Universidade de Aveiro Departamento de
2011 Electrónica, Telecomunicações e Informática

Miguel Vidal Drummond

Dispositivos fotónicos para processamento de sinais ópticos e de RF

Photonic devices for optical and RF signal processing

Universidade de Aveiro
2011

Departamento de
Electrónica, Telecomunicações e Informática

Miguel Vidal Drummond

Dispositivos fotónicos para processamento de sinais ópticos e de RF

Photonic devices for optical and RF signal processing

Dissertação apresentada à Universidade de Aveiro para cumprimento dos requisitos necessários à obtenção do grau de Doutor em Engenharia Electrotécnica, realizada sob a orientação científica do Doutor Paulo Miguel Nepomuceno Pereira Monteiro, Professor Associado do Departamento de Electrónica, Telecomunicações e Informática da Universidade de Aveiro, e do Doutor Rogério Nunes Nogueira, Investigador Auxiliar do Instituto de Telecomunicações.

Apoio financeiro da FCT e do FSE no âmbito do Programa Operacional Potencial Humano (POPH) do QREN.

o júri

presidente

Prof. Doutor José Carlos da Silva Neves
Professor Catedrático da Universidade de Aveiro

Prof. Doutor Paulo Miguel Nepomuceno Pereira Monteiro
Professor Associado da Universidade de Aveiro (orientador)

Prof. Doutor Rogério Nunes Nogueira
Investigador Auxiliar do Instituto de Telecomunicações (co-orientador)

Leif Katsuo Oxenløwe
Professor Catedrático da Danmarks Tekniske Universitet

Henrique Manuel de Castro Faria Salgado
Professor Associado da Faculdade de Engenharia da Universidade do Porto

Henrique José Almeida da Silva
Professor Associado da Faculdade de Ciências e Tecnologia da Universidade de Coimbra

agradecimentos/ acknowledgements

This journey has given me the pleasure and privilege of learning from people around the world. First of all, I would like to thank my supervisors, Prof. Dr. Paulo Monteiro and Prof. Dr. Rogério Nogueira, for their tireless support and friendship. Prof. Dr. Rogério Nogueira was always present in key moments to prompt me forward. I am deeply appreciated for his countless contributions, his candor, and for fostering my creativity.

I would like to thank all my colleagues and friends at Instituto de Telecomunicações and at the University of Aveiro for many fruitful discussions and pleasant times. I must mention Liliana Costa, João Prata, Daniel Albuquerque, Miguel Veiga, Jacklyn Reis, Carlos Marques, Diana Fidalgo, Nelson Muga, among others. I would like to thank to Prof. Dr. António Teixeira and Prof. Dr. Manuel Violas for their friendship and help.

I am very appreciated to Dr. Carola Sterner and Dr. Pierre-Yves Fonjallaz for having welcomed me at Acreo in Kista, Sweden. The fiber Bragg gratings produced there were fundamental in my very first work. I am also very appreciated to Dr. Satoshi Shinada and Dr. Naoya Wada for giving me the opportunity to work at National Institute of Information and Communications Technology, in Tokyo, Japan. I spent two unforgettable months there working on cutting-edge devices, and also having lots of fun with Dr. Benjamin Puttnam, Dr. Zsigmond Szilárd and Dr. Kazi Abedin.

I acknowledge Instituto de Telecomunicações and University of Aveiro for providing me fantastic working conditions. I also acknowledge Fundação para a Ciência e a Tecnologia for invaluable support in funding.

I would like to thank my lifelong friends Daniel Paulino, Pedro Monteiro, João Vitor and Carmen Martins. I would also like to thank my family, in particular my cousins Isabel and Carlos for very pleasant times. My last acknowledgment is for my parents, Duarte Esmeraldo and Maria Irene Vidal, and for Carina Pereira. You have always been there for me.

To all of you, *um grande abraço*!

palavras-chave

Comunicações ópticas, fotónica aplicada a sinais RF, interferómetro de Mach-Zehnder, filtragem óptica, processamento óptico não linear.

resumo

O presente trabalho tem por objectivo o estudo de novos dispositivos fotónicos aplicados a sistemas de comunicações por fibra óptica e a sistemas de processamento de sinais RF. Os dispositivos apresentados baseiam-se em processamento de sinal linear e não linear.

Dispositivos lineares ópticos tais como o interferómetro de Mach-Zehnder permitem adicionar sinais ópticos com pesos fixos ou sintonizáveis. Desta forma, este dispositivo pode ser usado respectivamente como um filtro óptico em amplitude com duas saídas complementares, ou, como um filtro óptico de resposta de fase sintonizável. O primeiro princípio de operação serve como base para um novo sistema fotónico de medição em tempo real da frequência de um sinal RF. O segundo princípio de operação é explorado num novo sistema fotónico de direccionamento do campo eléctrico radiado por um agregado de antenas, e também num novo compensador sintonizável de dispersão cromática.

O processamento de sinal é não linear quando sinais ópticos são atrasados e posteriormente misturados entre si, em vez de serem linearmente adicionados. Este princípio de operação está por detrás da mistura de um sinal eléctrico com um sinal óptico, que por sua vez é a base de um novo sistema fotónico de medição em tempo real da frequência de um sinal RF. A mistura de sinais ópticos em meios não lineares permite uma operação eficiente numa grande largura espectral. Tal operação é usada para realizar conversão de comprimento de onda sintonizável. Um sinal óptico com multiplexagem no domínio temporal de elevada largura de banda é misturado com duas bombas ópticas não moduladas com base em processos não lineares paramétricos num guia de ondas de niobato de lítio com inversão periódica da polarização dos domínios ferroeléctricos. Noutro trabalho, uma bomba pulsada em que cada pulso tem um comprimento de onda sintonizável serve como base a um novo conversor de sinal óptico com multiplexagem no domínio temporal para um sinal óptico com multiplexagem no comprimento de onda. A bomba é misturada com o sinal óptico de entrada através de um processo não linear paramétrico numa fibra óptica com parâmetro não linear elevado.

Todos os dispositivos fotónicos de processamento de sinal linear ou não linear propostos são experimentalmente validados. São também modelados teoricamente ou através de simulação, com a excepção dos que envolvem mistura de sinais ópticos. Uma análise qualitativa é suficiente nestes últimos dispositivos.

keywords

optical communications, microwave photonics, Mach-Zehnder interferometer, optical filtering, nonlinear optical processing.

abstract

This work investigates novel photonic devices for optical fiber communication systems and microwave photonics. Such devices rely on linear and nonlinear optical signal processing.

Basic linear optical devices such as the Mach-Zehnder delay interferometer enable delaying and adding optical signals with fixed or variable weights. Therefore, such device can be respectively used as an optical amplitude filter with two complementary optical outputs, or, as an optical phase filter with tunable group delay response. The first operation principle is explored in a novel instantaneous RF frequency measurement system, whereas the latter serves as basis to a novel photonic beamforming system for a phase array antenna, and also to a novel tunable optical dispersion compensator.

Nonlinear optical signal processing is obtained when optical signals are delayed and mixed, instead of being linearly added. Such operation principle is behind electro-optical mixing, which is explored in a novel instantaneous RF frequency measurement system. All-optical mixing enables ultra-fast and thereby broad bandwidth operation. This operation principle is explored to obtain tunable wavelength conversion. An optical time division multiplexed signal with a large spectral width is parametrically mixed with two continuous wave pumps in a periodically-poled lithium niobate waveguide. Instead of continuous wave pumps, a pulsed pump in which each pulse has a tunable wavelength enables a novel routable optical time-to-wavelength division converter. The pump signal is parametrically mixed with the input optical signal in a highly nonlinear optical fiber.

All the proposed linear and nonlinear optical signal processing devices are experimentally validated. In addition, theoretical modeling and simulations are presented in all concepts, with the exception of the ones which employ all-optical mixing. A qualitative analysis is sufficient for the latter devices.

"I've been waiting for you Obi-Wan.
We meet again at last. The circle is now complete.
When I left you I was but the learner. Now, I am the master!"
— Darth Vader, *in* Star Wars Ep. IV: A new hope

To my parents,
To Carina.

Contents

Main contributions

[J1] M. V. Drummond, P. P. Monteiro, and R. N. Nogueira. Photonic RF instantaneous frequency measurement system by means of a polarization-domain interferometer. *Optics Express*, 17(7):5433–5438, Mar. 2009.

[J2] M. V. Drummond, C. A. F. Marques, P. P. Monteiro, and R. N. Nogueira. Photonic instantaneous frequency measurement system using complementary modulation. *Photonics Technology Letters, IEEE*, 23(3): 143–145, Feb. 2011

[J3] M. V. Drummond, P. P. Monteiro, and R. N. Nogueira. Photonic true-time delay beamforming based on polarization-domain interferometers. *Journal of Lightwave Technology, IEEE/OSA*, 28(17):2492–2498, Sep. 2010.

[J4] M.V. Drummond, R.N. Nogueira, P. P. Monteiro, M.A. Violas, C. Sterner, and P.-Y. Fonjallaz. Tunable optical dispersion compensator based on power splitting between two dispersive media. *Journal of Lightwave Technology, IEEE/OSA*, 28(8):1164–1175, Apr. 2010.

[J5] M. V. Drummond, R. N. Nogueira, M.A. Violas, P. P. Monteiro, C. Sterner, and P.-Y. Fonjallaz. All-optical generation of 40 Gb/s single sideband signals using a fiber bragg grating. *Optics Communications*, 283(12):2492–2495, Jun. 2010.

[J6] M. V. Drummond, C. A. F. Marques, P. P. Monteiro, and R. N. Nogueira. Photonic instantaneous microwave frequency measurement system based on signal remodulation. *Photonics Technology Letters, IEEE*, 22(16):1226–1228, Aug. 2010.

[J7] M. V. Drummond, J. D. Reis, R. N. Nogueira, P. P. Monteiro, A. L. Teixeira, S. Shinada, N. Wada, and H. Ito. Error-free wavelength conversion at 160 Gbit/s in PPLN waveguide at room temperature. *Electronics Letters*, 45(22):1135–1137, Oct. 2009.

[J8] M. V. Drummond, A. L. Teixeira, P. P. Monteiro, and R. N. Nogueira. Flexible OTDM to WDM conversion based on a programmable optical processor. *Submitted to Optics Express.*

[C1] M. V. Drummond, P. P. Monteiro, and R. N. Nogueira. RF instantaneous frequency measurement system using a polarization-based interferometer. *Proc. OSA Optical Fiber Conf. (OFC)*, paper OTuE3, Mar. 2009, San Diego, United States.

[C2] M. V. Drummond, P. P. Monteiro, and R. N. Nogueira. Novel photonic RF instantaneous frequency measurement system using a HiBi fiber-based interferometer. *Proc. International Conf. on Transparent Networks (ICTON)*, paper Mo.D5.5, Jun. 2009, S. Miguel, Portugal.

[C3] M. V. Drummond, P. P. Monteiro, and R. N. Nogueira. Novel photonic RF instantaneous frequency measurement system using a HiBi fiber-based interferometer. *Proc. Conf. Telecommunications (ConfTele)*, paper 113, May 2009, Santa Maria da Feira, Portugal.

[C4] M. V. Drummond, P. P. Monteiro, and R. N. Nogueira. HiBi-fiber-based photonic RF instantaneous frequency measurement system. *Proc. Symposium on Enabling Optical Networks (SEON)*, Jun. 2009, Amadora, Portugal.

[C5] M. V. Drummond, C. A. F. Marques, P. P. Monteiro, and R. N. Nogueira. Photonic instantaneous RF frequency measurement system based on complementary E/O modulation *Proc. Opto-Electronics and Communications Conference (OECC)*, paper 6G2-2, Jul. 2011, Kaohsiung, Taiwan.

[C6] M. V. Drummond, C. A. F. Marques, P. P. Monteiro, and R. N. Nogueira. Photonic instantaneous RF frequency measurement system based on complementary modulation *Proc. EuroCon/ConfTele 2011*, Apr. 2011, Lisbon, Portugal.

[C7] M. V. Drummond, P. P. Monteiro, and R. N. Nogueira. Photonic true-time delay antenna beamformer based on a tunable polarization-domain interferometer 4^{th} *RadioNet Engineering Forum Workshop*, Sep. 2010, Amadora, Portugal.

[C8] M. V. Drummond, R. N. Nogueira, P. P. Monteiro, M. A. Violas, C. Sterner, and P.-Y. Fonjallaz. Novel opto-electrical tunable dispersion compensator for IM signals. *Proc. European Conf. on Optical Communications (ECOC)*, paper P3.05, Sep. 2010, Vienna, Austria.

[C9] M. V. Drummond, J. D. Reis, R. N. Nogueira, P. P. Monteiro, A. L. Teixeira, S. Shinada, N. Wada, and H. Ito. Wavelength conversion of a 160 Gbit/s RZ OTDM Signal in a PPLN waveguide at room temperature. *International Conf. on Photonics in Switching (PiS)*, post-deadline paper, Sep. 2009, Pisa, Italy.

[C10] M. V. Drummond, J. D. Reis, R. N. Nogueira, P. P. Monteiro, A. L. Teixeira, S. Shinada, N. Wada, and H. Ito. Wavelength conversion of a 160 Gbit/s RZ OTDM Signal in a PPLN waveguide at room temperature. *Proc. OSA Nonlinear Photonics (NP) Topical Meeting*, paper NMB3, Jun. 2010, Karlsruhe, Germany.

[C11] M. V. Drummond, A. L. Teixeira, P. P. Monteiro, and R. N. Nogueira. Tunable OTDM to WDM conversion based on a Programmable Optical Filter. *Proc. Opto-Electronics and Communications Conference (OECC)*, paper 8D1-2, Jul. 2011, Kaohsiung, Taiwan.

[C12] M. V. Drummond, A. L. Teixeira, P. P. Monteiro, and R. N. Nogueira. Routable OTDM to WDM converter based on a programmable optical processor. *Proc. European Conf. on Optical Communications (ECOC)*, paper We.10.P1.58, Sep. 2011, Geneva, Switzerland.

[C13] M. V. Drummond, R. N. Nogueira, and P. P. Monteiro. All-optical processing for future optical communication networks. *in Proc. Cranfield Multi-Strand Conference (CMC)*, May 2008, Cranfield, United Kingdom.

[C14] R. N. Nogueira, M. V. Drummond, M.A. Violas, and M. P. P. Monteiro. Tunable passive compensating devices for high bit rate optical systems. *Proc. International Conf. on Transparent Networks (ICTON)*, paper Th.B1.2, Jun. 2008, Athens, Greece.

[C15] R. N. Nogueira, M. V. Drummond, C. A. F. Marques, A. Albuquerque, R. Monteiro, A. Navarro, and A. L. Teixeira, P. S. André, M. A. Violas, P. P. Monteiro, C. Sterner, and P.-Y. Fonjallaz. All-optical signal processing techniques with fiber based devices, *Proc. International Conf. on Transparent Networks (ICTON)*, paper Tu.D2.1, Jun. 2009, S. Miguel, Portugal.

[C16] R. N. Nogueira, M. V. Drummond, C. A. F. Marques, R. Monteiro, A. Albuquerque, A. L. Teixeira, P. S. André, and R. F. Rocha. Advanced applications of fiber Bragg gratings for telecom systems. *Proc. Progress in Electromagnetics Research Symposium (PIERS)*, Aug. 2009, Moscow, Russia.

[W1] M. V. Drummond, P. P. Monteiro, and R. N. Nogueira. Photonic RF instantaneous frequency measurement system by means of a polarization polarization domain interferometer. *presented at the IEEE-MTT International Microwave Symposium (IMS)*, May 2010, Anaheim, United States.

[BC1] M. V. Drummond, C. A. F. Marques, P. P. Monteiro, and R. N. Nogueira. Optical Network Analyser for characterization of optical devices. *Book chapter to appear in the EURO-FOS scientific handbook of experimental fiber-optic systems for telecommunications.*

[P1] R. N. Nogueira, M. A. Violas, and M. V. Drummond. Filtro óptico com resposta sintonizável de forma contínua baseado na combinação de diferentes filtros ópticos. *PT104237*, Oct. 2008.

[P2] M. V. Drummond and R. N. Nogueira. Phased array antenna beamforming system and method based on optical Mach-Zehnder delay interferometers. *World patent pending.*

[P3] M. V. Drummond and R. N. Nogueira. Instantaneous frequency measurement system based on complementary electro-optic modulation. *World patent pending.*

List of Acronyms

ACF	amplitude comparison function	10
AE	antenna element	23
AF	array factor	25
ASE	amplified spontaneous emission	2
BER	bit error rate	39
CD	chromatic dispersion	2
COF	complementary optical filter	10
CR	contrast ratio	59
CW	continuous wave	9
DCF	dispersion compensating fiber	30
DC	direct current	48
DE	dual electrode	4
DFG	difference-frequency generation	44
DGD	differential group delay	13
DO	dual output	4
DPSK	differential phase shift keying	15
DSB	double sideband	31
DSP	digital signal processor	30
E/O	electrical to optical	9
EAM	electro-absorption modulator	49
EDFA	erbium-doped fiber amplifier	55
EDL	electrical delay line	15
EMI	electromagnetic interference	25
EOP	eye opening penalty	33
ER	extinction ratio	14
FBG	fiber Bragg grating	17
FWHM	full width at half maximum	58
FWM	four-wave mixing	2

PM	polarization maintaining	11
POF	programmable optical filter	58
PPLN	periodically poled lithium niobate	2
PS	phase shifter	17
QPM	quasi-phase-matching	46
RF	radio frequency	3
RLCM	reference-lobe comparison method	51
SFG	sum-frequency generation	44
SHG	second-harmonic generation	44
SOA	semiconductor optical amplifier	2
SOP	state-of-polarization	11
SPM	self-phase modulation	2
SPT	sampling pulse train	43
SP	sampling pulse	58
SSB	single sideband	32
SSMF	standard single mode fiber	32
SSOF	sideband suppression optical filter	33
SSR	sideband suppression ratio	33
TCR	tunable coupling ratio	4
TEDC	tunable electrical dispersion compensation	30
TEDL	tunable electrical delay line	17
TODC	tunable optical dispersion compensator	4
TODL	tunable optical delay line	21
TTD	true time delay	25
VOA	variable optical attenuator	17
WDM	wavelength-division multiplexing	1
XPM	cross-phase modulation	2
cSFG-DFG	cascaded sum-frequency generation with difference-frequency generation	43

List of Figures

Chapter 1

Introduction

A great deal of our daily routine involves communicating and sharing information with others. Thanks to the enormous advances made in telecommunications, we can seamlessly access to virtually any point of the globe. We now have multiple digital communication tools such as voice calls, text messaging, email, photo and video sharing, social networks and blogs. All these services generate huge amounts of data, which must be carried around the globe. The data is carried in networks, which basically aggregate the data originated from a given location, transport the aggregated data in pipelines, and disaggregate the data at the destination. Such data pipelines are generally optical fiber communication systems, which are nowadays unarguably the best solution to handle such enormous amounts of data traffic.

1.1 Optical fiber communication systems

Optical fiber communication systems generally convert the information of input electrical signals to the optical domain, transmit the resulting optical signals, and reconvert the received optical signals back to the electrical domain. This is depicted in Fig. 1.1. The information of the input data signals can be modulated in the three dimensions of light – amplitude (or intensity), phase and polarization. The phase (or frequency/wavelength) dimension can be firstly explored to distribute the information by various channels, which may or may not differ in wavelength. When the optical channels have different wavelengths, different portions of the input information data modulate different input optical carriers (OCs). The output optical signals of the transmitters are multiplexed in the wavelength domain, originating wavelength-division multiplexing (WDM) [1]. A WDM transmitter is depicted in Fig. 1.1. When the optical channels share the same wavelength, different portions of the input information data occupy different time slots. This results in optical time-domain multiplexing (OTDM) [2], also depicted in Fig. 1.1. An optical clock source generates short optical pulses at a repetition rate of $\frac{1}{N\tau_p}$. N copies of the optical clock signal are modulated by different transmitters. The output optical signal of the k^{th} transmitter is delayed by $k\tau_p$, and combined with the other output optical signals. The resulting OTDM signal has N tributaries, in which each tributary has a symbol rate of $\frac{1}{N\tau_p}$. The symbol rate of the OTDM signal is therefore of $1/\tau_p$. The input information can be hybridly mapped in time and frequency, as in orthogonal frequency division multiplexing (OFDM) [3]. WDM, OTDM and OFDM are multiplexing schemes, which define how information is distributed by channels or tributaries. The modulation format defines how the three dimensions of light of each channel or tributary are modulated by the input

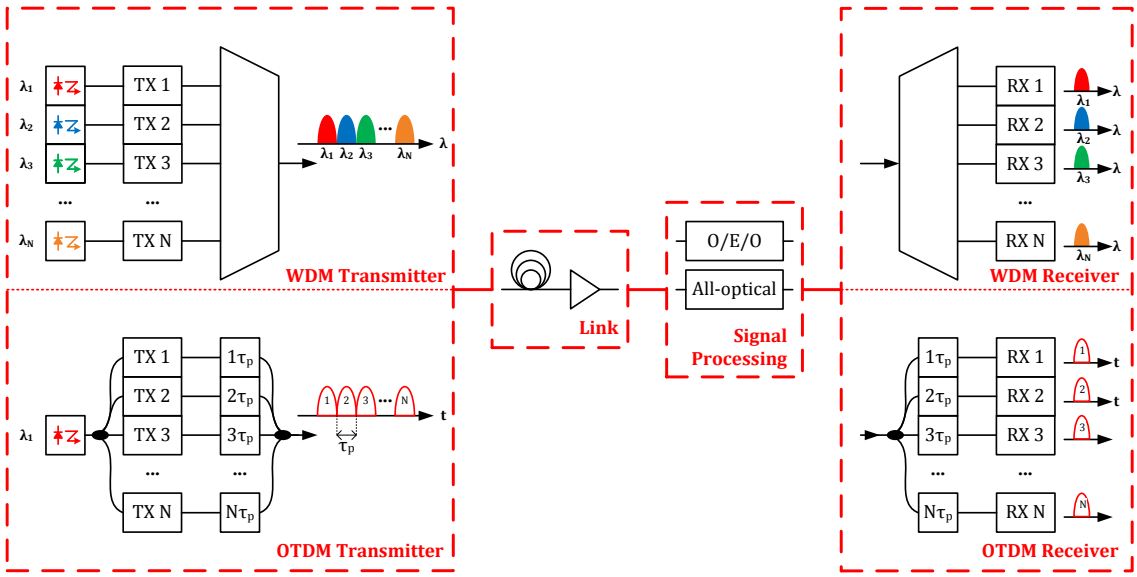

Figure 1.1: General scheme of an optical fiber communication system using wavelength or time-domain multiplexing.

information data [4]. Different modulation formats may therefore require different transmitter architectures.

The multiplexed optical signals are transmitted through a link, which is generally composed by spans of optical fiber interleaved by optical amplifiers [1]. Optical fibers impair the propagating optical signals with linear and nonlinear effects. Linear effects include loss, chromatic dispersion (CD) and polarization-mode dispersion (PMD). Nonlinear effects are stimulated light scattering and nonlinear phase modulation. The latter effect is highly deleterious in high bit rate transmission over long links, as channels are impaired by self-phase modulation (SPM), cross-phase modulation (XPM) and four-wave mixing (FWM). Optical amplifiers add amplified spontaneous emission (ASE) noise to the optical signals, reducing their optical signal-to-noise ratio (OSNR).

Before being detected at the receiver, the optical signals can be processed all-optically or in the electrical domain. The latter option requires optical to electrical to optical (O/E/O) conversion. In this case, electrical signal processing is usually employed to regenerate the detected optical signals after having propagated a significant link length. All-optical signal processing can perform different functions such as switching, regeneration, modulation, format conversion, compensation of CD or PMD, and add/drop multiplexing [5, 6]. All-optical signal processors are generally based on optical filters (passive devices) and nonlinear effects in highly nonlinear media such as highly nonlinear fibers (HNLFs) [J8], semiconductor optical amplifiers (SOAs) [7] and periodically poled lithium niobate (PPLN) waveguides [J7] (active devices).

At the receiver, the WDM channels are passively separated using a WDM demultiplexer. Each WDM channel is converted to the electrical domain after detection. Depending on the modulation format, direct detection or coherent detection can be employed. Coherent detection does not require WDM demultiplexing, as the WDM channel to be detected can be selected by tuning the wavelength of the local oscillator [1]. In addition, coherent detection

enables an efficient compensation of transmission impairments by means of digital signal processing. In OTDM, the separation of a given tributary requires active processing, such as electro-optical [8] or all-optical gating [J7]. Depending on the modulation format of each tributary, direct, differential or coherent detection can be employed.

Optical fiber communication systems are currently at the fifth generation. The transition to a new generation has been marked by breakthroughs, which have enabled a significant increase of the system's capacity. The breakthroughs were the introduction of single mode fiber, low-loss operation at 1550 nm, optical amplification and WDM [1]. A further capacity increase is expected to be based on novel optical fibers, less noisier optical amplifiers, and advanced modulation formats enabled by coherent detection and digital signal processing.

1.2 Microwave photonics

The unique advantages of photonic technologies such as broad bandwidth, low loss and immunity to electromagnetic interference have spurred the development of optical fiber communication systems, which deal with digital signals. Such unique advantages have been also explored to generate, process, control and transmit microwave[1] signals. Microwave photonics is an interdisciplinary area that studies the interaction between microwave and optical signals, and therefore investigates photonic techniques to perform RF signal processing [9]. Microwave photonics can be applied to broadband wireless access networks, sensors, radar systems, satellite communications, instrumentation and warfare systems. The topics covered by microwave photonics techniques generally include photonic generation of RF signals, photonic processing of RF signals, photonic beamforming of phased array antenna (PAA), radio-over-fiber systems and photonic analog-to-digital conversion [9]. Microwave photonics techniques and devices are comprehensively reviewed in [9, 10], respectively.

Contrarily to fiber optical communication systems, the implementation and commercialization of microwave photonics devices and systems has not been so successful. In comparison with coaxial cables, optical fibers have a much higher capacity and also much lower losses. Such impressive advantages enabled transmitting huge volumes of data by fiber optical communication systems, thereby turning coaxial cable based communication systems obsolete. Microwave photonics systems and particularly devices currently do not offer such distinguishable advantages relatively to their electrical counterparts. Without cost-effective integration of optical components, microwave photonics systems are costly and bulky [9]. It is therefore expected that advances in silicon photonics should enable the deployment of microwave photonics systems and devices.

1.3 Motivation and outline

The motivation for this thesis was to investigate novel devices for optical fiber communication systems and microwave photonics based on linear and nonlinear optical signal processing. The basic operation principle behind all the proposed concepts was to individually delay optical signals with different weights, and to add or mix them thereafter. Experimental work was carried out with the purpose of validating all concepts. Theoretical modeling and simulations were also performed whenever possible or useful. This was the case of linear optical signal processing systems.

[1] In the remainder of this text the terms microwave and radio frequency (RF) are used interchangeably.

The introductory part of the thesis provides a brief background about the areas of optical fiber communication systems and microwave photonics, to which all the work performed for this thesis belongs. Chapters 2 and 3 discuss photonic devices based on linear optical signal processing. More specifically, the photonic devices addressed in chapters 2 and 3 rely on Mach-Zehnder delay interferometers (MZDIs) without and with tunable coupling ratio (TCR), respectively. Nonlinear optical signal processing devices are discussed in chapter 4. Such devices explore electro-optical and all-optical signal mixing. The last chapter presents the final conclusion and an outlook on future projects originated from the work done for this thesis.

As detailed in the following section, all the concepts discussed in this thesis were either published or submitted to prestigious scientific journals of the present research areas [J1]–[J8], and also presented in international conferences [C1]–[C12]. This thesis was therefore written as a comprehensive complement to the published journal papers, which contain most of the information. Consequently, chapters 2 to 4 begin with an introduction to the basic operation principles. The operation principle and state-of-the-art related with each proposed device are presented and referenced at the beginning of each section. The remaining part of each section is devoted to the proposed implementation.

1.4 Contributions

The contributions described in this work are novel applications that rely on the operation principles by which the structure of this thesis is organized. Linear optical signal processing based on the MZDI without TCR, as explained in chapter 2, serves as basis to the following contributions:

- A novel instantaneous frequency measurement system (IFMS) based on a MZDI with two outputs. A journal paper [J1], four conferences papers [C1, C2, C3, C4] and a workshop [W1] were written on this topic.

- A new IFMS based on a dual electrode (DE) dual output (DO) Mach-Zehnder modulator (MZM), which does not require complementary optical filtering. A journal paper [J2], two conferences papers [C5, C6] and a patent [P3] were written on this topic.

Linear optical signal processing based on the Mach-Zehnder delay interferometer with tunable coupling ratio (MZDI-TCR), as explained in chapter 3, serves as basis to the following contributions:

- A novel photonic beamforming system for a PAA which uses a single piece of polarization maintaining fiber (PMF). A journal paper [J3], a conference paper [C7] and a patent [P2] were written on this topic.

- A novel tunable optical dispersion compensator (TODC) with a fast tuning response. Two journal papers [J4, J5], a conference paper [C8] and a patent [P1] were written on this topic.

Nonlinear optical signal processing, which as explained in chapter 4 consists in delaying and mixing optical signals by electro-optic or all optical means, serves as basis to the following contributions:

- A novel IFMS based on electro-optical signal remodulation. A journal paper [J6] was written on this topic.
- Tunable wavelength conversion of a 160 Gb/s OTDM signal in a PPLN waveguide at room temperature. A journal paper [J7], and a regular [C10] and post-deadline [C9] conference papers were written on this topic.
- A novel OTDM to WDM converter enabling wavelength tunability of the converted signals, flexible OTDM tributary to WDM channel mapping, and modulation format transparency. A journal paper [J8] and two conference papers [C11, C12] were written on this topic.

The remaining conference papers [C13]–[C16] do not focus exclusively on the operation principles covered in this theses. In addition to these contributions, a book chapter [BC1] was written within the frame of the EURO-FOS Network of Excellence. All contributions are referenced at pages iii–v. With the permission of the involved publication editors the content of all journal papers is found at the appendix A.

Chapter 2

Photonic devices based on a Mach-Zehnder delay interferometer

This chapter is devoted to photonic devices whose operation principle relies on a MZDI. A theoretical description of a MZDI is presented in the first section. Two IFMSs based on two different implementations of a MZDI are assessed in section 2.2. Section 2.3 states the conclusions drawn from both implementations.

2.1 Operation principle of a Mach-Zehnder delay interferometer

The scheme of a MZDI is shown in Fig. 2.1. A MZDI is composed by an input optical coupler, two optical delay lines (ODLs) and an output optical coupler. The ODLs of the upper and lower arm have a transfer function given by $\tau_1(f)$ and $\tau_2(f)$, respectively. The MZDI has two input ports and two output ports. The transfer function of the MZDI is given by the product of the transfer matrices of the input coupler, delay lines and output coupler,

$$\begin{bmatrix} O_1(f) \\ O_2(f) \end{bmatrix} = \frac{1}{\sqrt{2}} \begin{bmatrix} 1 & j \\ j & 1 \end{bmatrix} \cdot \begin{bmatrix} \tau_1(f) & 0 \\ 0 & \tau_2(f) \end{bmatrix} \cdot \frac{1}{\sqrt{2}} \begin{bmatrix} 1 & j \\ j & 1 \end{bmatrix} \cdot \begin{bmatrix} E_1(f) \\ E_2(f) \end{bmatrix}$$
$$\begin{bmatrix} O_1(f) \\ O_2(f) \end{bmatrix} = \frac{1}{2} \begin{bmatrix} \tau_1(f) - \tau_2(f) & j(\tau_1(f) + \tau_2(f)) \\ j(\tau_1(f) + \tau_2(f)) & \tau_2(f) - \tau_1(f) \end{bmatrix} \cdot \begin{bmatrix} E_1(f) \\ E_2(f) \end{bmatrix}, \tag{2.1}$$

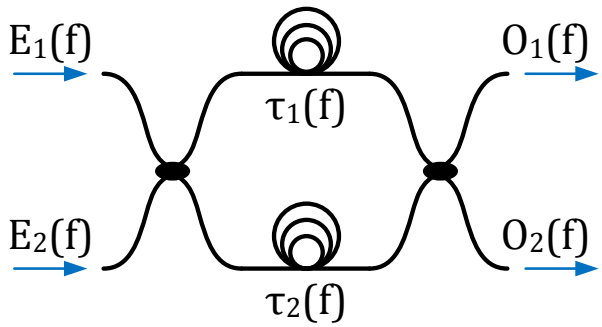

Figure 2.1: Scheme of a Mach-Zehnder delay interferometer.

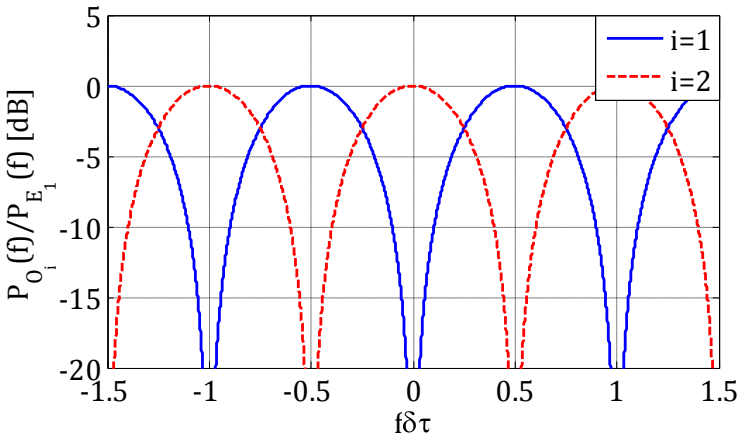

Figure 2.2: Amplitude response of the two outputs of a MZDI.

where $O_1(f)$ and $O_2(f)$ are the electrical fields of the output optical signals, and $E_1(f)$ and $E_2(f)$ are the electrical fields of the input optical signals.

Let us consider only one input optical signal, i.e., $E_2(f) = 0$. Let us also consider ideal ODLs, given by $\tau_i(f) = \exp\{-j2\pi f\tau_i\}$, $i = 1, 2$. Equation (2.1) can be written as

$$\begin{bmatrix} O_1(f) \\ O_2(f) \end{bmatrix} = \frac{1}{2} \begin{bmatrix} \exp\{-j2\pi f\tau_1\} - \exp\{-j2\pi f\tau_2\} \\ j(\exp\{-j2\pi f\tau_1\} + \exp\{-j2\pi f\tau_2\}) \end{bmatrix} \cdot E_1(f). \tag{2.2}$$

The optical power and phase of the output optical signals are given by

$$\begin{bmatrix} P_{O_1}(f) \\ P_{O_2}(f) \end{bmatrix} = \frac{1}{2} \begin{bmatrix} 1 - \cos(2\pi f\delta\tau) \\ 1 + \cos(2\pi f\delta\tau) \end{bmatrix} \cdot P_{E_1}(f) \tag{2.3}$$

$$\begin{bmatrix} \Phi_{O_1}(f) \\ \Phi_{O_2}(f) \end{bmatrix} = -\frac{1}{2} \begin{bmatrix} 2\pi f\frac{\tau_1+\tau_2}{2} \\ 2\pi f\frac{\tau_1+\tau_2}{2} \end{bmatrix} + \Phi_{E_1}(f), \tag{2.4}$$

where $P_{O_1}(f)$ and $P_{O_2}(f)$ are the powers of the output optical signals, $P_{E_1}(f)$ is the power of the input optical signal, $\delta\tau = \tau_1 - \tau_2$, $\Phi_{O_1}(f)$ and $\Phi_{O_2}(f)$ are the phases of the output optical signals and $\Phi_{E_1}(f)$ is the phase of the input optical signal. Equation (2.4) shows that the MZDI has a linear phase response to which corresponds a constant group delay of $\frac{\tau_1+\tau_2}{2}$. The amplitude response of both MZDI outputs are shown in Fig. 2.2. The amplitude responses have a periodical variation with a period of $1/\delta\tau$, and each period has a -3 dB bandwidth of $\frac{1}{2\delta\tau}$. At the maxima, the optical signals at the output of the ODLs interfere constructively. At the minima, such interference is destructive. As the MZDI is a lossless device one has $P_{O_1}(f) + P_{O_2}(f) = P_{E_1}(f)$. Hence, for frequencies where $P_{O_1}(f)$ is maximum, $P_{O_2}(f)$ is minimum. Furthermore, the variation of P_{O_1} with the frequency is opposite to the variation of P_{O_2}.

2.2 Instantaneous frequency measurement system

The purpose of an IFMS is to measure the frequency of an input RF signal in real-time. Several IFMSs based on different microwave photonic techniques have been investigated. As nicely reviewed in the introduction of [11], IFMSs can be divided in two categories. In the

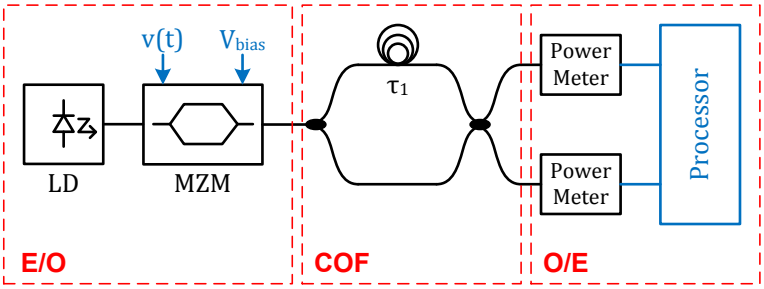

Figure 2.3: Basic scheme of the proposed IFMSs.

first category the input RF signal is allowed to have multiple RF frequencies, as the frequency measurement is performed by means of an optical channelizer. In the second category only one RF frequency is allowed. In both categories the frequency measurement is generally obtained by RF frequency to power mapping. For instance, the average power of an optical signal is proportional to the RF frequency, or the power of an optical signal at a given instant is proportional to the power of a given RF frequency. The techniques presented in this section belong to the second category, and rely on RF frequency to average optical power mapping.

The basic scheme of the proposed IFMSs is shown in Fig. 2.3. The operation of the photonic IFMS is divided in three stages: electrical to optical (E/O) conversion, complementary optical filtering and optical to electrical (O/E) conversion. E/O conversion is achieved using a laser diode (LD) and a MZM.

The optical signal at the output of the MZM can be given by

$$E_{\mathrm{MZM}}(t) = \frac{1}{2}\left[1 + \exp\left(j\frac{\pi}{V_\pi}(v(t) + V_{\mathrm{bias}})\right)\right] \cdot E_{\mathrm{LD}}(t), \tag{2.5}$$

where V_π is the switching voltage of the modulator, $v(t)$ is the input RF signal, V_{bias} is the bias voltage applied to the modulator and $E_{\mathrm{LD}}(t)$ is the electrical field of the optical continuous wave (CW) signal generated by the LD. The input RF signal is given by $v(t) = V_{\mathrm{RF}}\sin(\omega_{\mathrm{RF}}t)$, where $\omega_{\mathrm{RF}} = 2\pi f_{\mathrm{RF}}$ is the RF angular frequency, and f_{RF} is the RF frequency. In order to obtain optical carrier suppression (OCS) the bias voltage is set to $V_{\mathrm{bias}} = V_\pi$. Considering the Jacobi-Anger expansion, (2.5) can be written as

$$E_{\mathrm{MZM}}(t) = \frac{1}{2}\left[1 - J_0(z) - 2\sum_{n=1}^{+\infty} j^n J_n(z)\cos(n\omega_{\mathrm{RF}}t)\right] \cdot E_{\mathrm{LD}}(t), \tag{2.6}$$

where $J_n(z)$ is a Bessel function of the first kind, and $z = \frac{\pi}{V_\pi}V_{\mathrm{RF}}$ is the modulation index. For low modulation indexes (2.6) can be approximated in the following way,

$$E_{\mathrm{MZM}}(t) \approx \frac{1}{2}\left[-2jJ_1(z)\cos(\omega_{\mathrm{RF}}t)\right] \cdot E_{\mathrm{LD}}(t). \tag{2.7}$$

Let us consider an ideal LD, i.e., $E_{\mathrm{LD}}(t) = E_{\mathrm{LD}}\exp(j\omega_o t)$, where $\omega_o = 2\pi f_o$ is the angular frequency of the OC, and f_o is the respective frequency. Using the Fourier transform, (2.7) can be written in the frequency domain

$$E_{\mathrm{MZM}}(f) \approx -\frac{j}{2}J_1(z)E_{\mathrm{LD}}\left\{\delta(f - (f_o - f_{\mathrm{RF}})) + \delta(f - (f_o + f_{\mathrm{RF}}))\right\}. \tag{2.8}$$

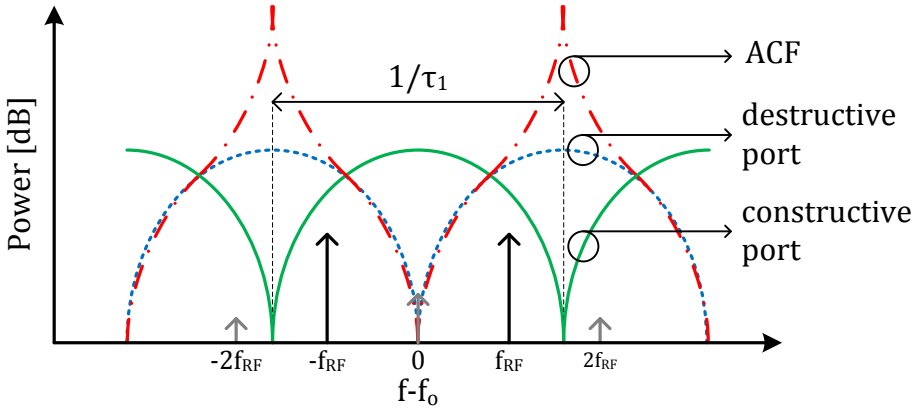

Figure 2.4: Amplitude responses of the MZDI and spectral lines of the MZM's output optical signal. ACF – amplitude comparison function.

The following stage comprises a MZDI where it is considered $\tau_2 = 0$. The transfer function and amplitude responses of the MZDI were derived in the previous section, and are given by (2.2) and (2.3). The outputs of the MZDI provide a complementary optical filter (COF) pair. Such complementarity results from the opposite frequency dependence of the MZDI's output optical powers. Figure 2.4 depicts the amplitude responses of the COF pair and the spectrum of the MZM's output optical signal. The OC frequency is set at a maximum of one amplitude response (green solid line) and consequently at a minimum of the other amplitude response (blue dashed line). The output port associated with the first amplitude response is designated by constructive port, whereas the other output port is designated by destructive port. According to (2.8), the spectrum of the RF signal consists in two lines located at frequencies $f_o \pm f_{\mathrm{RF}}$. These lines are filtered by the COF pair according to (2.3),

$$\begin{bmatrix} P_D(f) \\ P_C(f) \end{bmatrix} = \frac{1}{2} \begin{bmatrix} 1 - \cos(2\pi f \tau_1) \\ 1 + \cos(2\pi f \tau_1) \end{bmatrix} \cdot P_{\mathrm{MZM}}(f), \tag{2.9}$$

where $P_D(f)$ and $P_C(f)$ are the powers of optical signals at the output of the destructive and constructive ports, respectively. $P_{\mathrm{MZM}}(f)$ is the power of MZM's output optical signal. Equations (2.9) and (2.8) show that $P_D(f)$ and $P_C(f)$ depend not only on the RF frequency, but also on the modulation index and power of the optical source. Therefore, the calculation of the RF frequency from $P_D(f)$ or $P_C(f)$ would have to take into account the modulation index and power of the optical source.

The advantage of having two optical powers with a complimentary dependence on the RF frequency is that a function only dependent on the RF frequency can be defined. Such function is designated by amplitude comparison function (ACF), and is given by

$$\mathrm{ACF}(f) = \frac{P_D(f)}{P_C(f)} = \frac{1 - \cos(2\pi f \tau_1)}{1 + \cos(2\pi f \tau_1)} = \tan^2(\pi f \tau_1). \tag{2.10}$$

The RF frequency can be obtained by inverting the ACF,

$$f_{\mathrm{RF}} = \frac{1}{\pi \tau_1} \tan^{-1}(\sqrt{\mathrm{ACF}}). \tag{2.11}$$

The purpose of the third stage is therefore to measure the average power of $P_D(f)$ and $P_C(f)$ using two power meters. The RF frequency is derived from the ACF using a processor.

Figure 2.4 and (2.10) show that the RF frequency can be measured without ambiguity over a frequency range of $\frac{1}{2\tau_1}$. The increase of the measurement range results in a decrease of the slope of the ACF, whose units are dB/GHz. Therefore there is a trade-off between measurement range and sensitivity, where the sensitivity is also given in dB/GHz. The derivation of (2.7) until (2.11) considers low modulation indexes. For high modulation indexes the OCS of the modulated signal is reduced. This is not very important as the power of the RF carriers also increases with the modulation index. Other important detail is that the series in (2.6) cannot be approximated to its first term. Therefore the power of the spectral lines at harmonics $f_o \pm k \cdot f_{\mathrm{RF}}$, $k = 1, 2, ...$ can no longer be neglected. Both cases are illustrated in Fig. 2.4. If the modulation index and the power of the LD are known, a precise simulation of the ACF can be performed. This enables obtaining a precise calculation of the RF frequency for an arbitrary modulation index.

2.2.1 System implementation

The first work reporting an IFMS based on two complementary optical powers does not employ a MZDI with two outputs [12]. IN that work, the RF signal modulates two OCs with different wavelengths. An optical filter with a sinusoidal amplitude response and a single output is used. One OC is centered at a maximum of the filter's amplitude response, whereas the other OC is centered at a minimum. In this way, the OCs are subject to complementary optical filtering. After the optical filter, the OCs are separated using an optical demultiplexer. The average power of the OCs is measured resorting to two optical power meters. This technique has the advantage of requiring a single output optical filter. However, it requires two LDs along with an optical multiplexer and a demultiplexer. Furthermore, the frequency measurement is not independent of the optical powers, as the optical powers of the two LDs are uncorrelated. As shown in the previous sections, such disadvantages can be easily solved using a MZDI.

A important part of the proposed system shown in Fig. 2.3 can be implemented resorting to commercially available discrete fiber-based components. The LD, MZM and power meters are off-the-shelf components. However, there are many different ways of implementing a MZDI. All-optical implementations of a MZDI may resort to free-space optics, discrete fiber-based components, all-fiber devices or integrated optics. A free-space optics implementation is not considered in this work since it does not offer significant advantages over a fiber-based implementation. The MZDI can be implemented using discrete fiber-based components such as an input 3-dB optical coupler, two patch-cords and an output 3-dB optical coupler. Such a straightforward implementation presents three challenges. First, the optical signals at the inputs of the output 3-dB optical coupler must have the same state-of-polarization (SOP) so that the two optical signals may be coherently added instead of being combined in orthogonal polarizations. Secondly, the power of the optical signals at the inputs of the output 3-dB optical coupler should be exactly the same, as assumed in (2.1). Thirdly, the phase deviations experienced by the optical signals propagating through the patch-cords must be equal.

The first issue can be easily taken care of using polarization maintaining (PM) components. As for the second challenge, the power of the optical signals at the input of the output 3-dB optical coupler can be tuned using one optical coupler with tunable coupling ratio. The third

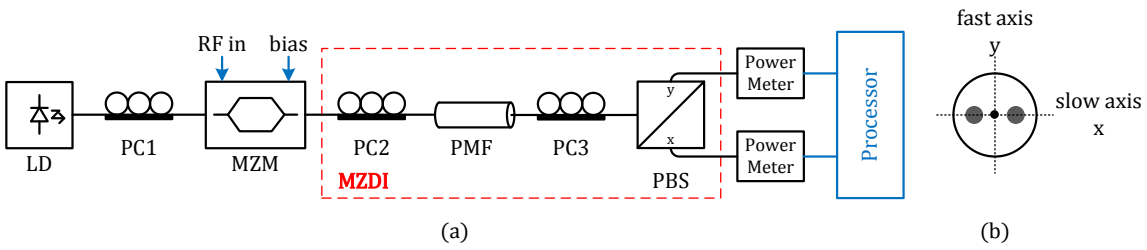

Figure 2.5: (a) Scheme of the IFMS based on a PMF. (b) cross-section of a PANDA PMF.

challenge can be modeled on (2.3),

$$\begin{bmatrix} P_{O_1}(f) \\ P_{O_2}(f) \end{bmatrix} = \frac{1}{2} \begin{bmatrix} 1 - \cos\left(2\pi(f + \Psi(f))\delta\tau\right) \\ 1 + \cos\left(2\pi(f + \Psi(f))t\delta\tau\right) \end{bmatrix} \cdot P_{E_1}(f), \tag{2.12}$$

where $\Psi(f) = \mathscr{F}\{\psi(t)\}$, and $\mathscr{F}$ represents the Fourier transform. $\psi(t)$ represents the difference between the phase deviations experienced by the optical signal propagating through a patch-cord with respect to the other. As shown in Fig. 2.4 the amplitude responses of the MZDI should be precisely centered with the OC. Therefore, it is required that $\psi(t) = 0$. In practice, this means that mechanical and thermal variations experienced by both patch-cords should affect the optical signals propagating by them in the same way. This is quite difficult to achieve using discrete fiber-based components. A simple way to achieve this is by placing all the components closely together. Hence, one should consider a system implementation based on all-fiber devices or integrated optics.

2.2.1.1 Implementation on the polarization domain [papers J1, C1–C4]

An IFMS based on all-fiber devices was proposed in [J1, C1, C2, C3, C4]. The system setup is shown in Fig. 2.5 (a). The key component of the MZDI is a PMF. A single-mode optical fiber supports two orthogonally polarized light propagation modes, which propagate on two orthogonal polarization axes. The structure of a PMF is designed to allow that a linearly polarized optical signal propagating on one of the polarization axes maintains its SOP unchanged from the beginning of the fiber to its end. Figure 2.5 (b) depicts the cross-section of a Polarization-maintaining AND Attenuation-reducing (PANDA) PMF. Such name was inspired on the similarities between the cross section of the fiber and the face of a panda bear. Near the fiber's core there are two rods made from a material which can be the same as the core or a different one. As a result, the polarization axes are aligned with the rods as depicted in the figure. The mode which propagates on the same plane of the rods has a lower group velocity in comparison to the orthogonal mode. This is the reason why the axis coincident with the plane of the rods is designated by slow axis, whereas the other one is the fast axis. The difference between the group velocity of the two orthogonally polarized modes is caused by birefringence, defined as

$$B = n_x - n_y, \tag{2.13}$$

where n_x and n_y are the refractive indices of the slow and fast axes, respectively. The group velocities of the optical signals which propagate on the slow and fast axes are given by,

$$v_{x,y} = \frac{c}{n_{x,y}}, \tag{2.14}$$

where c is the speed of light in vacuum. The differential group delay (DGD) between the two orthogonally polarized modes is given by

$$\text{DGD} = t_x - t_y = \frac{n_x}{c}L - \frac{n_y}{c}L = \frac{BL}{c}, \tag{2.15}$$

where t_x and t_y are the propagation times of an optical signal with a SOP aligned at the slow and fast axes. L is the length of the fiber. The two polarization axes of the PMF provide the two ODLs which compose the MZDI. Therefore, the length of the PMF should be chosen in order to obtain

$$\text{DGD} = \tau_1 - \tau_2. \tag{2.16}$$

The MZDI depicted in Fig. 2.5 is composed by two polarization controllers (PCs), a PMF and a polarization beam splitter (PBS). The PCs are tunable all-fiber devices which allow transforming the SOP of its input optical signal to any given SOP. PC2 is the input optical coupler. Its function is to align the linearly polarized output optical signal of the MZM at 45° relatively to the slow axis of the PMF. In this way, at the output of the PMF there are two orthogonally polarized signals with the same average optical power and with a DGD given by (2.16). The output optical coupler consists of PC3 and the PBS. The PBS separates the x and y polarization components of its input optical signal, sending them to two output ports. The function of the PC3 is to align the slow axis of the PMF at 45° relatively to the x axis of the PBS. Under these conditions, the proposed MZDI is mathematically modeled by (2.2).

In [J1], a comprehensive mathematical model of the proposed MZDI was presented. PC2 and PC3 provide a tunable coupling ratio to the input and output optical couplers. Such tunable coupling ratios are related with the polarization rotation angles imposed by the PCs in the following way,

$$\begin{bmatrix} O_1(f) \\ O_2(f) \end{bmatrix} = \frac{1}{2}\begin{bmatrix} \cos(\theta_1)\cos(\theta_2)\exp\{-j2\pi f\tau_1\} - \sin(\theta_1)\sin(\theta_2) \\ j(\cos(\theta_1)\sin(\theta_2)\exp\{-j2\pi f\tau_1\} - \sin(\theta_1)\cos(\theta_2)) \end{bmatrix} \cdot E_1(f), \tag{2.17}$$

where θ_1 and θ_2 are the polarization rotation angles imposed by PC2 and PC3. It was considered $\tau_2 = 0$, and therefore DGD $= \tau_1$. As mentioned in the previous paragraph, one should have $\theta_1 = \theta_2 = 45°$. As a result, (2.17) equals (2.2). Figure 2.4 shows that the ACF has a very steep variation at the maxima and minima of the amplitude responses. Such a steep variation results from the also steep variation of the amplitude responses at their minima. The optical power at the minima is zero only if ideal destructive interference occurs. In practice, this does not happen. Part of the x and y polarization components of the PBS's input optical signal leak to the output ports corresponding to the y and x polarization, respectively. This is particularly deleterious in the proposed MZDI configuration. When to a given output port of the PBS corresponds a maximum of the amplitude response, to the other port corresponds a minimum. Therefore, the power leaking from the output port to which corresponds a maximum of the amplitude response can significantly affect the amplitude response on the

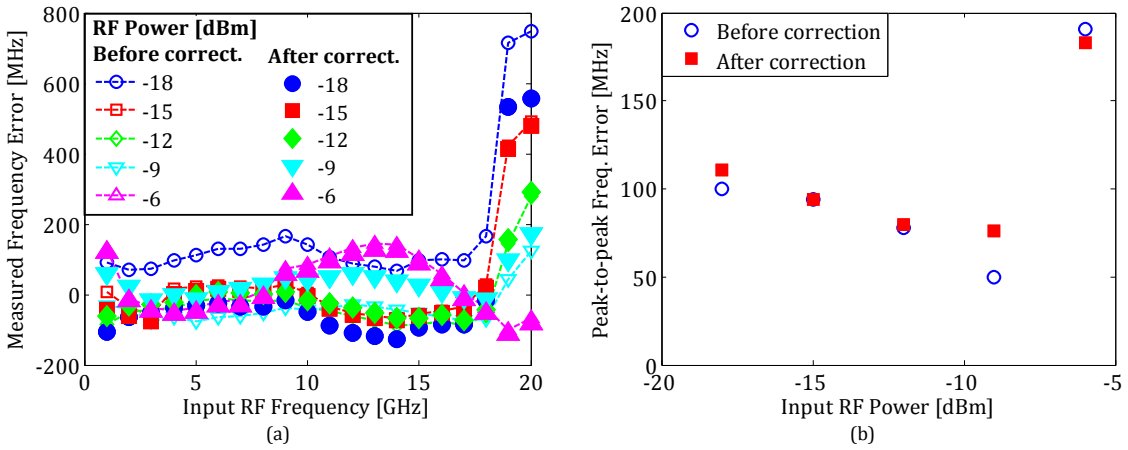

Figure 2.6: (a) Measured frequency errors considering different input RF powers. (b) peak-to-peak frequency errors for the considered input RF powers. Before correction: results taken from [J1, Fig. 4]. After correction: results obtained after correcting the expression of the ACF, now given by (2.18).

other port. The power leakage from one output port of the PBS to the other can be modeled on the ACF in the following way

$$\mathrm{ACF}(f) = \frac{P_D(f) + P_C(f) \cdot 10^{-\frac{\mathrm{ER}_x}{10}}}{P_C(f) + P_D(f) \cdot 10^{-\frac{\mathrm{ER}_y}{10}}}, \tag{2.18}$$

where ER_x and ER_y are the extinction ratios (ERs) of the x and y output ports of the PBS. Off-the-shelf PBSs have similar ERs on both output ports of about 25 dB.

Experiment An experimental assessment of the proposed IFMS was performed considering a PMF with a DGD of 22 ps and a RF frequency from 1 GHz up to 20 GHz [J1]. It was observed that the powers at the output of the PBS, $P_C(f)$ and $P_D(f)$ deviated significantly from the theoretical predictions with the increase of the RF frequency [J1, Fig. 3 (a)]. This was caused by the electrical low-pass filtering characteristics of the electrical circuitry feeding the MZM. Due to the complementarity of $P_C(f)$ and $P_D(f)$, such deviations do not affect the ACF. The RF frequency measurement was repeated for different input RF powers. The measured RF frequency and corresponding frequency errors are shown in Fig. 2.6. There are two sets of results. The first ones, labeled "Before correction", are the ones presented in [J1, Fig. 4]. Such results are based on [J1, Eq. 7], which incorrectly divides the ERs of the PBS by 20. The correct factor is of 10, as presented in (2.18). Corrected results, labeled "After correction", were obtained using (2.18). Figure 2.6 (a) shows that the results obtained before and after correction are very similar, apart from a vertical offset. Such offset has no impact on the peak-to-peak frequency error. The frequency errors increased for high RF frequencies as the residual power of the OC interfered on the measurement taken at the constructive port. It should be noted that a limited OCS is unavoidable in commercial MZMs as ideal destructive interference is again impossible to achieve. Consequently, a low OCS is obtained for low RF powers, which results in higher RF frequency measurement errors. For high RF powers the RF frequency errors are also significantly high. The reason for this lies in the power of the

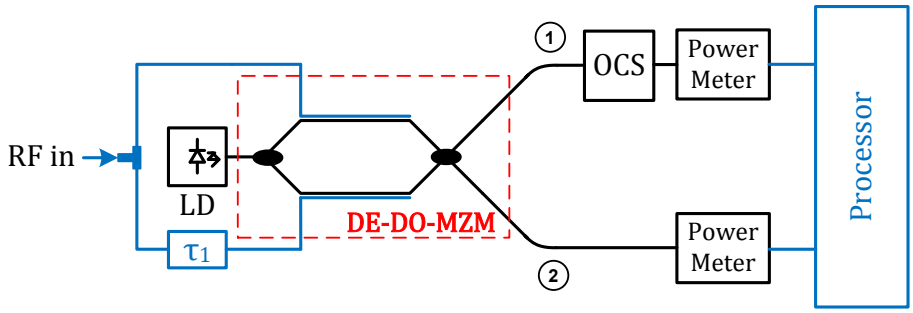

Figure 2.7: Scheme of the IFMS based on complementary E/O modulation.

spectral lines at harmonics $f_o \pm k \cdot f_{RF}$, $k = 1, 2, ...$, which is non-negligible for high modulation indexes. A minimum peak-to-peak frequency error of 76 MHz over a frequency range of 1–18 GHz was achieved for an input RF power of −9 dBm.

The key in obtaining low frequency errors is the stability of the system. Even though the proposed MZDI is based on all-fiber components such as the PCs and the PMF, its experimental implementation was considerably bulky and therefore sensitive to mechanical and thermal variations. Such variations are modeled by $\Psi(f)$ in (2.12). This was the reason why the frequency measurement process was performed using LabVIEW©. The automation of the frequency measurement process allowed doing the measurements in less time in comparison to manual operation. Hence, the measurements were subject to less mechanical and thermal variations, yielding lower frequency errors.

An improved IFMS should therefore employ a compact MZDI, resorting to an implementation in integrated optics. Integrated MZDIs are commercially available since they are commonly used in the demodulation of differential phase shift keying (DPSK) optical signals. An IFMS using such a MZDI was proposed in [13]. Although the resilience of the system to mechanical and thermal variations improved in comparison with the proposed scheme, the instability of the MZDI was still dominant over the wavelength drifts of the LD.

2.2.1.2 Implementation based on complementary electro-optic modulation [papers J2, C5, C6]

The IFMS proposed in Fig. 2.3 separates E/O conversion from COF. As observed in [J1] and [13], this approach was limited by the sensitivity of the MZDI to environmental variations. In order to avoid this limitation a different approach was assessed: E/O conversion and COF were simultaneously achieved in a single stage [J2]. Therefore, both operations should be performed within the MZM, resulting in a compact and stable implementation. The scheme of the proposed IFMS is shown in Fig. 2.7.

The key device of the IFMS is a DE DO MZM. A MZM is essentially a MZDI with $\tau_1 = \tau_2$. Therefore, it may have one or two inputs and one or two outputs. Off-the-shelf modulators commonly have one input, one output and one or two electrodes. An electrode is an electrical transmission line located near one of the optical waveguides that connect the input optical coupler to the output optical coupler. By applying a voltage to the electrical delay line (EDL), the phase of the optical signal propagating on the waveguide can be controlled. The optical phase is proportional to the applied voltage. Since the considered modulator has two electrodes

and two outputs, its output optical signals are given by

$$E_{1,2}(t) = \frac{1}{2}\left[\exp\left(\frac{\pi}{V_\pi}(v_1(t) + V_{\text{bias}})\right) \mp \exp\left(\frac{\pi}{V_\pi}(v_2(t) - V_{\text{bias}})\right)\right] \cdot E_{\text{LD}}(t), \tag{2.19}$$

where $v_1(t)$ and $v_2(t)$ represent the electrical signals applied to electrodes one and two, respectively. According to Fig. 2.7, the input RF signal is split into two copies with identical amplitudes. Each copy is fed to one of the modulator electrodes. An EDL is used to set a time delay of τ_1 between the two copies. Therefore, $v_1(t)$ and $v_2(t)$ are given by

$$v_1(t) = V_{\text{RF}} \sin(\omega_{\text{RF}} t) \tag{2.20}$$

$$v_2(t) = V_{\text{RF}} \sin(\omega_{\text{RF}}(t - \tau_1)), \tag{2.21}$$

where the attenuation imposed by the electrical splitter is neglected. Let us consider $V_{\text{bias}} = \frac{V_\pi}{2}$ and a low modulation index. By applying the Jacobi-Anger expansion, (2.20) and (2.21) can be approximated as

$$E_1(t) \approx j\left\{J_0(z) + 2jJ_1(z) \cdot \left[\cos\left(\omega_{\text{RF}}\left(t - \frac{\tau_1}{2}\right)\right)\cos\left(\frac{\omega_{\text{RF}}\tau_1}{2}\right)\right]\right\} \cdot E_{\text{LD}}(t) \tag{2.22}$$

$$E_2(t) \approx j\left\{-2jJ_1(z) \cdot \left[\sin\left(\omega_{\text{RF}}\left(t - \frac{\tau_1}{2}\right)\right)\sin\left(\frac{\omega_{\text{RF}}\tau_1}{2}\right)\right]\right\} \cdot E_{\text{LD}}(t). \tag{2.23}$$

Equations (2.22) and (2.23) show that the RF carriers of the optical signals at the output 1 and 2 of the MZM are multiplied by the term $\cos(\frac{\omega_{\text{RF}}\tau_1}{2})$ and $\sin(\frac{\omega_{\text{RF}}\tau_1}{2})$, respectively. These terms depend on the RF frequency. Therefore, the optical signals at the outputs of the modulator are subject to complementary filtering. This proves that E/O conversion and COF are achieved in a single stage, thanks to the electrical circuitry driving the DE DO MZM. The average optical power at the output 2 of the modulator, given by $P_2 = \overline{\|E_2(t)\|^2}$ is proportional to $\sin(\frac{\omega_{\text{RF}}\tau_1}{2})$. However, $P_1 = \overline{\|E_1(t)\|^2}$ is proportional to $\cos(\frac{\omega_{\text{RF}}\tau_1}{2})$ only if the first term of (2.22) is eliminated. In practice, this means suppressing the OC of the optical signal at modulator's output 1, as depicted in Fig. 2.7. If OCS is accomplished at the modulator's output 1, the ACF can be defined as follows,

$$\text{ACF}(\omega_{\text{RF}}) = \frac{P_2}{P_1} = \tan^2\left(\frac{\omega_{\text{RF}}\tau_1}{2}\right), \tag{2.24}$$

which is identical to (2.10).

There are two main challenges in the implementation of the proposed IFMS. As shown in (2.20) and (2.21), the amplitudes of $v_1(t)$ and $v_2(t)$ should be identical. In practice, this requires a low-loss EDL. As τ_1 is on the order of 10 ps, an electrical length of less that one centimeter is required. Such low lengths involve negligible losses. Furthermore, the impact of having different amplitudes can be taken into account at the processor. The other challenge is how to perform OCS at the output 1 of the modulator.

There are two possible ways to perform OCS: using a notch filter (NF), or resorting to destructive interference. Both ways are depicted in Fig. 2.8. The first way consists in using a NF at the modulator's output 1, centered at the frequency of the OC. This method is quite straightforward. However, the OC frequency must be carefully centered with the NF's center frequency. Nonetheless, a deviation between the OC and notch frequencies can be easily monitored as it only affects P_1. Another important detail is that the NF should have a low

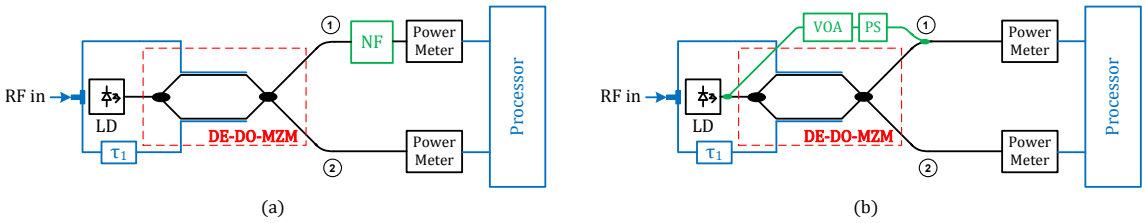

Figure 2.8: IFMS schemes in which OCS at the output 1 of the modulator is performed through (a) notch filtering and (b) destructive interference.

bandwidth in order to enable the measurement of low RF frequencies. The other way is to suppress the OC by destructive interference. As shown in Fig. 2.8 (b), a portion of the LD has its amplitude and phase adjusted by a variable optical attenuator (VOA) and a phase shifter (PS), respectively. The resulting optical signal is coherently added with the optical signal at the output 1 of the modulator, yielding

$$E_{1,\mathrm{OCS}}(t) = \sqrt{1-\alpha}E_1(t) + \sqrt{\alpha}E_{\mathrm{LD}}(t) \cdot A_{\mathrm{VOA}} \exp(j\phi_{\mathrm{PS}}), \tag{2.25}$$

where α is the power coupling ratio of the optical coupler at the output of the LD, A_{VOA} is the attenuation set by the VOA and ϕ_{PS} is the phase set by the PS. By using (2.25) on (2.22), it can be derived that the OC is suppressed when $\phi_{\mathrm{PS}} = (2k+1)\pi$, $k = 1, 2, ...$ and $A_{\mathrm{VOA}} = \sqrt{\frac{1-\alpha}{\alpha}}J_0(z)$. This method has the advantage of being insensitive to the wavelength drifts of the LD. However, the DE DO MZM should be integrated with the VOA, PS and additional optical couplers in order to achieve stable operation.

Experiment Due to the unavailability in the laboratory of a DE DO MZM, a proof-of-concept experiment was conducted using a DE single output MZM. Therefore, the experiment was divided in two steps, in which P_2 was firstly measured. Then, V_{bias} was adjusted and a NF was set at the output of the MZM, enabling the measurement of P_1. A tunable electrical delay line (TEDL) was adjusted to provide $\tau_1 = 16.67$ ps. Even though such delay enabled a measurement range of $\frac{1}{2\tau_1} = 30$ GHz, the electrical bandwidth of the system was limited to 20 GHz. The cause was electrical impedance mismatch between the TEDL and the RF cable that connected it to the respective modulator's electrode.

The NF consisted in a uniform fiber Bragg grating (FBG) operating in reflection. A uniform FBG with a length of 7 mm and an average refractive index variation of 2×10^{-4} was employed. Figure 2.9 displays the reflectivity of the FBG, measured by an optical network analyzer (ONA). The OC was aligned with a first-order zero of the FBG. As a result an OCS of 20 dB was achieved. The highest frequency zero was chosen since it provides the narrowest notch filtering. The FBG does not provide ideal notch filtering, as it attenuates the RF tone at $f_o + f_{\mathrm{RF}}$. Therefore, the FBG's reflectivity was considered on the simulation of P_1, and consequently also of the ACF. Two other NF options also based on FBGs were considered. The first consisted in using a long and weak uniform FBG in transmission with the purpose of reflecting the OC and transmitting the RF carriers. The other one was to use a phase shifted FBG centered at the OC frequency. These two options were discarded discarded since such FBGs were more complex and thus harder to produce. Furthermore, and to the best of the author's knowledge, the proposed approach had never been reported.

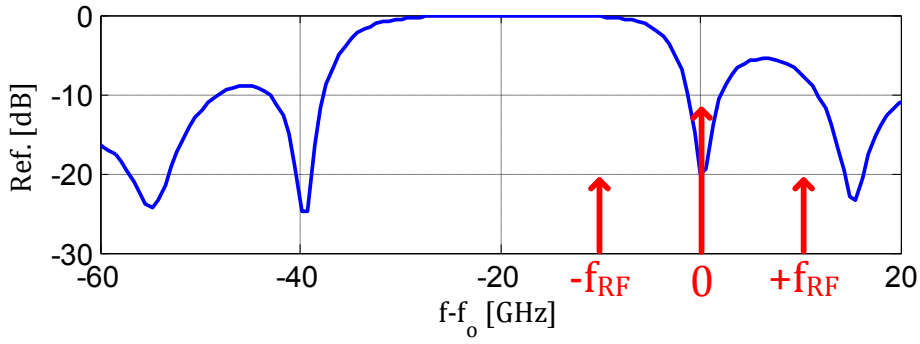

Figure 2.9: Reflectivity of the uniform FBG. The optical spectrum of the input optical signal should be centered at a zero of the reflectivity of the FBG.

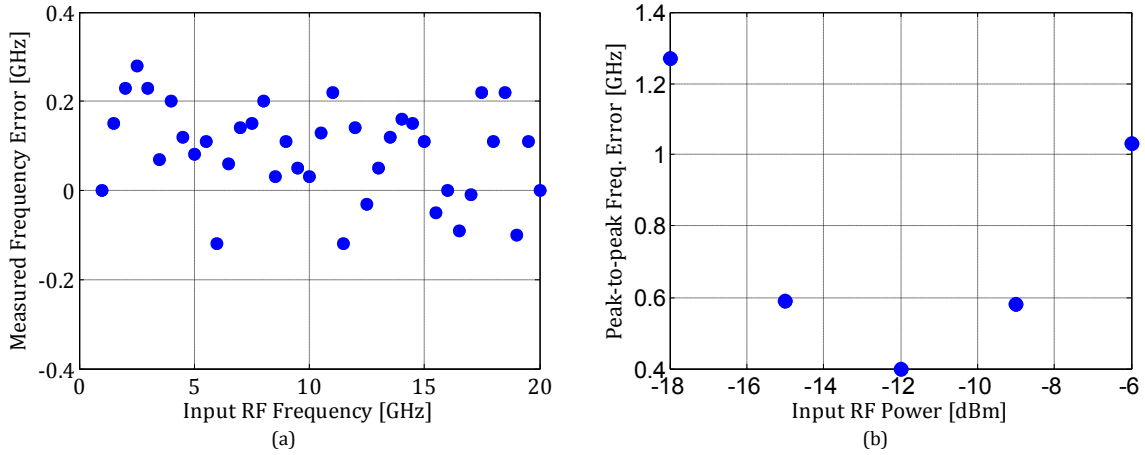

Figure 2.10: (a) Measured frequency errors for an input RF power of −12 dBm. (b) peak-to-peak frequency errors for the considered input RF powers.

An important detail in the experiment not mentioned in [J2] was that a PC was inserted before the FBG. When a FBG is written on an originally non-birefringent optical fiber, a residual birefringence is induced [14]. This results in having equal reflectivities on the x and y polarization of the fiber, however with different center frequencies. This is particularly serious at the zeros of the reflectivity, as a change in the input polarization results in a significant variation of the reflectivity. In the experimental tests, this detail turned to be very useful. The LD could be tuned with a minimum step of 1.25 GHz. Such a large step did not allow fine tuning the OC with the FBG's zero frequency. However, tuning the PC and thereby the input SOP enabled fine tuning the center frequency of the reflectivity, maximizing the OCS. The FBG was set on a Peltier device, controlled by a temperature controller. The temperature was kept constant at 25 °C in order to avoid temperature-dependent frequency deviations.

The experimental results are shown in Fig. 2.10. A peak-to-peak frequency error of 400 MHz was obtained. Measurement errors were mainly caused by wavelength drifts between the laser source and the FBG. Hence, the system's stability was mainly dependent of such drifts, as the MZM modulator provided stable operation. Low frequency errors at low RF frequencies were achieved thanks to the narrow notch bandwidth of the uniform FBG. As shown in

Fig. 2.10, for low input RF powers the measurement error increases. This is explained by the increasing significance of the residual OC in P_1, which degrades the complementarity of the power measurements and also reduces the slope of the ACF. For higher RF powers the frequency errors increase as the experimental results deviate from the simulation predictions. This can be explained by the gain compression of the input electrical amplifier, which was not considered on simulations. Improved results can be achieved with precise electrical impedance matching, and high OCS at both modulator outputs.

2.3 Conclusions

In this chapter, two novel IFMSs based on complementary filtering were presented. Complementary filtering is provided by a MZDI with a single input and two outputs. The RF frequency is derived from the two average optical powers measured at the outputs of the MZDI. The complementarity of both measurements provides a RF frequency measurement independent of the optical and input RF powers.

The two proposed IFMSs differ in the implementation of the MZDI. In the first implementation, an all-fiber MZDI operating in the polarization domain was implemented resorting to PCs, a PMF and a PBS. An peak-to-peak RF frequency error lower than 200 MHz was achieved within a RF frequency range of 1–18 GHz. However, the system was significantly sensitive to the environmental conditions as the MZDI was implemented with discrete components.

Such drawback motivated the proposal of the second implementation. E/O modulation and complementary filtering were simultaneously achieved using a DE DO MZM driven by differentially delayed copies of the input RF signal. An optical NF was used at one of the modulator's outputs to perform OCS. A peak-to-peak RF frequency error of 400 MHz was achieved over a measurement range of 1—20 GHz. The robustness of the system to environmental conditions clearly improved, as it is only dependent on the drifts between the OC frequency and NF's center frequency. The center frequency of the NF was stabilized by keeping its temperature controlled.

Chapter 3

Photonic devices based on a Mach-Zehnder delay interferometer with tunable coupling ratio

This chapter presents the research carried out on photonic devices whose operation principle is based on a MZDI-TCR. A theoretical description of the MZDI-TCR is presented in the first section. Two kinds of ODLs are considered, non-dispersive media and ideal second-order dispersive media. Section 3.2 presents a photonic beamforming system for a PAA transmitter which employs a tunable optical delay line (TODL) based on a MZDI-TCR with non-dispersive media. The concept behind the proposed TODL is further explored in section 3.3. A MZDI-TCR with second-order dispersive media is exploited to implement a TODC. The conclusions of this chapter are drawn in section 3.4.

3.1 Operation principle of a Mach-Zehnder delay interferometer with tunable coupling ratio

The scheme of a MZDI-TCR is depicted in Fig. 3.1. In order to simplify the theoretical assessment of this device, only one input and output optical signals are considered. The interferometer's TCR is obtained by employing an input and/or output optical coupler with TCR. If the ODLs have a linear response, there is no difference in having TCR on the input or output optical coupler. In the following analysis the input optical coupler has a TCR, whereas the output optical coupler has a coupling ratio of 50%. The relation between the input and output optical signals can be written as

$$O_1(f) = \frac{1}{\sqrt{2}} \left(\alpha \tau_1(f) + \sqrt{1-\alpha^2}\tau_2(f) \right) E_1(f), \tag{3.1}$$

where $\alpha^2 \in [0,1]$ is the coupling ratio. Let us consider that the ODLs are ideal second-order dispersive media,

$$\tau_{1,2}(f) = \exp\left[-j\phi_{1,2}(f)\right] = \exp\left[-j2\pi \left(\frac{D_{1,2}\lambda_o^2}{2c} f^2 + \tau_{1,2} f \right) \right], \tag{3.2}$$

where $D_{1,2}$ and $\tau_{1,2}$ are the cumulative dispersions and time delays of the dispersive media, and λ_o is the center wavelength of the dispersive media. The amplitude response of the

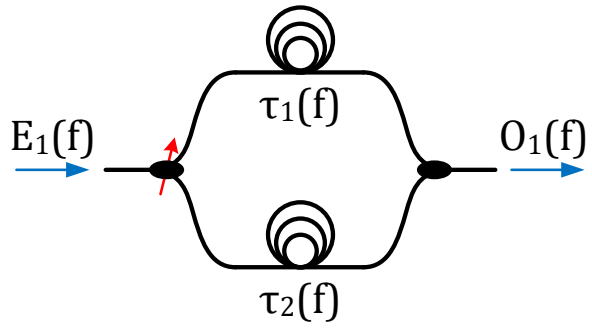

Figure 3.1: Scheme of a Mach-Zehnder delay interferometer with tunable coupling ratio.

MZDI-TCR is given by

$$P_{O_1}(f) = \frac{1}{2}\left[1 + 2\alpha\sqrt{1-\alpha^2}\cos\left[\phi_1(f) - \phi_2(f)\right]\right] \cdot P_{E_1}(f). \tag{3.3}$$

The group delay response can be obtained by derivating the phase response of the interferometer, $\phi(f)$, using the relation $\tau(f) = \frac{1}{2\pi}\frac{d\phi}{df}$. Hence, the group delay response is given by

$$\tau(f) = \frac{1}{2\pi}\frac{\alpha^2\phi_1'(f) + (1-\alpha^2)\phi_2'(f) + \alpha\sqrt{1-\alpha^2}(\phi_1'(f) + \phi_2'(f))\cos\left[\phi_1(f) - \phi_2(f)\right]}{1 + 2\alpha\sqrt{1-\alpha^2}\cos\left[\phi_1(f) - \phi_2(f)\right]}, \tag{3.4}$$

where

$$\phi_{1,2}'(f) = \frac{d\phi_{1,2}(f)}{df} = 2\pi\left(\frac{D_{1,2}\lambda_o^2}{c}f + \tau_{1,2}\right). \tag{3.5}$$

The theoretical analysis presented up to this point consists in a generalization of a MZDI-TCR whose ODLs are second-order dispersive media.

Let us firstly consider non-dispersive media, i.e., $D_1 = D_2 = 0$, and also $\tau_2 = 0$. Let us define $\alpha = \cos\theta$, and therefore $\sqrt{1-\alpha^2} = \sin\theta$. Equations (3.3) and (3.4) are simplified to

$$P_{O_1}(f) = \frac{1}{2}\left[1 + 2\cos(\theta)\sin(\theta)\cos\left[2\pi f\tau_1\right]\right] \cdot P_{E_1}(f) \tag{3.6}$$

$$\tau(f) = \tau_1\frac{\cos^2(\theta) + \cos(\theta)\sin(\theta)\cos\left[2\pi f\tau_1\right]}{1 + 2\cos(\theta)\sin(\theta)\cos\left[2\pi f\tau_1\right]}. \tag{3.7}$$

$P_{O_1}(f)$ and $\tau(f)$ are displayed in Fig. 3.2. Different amplitude and group delay responses are obtained for different values of θ. Let us consider the frequencies at which $P_{O_1}(f)$ is maximum, i.e., $f\tau_1 = k$, where $k = 0, \pm1, \pm2, \ldots$. At such frequencies the MZDI-TCR behaves like a TODL, with a tuning range of 0 up to τ_1 and an insertion loss of 0 up to 3 dB.

Let us now consider the general expressions (3.3) and (3.4). For $\phi_1(f) - \phi_2(f) \approx 0$ these equations can be approximated by

$$P_{O_1}(f) \approx \frac{1}{2}\left[1 + 2\cos(\theta)\sin(\theta)\right] \cdot P_{E_1}(f) \tag{3.8}$$

$$\tau(f) \approx \frac{1}{2\pi}\frac{\left(\cos^2(\theta) + \cos(\theta)\sin(\theta)\right)\phi_1'(f) + \left(\sin^2(\theta) + \cos(\theta)\sin(\theta)\right)\phi_2'(f)}{1 + 2\cos(\theta)\sin(\theta)}. \tag{3.9}$$

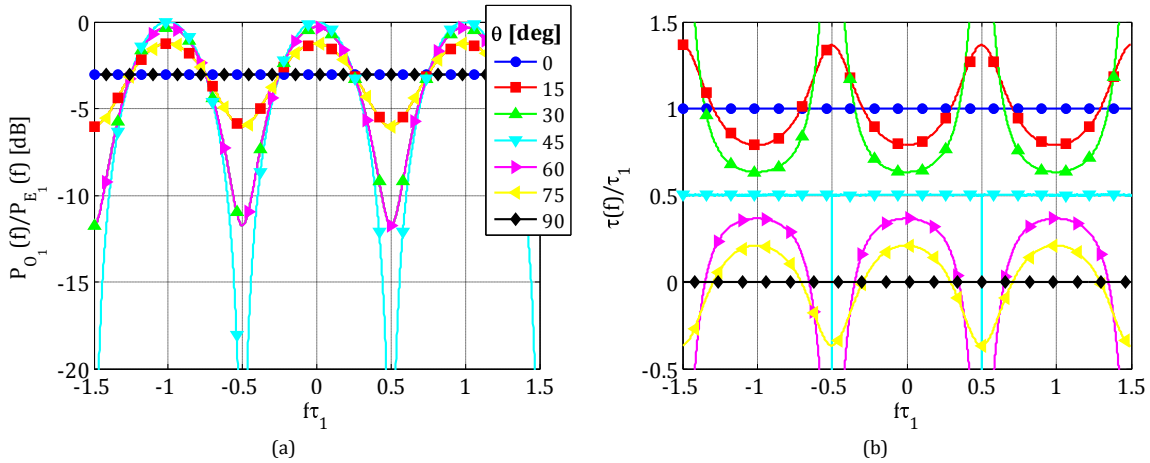

Figure 3.2: Normalized (a) amplitude and (b) group delay responses of a MZDI-TCR with non-dispersive media for different coupling ratios.

Equation (3.9) shows that the group delay is a weighted mean between $\phi_1'(f)$ and $\phi_2'(f)$, where the weight associated with both functions depends on θ and thereby on the coupling ratio. Hence, for frequencies at which the condition $\phi_1(f) - \phi_2(f) \approx 0$ is valid, the MZDI-TCR behaves like a TODC with a tuning range of D_1 up/down to D_2, and an insertion loss of 0 up to 3 dB. The amplitude and group delay responses of a MZDI-TCR with $D_1 = -340$ ps/nm and $D_2 = 0$ are shown in Fig. 3.3. This figure shows that all variables $D_{1,2}$, $\tau_{1,2}$ and θ have a significant impact on the amplitude and group delay responses of the MZDI-TCR. Consequently, the design of a TODC based on a MZDI-TCR should take into account all these variables, with the purpose of optimizing the amplitude and group delay responses within the condition $\phi_1(f) - \phi_2(f) \approx 0$.

3.2 Photonic beamforming system for a PAA transmitter [papers J3, C7]

The scheme of a PAA is shown in Fig. 3.4. A PAA is composed by N antenna elements (AEs), which usually are identical antennas. The AEs may be arranged in one, two or three spacial dimensions, with arbitrary distances between them. Each AE is fed with a copy of the input RF signal, which has its amplitude and phase adjusted. By controlling the number of AEs and their disposition, and also the amplitude and phase of the RF signals fed to each AE, it is possible to optimize the radiation diagram of the PAA. As there is a significant number of parameters which can be optimized, PAAs are highly flexible with respect to the desired radiation diagram.

A fast adjustment of the radiation diagram is generally obtained by controlling only the amplitudes and phases of the N RF signals, since spacial displacements are avoided. Therefore, the input signal splitter, amplitude controllers and phase adjusters are used to shape the radiation diagram. These components compose the beamforming system. Let us consider a PAA with N AEs arranged in a single dimension. The distance between two adjacent AEs,

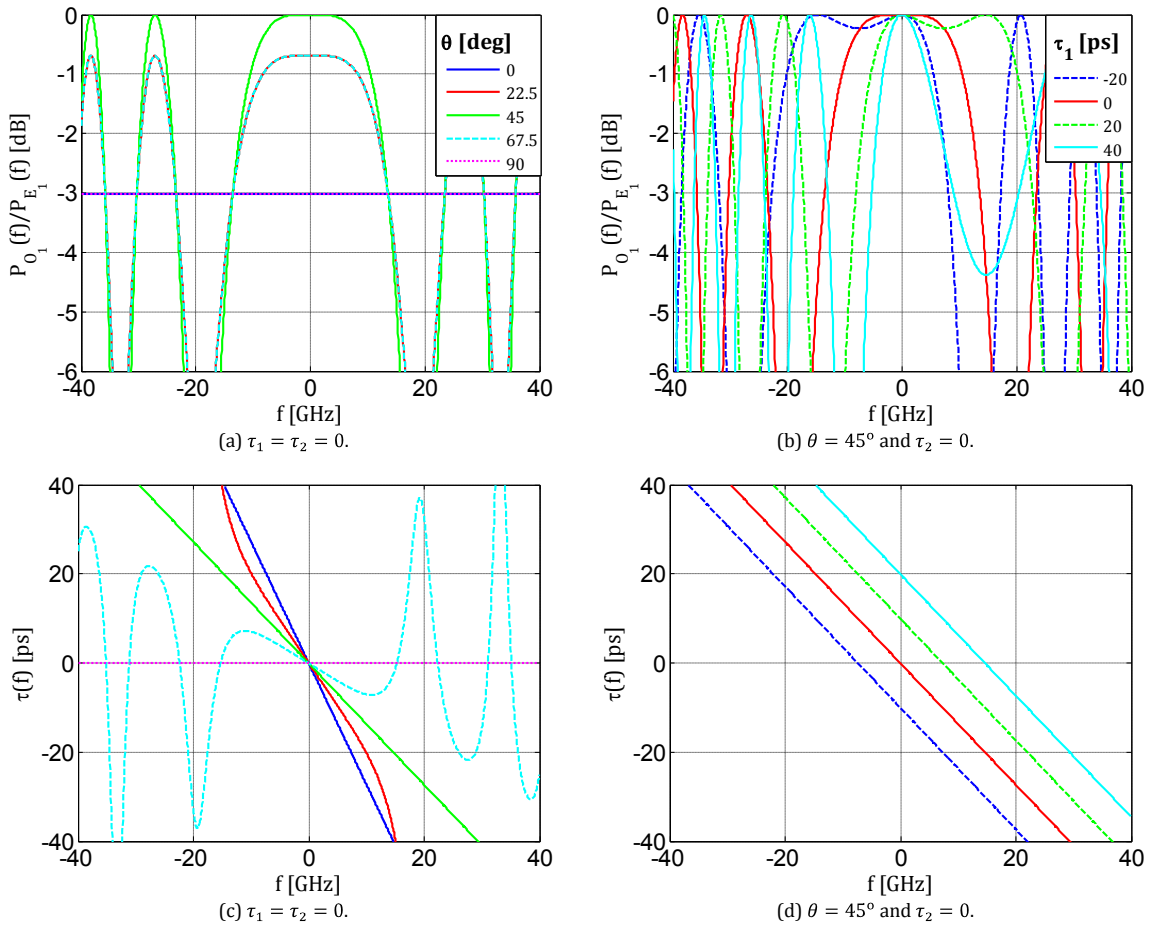

(a) $\tau_1 = \tau_2 = 0$. (b) $\theta = 45^o$ and $\tau_2 = 0$.

(c) $\tau_1 = \tau_2 = 0$. (d) $\theta = 45^o$ and $\tau_2 = 0$.

Figure 3.3: (Top) amplitude and (bottom) group delay responses of a MZDI-TCR with $D_1 = -340$ ps/nm and $D_2 = 0$ for (left) different coupling ratios, and (right) different values of τ_1.

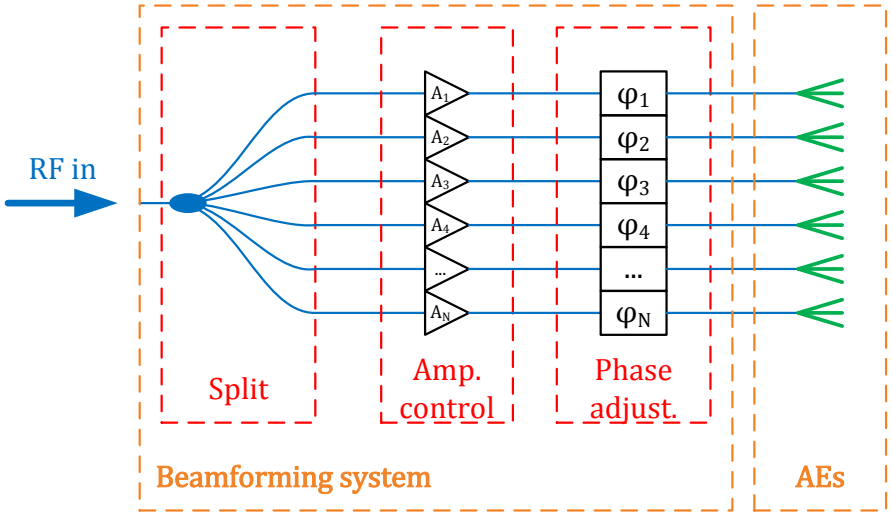

Figure 3.4: Scheme of a PAA.

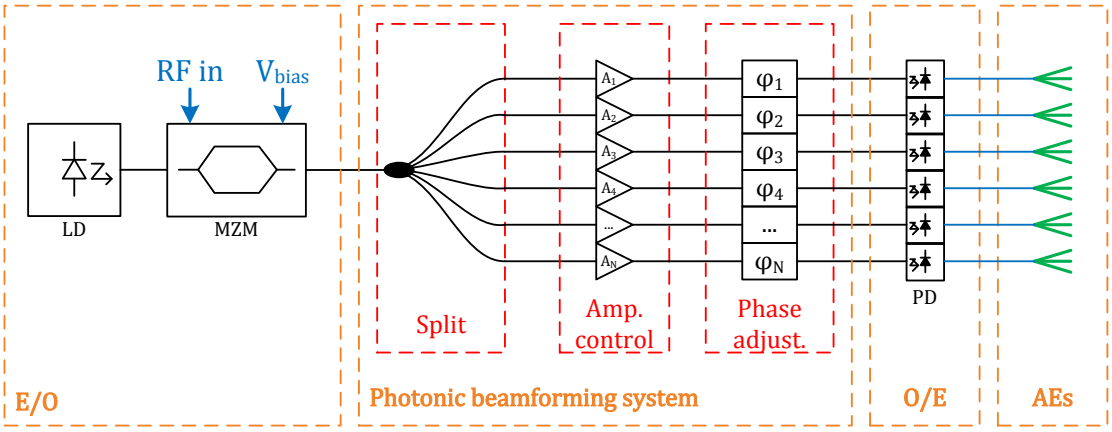

Figure 3.5: Scheme of a PAA with a photonic beamforming system.

d, is constant. The array factor (AF) of the PAA is given by

$$\mathrm{AF}(\Theta) = \frac{1}{N}\sum_{i=0}^{N-1} A_i \cdot \exp\left[j\left(ikd\cos(\Theta) + \beta_i\right)\right], \tag{3.10}$$

where Θ is the spacial angle around the orientation axis of the PAA and $k = 2\pi f_{\mathrm{RF}}/c$ is the wavenumber of the RF signal. A_i and β_i are the amplitude and phase of the RF signal fed to the i^{th} AE, respectively. Equation (3.10) shows that the radiation diagram of a PAA is the superposition of the electric fields radiated by the AEs. The phase term of (3.10) consists in the sum of two terms. The first one depends on the physical distance between AEs, whereas the second one can be controlled by the phase adjusters. The first phase term is proportional to the RF frequency. Consequently, if β_i are constants, different RF frequencies experience different phases. As a result, different RF frequencies are radiated to different directions. Such phenomenon is designated by beam squinting. On the other hand, if β_i are proportional to f_{RF}, beam squinting is avoided. In this case, β_i represents a time delay defined as

$$\beta_i = 2\pi f_{\mathrm{RF}} \tau_i^{\mathrm{PA}}, \tag{3.11}$$

where τ_i^{PA} is the time delay induced by the i^{th} phase adjuster. A beamforming system whose phase adjusters consist of tunable delay lines is designated by true time delay (TTD) beamformer. Such beamforming systems have the advantage of handling broad bandwidth RF signals without causing beam squinting.

Photonic TTD beamforming systems have been investigated, as they share the advantages that microwave photonics techniques have in comparison to electrical implementations [15]. Important advantages include small size and light weight, low propagation losses, immunity to electromagnetic interference (EMI) and wide available bandwidth. A general scheme of a PAA with a photonic beamforming system is shown in Fig. 3.5. The first step consists in converting the RF signal to the optical domain. The modulated optical signal is then processed by the photonic beamforming system. The N output optical signals are converted to the electrical domain using an array of photodetectors (PDs). Each detected signal is fed to the respective AE.

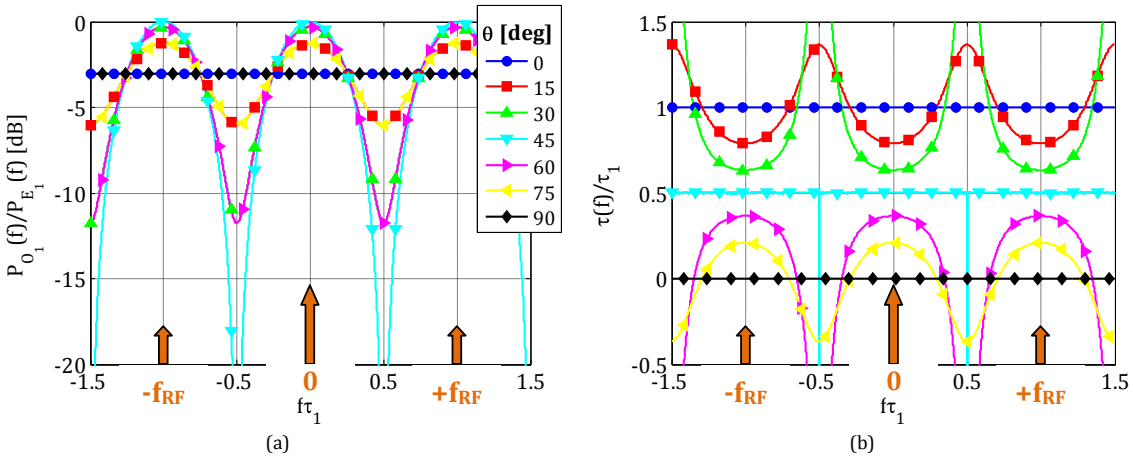

Figure 3.6: Normalized (a) amplitude and (b) group delay responses of a MZDI-TCR with non-dispersive media, properly centered with the spectrum of the optical signal.

The brief review of photonic TTD beamforming systems found at the introduction of [J3] shows that different beamforming systems rely on different TODLs. Therefore, the research on photonic beamforming systems has been mainly focused on the used TODLs. In [J3], the TODLs are based on MZDI-TCRs with non-dispersive media. As described in section 3.1, the MZDI-TCR behaves as an TODL for frequencies at which its amplitude response is maximum. Therefore, this TODL should only be employed on optical signals with a spectral content limited to such frequencies. As shown in Fig. 3.6, the proposed TODL can be employed on RF signals converted to the optical domain which comply with

$$f_{\mathrm{RF}}\tau_1 = n, \tag{3.12}$$

where $n = 0, 1, 2, 3, ...$ Equation (3.12) shows that τ_1 should be a multiple of the RF period, $1/f_{\mathrm{RF}}$. Let us define the beampointing angle $\Theta_{\max}$, which corresponds to the spacial angle at which the absolute value of the AF is maximum. A fully tunable beamforming system allows varying $\Theta_{\max}$ from 0 to 2π. This requires that the differential phase between two adjacent AEs is also tunable between 0 and 2π, i.e.,

$$\beta_i - \beta_{i-1} = 2\pi f_{\mathrm{RF}}(\tau_i^{\mathrm{PA}} - \tau_{i-1}^{\mathrm{PA}}) \in [0, 2\pi]\,. \tag{3.13}$$

Therefore, the maximum time delay between two adjacent AEs is of $1/f_{\mathrm{RF}}$. As a result, the time delay related to the i^{th} AE should be tunable from 0 up to $\frac{i-1}{f_{\mathrm{RF}}}$. This means that the i^{th} MZDI-TCR should have $\tau_1 = \frac{i-1}{f_{\mathrm{RF}}}$. Such condition complies with (3.12). For a matter of simplicity that is explained in the next subsection, let us consider all the N MZDI-TCRs with the same value of τ_1. In this case, the value of τ_1 is given by the highest value of τ_i^{PA}, which is $\frac{N-1}{f_{\mathrm{RF}}}$. The tunable time delay range can be of $[0, \tau_1]$, or $[-\tau_1/2, +\tau_1/2]$, which corresponds to a beampointing angle range of $[0, 2\pi]$ or $[-\pi, +\pi]$, respectively. In the latter case, a positive steering angle, i.e., $\Theta_{\max} \in [0, +\pi]$, requires $\tau_0^{\mathrm{PA}} = 0$, $\tau_1^{\mathrm{PA}} = +\frac{1}{2}\frac{\delta}{f_{\mathrm{RF}}}$, ..., $\tau_{N-1}^{\mathrm{PA}} = +\frac{N-1}{2}\frac{\delta}{f_{\mathrm{RF}}}$. $\delta \in [0, 1]$ is a constant defined by $\Theta_{\max}$. A negative steering angle, i.e., $\Theta_{\max} \in [-\pi, 0]$, requires $\tau_0^{\mathrm{PA}} = 0$, $\tau_1^{\mathrm{PA}} = -\frac{1}{2}\frac{\delta}{f_{\mathrm{RF}}}$, ..., $\tau_{N-1}^{\mathrm{PA}} = -\frac{N-1}{2}\frac{\delta}{f_{\mathrm{RF}}}$. This is equivalent to having $\tau_{N-1}^{\mathrm{PA}} = 0$, $\tau_{N-2}^{\mathrm{PA}} = \frac{1}{2}\frac{\delta}{f_{\mathrm{RF}}}$, ..., $\tau_0^{\mathrm{PA}} = \frac{N-1}{2}\frac{\delta}{f_{\mathrm{RF}}}$. Therefore, the tuning range of all TODLs

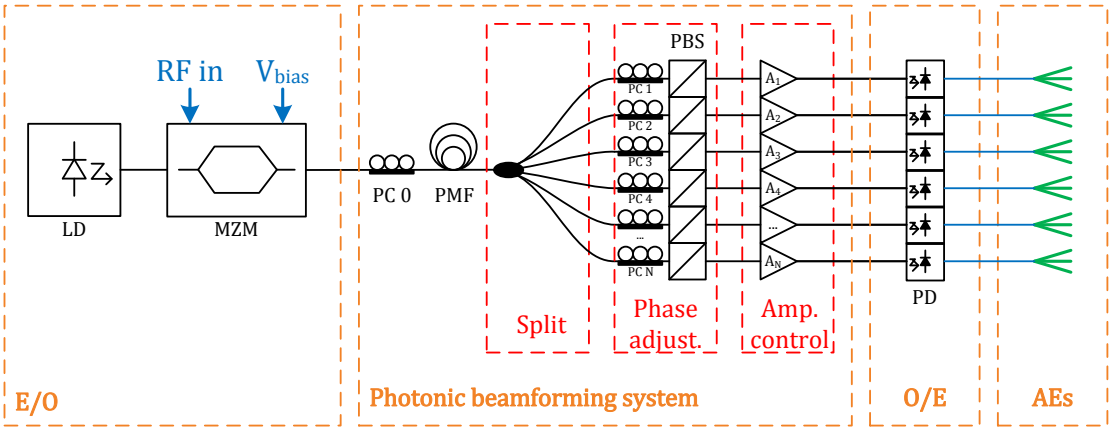

Figure 3.7: Scheme of a PAA with the proposed optimized implementation of the photonic beamforming system.

can be of $\left[0, \frac{N-1}{2f_{\mathrm{RF}}}\right]$, instead of $\left[-\frac{N-1}{2f_{\mathrm{RF}}}, \frac{N-1}{2f_{\mathrm{RF}}}\right]$ or $\left[0, \frac{N-1}{f_{\mathrm{RF}}}\right]$. Such a new value of $\tau_1 = \frac{N-1}{2f_{\mathrm{RF}}}$ is compliant with (3.12) when $\frac{N-1}{2f_{\mathrm{RF}}} = 0, 1, 2, 3, \ldots$. This condition is valid only for odd values of N. Therefore, the time delay τ_1 of the MZDI-TCRs is given by

$$\tau_1 = \begin{cases} \frac{N-1}{2f_{\mathrm{RF}}}, & \text{when } N \text{ is odd} \\ \\ \frac{N}{2f_{\mathrm{RF}}}, & \text{when } N \text{ is even.} \end{cases} \tag{3.14}$$

Equation (3.6) shows that the bandwidth of the MZDI-TCR's amplitude response decreases with τ_1. Therefore, it is very important to minimize τ_1 in order to accommodate broad bandwidth RF signals.

3.2.1 System implementation

A straightforward implementation of a photonic beamforming system using the proposed TODL would be based on the scheme shown in Fig. 3.5, on which the phase adjusters would be MZDI-TCRs with τ_1 given by (3.14). In this case, the N MZDI-TCRs share the same values of τ_1 and τ_2, and have an optical coupler with a coupling ratio of 50%. They only differ in the coupling ratio of the optical coupler with TCR. Such a little difference can be explored towards an optimized implementation.

Let us consider MZDI-TCRs implemented on the polarization domain, as depicted in Fig. 2.5. The input PC sets an input coupling ratio of 50%. The DGD of the PMF is of τ_1. The output PC and PBS compose the output optical coupler. Since the output PC is tunable, the output optical coupler and consequently the MZDI have TCR. The N MZDI-TCRs required by the proposed photonic beamforming system can all share the input PC and PMF, but not the output PC and PBS. An optimized implementation of a photonic beamforming system considering this is shown in Fig. 3.7. The shared components of the N MZDI-TCRs are set before the optical splitter, whereas the output optical couplers with TCR, i.e., PC i and respective PBS, are located after the splitter. It should be emphasized that the proposed implementation uses a single piece of PMF only because all interferometers have the same

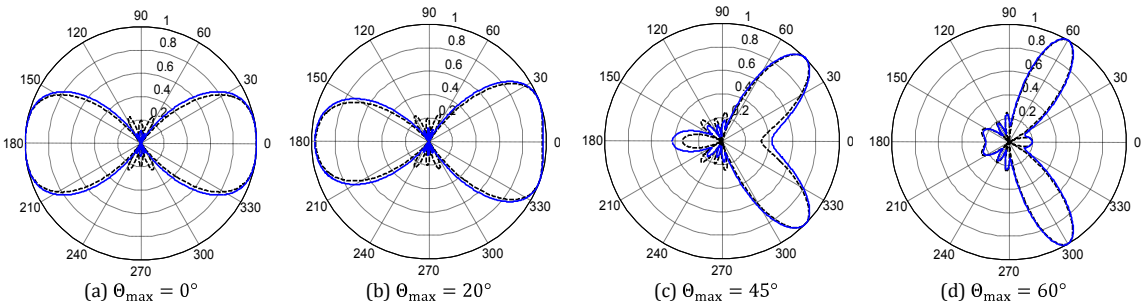

Figure 3.8: Radiation diagrams obtained for different beampointing angles. The solid line represents the proposed beamformer. The dashed line represents an ideal TTD beamformer.

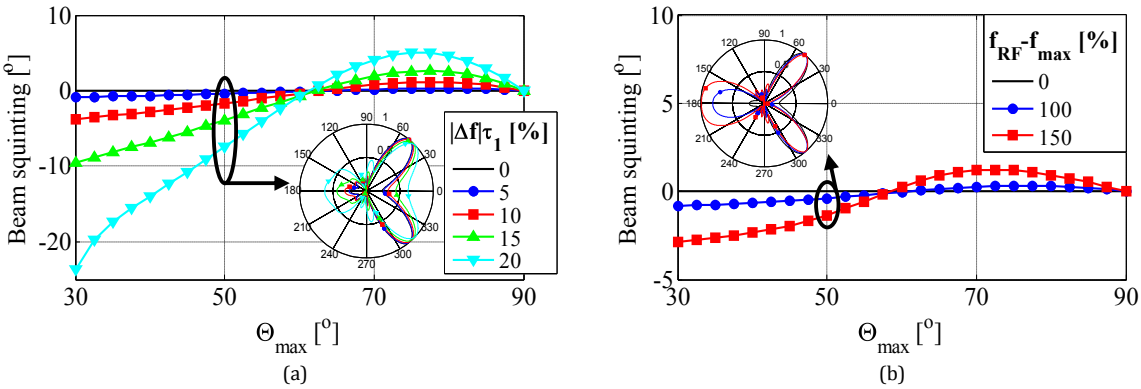

Figure 3.9: Beam squinting obtained for two different scenarios. (a) frequency detuning between the optical signals and interferometer's amplitude response. $\Delta f = f_o - f_{\max}$, where $f_{\max}$ is the frequency corresponding to a maximum of the interferometer's amplitude response. (b) RF frequency not compliant with (3.14). $f_{\mathrm{RF}} - f_{\max}$ is normalized to the 3 dB cutoff frequency. Insets: radiation diagrams obtained for $\theta_{\max} = 50°$.

value of τ_1. The proposed optimization only applies to MZDI-TCRs implemented on the polarization domain, as the differentially delayed optical signals are split before being added.

Simulations The proposed photonic beamforming system has a significant number of parameters, such as the RF frequency, number of AEs, and the amplitudes and phases of the N optical signals. Therefore, a suitable and simple simulation scenario had to be chosen. The proposed photonic beamforming system was simulated considering $N = 5$, $f_{\mathrm{RF}} = 60$ GHz, and a distance between two adjacent AEs of $d = \lambda_{\mathrm{RF}}/2 \approx 5$ mm. According to (3.14), $\tau_1 = 2/f_{\mathrm{RF}} \simeq 33.3$ ps. Amplitude adjusters were not employed.

Different beampointing angles were considered on simulations. The resulting radiation diagrams are shown in Fig. 3.8. Beam squinting is not observed. However, there is beam shaping caused by the dependence of the attenuation imposed by the MZDI-TCRs with the time delays τ_i^{PA}. This is depicted in Fig. 3.6. The different attenuations induced by the different values of τ_i^{PA} can be equalized using optical or electrical amplifiers with tunable gain. Tunable attenuators can be used instead of amplifiers. A perfect equalization results in ideal radiation diagrams.

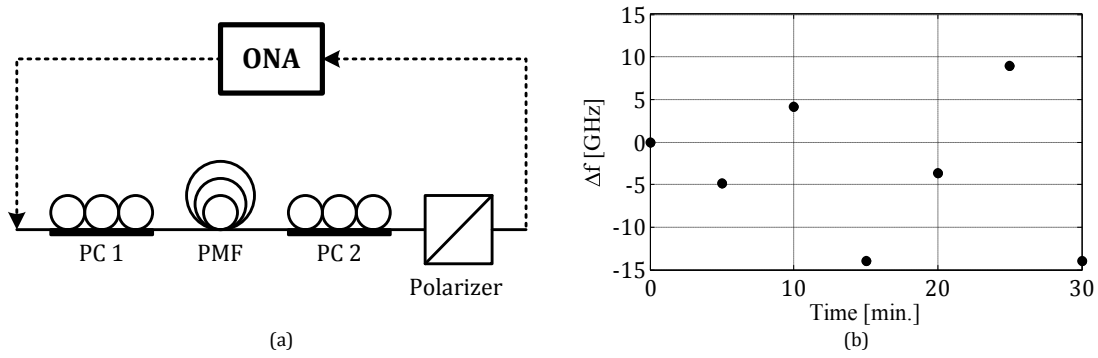

Figure 3.10: (a) Experimental setup. (b) temporal variation of the frequency detuning of the amplitude response.

As depicted in Fig. 3.6, the proposed photonic beamforming system requires that the two RF carriers and OC of the N optical signals are precisely centered at maxima of the MZDI-TCR's amplitude response. There are two possible scenarios which do not comply with this requirement. First, the RF carriers and OC of the N optical signals are detuned from maxima of the MZDI-TCR's amplitude response. Second, the OC of the N optical signals is properly centered at maxima of the MZDI-TCR's amplitude response, but the RF carriers are not. This scenario occurs when the RF frequency is not compliant with (3.14). Simulations regarding both scenarios were performed. The results are shown in Fig. 3.9. Beam squinting and distortion are achieved in both cases, as the amplitude and group delay responses of the MZDI-TCRs do not correspond to the expected. However, a much higher beam squinting is obtained for the first scenario in comparison to the second. This can be explained by the importance of having the OC centered at a maxima of the interferometer's response. The time delay added to the optical signal by the interferometer's response is mainly given by $\tau(f_o)$. Conversely, having a RF frequency not compliant with (3.14) only results in a slight phase shift. Two conclusions can be drawn from these results. First, the OC must be properly centered with the interferometer's response. Secondly, the proposed system is able to handle broad bandwidth RF signals, composed by different RF frequencies, with reduced beam squinting.

Experiment A simple proof-of-concept experiment was performed with the purpose of assessing the operation principle of the proposed polarization-domain implementation of the MZDI-TCR. The experimental setup is shown in Fig. 3.10. The PMF had a DGD of 33.3 ps. Different coupling ratios were set through the adjustment of PC 2. The amplitude and group delay responses were measured using an ONA. The measured responses were very close to the theoretical curves.

As observed in simulations, the OC should be precisely centered at a maxima of the interferometer's response. Consequently, the interferometer's frequency response should be stable over time. In order to assess the stability of the MZDI-TCR, PC 2 was firstly adjusted to set θ at 45°. Amplitude and group delay responses were then measured with a time interval of 5 minutes between them. The frequency detuning between the measured amplitude responses relatively to the first measurement are shown in Fig. 3.10 (b). Although not shown in the figure, the shape of the amplitude responses remained nearly unchanged in all measurements. These results demonstrate that the coupling ratio was stable, whereas the

frequency response drifted significantly over time. Such frequency drifts were originated by thermal and mechanical vibrations. As previously discussed in the experimental setup in subsection 2.2.1.1, a stable implementation of the MZDI-TCR and therefore of the proposed beamforming system should resort to photonic integration.

3.3 Tunable optical dispersion compensator [papers J4, J5, C8]

The propagation of an optical signal along an optical fiber is impaired by linear and nonlinear phenomena. Generally, the dominant linear impairment is CD, in which the phase velocity depends on the signal's wavelength. The CD of an optical fiber can be modeled by the following transfer function

$$H_{\mathrm{CD}}(f) = \exp\left(j \cdot k(f)\right), \tag{3.15}$$

where $k(f)$ is related with the propagation velocity. $k(f)$ is commonly approximated by the first two terms of its Taylor expansion,

$$H_{\mathrm{CD}}(f) \approx \exp\left(j \cdot 2\pi \left[k_1 f^2 + k_0 f\right]\right) \tag{3.16}$$

, where $k_1 = \frac{DL\lambda_o^2}{2c}$. D is the chromatic dispersion, L is the length of the optical fiber and λ_o is the center wavelength of the optical signal. The second term corresponds to a constant time delay of k_0. The first term corresponds to a time delay that is proportional to the signal's frequency. This term results in spectral phase distortion of the optical signal, leading to pulse broadening. In order to avoid signal degradation, a CD compensator should be employed. The transfer function of such device should be

$$H_{\mathrm{CDC}}(f) = \exp\left(j \cdot 2\pi \left[-k_1 f^2 + \tau f\right]\right), \tag{3.17}$$

where the value of τ is irrelevant for dispersion compensation purposes.

The CD experienced by optical signals in optical communication systems is not constant over time. It depends on the routing path, which may employ more than one kind of transmission fiber with arbitrary length. The CD can be compensated in all routing paths using CD compensators with fixed dispersion, such as dispersion compensating fibers (DCFs). However, perfectly matched dispersion compensation is usually unachievable for the following reasons. Firstly, the CD compensator only performs perfectly matched compensation over a limited bandwidth. Secondly, the CD of an optical fiber is sensitive to temperature variations [16]. Thirdly, the interplay of dispersion with nonlinear effects should be taken into account, resulting in a variation of the amount of CD to be compensated. As nonlinear effects depend on dynamic parameters such as channel allocation and data traffic, the optimum amount of CD to be compensated is also dynamic. These reasons have motivated research on tunable chromatic dispersion compensation. Digital tunable electrical dispersion compensation (TEDC) using a digital signal processor (DSP) has been intensively investigated over the last few years, due to the increased interest in coherent optical communication systems [17]. Such technique is highly flexible and does not require any optical component. However, the processing of CD algorithms increases the DSP's power consumption. Furthermore, the power consumption increases with the baud rate and amount of CD to be compensated. A TODC is a single or multi-channel optical filter with a given bandwidth, and an adjustable phase response which cancels the CD induced to the input optical signal. Many different TODCs have been proposed, as briefly

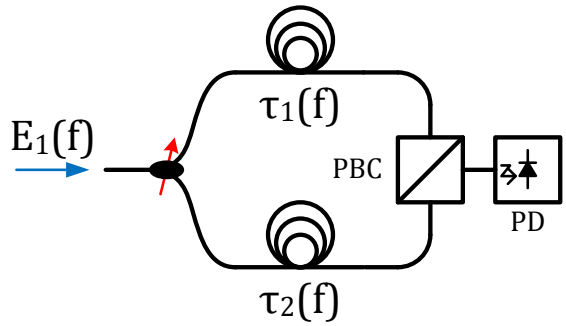

Figure 3.11: Scheme of the TODC with the addition of the dispersive media output signals performed in the electrical domain.

reviewed in the introduction of [J4]. In comparison with electrical tunable dispersion compensators, TODCs have lower power consumption. Furthermore, some implementations enable multi-channel operation with individual channel control. A commercially available example of such implementation is the WaveShaper wavelength selective switch developed by Finisar®.

The previous section described a photonic beamforming system employing a MZDI-TCR based TODL. The TODC proposed in [J4] is an extension of such TODL. The TODC consists in a MZDI-TCR with second-order dispersive media, as depicted in Fig. 3.1. Its frequency response is governed by (3.8) and (3.9).

3.3.1 System implementation

The experiment presented in the previous section revealed that the implementation of a MZDI-TCR with non-dispersive media using discrete components is extremely sensitive to temperature and mechanical perturbations. The same conclusion can be drawn to the proposed TODC. Since an implementation in integrated photonics was not an option, a novel approach with discrete components was investigated. Such approach is depicted in Fig. 3.11. The difference between the proposed scheme and the original one shown in Fig. 3.1 lies in the output optical coupler. The output optical signals of the dispersive media are combined in orthogonal polarizations using a polarization beam combiner (PBC), instead of being coherently added in the optical domain. The photocurrent produced by direct detection of two orthogonally polarized optical signals is given by

$$I(t) = \mathscr{R}\left(||E_x(t)||^2 + ||E_y(t)||^2\right), \tag{3.18}$$

where $\mathscr{R}$ is the responsivity of the PD, and $E_x(t)$ and $E_y(t)$ are the electrical fields of the orthogonally polarized optical signals. Equation (3.18) shows that the direct detection of two orthogonally polarized optical signals yields the same result as detecting each signal independently, and adding the resulting photocurrents thereafter. Hence, the output optical signals of the dispersive media are simultaneously detected and added thereafter. This scheme does not have any coherent optical signal addition. As a result, it is insensitive to environmental perturbations. However, the TODC requires that signal addition is performed before direct detection. Direct detection destroys the phase information carried by optical double sideband (DSB) signals due to spectrum back-folding. Since CD affects the phase of the optical signal, it cannot be effectively compensated after direct detection. Spectrum back-folding does

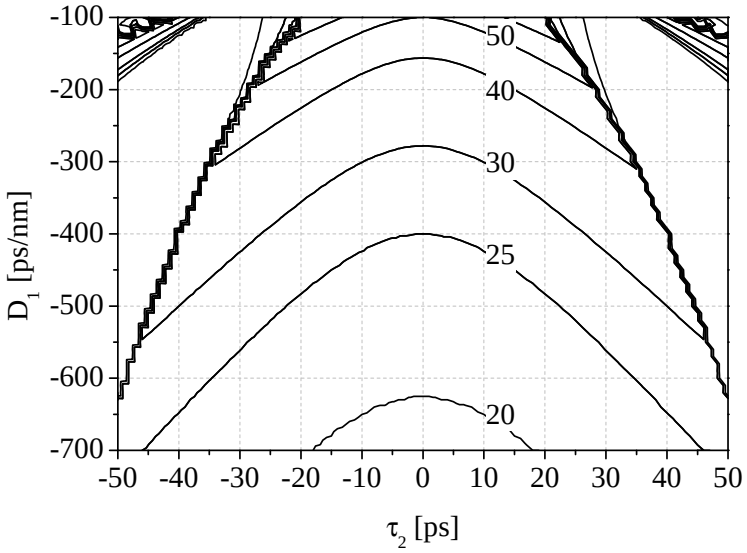

Figure 3.12: -3 dB bandwidth of the TODC's amplitude response obtained for different values of D_1 and τ_2, considering $\theta = \pi/4$.

not occur on direct detection of optical single sideband (SSB) signals [18]. Hence, the phase information carried by an optical SSB signal is not destroyed by direct detection. As a result, the proposed implementation is valid only for optical SSB signals. This is mathematically demonstrated in [J4]. Even though the use of SSB modulation format is only a consequence of the proposed TODC's implementation, it is worth mentioning that such a modulation format has been intensively researched with the purpose of increasing the capacity of optical communication systems [J5]. Optical SSB modulation has attractive features in comparison with DSB modulation. SSB modulation has twice the spectral efficiency, and consequently twice the tolerance to CD. In addition, the phase information of the optical signal is preserved after direct detection, which enables linear electrical CD compensation.

Simulations The adopted simulation scenario considered a non return to zero (NRZ) input optical DSB signal with a bit rate of 40 Gb/s. The frequency response of the TODC, given by (3.8) and (3.9) is valid for the condition

$$\phi_1(f) - \phi_2(f) = 2\pi \left[(D_1 - D_2)\frac{\lambda_o^2}{2c} f^2 + (\tau_1 - \tau_2) f \right] \approx 0. \tag{3.19}$$

The bandwidth over which this condition applies depends on $D_1 - D_2$ and $\tau_1 - \tau_2$. Therefore, one can consider $\tau_1 = 0$ and $D_2 = 0$. This means that the first ODL is purely dispersive, whereas the second one is non-dispersive. The first considered figure of merit was the bandwidth of the TODC's amplitude response. The bandwidth depends on D_1, τ_2 and the coupling ratio's variable θ, being minimum for $\theta = \pi/4$. Figure 3.12 plots the bandwidth as function of D_1 and τ_2. Negative dispersions were considered as the standard single mode fiber (SSMF) has a positive dispersion of 17 ps/nm/km. The bandwidth decreases with the increase of the compensation range, i.e., of D_1, and increases with the increase of $|\tau_2|$. However, the increase of $|\tau_2|$ results in ripple on both amplitude and group delay responses. Such ripple increases

with $|\tau_2|$. When the amplitude ripple reaches 3 dB the contour lines in Fig. 3.12 merge into two lines, one for $\tau_2 < 0$ and other for $\tau_2 > 0$. The optical SSB signal has a spectral width of approximately 20 GHz. Therefore, the TODC should have a bandwidth slightly higher than 20 GHz with the purpose of maximizing the compensation range, while keeping the condition (3.19) valid within the entire spectral bandwidth of the optical SSB signal. Furthermore, $|\tau_2|$ should be low in order to minimize the ripple. By taking into account these guidelines, D_1 was set at -340 ps/nm. This results in a -3 dB bandwidth of 27 GHz for $\tau_2 = 0$. Such bandwidth is sufficiently high in order to set τ_2 at 0, thereby avoiding amplitude and group delay ripple.

The input optical signal is DSB modulated. Hence, it must be converted to SSB modulation. This can be achieved using optoelectronic filters or all-optical techniques, as discussed in [J5]. The use of a sideband suppression optical filter (SSOF) is a well known all-optical technique, and was the employed approach. A detuned optical filter with a given bandwidth is used to filter only one sideband of an input optical DSB signal, therefore converting it to SSB. The quality of the output optical SSB signal depends on the transfer function of the SSOF, which was optimized for the input optical DSB signal. The optimization of the SSOF's transfer function was based on simulations performed in optical simulation platform (OSiP) [19], which is an in-house software written in Matlab®. The important parameters of the input optical DSB signal are its spectral width, which can be defined by the frequency response of the MZM that generates the signal, and the ER. The ER depends on the spectral power of the OC, which is affected by the SSOF. The frequency response of the MZM was modeled by a third-order Bessel filter with a -3 dB bandwidth of 30 GHz, and the ER of the input optical DSB signal was of 10 dB. These parameters provided an optical DSB signal very similar to the one obtained in the experiments. The parameters of the SSOF are the amplitude and group delay responses, bandwidth, and frequency detuning relatively to the OC frequency of the input optical signal. The amplitude response of the optical filter was modeled by a second-order super-Gaussian function. The group delay response was constant over frequency in order to avoid spectral phase distortion. Therefore, the optimization parameters were the bandwidth and frequency detuning. The figures of merit of the optimization were the eye opening penalty (EOP) of the filtered optical signal, the filtering loss, and the obtained sideband suppression ratio (SSR). The EOP (in dB) is given by

$$\mathrm{EOP} = -10 \log_{10} \frac{O_s}{O_{\mathrm{ref}}}, \tag{3.20}$$

where O_s and O_{ref} are the eye apertures obtained at the input of the decision circuit of the analyzed and reference signals, respectively. The reference signal was an optical DSB signal with an ER of 9 dB. The SSR is the difference in dB between the power of the spectral components located 20 GHz apart from the OC frequency. The optimization results are shown in Fig 3.13. A detailed analysis of the obtained curves can be found in [J4] and [J5]. The purpose of the optimization was to find a bandwidth and frequency detuning which results in reduced signal distortion, improved resilience to CD, high SSR and low filtering losses. The first two goals were assessed through the measurement of the EOP of the detected optical SSB signal after being subject to cumulative dispersions of 0 and 85 ps/nm, respectively. According to these guidelines, a bandwidth of 40 GHz and a frequency detuning of 23 GHz were adopted. These parameters correspond to the blue dot shown in Fig. 3.13. Even though higher bandwidths provide lower EOPs without significantly affecting the SSR and filtering loss, such improvement is negligible. Other functions for the amplitude response were also

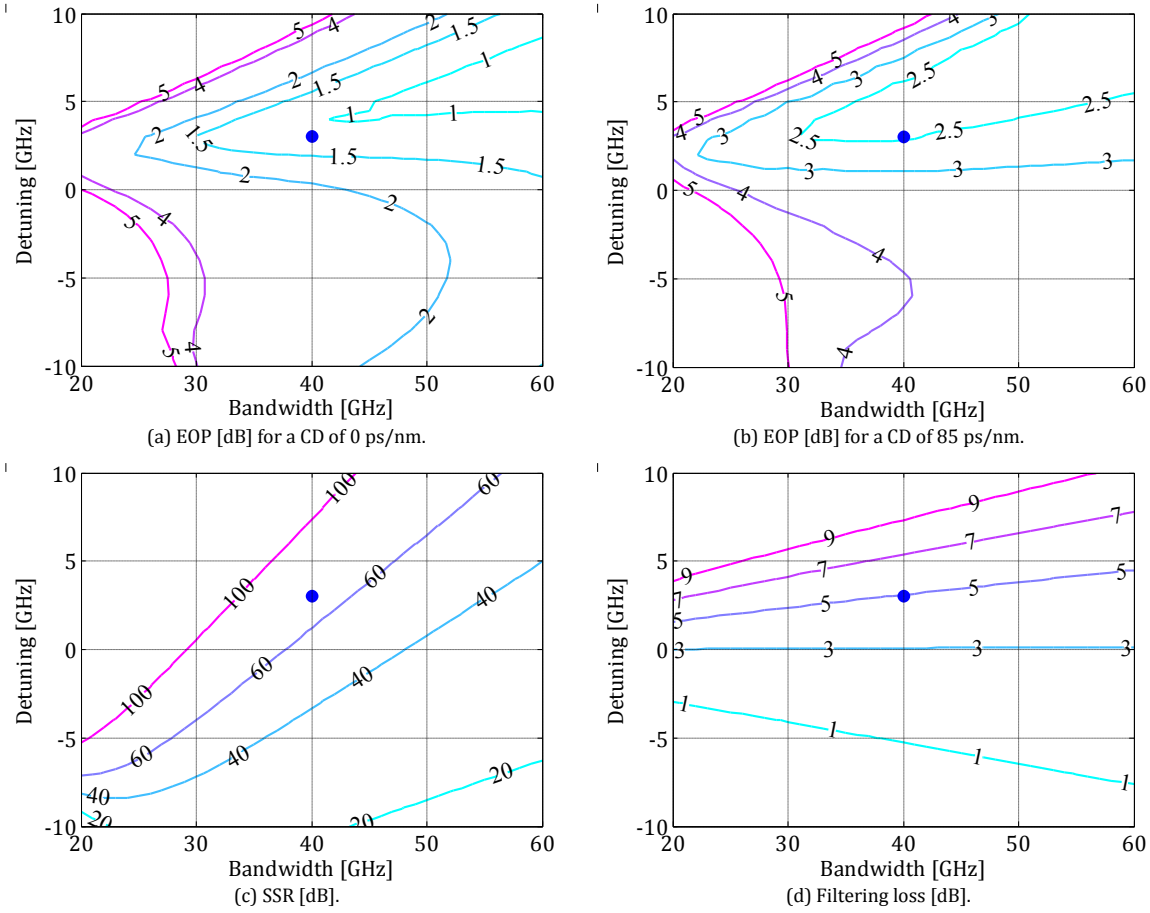

(a) EOP [dB] for a CD of 0 ps/nm.

(b) EOP [dB] for a CD of 85 ps/nm.

(c) SSR [dB].

(d) Filtering loss [dB].

Figure 3.13: Optimization results of the SSOF's parameters. Half of the bandwidth was subtracted to the frequency detuning. The blue dot represents the optimum bandwidth (40 GHz) and detuning (23 GHz).

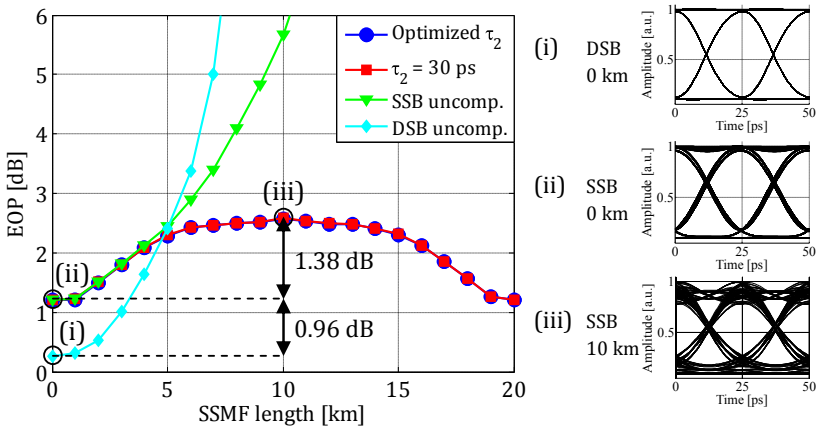

Figure 3.14: Results obtained from simulations considering linear transmission. Insets: eye diagrams of the detected optical signals.

assessed, such as super-Gaussian with higher orders, Blackman and hyperbolic tangent. No improvements were observed in comparison with the adopted second-order super-Gaussian function.

After defining the specifications of the TODC and SSOF, the performance of the SSOF together with the TODC was assessed. CD was added to the optical signals. The dispersion compensated optical SSB signals were compared with uncompensated optical SSB and DSB signals. Fixed and optimized values of τ_2 for each fiber length were assessed. SSMF lengths from 0 up to 20 km were considered, as the corresponding cumulative CDs cover the entire compensation range of the TODC. The figure of merit was the EOP of the detected optical signals. The obtained results are shown in Fig. 3.14. A detailed analysis of these results can be found in [J4]. Sideband suppression optical filtering results in an EOP difference between the optical SSB and DSB signals of 0.96 dB. Such difference decreases as the cumulative CD increases, due to the higher resilience to CD of the optical SSB signal. The TODC's transfer function is ideal only for fiber lengths of 0 and 20 km, resulting in no compensation penalty for such fiber lengths. However, the bandwidth of the TODC's amplitude response varies with the fiber length, reaching its minimum at a length of 10 km, i.e., half the compensation range. This explains why the compensation gain for SSMF lengths lower than 5 km is negligible, and also the maximum compensation penalty of 1.38 dB at a fiber length of 10 km. The optimization of τ_2 for each considered fiber length did not yield any improvement. The minimum bandwidth of the TODC's amplitude response is already sufficiently broad for $\tau_2 = 30$ ps. Therefore, there is no advantage in trading off frequency response degradation for higher bandwidth by tuning τ_2. It should be noted that 30 ps was merely a value used in simulations, which in theory corresponds to $\tau_2 = 0$. These simulations proved very helpful in predicting and analyzing the experimental results.

Experiment The previously discussed simulations have shown that the performance of the CD compensation depends on the optimized parameters of the SSOF and dispersive media. Therefore, the experimental implementation of these devices should faithfully follow the optimized parameters. The SSOF and the first ODL were implemented in FBGs operating in reflection. Such devices allow the much needed custom made design at a reduced cost, and its

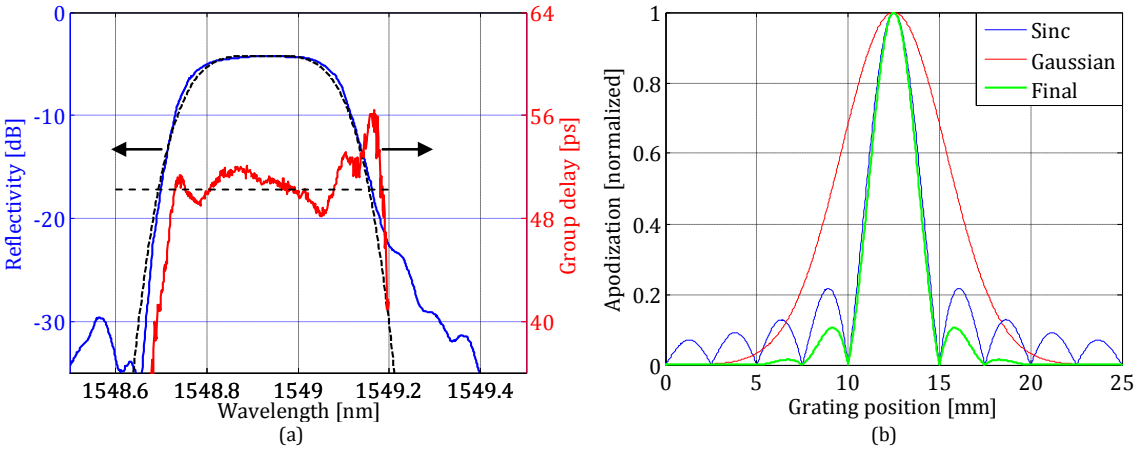

Figure 3.15: (a) Reflectivity and group delay responses of the written FBG. The dashed lines represent the target responses. (b) the final apodization function was the product between a sinc and a super-Gaussian function.

production can be made with a relatively simple experimental apparatus. The basic design rule of a FBG is that the Fourier transform of the apodization function should be based on the target filter's transfer function [20]. This rule is particularly accurate for weak gratings, i.e., with a maximum reflectivity lower than −3 dB. The design and simulation of all FBGs described in this thesis were performed on a Matlab® simulation software written by the author. The software was designated by gratings in OSiP (GOSiP). It allows designing arbitrary apodization and grating period profiles. The frequency response of a FBG is calculated through the transfer matrix method [20], and can be used in OSiP.

The SSOF should have a second-order super-Gaussian reflectivity with a −3 dB bandwidth of 40 GHz, and a constant group delay response. According to the basic design rule, a super-Gaussian reflectivity is achieved using a super-Gaussian apodization. Due to the resonant nature of the FBG, the corresponding group delay response is far from being constant over frequency. This can be observed in [21, Fig. 3.11]. As firstly proposed in [22] and explored in [J5], both a super-Gaussian reflectivity and a constant group delay response can be achieved using a different apodization function. Such apodization function is the product of a sinc and super-Gaussian functions. The sinc function alone yields a rectangularly shaped reflectivity and a rippled group delay response. The application of the super-Gaussian function transforms the rectangular shape into a super-Gaussian function, and significantly smooths the group delay ripple. As a result, a super-Gaussian reflectivity and a quasi-constant group delay are achieved. The order of the super-Gaussian reflectivity can be optimized through the parameters of the super-Gaussian function. Further details about the optimization and design of the FBG can be found in [J5]. The reflectivity and group delay responses of the written FBG and the employed apodization functions are shown in Fig. 3.15. The measured reflectivity closely matches the target amplitude response. The group delay ripple is of about 8 ps within the −10 dB passband. The deviations from the target responses are mainly due to experimental errors which occurred during the writing process of the FBG. These results prove that the implementation of the SSOF in such a complex FBG is feasible.

The first ODL should have a cumulative CD of −340 ps/nm, and a sufficiently broad band-

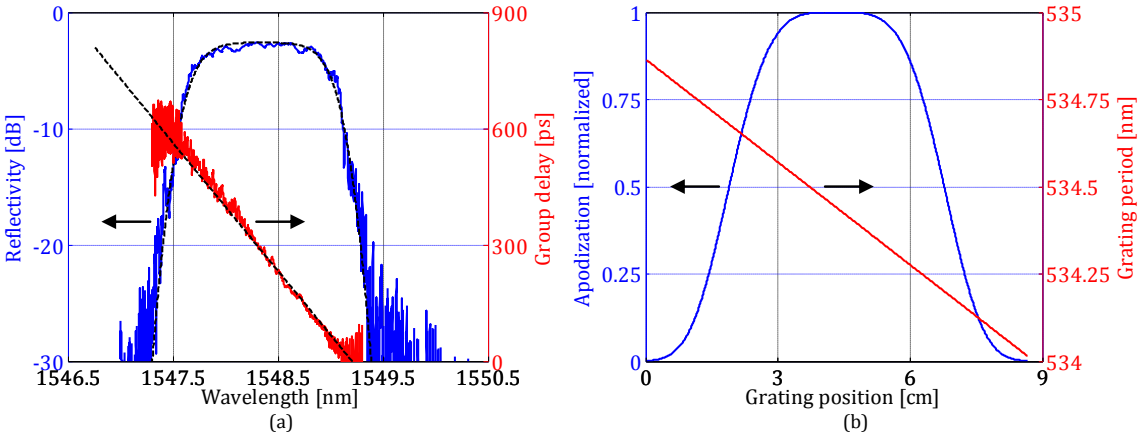

Figure 3.16: (a) Reflectivity and group delay responses of the written LCFBG. The dashed lines represent the target responses. (b) super-Gaussian apodization function and grating period.

width to avoid narrow optical filtering. A linearly chirped fiber Bragg grating (LCFBG) was designed to provide the target cumulative CD over a bandwidth of 160 GHz. The apodization function consisted in a fourth-order super-Gaussian function. The purpose of the apodization was to reduce the amplitude of the reflectivity's sidelobes, but more importantly to reduce the group delay ripple [20]. Further details on the characteristics of the LCFBG can be found in [J4]. The reflectivity and group delay responses of the written LCFBG and the employed apodization and grating period profiles are shown in Fig. 3.16. The measured reflectivity closely matches the target amplitude response. However, a slightly lower cumulative CD of -370 ps/nm was obtained due to imperfect calibration of the FBG writing system. Such deviation did not limit the subsequent experiments. It is interesting to note that the previously mentioned basic FBG design rule is evident when comparing Fig. 3.16 (b) with (a). Considerable amplitude and group delay ripple is observable in Fig. 3.16 (a). Even though the FBG depicted in Fig. 3.15 has a more complex apodization profile, it has a constant grating period. On the other hand, the LCFBG has an equally complex apodization profile and a linearly chirped grating period. Furthermore, the LCFBG was almost four times longer than the SSOF FBG. The combination of a complex apodization profile with a non-constant grating period over a long grating length is extremely demanding on a FBG writing system not based on a chirped phase mask [21], as was the case. Deviations of the grating period at certain positions of the grating caused amplitude and group delay ripple at certain wavelengths.

The second ODL should be non-dispersive. Similarly to the first ODL, its bandwidth should be sufficiently broad to avoid narrow optical filtering. The induced time delay should be tunable with the purpose of precisely setting $\tau_2 = \tau_1$. In addition, the ODL should also be reflective. As shown later in the text, there are advantages in having both ODLs operating in reflection. A nearly ideal implementation resorting to a free-space TODL and a fiber mirror reflector was employed. The TODL provided continuous time delay tunability, whereas the fiber mirror reflector had an almost perfect frequency response and negligible insertion losses.

The performance of the TODC was assessed using the experimental setup shown in Fig. 3.17. The experiment comprised the steps of generating a 40 Gb/s NRZ optical DSB signal,

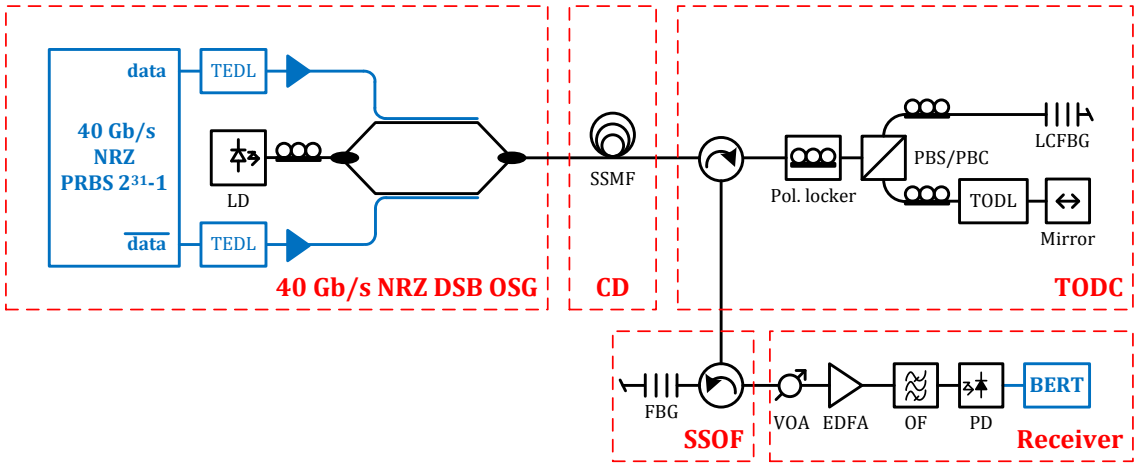

Figure 3.17: Experimental setup used to assess the performance of the proposed TODC.

adding CD, compensating the added CD, performing sideband suppression optical filtering and detecting the resulting optical signal. Since the addition of CD, tunable optical dispersion compensation and sideband suppression optical filtering are linear operations, the order by which they are performed is irrelevant. The 40 Gb/s NRZ DSB optical signal generator (OSG) was based on a DE MZM operating in push-pull. Such operation provides chirp-free modulation, which is required as the output optical signal is converted to SSB modulation afterwards. The TEDLs and electrical paths used in the driving circuitry of the MZM were carefully adjusted to obtain identical time delays and signal amplitudes at the electrodes of the MZM's. CD was added to the modulated optical signal using spools of SSMF. Spools with different fiber lengths provided different amounts of cumulative CD. The optical power at the input of the SSMF was approximately 0 dBm, which is sufficiently low to avoid nonlinear effects. The TODC's setup takes advantage of having both ODLs operating in reflection. The input optical coupler with TCR was composed by the polarization locker (Thorlabs PL100S) and PBS. The coupling ratio depends on the SOP of the PBS's input optical signal, which was defined by the polarization locker. This device is basically a PC with a feedback loop, which enables locking an arbitrary output SOP independently of the input SOP. The microsecond response time of the polarization locker to variations of the input SOP significantly minimized the polarization sensitivity of the TODC. The LCFBG and fiber mirror reflector presented a non-negligible polarization sensitivity. Two PCs were used to maximize the power of the reflected signals. The reflected signals were combined in orthogonal SOPs by the PBC, which was therefore simultaneously a PBS and a PBC. The polarization transformation produced on the reflected signals by the polarization locker was not important, since all the components of the SSOF and receiver were polarization insensitive. After DSB to SSB modulation format conversion performed by the SSOF the optical signal was converted to the electrical domain using an optically pre-amplified receiver. A quantitative description of the experimental setup can be found in [J4].

The center wavelengths of the LCFBG and SSOF were adjusted by tuning the longitudinal strain and temperature, respectively. As observed in Fig. 3.16 (a), excellent fitting between the target and measured group delays and a reduced group delay ripple is obtained within the wavelength interval of 1548.25 nm and 1548.75 nm. The strain applied to the LCFBG was

tuned until such wavelength interval was centered with the input optical signal. The strain-based tuning mechanism enabled the required large wavelength detuning at the cost of being highly sensitive to mechanical vibrations. This was deleterious in the TODC's operation, as it induced a random fluctuation of τ_2. The wavelength detuning of the SSOF FBG was considerably lower, enabling the use a temperature-based tuning mechanism. The temperature of the FBG and thereby the detuning of the SSOF were precisely tuned using a thermoelectric device.

The input optical DSB signal can be converted to SSB by suppressing either the lower or the upper sideband. The terms "upper" and "lower" are here associated with higher and lower wavelengths, respectively. For an ideally chirp-free input optical DSB signal it is irrelevant which sideband is removed. In practice, there is a residual chirp due to imperfections in the modulation circuitry and in the MZM itself. Furthermore, the measured group delay of the FBG (Fig. 3.15 (a)) is not symmetric with respect to the center wavelength. The choice of the suppressed sideband was done by experimentally assessing both cases. The temperature of the FBG was adjusted to a set a positive and then negative wavelength detuning. The upper sideband was chosen as the suppressed one, since the obtained eye diagram was the less distorted.

The system's performance was firstly assessed from measurements of optical spectra and eye diagrams. The results are shown in Fig. 3.18 and 3.19. The optical spectra show that the upper sideband was significantly suppressed, whereas the lower sideband was actually enhanced. A SSR of 28 dB was obtained. These results are discussed in detail in [J5]. The eye diagrams were measured using an optical sampling scope (OSS) (PicoSolve PSO101) with an equivalent electrical bandwidth higher than 500 GHz. In comparison with the simulation results depicted in Fig. 3.14 inset (ii), the eye diagram obtained for optical DSB modulation in back-to-back has lower rise and fall times. This was expected since in simulations the bandwidth of the electrical receiver was of 30 GHz. The Q-factor penalties and EOP differences cannot be directly compared. Nonetheless, such different receiver bandwidths explain why the Q-factor penalty of 5.8 dB obtained after DSB to SSB conversion is higher than the EOP penalty of 0.96 dB depicted in Fig. 3.14. The eye diagrams obtained experimentally and in simulations for optical SSB modulation considering fiber lengths of 0, 5 and 10 km without CD compensation are compared in [J5, Fig. 5]. A nearly perfect match was obtained, which again shows that the implementation of the SSOF in a FBG was successful. The open eye diagrams obtained for a fiber length of 20 km show that the LCFBG correctly compensates the cumulative CD. These eye diagrams also prove that the amplitude and group delay ripple of the LCFBG were negligible, as no distortion is observed. The effectiveness of the CD compensation performed by the TODC can be assessed by comparing the eye diagrams of the last two columns in Fig. 3.19. Perfect compensation is achieved for fiber lengths of 0 and 20 km, which corresponds to a polarization rotation angle of $\theta = 90°$ and $\theta = 0°$. Partial compensation is obtained for fiber lengths of 5 and 15 km using the same angles. However, for a fiber length of 10 km with $\theta = 90°$ the eye is severely distorted. Tunable optical dispersion compensation clearly improves the eye opening when perfect compensation cannot be achieved. Identical Q-factors were obtained for fiber lengths of 0 and 20 km, and 5 and 15 km. The lowest Q-factor was obtained for a fiber length of 10 km. These results agree with the simulation results shown in Fig. 3.14. The measured polarization rotation angles were compared with the ones obtained in simulation. A maximum difference of only 7° was obtained. Such difference is explained in [J4].

The qualitative assessment of the system's performance was based on bit error rate (BER)

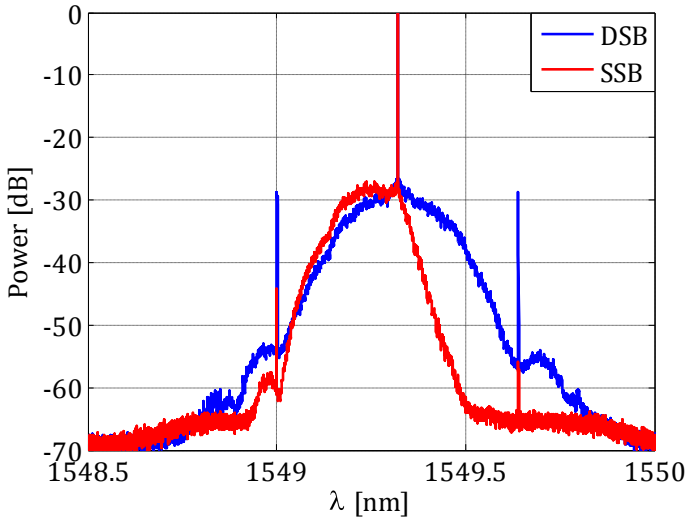

Figure 3.18: Optical spectra of the optical DSB and SSB signals with a resolution of 0.8 pm.

SSMF length [km]	DSB signal	SSB signal	Comp. SSB signal
0	θ=90° Q=24.6 dB	θ=90° Q=18.8 dB	θ=90° Q=18.8 dB
5	θ=90°	θ=90° Q=11.0 dB	θ=58° Q=13.6 dB
10	θ=90°	θ=90°	θ=42° Q=12.5dB
15	θ=0°	θ=0° Q=12.8 dB	θ=30° Q=14.0 dB
20	θ=0° Q=23.2 dB	θ=0° Q=18.3 dB	θ=0° Q=18.3 dB

Figure 3.19: Eye diagrams of the detected optical signals.

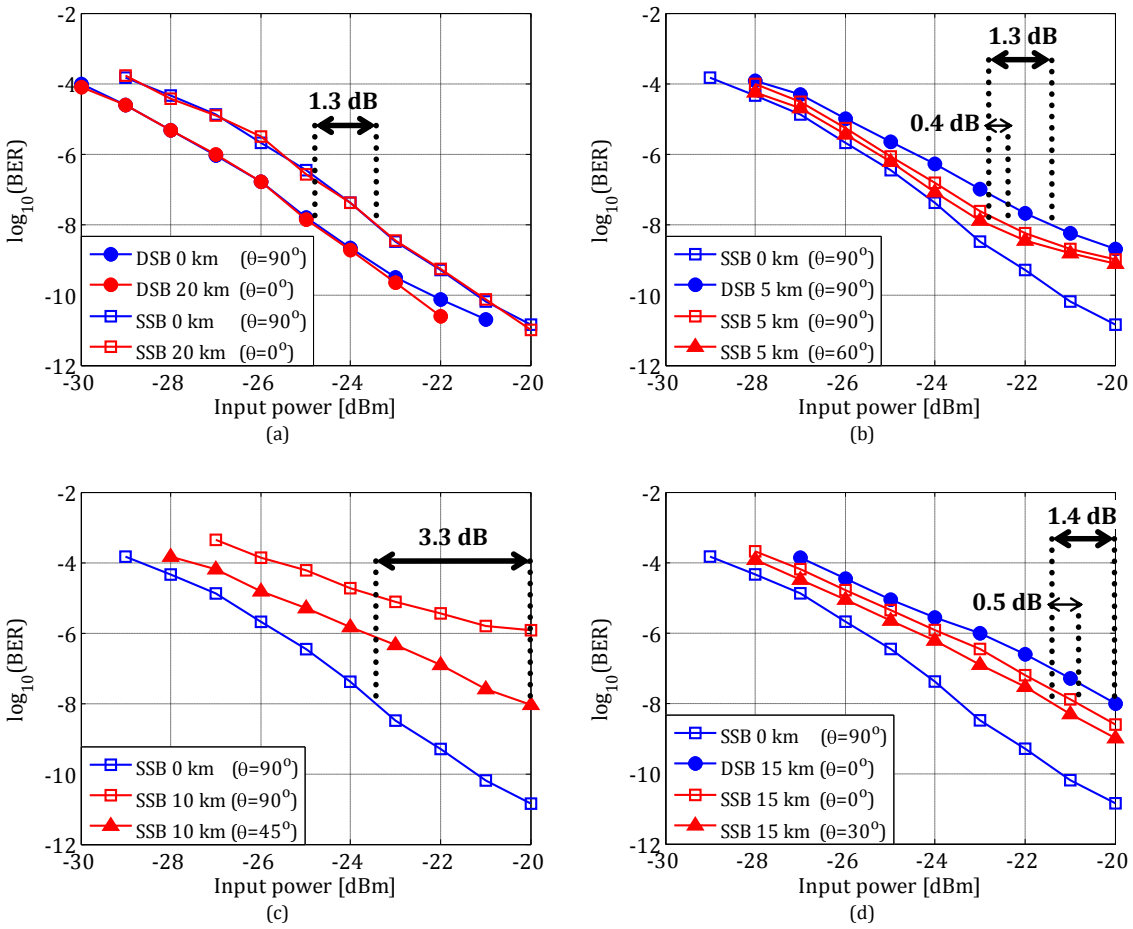

Figure 3.20: BERs measured for different output powers of the VOA.

measurements. The results are shown in Fig. 3.20. The BER of the optical DSB signal considering a fiber length of 10 km could not be measured due to severe distortion, as observed in the corresponding eye diagram of Fig. 3.19. In accordance with the eye diagrams, the BER curves also agree with the simulation results shown in Fig. 3.14. Identical compensation gains were obtained for fiber lengths of 5 and 15 km. In addition, the highest compensation gain was achieved for a fiber length of 10 km. The compensation gains are referenced at a BER of 10^{-8}, and not 10^{-9} as usually done. The reason was that the compensated optical signal for a fiber length of 10 km had a BER floor at 10^{-8}. A detailed analysis of the BER curves can be found in [J4].

3.4 Conclusions

This chapter has shown how the addition of TCR to a MZDI was explored to implement a photonic beamforming system for a PAA and a TODC. The former system relies on a MZDI-TCR with non-dispersive media, while the latter employs a MZDI-TCR with second-order dispersive media. The MZDI-TCRs are used as TODLs, in which the tunability is enabled by the TCR.

The photonic beamforming system is based on N MZDI-TCRs with non-dispersive media implemented on the polarization domain. The result of such implementation is that the N MZDI-TCRs share the same input optical coupler and delay lines, which in turn are implemented using a single piece of PMF. Simulation tests have shown that the system can handle RF signals carrying broadband data signals with negligible beam squinting and distortion. However, significant beam squinting and distortion are caused by detuning between the OC frequency and the center frequency of the N interferometers. A simple proof of concept experiment demonstrated that the implementation of the beamforming system using discrete components does not offer a stable control of such frequency detunings. This problem can be solved resorting to an implementation in integrated photonics.

The TODC is based on a MZDI-TCR with second-order dispersive media. In order to avoid stability problems analogous to the ones identified in the proof of concept experiment of the photonic beamforming system, part of the MZDI-TCR was implemented on the electrical domain. The output optical signals of the ODLs were combined in orthogonal polarizations. The direct detection of the resulting signal automatically resulted in the addition of the orthogonally polarized signals. The mathematical analysis of such system proved that it is limited to optical SSB signals. A simulation scenario considering a CD compensation range of -340 ps/nm up to 0 ps/nm was defined. The parameters of an all-optical DSB to SSB modulation format converter based on a SSOF were optimized. The performance of the SSOF together with the TODC was firstly investigated in simulations. Signal degradation is caused by sideband suppression optical filtering and non-ideal dispersion compensation. Ideal compensation is obtained only for cumulative CDs of 0 or 340 ps/nm. However, at half the compensation range, i.e., 170 ps/nm, the bandwidth of the TODC is minimum. Therefore, a maximum EOP of 1.38 dB is achieved at half the compensation range relatively to back-to-back operation. An experiment based on the defined simulation scenario was carried out to attest the simulation results. The TODC and an ODL were implemented in FBGs. The second ODL was implemented with a free-space TODL and a fiber mirror reflector. The frequency responses of the SSOF and ODLs corresponded closely with the target transfer functions. The measured eye diagrams, optical spectra and BER curves are completely in accordance with the simulation results. This proves that the proposed implementation of the TODC did not have stability problems.

A very important detail of the MZDI-TCR is the trade-off between bandwidth and time delay tuning range. In the photonic beamforming system, the required time delay tuning range of the MZDI-TCR-based TODLs is proportional to the number of antenna elements N. Therefore, the bandwidth of the photonic beamforming system decreases with the increase of N. Likewise, the CD tuning range of the TODC decreases with the increase of the bandwidth.

Chapter 4

Photonic devices based on nonlinear optical signal processing

This chapter is devoted to photonic devices which explore different nonlinear optical signal processing techniques with the purpose of mixing optical signals. A theoretical introduction to photonic mixing in general and to parametric processes in second- and third-order nonlinear media is presented in the first section. Section 4.2 presents a IFMS based on mixing two differentially delayed copies of the input RF signal. Photonic mixing by means of signal remodulation is employed. Cascaded parametric processes in a second-order nonlinear PPLN waveguide are investigated in section 4.3. An input OTDM signal is mixed with two CW pumps by means of cascaded sum-frequency generation with difference-frequency generation (cSFG-DFG), thereby resulting in wavelength conversion. Section 4.4 presents a flexible OTDM to WDM converter based on FWM in a HNLF. The converted WDM channels are the product of FWM between the input OTDM signal and a multi-wavelength sampling pulse train (SPT). The conclusions of this chapter are drawn in section 4.5.

4.1 Operation principles

The photonic systems presented in this chapter are based on the scheme shown in Fig. 4.1. N_s input optical signals are individually delayed by non-dispersive ODLs. The delayed optical signals are incoherently combined with the purpose of avoiding any filtering effects. The combined optical signals are then mixed. The output optical signal can be expressed by

$$O_1(t) = \left[\sum_{a=1}^{N_s} E_a(t-\tau_a)\right]^{\mathrm{O_{Mix}}} = \left[\sum_{a=1}^{N_s} E_{a,\mathrm{BB}}(t-\tau_a)\exp\left[j2\pi f_a(t-\tau_a)\right]\right]^{\mathrm{O_{Mix}}}, \tag{4.1}$$

where $E_{a,\mathrm{BB}}(t)$ is the baseband signal modulated onto the OC with a frequency of f_a. The order of the mixer, $\mathrm{O_{Mix}}$, defines how many input optical signals are mixed all together. The nonlinear optical signal processing systems presented in this chapter are based on three different mixing mechanisms, which are signal remodulation, FWM in optical fiber and cascaded parametric processes in a PPLN waveguide. Signal remodulation has a straightforward mathematical derivation that is presented in the next section.

The response of a dielectric medium to light is nonlinear when high-intensity electromagnetic fields are applied [23]. As a result, the polarization **P** induced by electric dipoles can be

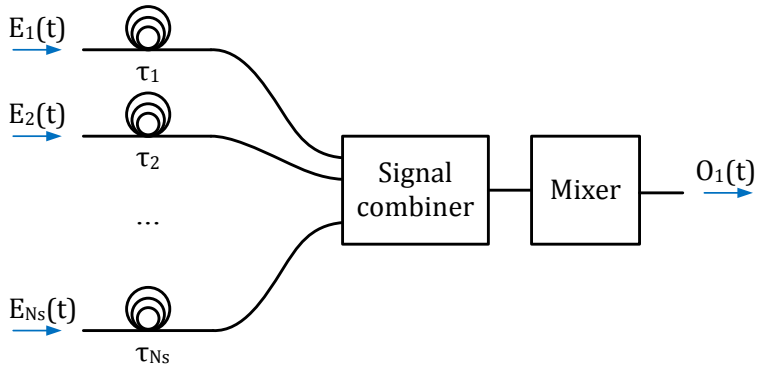

Figure 4.1: General scheme of the nonlinear optical signal processing systems presented in the following sections.

expressed by

$$\mathbf{P} = \varepsilon_0 \left[\chi^{(1)} \cdot \mathbf{E} + \chi^{(2)} : \mathbf{EE} + \chi^{(3)} \vdots \mathbf{EEE} + \dots \right], \tag{4.2}$$

where ε_0 is the vacuum permittivity, $\chi^{(a)}$, $a = 1, 2, \dots$ is the a^{th} order susceptibility and $\mathbf{E}$ is the electromagnetic field. The linear susceptibility $\chi^{(1)}$ represents the dominant contribution to $\mathbf{P}$. The second-order susceptibility $\chi^{(2)}$ is responsible for nonlinear effects such as second-harmonic generation (SHG), sum-frequency generation (SFG) and difference-frequency generation (DFG). The third-order susceptibility $\chi^{(3)}$ mainly results in FWM, SPM and XPM. As the dielectric medium of optical fibers is silica, the susceptibility terms in (4.2) other than first and third-order can be neglected [23]. Consequently, the optical fiber behaves like a third-order photonic mixer, i.e., $\mathrm{O}_{\mathrm{Mix}} = 3$, due to the third-order susceptibility of silica. A third-order photonic mixer can be characterized by four optical signals which include $N_s = 3$ input signals and the output signal, given by

$$\mathbf{E} = \frac{1}{2}\hat{x} \sum_{a=1}^{4} \Big(E_{a,\mathrm{BB}} \cdot \exp\left[j(k_a z - \omega_a t) \right] + \text{c.c.} \Big), \tag{4.3}$$

where k_a is the propagation constant given by $k_a = n_a \omega_a / c$, in which n_a is the refractive index, and $\omega_a = 2\pi f_a$. c.c. means complex conjugate. All optical signals are linearly polarized along the same axis $\hat{x}$. The third-order polarization term of (4.2), $\mathbf{P}_{\mathrm{NL}}$, can be derived from (4.2) and (4.3),

$$\mathbf{P}_{\mathrm{NL}} = \chi^{(3)} \vdots \mathbf{EEE} = \frac{1}{2}\hat{x} \sum_{a=1}^{4} \Big(P_a \cdot \exp\left[j(k_a z - \omega_a t) \right] + \text{c.c.} \Big). \tag{4.4}$$

The terms P_a are composed by a significant number of terms involving the product of three optical signals. For example, P_4 is given by

$$\begin{aligned} P_4 = \frac{3}{4}\varepsilon_0 \chi^{(3)} \Big[& |E_{4,\mathrm{BB}}|^2 E_{4,\mathrm{BB}} + \\ & 2\left(|E_{1,\mathrm{BB}}|^2 + |E_{2,\mathrm{BB}}|^2 + |E_{3,\mathrm{BB}}|^2 \right) E_{4,\mathrm{BB}} + \\ & 2E_{1,\mathrm{BB}} E_{2,\mathrm{BB}} E_{3,\mathrm{BB}} \cdot \exp(j\theta_+) + 2E_{1,\mathrm{BB}} E_{2,\mathrm{BB}} E^*_{3,\mathrm{BB}} \cdot \exp(j\theta_-) + \dots \Big], \end{aligned} \tag{4.5}$$

where θ_+ and θ_- are given by

$$\theta_+ = (k_1 + k_2 + k_3 - k_4)\, z - (\omega_1 + \omega_2 + \omega_3 - \omega_4)\, t \tag{4.6}$$

$$\theta_- = (k_1 + k_2 - k_3 - k_4)\, z - (\omega_1 + \omega_2 - \omega_3 - \omega_4)\, t. \tag{4.7}$$

The first and second lines of (4.5) represent the SPM and XPM nonlinear effects, respectively. The remaining terms result in FWM. These are the important terms for the photonic mixer, as the three input optical signals are mixed all together yielding the output optical signal with an angular frequency of ω_4. The power of the terms produced by FWM and consequently the mixing efficiency depends on the factors $\exp(j\theta_+)$, $\exp(j\theta_-)$, etc. These factors depend on the phase-matching between $E_{4,\mathrm{BB}}$ and P_4, governed by θ_+, θ_-, or a similar quantity. The FWM term containing θ_+ results in an output optical signal with an angular frequency of $\omega_4 = \omega_1 + \omega_2 + \omega_3$. Such a significant difference between the frequencies of the output optical signal and input optical signals usually results in very reduced phase-matching. This term can therefore be neglected. The FWM term containing θ_- produces an output optical signal with an angular frequency of $\omega_4 = \omega_1 + \omega_2 - \omega_3$. The phase-matching requirement for this term is given by

$$\Delta k = k_1 + k_2 - k_3 - k_4 = \frac{n_1\omega_1 + n_2\omega_2 - n_3\omega_3 - n_4\omega_4}{c} = 0. \tag{4.8}$$

The phase-matching requirement depends on the refractive index of the optical fiber, whose variation leads to CD. In general, there are two ways of maximizing the phase-matching requirement. The first consists in carefully optimizing the material composition, geometry and length of the optical fiber so that CD is minimized. Such optimization usually also includes the maximization of the third-order susceptibility. The other way is by densely spacing the four optical signals around the zero-dispersion wavelength, with the purpose of having a low spectral bandwidth in which the approximation $n_1 \approx n_2 \approx n_3 \approx n_4$ is valid. It is even possible to have $\omega_1 = \omega_2$. This case corresponds to degenerate FWM. It occurs when an optical signal is mixed with itself and with another optical signal. A seminal study about the mechanisms involved in FWM efficiency can be found in [24].

Lithium niobate ($LiNbO_3$) is a dielectric medium whose susceptibility terms in (4.2) other than first and second-order can be neglected [25]. Therefore, a lithium niobate waveguide can be used as a second-order photonic mixer, i.e., $\mathrm{O_{Mix}} = 2$. A similar analysis to the one previously performed on an optical fiber can be performed [25]. Three optical signals are required to characterize a second-order photonic mixer. In a first approach, the SOP of the optical signals is assumed arbitrary. The second-order polarization term of (4.2) is given by

$$\mathbf{P}_{\mathrm{NL}} = \chi^{(2)} : \mathbf{EE} = \frac{1}{2}\sum_{a=1}^{3} P_a \cdot \exp\left[j(k_a z - \omega_a t)\right] + \text{c.c.}. \tag{4.9}$$

Equation (4.9) can be easily expanded considering only the two input optical signals, $\mathbf{E_1}$ and $\mathbf{E_2}$,

$$\begin{aligned}\mathbf{P}_{\mathrm{NL}} = \frac{1}{4}\varepsilon_0\chi^{(2)}\Big[&E_{1,\mathrm{BB}}^2 \exp\left[j\left(2\omega_1 t - 2k_1 z\right)\right] + E_{2,\mathrm{BB}}^2 \exp\left[j\left(2\omega_2 t - 2k_2 z\right)\right] + \\ &2E_{1,\mathrm{BB}}E_{2,\mathrm{BB}} \exp\left[j\left((\omega_1 + \omega_2)t - (k_1 + k_2)z\right)\right] + \\ &2E_{1,\mathrm{BB}}^* E_{2,\mathrm{BB}} \exp\left[j\left((\omega_2 - \omega_1)t - (k_2 - k_1)z\right)\right] + \text{c.c.} + \\ &E_{1,\mathrm{BB}}E_{1,\mathrm{BB}}^* + E_{2,\mathrm{BB}}E_{2,\mathrm{BB}}^*\Big].\end{aligned} \tag{4.10}$$

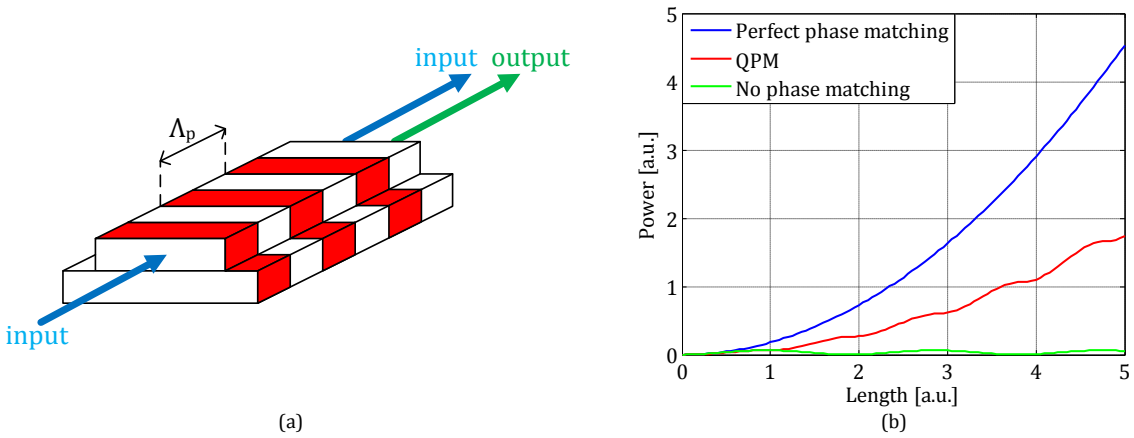

Figure 4.2: (a) Scheme of a PPLN waveguide. (b) depiction of the power of the output optical signal for different cases of phase-matching.

The first two terms describe SHG. The third and fourth terms represent SFG and DFG, respectively. The last two terms concern the rectification of the input optical signals, and are not important. The phase-matching requirements for SHG, SFG and DFG are given by

$$\Delta k_{\mathrm{SHG}}|_{\omega_3=2\omega_1} = k_3 - k_1 = 0 \tag{4.11}$$

$$\Delta k_{\mathrm{SHG}}|_{\omega_3=2\omega_2} = k_3 - k_2 = 0 \tag{4.12}$$

$$\Delta k_{\mathrm{SFG}}|_{\omega_3=\omega_1+\omega_2} = k_3 - k_2 - k_1 = 0 \tag{4.13}$$

$$\Delta k_{\mathrm{DFG}}|_{\omega_3=\omega_2-\omega_1} = k_3 - k_2 + k_1 = 0. \tag{4.14}$$

These expressions are very similar to (4.8). However, the phase-matching mechanisms involved in second-order nonlinear media are quite different from the ones involved in FWM. Firstly, the frequency of the output optical signal produced by either SHG, SFG or DFG is much higher or much lower than at least one of the input optical signals. Therefore, the refractive index n_3 is very different from n_1 or n_2. The birefringence of the lithium niobate crystal was explored to minimize such difference, and therefore to achieve phase-matching [25]. This explains why the SOP of the optical signals was considered arbitrary. However, such technique does not enable a flexible design of the phase-matching condition, and poses propagation problems when the SOPs of the optical signals are different from the required. A different technique consists in poling the lithium niobate crystal. The poling inverts the electrical domains of the crystal, and consequently switches the sign of the nonlinear coefficient. Since the poling pattern is often periodic with a period of Λ_p, a waveguide employing this technique is commonly referred as a PPLN waveguide. Such a device is depicted in Fig. 4.2 (a). Figure 4.2 (b) depicts the evolution of the average power of the output optical signal resulting from SHG, SFG or DFG for cases of no phase-matching, quasi-phase-matching (QPM) and perfect phase-matching. For the case of no phase-matching the power of the output optical signal has a periodic variation. The power of the output optical signal increases along a coherence length defined as

$$L_c = \frac{\pi}{\Delta k}, \tag{4.15}$$

where Δk refers to the phase-matching condition of the considered nonlinear process. After one coherence length, the power of the output optical signal decreases along another coherence

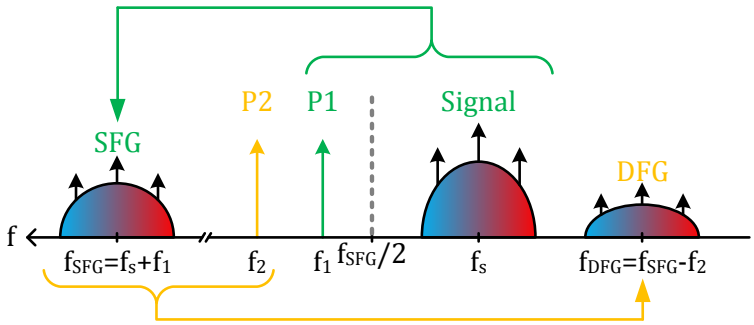

Figure 4.3: Depiction of the spectra of the optical signals involved in cSFG-DFG.

length, which means that the output optical signal returns energy to the input optical signals. This can be avoided by periodically poling the crystal, thereby enabling a steady increase of the power of the output optical signal. The result is QPM, which can be included in the phase-matching requirements (4.11) to (4.14) as

$$\Delta k_{\mathrm{SHG}}|_{\omega_3=2\omega_1} = k_3 - k_1 - 2\pi/\Lambda_p = 0 \tag{4.16}$$
$$\Delta k_{\mathrm{SHG}}|_{\omega_3=2\omega_2} = k_3 - k_2 - 2\pi/\Lambda_p = 0 \tag{4.17}$$
$$\Delta k_{\mathrm{SFG}}|_{\omega_3=\omega_1+\omega_2} = k_3 - k_2 - k_1 - 2\pi/\Lambda_p = 0 \tag{4.18}$$
$$\Delta k_{\mathrm{DFG}}|_{\omega_3=\omega_2-\omega_1} = k_3 - k_2 + k_1 + 2\pi/\Lambda_p = 0. \tag{4.19}$$

As explained in [26], the power of the output optical signal is proportional to $\mathrm{sinc}^2\frac{\Delta kL}{2}$. Δk is adjusted to define the center frequency of the QPM condition, as observed in (4.16) to (4.19). This leaves the length of the waveguide, L, as the parameter associated with the bandwidth of the QPM response. It is interesting to note that these remarks may also apply to the efficiency of FWM in optical fiber. Under certain conditions, the FWM efficiency varies with Δk according to a sinc^2 shape, as shown in [24, Fig. 2]. The nonlinear processes of SHG, SFG and DFG by themselves are generally uninteresting for applications related with optical communication systems. The reason is that at least one of the optical signals has a frequency much higher or lower than another. In fact, it is desirable that the frequencies of all optical signals lie within a reasonable wide spectral range, such as the C-band [26]. For instance, this eases the coupling of the optical signals to the input or output of the waveguide. Such purpose can be accomplished by cascading at least two basic nonlinear processes of SHG, SFG or DFG. Let us consider cSFG-DFG. This cascaded process is illustrated in Fig. 4.3. The input optical signal is mixed with a CW pump, P1, by means of SFG. The resulting optical signal is simultaneously mixed with another CW pump, P2, by means of DFG. The frequency of the output optical signal is given by

$$f_{\mathrm{DFG}} = f_{\mathrm{SFG}} - f_2 = f_s + f_1 - f_2. \tag{4.20}$$

Such frequency lies within the same frequency range as the input optical signal and pumps. Depending on the frequency of the input optical signal, f_1 should be tuned in order to minimize Δk_{SFG}. f_2 should be tuned according to the target frequency of the output optical signal. As a result, this configuration is flexible with respect to the frequencies of both the input and output optical signals. It is interesting to note that cSFG-DFG mimics FWM, where the four waves involved are the input optical signal, two pumps and the output optical signal.

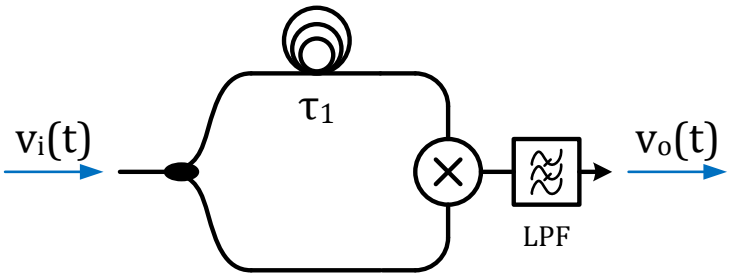

Figure 4.4: Scheme of a IFMS based on signal mixing.

FWM in optical fiber can also be cascaded, as reported in [27]. Parametric nonlinear effects in optical fiber and in a PPLN waveguide thus share many similarities, except for the phase-matching mechanisms. In a HNLF, the phase-matching is generally tailored with the purpose of maximizing conversion efficiency over broad a bandwidth. This can also be the case in a PPLN waveguide. However, by carefully engineering the poling pattern of the waveguide, an arbitrary variation of the phase-matching with the wavelength of the input optical signal can be achieved [28, 29].

4.2 IFMS based on signal remodulation [paper J6]

The IFMSs presented in chapter 2 are based on splitting the input RF signal in two copies, delaying the two copies between them, and adding them thereafter. This is performed on the optical domain by a MZDI. It is also possible to measure the RF frequency of an input RF signal by mixing the two copies instead of adding them. The schematic of such IFMS is shown in Fig. 4.4. Considering $v_i(t) = V_{\mathrm{RF}} \sin(\omega_{\mathrm{RF}} t)$, the signal at the output of the low-pass filter (LPF) is given by

$$v_o(t) = \frac{1}{4} V_{\mathrm{RF}}^2 \cos(\omega_{\mathrm{RF}} \tau_1) . \tag{4.21}$$

By knowing the amplitude of the RF signal and the differential delay between the copies of the RF signal, τ_1, the RF frequency can be derived. The first photonic implementation of such scheme was reported in [30]. Two MZMs are employed. The first one mixes the CW light produced by the laser source with the input RF signal, therefore acting like a modulator. The second one mixes the modulated optical signal with a delayed copy of the input RF signal. An improved photonic system capable of also measuring the RF amplitude was proposed in [31]. Such systems are fairly complex and costly, and are limited both in frequency resolution and range by the electrical circuitry which feeds the MZMs. In [32], the second MZM-based mixer was replaced by FWM in a HNLF. The limitations related with the electrical circuitry were solved. Nonetheless, the system remains complex and costly. The photonic IFMSs proposed in [30, 31, 32] employ optical signals with unsuppressed OC. This means that the input RF signal in Fig. 4.4 should be modeled as $v_i(t) = V_c + V_{\mathrm{RF}} \sin(\omega_{\mathrm{RF}} t)$, where V_c is a direct current (DC) term. Consequently,

$$v_o(t) = \frac{V_c^2}{2} + \frac{1}{4} V_{\mathrm{RF}}^2 \cos(\omega_{\mathrm{RF}} \tau_1) . \tag{4.22}$$

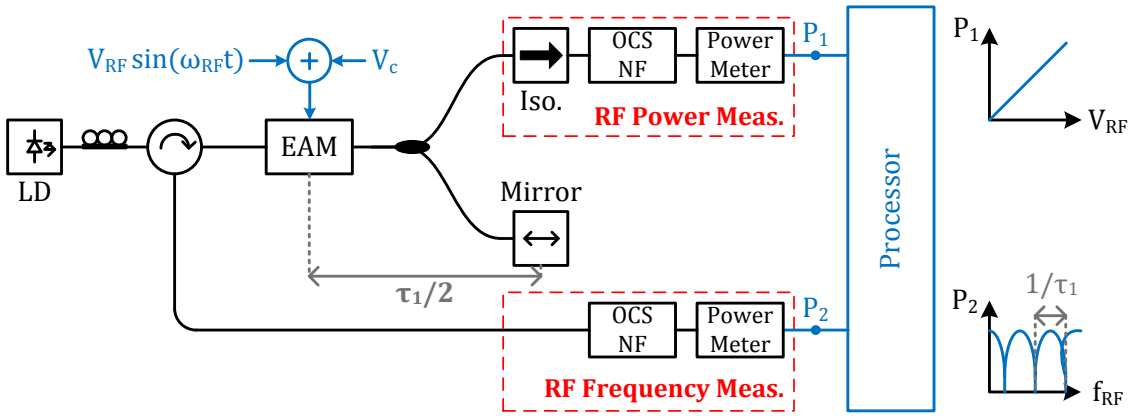

Figure 4.5: Scheme of the IFMS based on signal remodulation. Insets: variation of the measured average optical powers with the (top) amplitude and (bottom) frequency of the input RF signal.

In theory, the DC offset added to the output signal is not important as long as V_c is known. In practice, since the DC term is usually much higher than the second term it is difficult to measure the small variations of $v_o(t)$ related with the change of the RF frequency using a simple power meter.

4.2.1 System implementation

A simple photonic implementation of the IFMS depicted in Fig. 4.4 was proposed in [J6]. The scheme of the proposed system is shown in Fig. 4.5. The system relies on bidirectional operation of a single electro-absorption modulator (EAM). A lithium niobate MZM cannot be used, since it is not bidirectional. This is due to the traveling-wave operation of such device, which requires that the electrical and optical signals propagate in the same direction. The CW light is modulated by the input RF signal. Part of the modulated optical signal is reflected back to the EAM, and is thereby remodulated by the input RF signal. There is a temporal difference of τ_1 between modulation and remodulation. Therefore, signal remodulation performs exactly as schematized in Fig. 4.4. The value of τ_1 only depends on the length of the optical path between the EAM and the fiber mirror reflector. As a result, remodulation does not require a complex electrical circuitry. An EAM can only perform intensity modulation, which means that the modulated and remodulated optical signals have unsuppressed OC. Assuming that the EAM provides purely linear, chirp-free intensity modulation the power of the modulated optical signal is given by

$$P_{\mathrm{mod}}(t) = P_{\mathrm{in}} L_{\mathrm{mod}} \left[V_{\mathrm{RF}} \sin\left(\omega_{\mathrm{RF}} t\right) + V_c \right], \tag{4.23}$$

where P_{in} is the input power of the CW light and L_{mod} is a constant which accounts for losses. As the EAM can only provide intensity modulation, then $P_{\mathrm{mod}}(t) > 0$. This implies that $V_c > V_{\mathrm{RF}}$. In the spectral domain, the power of the OC of the modulated optical signal depends on the average value of $P_{\mathrm{mod}}(t)$, which is V_c. Therefore, OCS sets the value of V_c in (4.23) to zero. The average power of the modulated optical signal after OCS is given by

$$P_1 = P_{\mathrm{in}} L_{\mathrm{mod}} V_{\mathrm{RF}} \cdot \frac{2}{\pi}. \tag{4.24}$$

The amplitude of the RF signal can be measured from P_1 independently of the RF frequency. The power of the remodulated optical signal is given by

$$P_{\text{remod}}(t) = P_1 L_{\text{remod}} \left[V_{\text{RF}} \sin\left(\omega_{\text{RF}} t\right) + V_c\right] \cdot \left[V_{\text{RF}} \sin\left(\omega_{\text{RF}}(t-\tau_1)\right) + V_c\right], \tag{4.25}$$

where L_{remod} is a constant which accounts for losses. Equation (4.25) can be expanded, yielding

$$\begin{aligned} P_{\text{remod}}(t) = P_1 L_{\text{remod}} \Big[& V_c^2 + \frac{1}{2} V_{\text{RF}}^2 \cos(\omega_{\text{RF}} \tau_1) + \\ & 2 V_{\text{RF}} V_c \cos\left(\frac{\omega_{\text{RF}} \tau_1}{2}\right) \sin\left(\omega_{\text{RF}} t - \frac{\omega_{\text{RF}} \tau_1}{2}\right) - \\ & \frac{1}{2} V_{\text{RF}}^2 \cos\left(2\omega_{\text{RF}} t - \omega_{\text{RF}} \tau_1\right) \Big]. \end{aligned} \tag{4.26}$$

In the spectral domain, the first two terms represent the OC of the remodulated optical signal. The third term corresponds to the spectral lines at $f_o \pm f_{\text{RF}}$, and the fourth term represents the spectral lines at $f_o \pm 2f_{\text{RF}}$. The RF frequency could be derived from the average power of the spectral lines located at $f_o \pm f_{\text{RF}}$ without the influence of a constant DC term, such as the first one. In order to do so by means of a power meter, the other spectral lines should be suppressed. OCS nulls the first two terms in (4.26). The fourth term can be neglected if $V_{\text{RF}} \ll V_c$, which in practice is normally the case. As a result, the average power of the remodulated optical signal is given by

$$P_2 = P_{\text{in}} L_{\text{remod}} V_{\text{RF}} V_c \left|\cos\left(\frac{\omega_{\text{RF}} \tau_1}{2}\right)\right| \cdot \frac{4}{\pi}. \tag{4.27}$$

The RF frequency can be derived from P_2 within a frequency range of 0 up to $\frac{1}{2\tau_1}$, as depicted in the inset of Fig. 4.5. The derivation of the RF frequency requires that V_{RF} is known, which is achieved through P_1.

The key points in the implementation of the scheme shown in Fig. 4.5 are the OCS NFs and the linearity of the EAM. The limited OCS provided by the NFs results in limited suppression of the first two terms in (4.26). On one hand, the RF amplitude should be low in order to neglect the fourth term. On the other hand, decreasing the RF power results in the domination of the first term over the third one, even after OCS. As a result, there is an optimum RF amplitude which depends on the OCS provided by the NFs. The linearity of the EAM depends on how linear is the voltage to optical power conversion, and also on the frequency chirp which occurs simultaneously with intensity modulation [33]. Both effects produce additional spectral lines on the modulated or remodulated optical signals, located at $f_o \pm k \cdot f_{\text{RF}}$, $k = 2, 3, \ldots$.

Experiment The NFs were implemented with FBGs. Since this work was done before [J2], a different way as the one presented in Fig. 2.9 was adopted. A long and weak uniform FBG results in a very high reflectivity, and thereby very reduced transmission, over a reduced bandwidth. The OC of the input optical signal can be suppressed by centering it at the transmission minimum. A uniform FBG with a long length of 5 cm and a low average refractive index variation of 4×10^{-5} was written. The transmission spectrum of the FBG is shown in Fig. 4.6. A minimum transmission of -27 dB was obtained. For RF frequencies lower than 7 GHz the RF tones are significantly attenuated, thereby minimizing the effectiveness of OCS. The FBG was set on a Peltier device, controlled by a temperature controller. The temperature

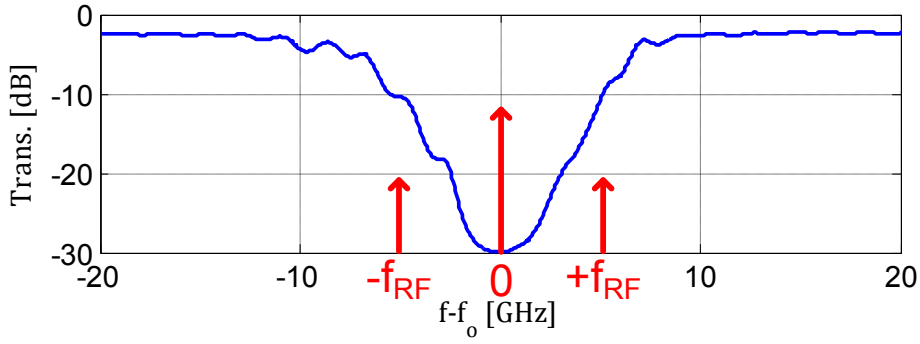

Figure 4.6: Transmission spectrum of the uniform FBG and depiction of the optical spectrum of the input optical signal.

was set at 25 °C in order to avoid temperature-dependent frequency drifts. A time delay of $\tau_1 = 47.375$ ns resulted from a patch-cord length of 4.91 m between the EAM and the fiber mirror reflector. The maximum measurable RF frequency of the system was limited by the 3 dB cutoff frequency of 20 GHz of the bias tee which fed the EAM.

RF frequencies from 1 up to 25 GHz with a step of 1 MHz were measured for input RF powers of −6, 0, and 6 dBm. The results are shown in Fig. 4.7. The maximum average optical powers oscillate with the input RF frequency. Such oscillations are due to impedance mismatch between the microwave signal generator and the EAM. This can be modeled in (4.23) to (4.27) by replacing V_{RF} with $V_{\mathrm{RF}}(f_{\mathrm{RF}})$. Since such oscillations affect both P_1 and P_2 in the same way, the measurement of the RF frequency is not affected. This is only true for RF frequencies higher than 10 GHz, as the NFs do not attenuate significantly the RF tones for such high RF frequencies. The peak-to-peak amplitude of P_2 is maximum for an input RF power of 0 dBm, as an optimum balance between OCS and minimization of the power of the spectral lines at $f_o \pm 2f_{\mathrm{RF}}$ was achieved. The RF frequency was derived from the measured values of P_1 and P_2 using two methods. The first one consists in comparing the measured average optical powers with the theoretical model summarized in (4.24) and (4.27). As depicted in Fig. 4.7 (a2), (b2) and (c2), the points of each period of P_2 are compared with the absolute value of the cosine term of (4.27). The RF frequency is derived from such comparison. This method assumes ideal OCS and negligible power of the spectral lines at $f_o \pm 2f_{\mathrm{RF}}$. In order to account for such limitations, a reference sinusoidal period can be modeled directly from the measured values of P_2, and used instead of the absolute value of the cosine term of (4.27). Such method was denoted by reference-lobe comparison method (RLCM). A better curve fitting is obtained. This approach is more straightforward than improving the derived mathematical model in order to address the referred limitations. Figures 4.7 (a3), (b3) and (c3) and the respective zoom-ins (a4), (b4) and (c4) show that lower frequency errors were obtained with the RLCM. The lowest peak-to-peak RF frequency error of 3 MHz was obtained for an input RF power of 0 dBm. The RF frequency measurement range of the system was of $\frac{1}{2\tau_1} \simeq 10.5$ MHz. Therefore, the obtained peak-to-peak error is quite high, which means that the system should be improved. Better results can be obtained over a broader frequency range using narrower NFs with lower transmission. The incoherent operation principle of the photonic IFMS has shown to provide a very stable setup. For an input RF power of 6 dBm, P_2 was repeatedly measured within an RF frequency range of 10 GHz ± 10 MHz during during five hours. The power of each point varied by less than 0.2 dB.

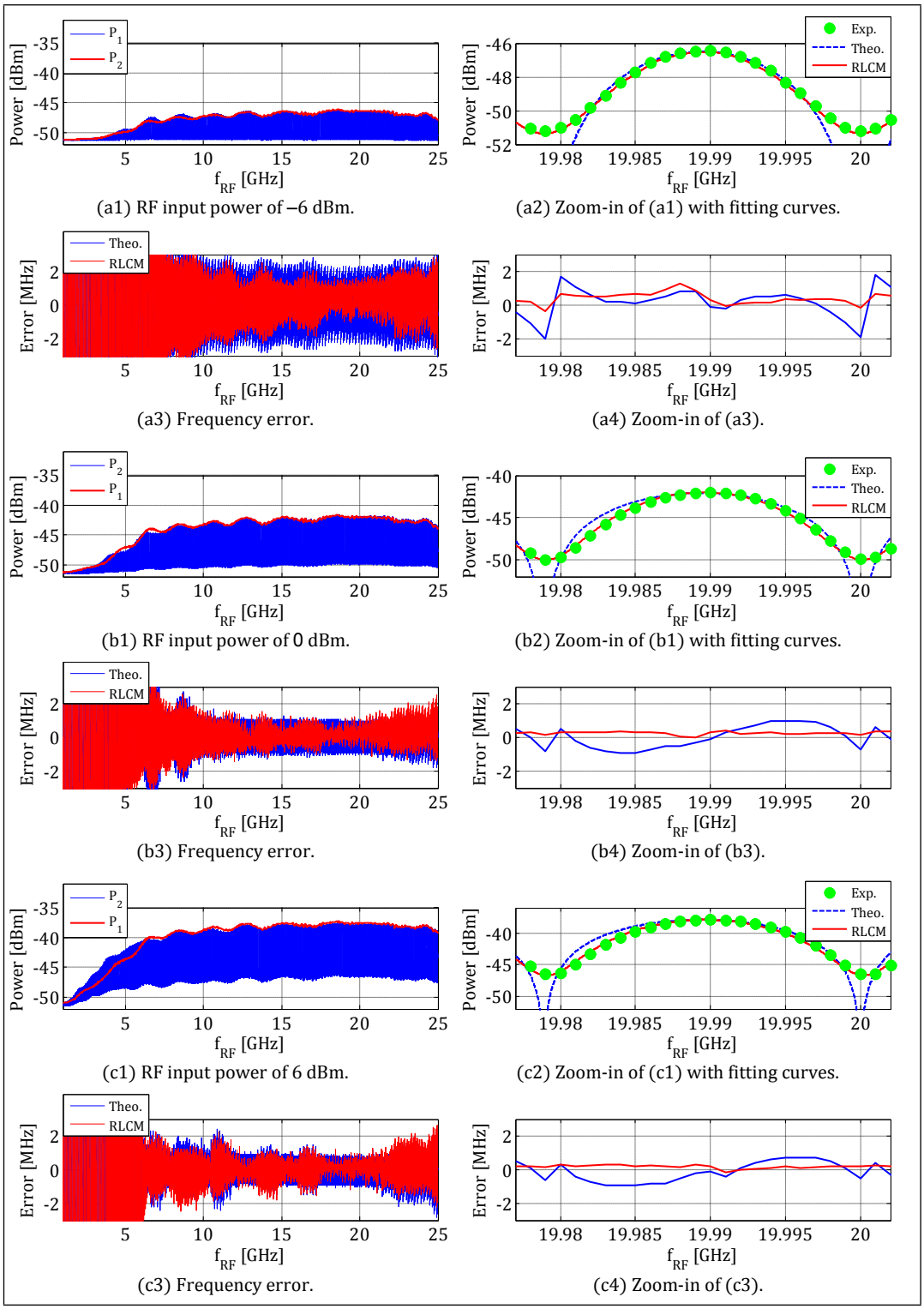

Figure 4.7: Experimental results obtained for input RF powers of (a) −6 dBm, (b) 0 dBm and (c) 6 dBm, respectively. (a2), (b2), (c2) are zoom-ins of the measured values of P_2 (dots), superimposed with the fitted lines.

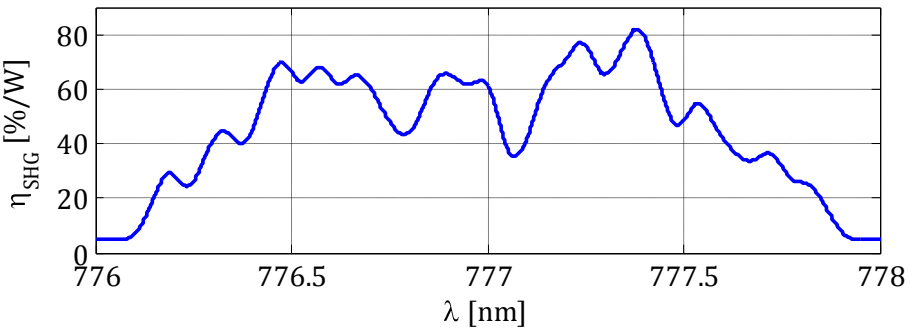

Figure 4.8: Measured conversion efficiency of SHG.

4.3 Wavelength conversion using a PPLN waveguide [papers J7, C9, C10]

Wavelength conversion of optical signals is the basis of important optical network applications such as all-optical routing [34], multicasting [7] and modulation [35]. There are many different wavelength conversion techniques based on different nonlinear subsystems [34]. Such techniques have been analyzed in terms of implementation complexity, energy efficiency, transparency to modulation format or bit rate, signal distortion, multi-wavelength operation, and other figures of merit. Recent research efforts on increasing the capacity of optical networks have been directed towards advanced modulation formats [36]. In this context, it is very important that a wavelength converter is transparent to the modulation format.

The simplest modulation format transparent wavelength converters are based on parametric mixing processes, such as FWM in optical fiber or SHG, SFG and DFG in a PPLN waveguide. The mathematical analysis presented in the first section of the current chapter clearly shows that the output optical signal is proportional to the product of the electrical fields of the input optical signals. Consequently, both the amplitude and phase of the output optical signal depend on the amplitudes and phases of the input optical signals. This enables modulation format transparency. Besides amplitude and phase transparency, polarization insensitive operation is also important to enable polarization-division multiplexing (PDM). Polarization insensitive parametric mixing was achieved both in optical fiber [37] and in a PPLN waveguide [38] by exploring the bidirectionality of these devices. As a result, both devices are able to provide intensity, phase and polarization transparent all-optical wavelength conversion.

In [J7], wavelength conversion was performed in a 4.5 mm long PPLN waveguide by means of cSFG-DFG, as depicted in Fig. 4.3. The used PPLN was designed with a linearly chirped polling pattern with the purpose of having a broad operational bandwidth while keeping the conversion efficiency sufficiently high. The obtained conversion efficiency of SHG, η_{SHG}, is shown in Fig. 4.8. The average poling period of $\Lambda_p = 19$ μm resulted in a center wavelength of approximately 777 nm. The chirped poling produced a rippled conversion efficiency over a broad bandwidth of about 1.43 nm, or 700 GHz. The cost of such a broad bandwidth was an average conversion efficiency of only 40 %/W. This bandwidth vs. efficiency trade-off is discussed in detail in [39]. The average power of the converted optical signal is approximately

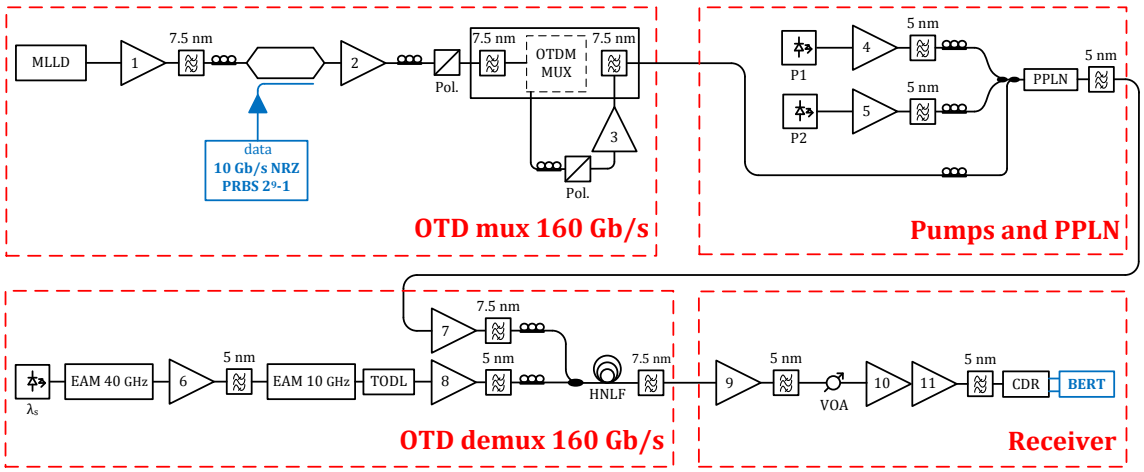

Figure 4.9: Experimental setup used to assess the performance of the PPLN waveguide. All amplifiers are EDFAs. Each optical filter has its 3 dB bandwidth written above it. CDR – clock and data recovery.

given by

$$P_{\text{conv}} = 4\eta_{\text{SHG}}^2 P_1 P_2 P_{\text{sig}}, \tag{4.28}$$

where P_1 and P_2 are the average powers of the CW pumps and P_{sig} is the average power of the input optical signal. In order to have a unitary conversion efficiency, i.e., $P_{\text{conv}} = P_{\text{sig}}$, and considering the average conversion efficiency of 40 %/W, $P_1 P_2$ must equal to 1.56 W^2. This estimate does not take into account the insertion losses of the waveguide, which were measured at 3.3 dB. These losses include coupling losses between the facets of the waveguide and fiber lenses, and waveguide propagation losses. Consequently, in order to achieve moderate conversion efficiencies without using high-power amplification on the input optical signal, pump powers in the order of 1 W are required. The use of such high power optical signals can be deleterious to the operation of the PPLN waveguide. The waveguide was fabricated using the annealed proton-exchange technique. As pointed in [26], high power optical signals affect the refractive index along the waveguide, thereby decreasing the conversion efficiency. This effect, which is commonly referred as photorefractive damage, can be mitigated by increasing the temperature of the waveguide to at least 100 °C, by mechanically defining the waveguide, or, by carefully doping the substrate. The fabrication of the used PPLN waveguide followed the latter strategy, using a 5 mol% MgO-doped lithium niobate wafer. As a result, the purpose of the work reported in [J7] was to validate room-temperature (25 °C) operation using broadband input optical signals and high power pumps. Optical fibers also pose challenges when high power optical signals are involved, such as stimulated Raman and Brillouin scattering [23]. Stimulated Brillouin scattering can be particularly deleterious in FWM using CW pumps, as it reduces the pump powers [40].

Experiment The experimental setup used to validate room-temperature operation of the PPLN waveguide is shown in Fig. 4.9. A mode-locked laser diode (MLLD) generated ultra-short optical pulses at a base rate of 10 GHz. The pulses were intensity modulated and then time-domain multiplexed by a phase-stable OTDM multiplexer. The resulting linearly polarized 160 Gb/s OTDM signal was mixed in the PPLN waveguide with two high power CW

pumps. The converted OTDM signal, which resulted from cSFG-DFG, was separated from the input optical signals of the PPLN using an optical filter. Single tributary demultiplexing was obtained by FWM the converted OTDM signal with short control pulses at the base rate in a HNLF. The control pulses were obtained by pulse carving a CW signal using two cascaded EAMs. The demultiplexed tributary was converted to the electrical domain using an optically pre-amplified receiver. A quantitative description of the experimental setup can be found in [J7]. The input power of the PPLN waveguide was of 32.6 dBm. The combination of such a high input power with room temperature operation allowed determining if there was photorefractive damage. The occurrence of such effect would clearly degrade the conversion efficiency. cSFG-DFG enables wavelength tunability both in the input and converted optical signals. However, the wavelength of the input optical signal could not be tuned due to limitations of the MLLD. The wavelength of the output optical signal was tuned by varying the wavelength of P2.

The energy efficiency of the system was fairly low. Firstly, the coupling of the two CW pumps and OTDM signal resulted in inherent losses of 6 dB and 3 dB, respectively, due to the use of optical couplers. Secondly, the insertion losses of the waveguide and the reduced conversion efficiency further decreased the energy efficiency. Thirdly, coupling losses and limited FWM conversion efficiency also existed in the HNLF. Such high accumulated losses were compensated by many erbium-doped fiber amplifiers (EDFAs), which degraded the OSNR of the optical signals.

The eye diagrams and optical spectra of the input and converted optical signals are shown in Fig. 4.10. The optical spectrum of the input optical signal has five clearly defined clock tones, which account for a spectral width of 640 GHz. Such spectral width is lower than the conversion bandwidth of the PPLN waveguide, which was of 700 GHz. As a result, the entire spectral width of the input optical signal was successfully converted. This is not evident in Fig. 4.10 (d3), as the converted signal was subject to detuned optical filtering in order to strongly suppress P1, located at 1560.92 nm. Undistorted eye diagrams were obtained both in the converted and demultiplexed optical signals. The eye diagram of the converted signal at 1565 nm shows noisy pulses. This was due to detuned optical filtering, and thereby lower signal power. Furthermore, the wavelength of the converted signal was at the limit of the gain bandwidth of the EDFAs, which further degraded the OSNR. The BERs of the input and converted optical signals are plotted in Fig. 4.11. Error-free performance (BER$<10^{-9}$) was measured in all tributaries of all optical signals. A maximum power penalty of 2.1 dB was obtained for a BER of 10^{-9} relatively to the input optical signal. The worst performance was obtained in the converted signal at 1565 nm, which was expected as previously discussed. A conversion efficiency of -25 dB was obtained. This value was expected due to the inherent losses in the coupling of the pumps and input optical signal, and also due to the insertion losses of the PPLN waveguide. These results show that wavelength conversion was successfully performed at room temperature over an output wavelength tuning range on nearly 30 nm, which was limited by the gain bandwidth of the used EDFAs. The negligible distortion observed in the converted optical signals and the obtained conversion efficiency allow concluding that photorefractive damage did not limit the operation of the PPLN waveguide.

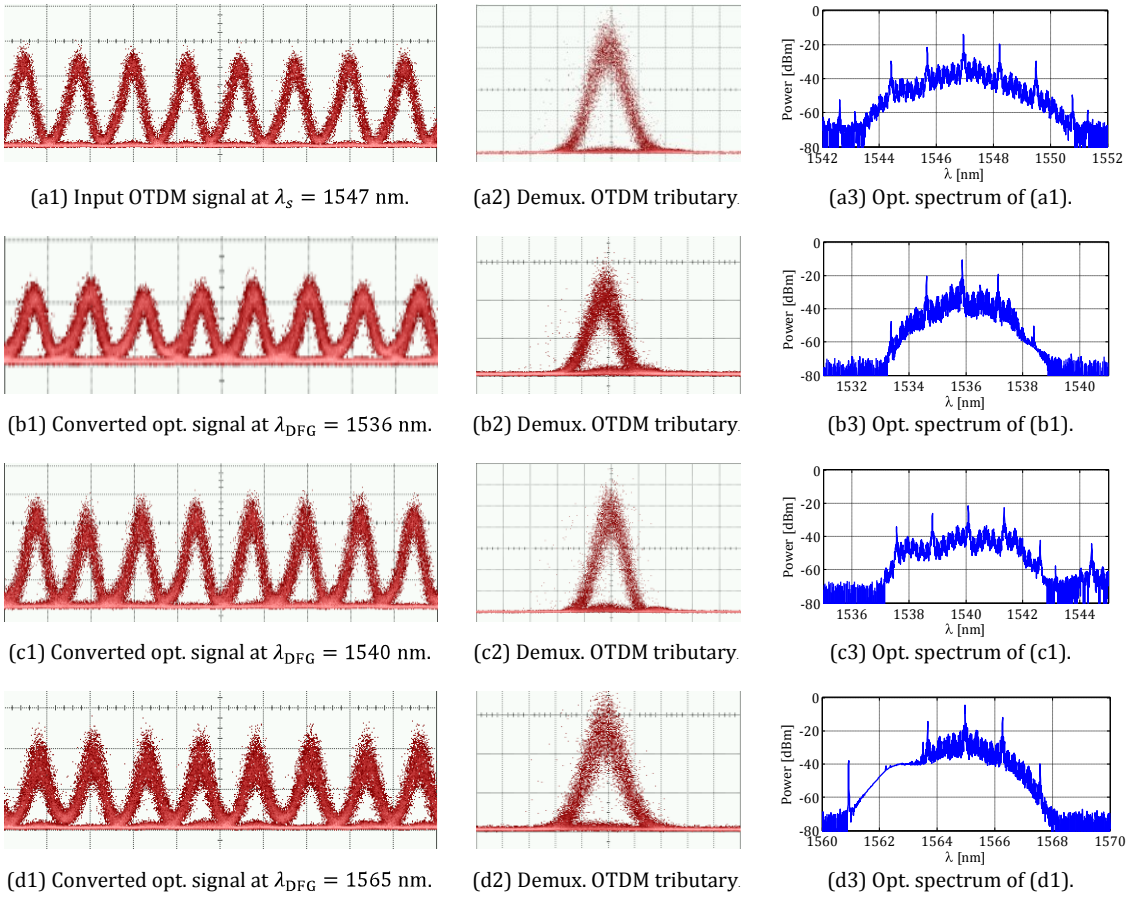

Figure 4.10: First column: eye diagrams of the input and converted optical signals. Second column: eye diagrams of a demultiplexed OTDM tributary. Third column: optical spectra of the input and converted optical signals.

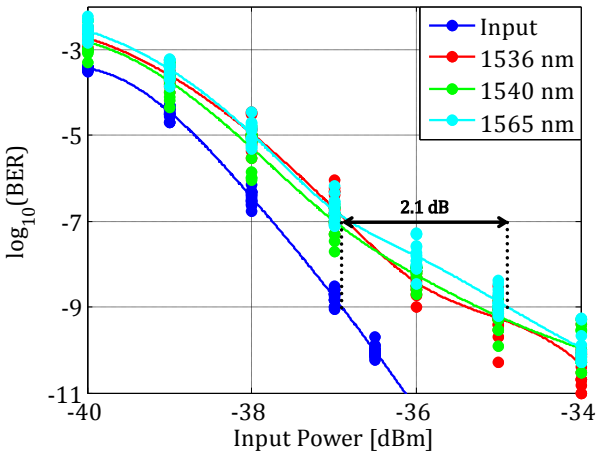

Figure 4.11: BERs of the input and converted optical signals. Each dot represents the BER of one of the sixteen tributaries. The lines are the interpolation of the average BER between all tributaries.

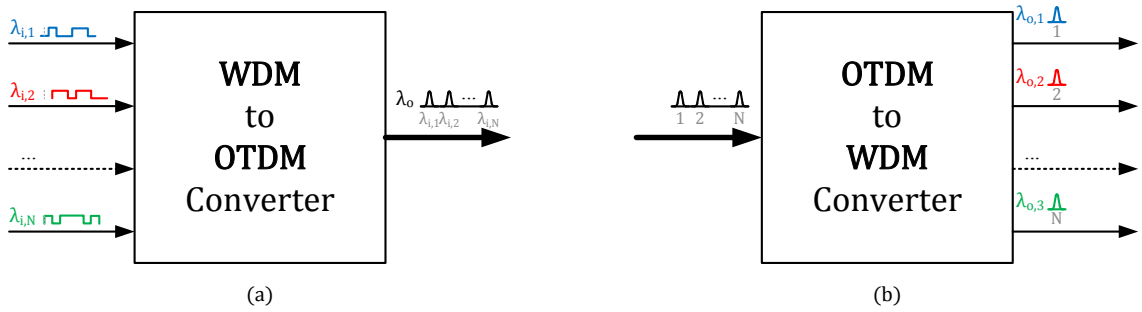

Figure 4.12: Scheme of a (a) WDM to OTDM converted and (b) OTDM to WDM converter. In (a), the information of an arbitrary input optical signal $\lambda_{i,1}$, $\lambda_{i,2}$ or $\lambda_{i,N}$ is mapped into the tributary $1, 2, \ldots, N$ of the output OTDM signal, respectively. In (b), the information of the tributary $1, 2, \ldots, N$ of the input OTDM signal is mapped into output optical signals with an arbitrary wavelength of $\lambda_{o,1}$, $\lambda_{o,2}$ or $\lambda_{o,N}$, respectively.

4.4 OTDM to WDM conversion in a HNLF [papers J8, C11, C12]

The experiment presented in the previous section dealt with OTDM signals due to its broad spectral width. OTDM communication systems generally involve the operations of tributary multiplexing, signal transmission, all-optical signal processing, and tributary demultiplexing, as recently reviewed in [41]. All these operations except for signal transmission were part of the previously presented experiment. As pointed in [41], WDM and OTDM networks have different advantages in terms of capacity, complexity, resiliency to transmission impairments and energy efficiency. As a result, future networks may employ different multiplexing schemes in different parts of the network, depending on the suitability of each multiplexing scheme to the presented scenario. The use of different multiplexing schemes in a network requires interfaces which enable transparent and flexible data flow from one multiplexing scheme to the other. These interfaces must include OTDM to WDM and WDM to OTDM converters. Such converters are depicted in Fig. 4.12. The flexibility of the converters depends on the wavelength tunability of the input and output optical signals, OTDM tributary to WDM channel mapping, and modulation format and bit rate transparency.

The basic architecture of a converter can be based on two approaches. The conversion of N input optical signals to N output optical signals can be performed by N multiple input to single output converters [42]. This approach resorts to the parallelization of N single output converters, and therefore scales with the number of optical signals N. The other approach avoids scalability problems by performing the conversion of N input signals to N output signals in a single subsystem. The state-of-the-art of OTDM to WDM converters employing both approaches is reviewed in [J8].

4.4.1 System implementation

A flexible OTDM to WDM converter which performs the conversion of N input OTDM tributaries to N output WDM channels in a single subsystem is depicted in Fig. 4.13. The scheme is divided in two steps, which are the generation of a SPT, and mixing of the input OTDM with a SPT. Part of the input OTDM signal feeds a clock recovery system, which

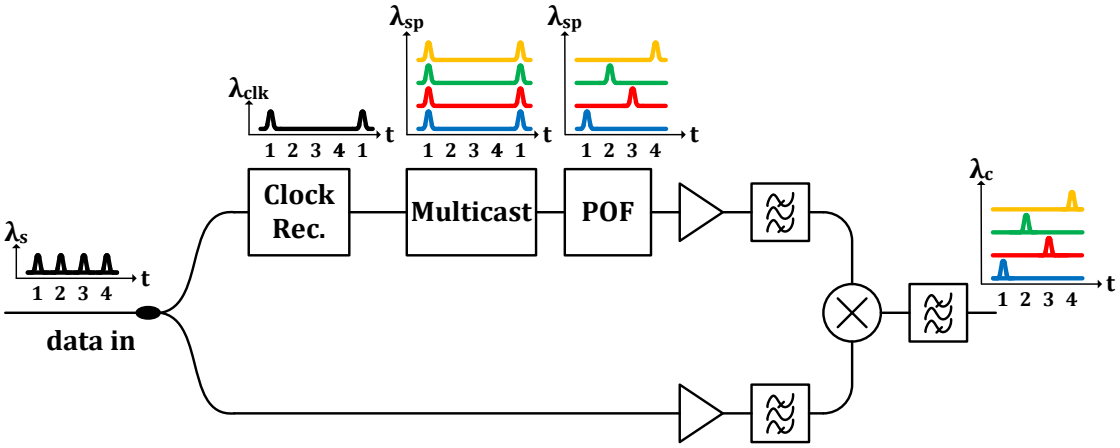

Figure 4.13: Scheme of a flexible OTDM to WDM converter considering four OTDM tributaries ($N = 4$). The insets depict the generation of the SPs and the converted WDM channels.

outputs an optical clock signal at the tributary rate synchronized with the input optical signal. The optical clock signal is multicast to N different wavelengths. A programmable optical filter (POF) individually reshapes and delays each of the multicast optical clock signals. As a result, a SPT composed by N sampling pulses (SPs) with different wavelengths is obtained. After amplification and noise filtering, the input OTDM signal is mixed with the SPT. The mixing products are the converted WDM channels. An optical bandpass filter separates the converted WDM channels from the input signals of the mixer.

The proposed scheme enables flexible conversion if the following conditions are fulfilled. Wavelength tunability of the input and output optical signals depends on wavelength tunability of the SPs, which should be enabled by the multicasting subsystem and POF. It also depends on the operational bandwidth of the mixer. Flexible OTDM tributary to WDM channel mapping only depends on the tunability of the frequency response of the POF. By shaping the frequency response of the POF, a SPT composed by undistorted SPs with an arbitrary disposition of wavelengths can be obtained. The notation adopted for the wavelength disposition of the SPT is $[\lambda_i \lambda_j \dots \lambda_N]$. The wavelengths of the output WDM channels are given by $[\lambda_{o,i} \lambda_{o,j} \dots \lambda_{o,N}]$, and contain the information of the tributary $1, 2, \dots, N$ of the input OTDM signal, respectively. Modulation format transparency is enabled if the mixer is intensity, phase and polarization transparent. Bit rate tunability mainly depends on the clock recovery system, which usually operates within a narrow bandwidth. It also depends on the limitations of the POF, such as its frequency resolution and minimum bandwidth.

Experiment The OTDM to WDM converter schematized in Fig. 4.13 was implemented in the experimental setup shown in Fig. 4.14. As the converter was tested in back-to-back, clock recovery was not needed. A mode-locked fiber laser (MLFL) was used to generate an optical clock signal at 40 GHz, composed by pulses with a full width at half maximum (FWHM) of 1.5 ps and centered at 1539 nm. Two copies of the output optical clock signal were required. One was used to obtain a 160 Gb/s intensity modulated OTDM signal, composed by four tributaries ($N = 4$) at 40 Gb/s. The other copy was multicast to three different channels spaced by 600 GHz using a multi-wavelength converter based on a Mach-Zehnder interferometer semiconductor optical amplifier (MZI-SOA) (CIP 40G-2R2-ORP). Such multi-wavelength

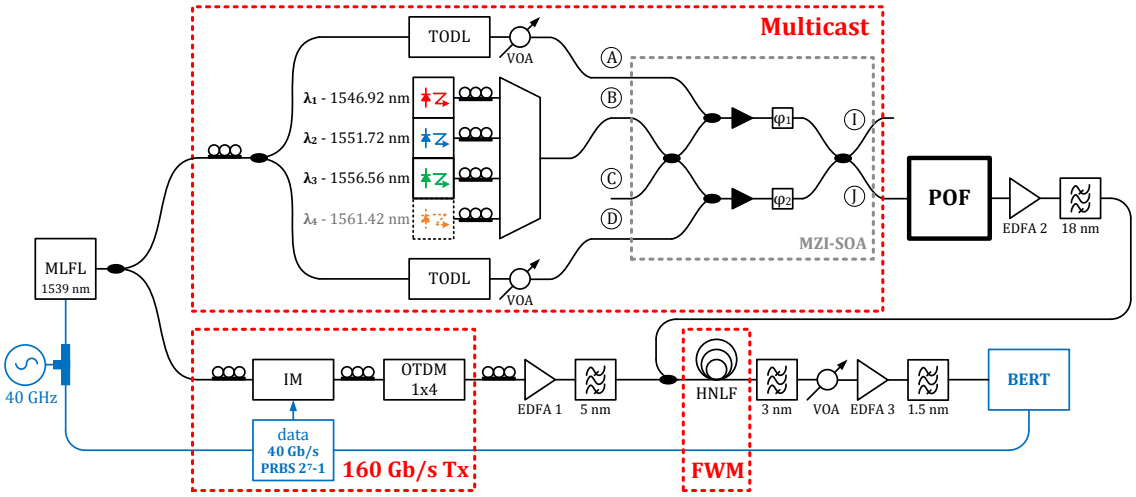

Figure 4.14: Experimental setup of the OTDM to WDM converter. IM – intensity modulator.

Operating range	1527.4 – 1567.4 nm	Insertion loss	5 dB
Maximum CD	±10 ps/nm	Minimum bandwidth	5 GHz
Frequency resolution	1 GHz	Maximum attenuation	35 dB
Attenuation resolution	0.1 dB	Settling time	500 ms

Table 4.1: Specifications of the POF.

converter is assessed in [7]. The fourth wavelength was not considered as the corresponding WDM channels would be out of the gain bandwidth of the EDFAs. The used multicasting subsystem allows continuous wavelength tunability within the gain bandwidth of the SOAs. It also has a low polarization sensitivity. Nonetheless, the SOPs of the input CW signals were aligned along the polarization axis of the MZI-SOA which enabled the highest gain. The purpose was to obtain co-polarized SPs. As observed in [7], this multicasting scheme impairs the multicast optical signals with patterning effects, ASE noise, limited ER[1], FWM and gain competition between channels. In the proposed converter there are no patterning effects, as the input optical signal of the multicasting subsystem is not modulated by data. A multiport optical processor (Finisar WaveShaper 4000S) was used as a POF. Its main specifications are summarized in Table 4.1. The POF was firstly configured to apply a rectangular bandpass filter with a bandwidth of 400 GHz to each multicast optical signal. Time delays of 12.5, 6.25 and 0 ps were configured to the SPs centered at λ_1, λ_2 and λ_3, respectively. As a result a SPT with a wavelength disposition of $[\lambda_3\lambda_2\lambda_1]$ was obtained. The frequency response of the POF, spectrum of the SPT and waveforms of the SPs is shown in Fig. 4.15 (a1) – (a2). Figure 4.15 (a6) shows that the configured phase response of the POF correctly delayed the SPs. However, Fig. 4.15 (a2) shows that the pulses are impaired by a noise floor and FWM idlers. Furthermore, the amplitudes of the SPs were not properly equalized due to gain competition in the SOAs between optical signals, and also due to the trade-off between insertion losses and added time delay of the used POF [43]. All these impairments can be mitigated simply by

[1]For optical signals without data modulation, the term contrast ratio (CR) is used instead of ER.

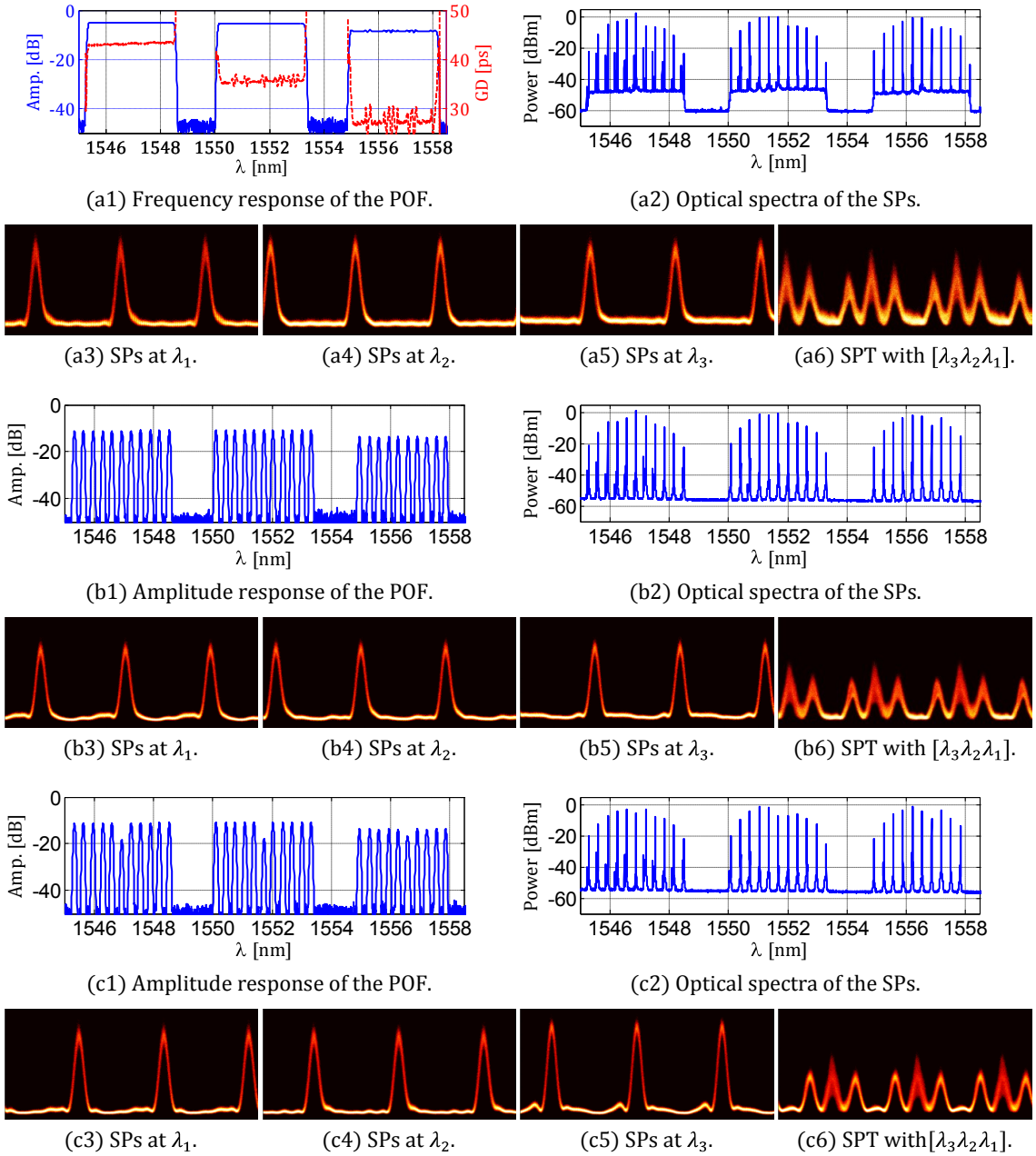

(a1) Frequency response of the POF. (a2) Optical spectra of the SPs.

(a3) SPs at λ_1. (a4) SPs at λ_2. (a5) SPs at λ_3. (a6) SPT with $[\lambda_3\lambda_2\lambda_1]$.

(b1) Amplitude response of the POF. (b2) Optical spectra of the SPs.

(b3) SPs at λ_1. (b4) SPs at λ_2. (b5) SPs at λ_3. (b6) SPT with $[\lambda_3\lambda_2\lambda_1]$.

(c1) Amplitude response of the POF. (c2) Optical spectra of the SPs.

(c3) SPs at λ_1. (c4) SPs at λ_2. (c5) SPs at λ_3. (c6) SPT with$[\lambda_3\lambda_2\lambda_1]$.

Figure 4.15: Waveforms and optical spectra of the SPs and corresponding SPTs obtained for the plotted frequency responses of the POF. The group delay in (b1) and (c1) could not be measured due to the significant discontinuities in the amplitude response.

reconfiguring the amplitude response of the POF, as shown in Fig. 4.15 (b1). The amplitude response of the POF between the spectral lines of the SPs was set at maximum attenuation, thereby suppressing the noise floor and FWM idlers. As observed in Fig. 4.15 (b2) the noise floor and FWM idlers near the spectral lines could not be fully suppressed due to the minimum bandwidth of the optical filters centered at each spectral line. The equalization of the SPs was performed by adjusting the attenuation of the optical filters. As shown in Fig. 4.15 (b6). The quality of the SPs clearly improved. The pulses falsely appear to be noisy and unequalized. This was due to the beat between one of the SPs and the zero level of the adjacent SPs, which was captured by the broad bandwidth of the used OSS. The ER of the converted WDM channels depends on the ER of the input OTDM signal and on the CR of the SPs. The ER of the input OTDM signal was of 15 dB, whereas the CR of the SPs centered at λ_1, λ_2 and λ_3 was of 12.1, 13.1 and 12.0 dB, respectively. Such low CRs can be improved by once again reconfiguring the amplitude response of the POF, as shown in Fig. 4.15 (c1). The CR of each SP significantly depends on the power of its center spectral line, located at λ_1, λ_2 or λ_3. Therefore, the CR of each SP can be maximized by tuning the attenuation of the optical filters centered at λ_1, λ_2 and λ_3. The CR of the SPs centered at λ_1, λ_2 and λ_3 improved to 15.7, 16.8 and 18.6 dB, respectively. The shape of each SP could be further improved by individually shaping each spectral line. Such time-consuming optimization was not performed due to time constraints.

Besides the SPT shown in Fig. 4.15 (c6), three additional SPTs were generated by configuring the phase response of the POF. Each SPT was mixed with the input OTDM signal by means of degenerate FWM in a HNLF. The HNLF had a length of 150 m, nonlinear coefficient of $\gamma = 10.5$ W^{-1}km^{-1}, zero-dispersion wavelength of 1550 nm and a dispersion slope of 0.005 ps/nm^2/km. The back-to-back 40 Gb/s and 160 Gb/s optical signals, optical spectrum at the output of the HNLF, SPTs and corresponding converted WDM channels are shown in Fig. 4.16. Figure 4.16 (a3) shows that a conversion efficiency between -20 and -25 dB was obtained. It also shows that all optical signals fill the entire gain bandwidth of the used C-band EDFAs. The fourth converted WDM signal, located at $\lambda_{o,4} = 1518.5$ nm, would be completely out of the EDFAs gain bandwidth. All SPTs produced undistorted converted WDM channels. However, the adjacent OTDM tributaries were not completely suppressed due to the following reasons. Firstly, the SPs contained a significant power before the rising edge and after the falling edge of the pulses. Secondly, the tight channel spacing and reduced roll-off the the optical filters used to select one of the converted WDM channels resulted in non-negligible inter-channel crosstalk. In addition, the bandwidth of the used OSS is sufficiently broad to capture the inter-channel crosstalk between two spectrally adjacent WDM channels. The Q-factors of all converted WDM channels are higher than 16 dB, except for Fig. 4.16 (e2)–(e4), which correspond to the multicasting of an OTDM tributary to the three converted WDM channels. When time-overlapped SPs are used inter-channel crosstalk overlaps in time with the pulses of the converted WDM channel, thereby decreasing the Q-factor. The inter-channel crosstalk can be significantly averaged in all converted WDM channels by using a photoreceiver with lower bandwidth (e.g., 30 GHz) instead of the broad bandwidth OSS.

Such a photoreceiver was employed to perform the measurement the BERs of the converted WDM channels. The results are plotted in Fig. 4.17. The converted WDM channels achieved error-free operation (BER$<10^{-9}$) with power penalties between 3.6 and 6.3 dB relatively to the 40 Gb/s input optical signal. Such power penalties were mainly due to ASE noise and inter-channel crosstalk. The highest power penalties were measured in the converted WDM

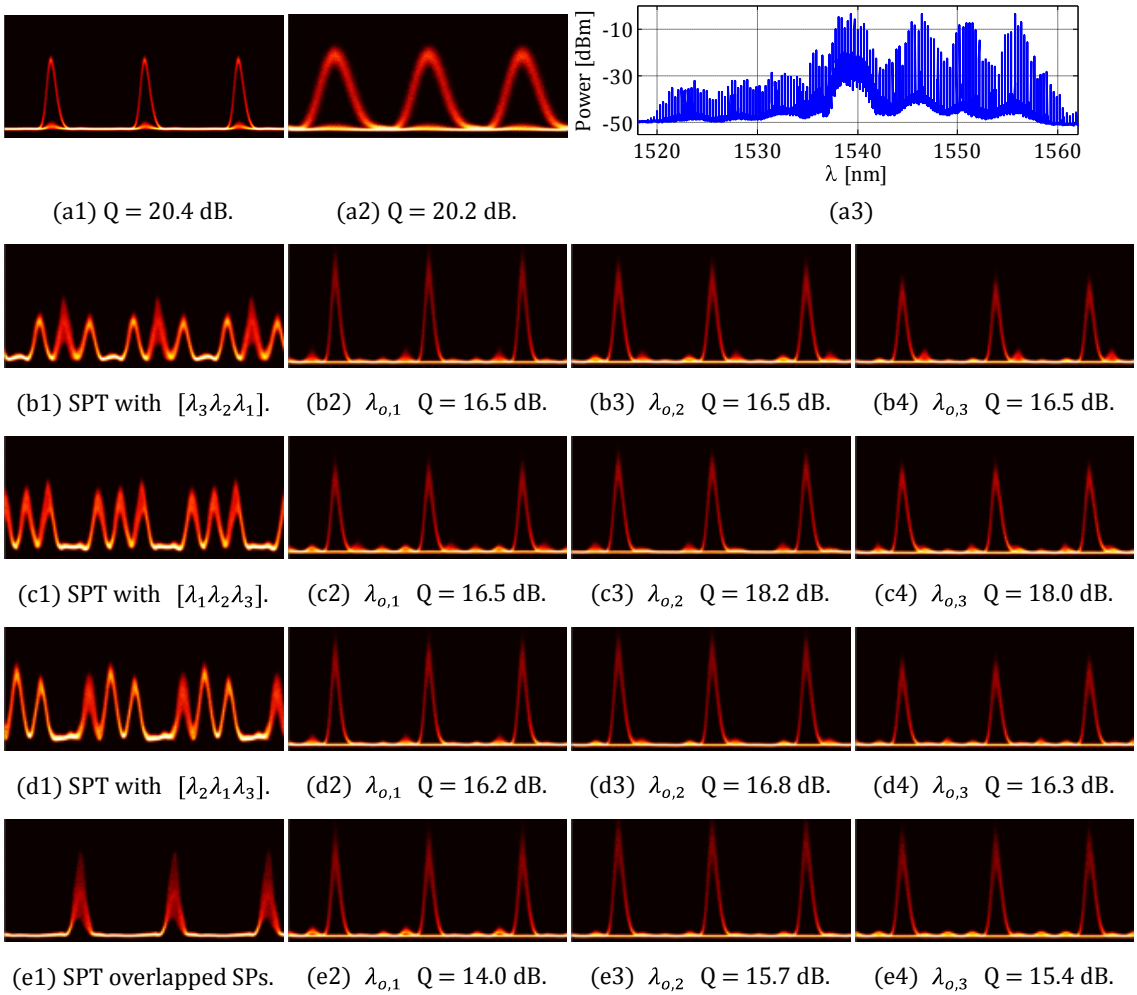

Figure 4.16: Input optical signals (a1) before and (a2) after OTDM. (a3) optical spectrum at the output of the HNLF obtained for a SPT with a wavelength disposition of $[\lambda_3\lambda_2\lambda_1]$. Remaining rows: SPTs and corresponding converted WDM channels. The wavelengths of the converted WDM channels are $\lambda_{o,1} = 1532.7$ nm, $\lambda_{o,2} = 1528.2$ nm and $\lambda_{o,3} = 1523.1$ nm.

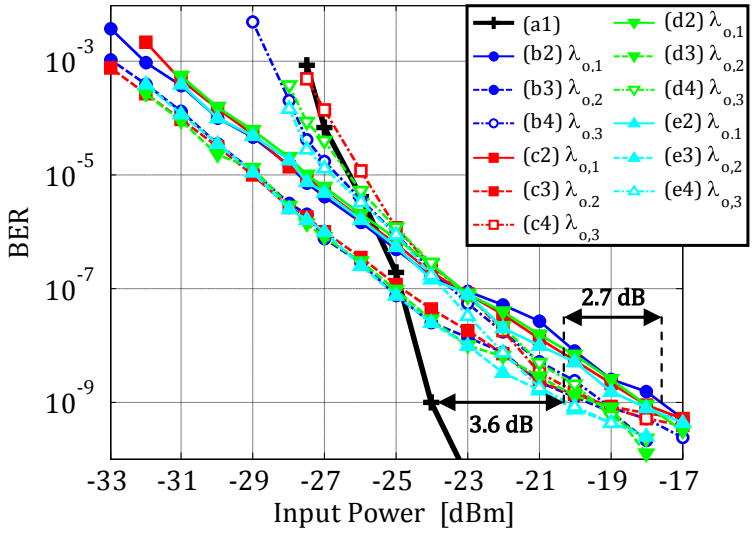

Figure 4.17: BERs of the input and converted optical signals, as labeled in Fig. 4.16.

channel centered at $\lambda_{o,1}$, as it was spectrally adjacent to the input optical signal. The BER of the input optical signal has the steepest variation with the input optical power. For input optical powers lower than -25 dBm the BERs of the input optical signal are amongst the highest ones. The converted WDM channels are clearly more distorted and noise loaded than the input optical signal. This means that decreasing the OSNR by decreasing the input optical power only severely impairs the converted optical signal if the added noise power is sufficiently high. This only occurs for very low OSNRs, and thereby very low input optical powers. In this case, the impairments arising from the added ASE noise dominate over signal distortions, and the slope of the BER curve increases. On the other hand, the input optical signal is undistorted, and thereby its BER depends exclusively on the OSNR. This is why the BER of the input optical signal varies so steeply with the OSNR, and therefore with the input optical power. The presented results demonstrate that the experimental setup successfully implemented the scheme depicted in Fig. 4.13 in terms of wavelength tunability of the input and output optical signals, and OTDM tributary to WDM channel mapping. However, modulation format transparency was not demonstrated, as the employed degenerate FWM scheme is neither phase nor polarization transparent. Assuming negligible CD in the HNLF, the phase of the converted WDM channels is given by $\theta_{o,i} = 2\theta_s - \theta_i$, where θ_s is the phase of the input OTDM signal and θ_i is the phase of the i^{th} SP. As a result, the phase of the converted WDM channel depends on twice the phase of the OTDM signal. In order to obtain the correct phase relation, which is $\theta_{o,i} = 2\theta_i - \theta_s$, the SPs must be spectrally located between the converted WDM channels and the input OTDM signals. Polarization insensitive operation can be achieved by using two orthogonal pumps [44] or a polarization diversity scheme [37]. The schemes proposed for phase and polarization transparency require high power SPs or CW pumps instead of a high power input OTDM signal, thereby alleviating the amplification of the input OTDM signal. Hence, such schemes should provide a lower power penalty relatively to back-to-back operation. These schemes could not be tested due to experimental constraints. Bit rate transparency could not be assessed as the MLLD operated only between 38 and 43 GHz. Nonetheless, the highest bit rate depends on the operational bandwidths of the MZI-

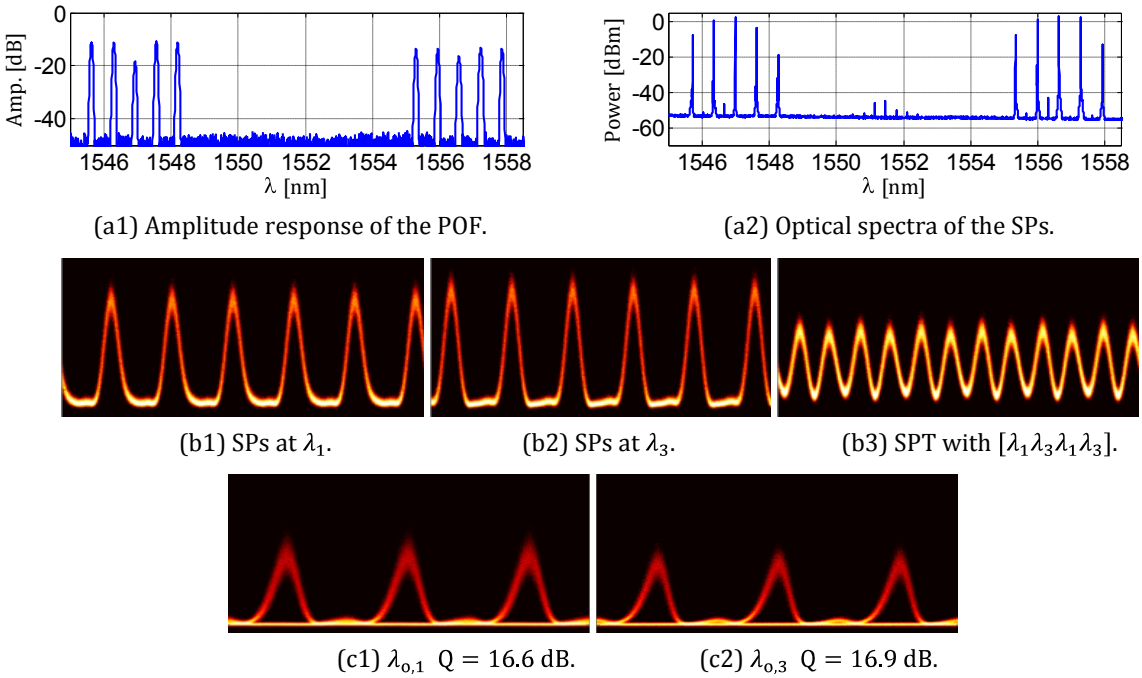

(a1) Amplitude response of the POF. (a2) Optical spectra of the SPs.

(b1) SPs at λ_1. (b2) SPs at λ_3. (b3) SPT with $[\lambda_1\lambda_3\lambda_1\lambda_3]$.

(c1) $\lambda_{o,1}$ Q = 16.6 dB. (c2) $\lambda_{o,3}$ Q = 16.9 dB.

Figure 4.18: Experimental results obtained for intermediate rate conversion (2×80 Gb/s).

SOA, POF, EDFAs, and FWM in the HNLF. The operational bandwidth of the MZI-SOA is the lowest one. The gain dynamics of the SOAs limits the operation of the used MZI-SOA to intensity modulated optical signals at a maximum bit rate of 40 Gb/s. However, since the MZI-SOA operates with optical signals without data modulation, such limitation does not apply. Firstly, the FWHM of the multicast optical signals can be defined by tuning the average power and time delays of the MZI-SOA's input optical signals [7]. A lower FWHM can be obtained at the cost of a lower output power. The minimum FWHM ultimately depends on the timing jitter of the input optical signals. The FWHM can also be defined by shaping the amplitude response of the POF. Secondly, the repetition rate of the SPs can be increased by a power of two by suppressing spectral lines with the amplitude response of the POF. The remaining spectral lines should be spaced by a frequency equal to the target repetition rate. This configuration was experimentally assessed with the purpose of performing intermediate rate OTDM to WDM conversion.

The repetition rate of the SPs centered at λ_1 and λ_3 was doubled to 80 GHz by suppressing half of their spectral lines, as shown in Fig. 4.18 (a1) and (a2). The SPs centered at λ_2 were suppressed by the POF. The time delays added by the POF to the SPs centered at λ_1 and λ_3 were of 0 and 12.5 ps, respectively. Figure 4.18 (b1)–(b3) shows that high quality SPs and SPT were obtained. Half of the OTDM tributaries were converted to each output WDM channel, shown in Fig. 4.18 (c1) and (c2). The measured Q-factors show that successful intermediate rate conversion was achieved. SPTs with arbitrary disposition of wavelengths such as $[\lambda_3\lambda_3\lambda_1\lambda_2]$, or time-overlapped $[\lambda_1\lambda_2\lambda_3]$ with $[\lambda_3\lambda_2\lambda_1]$ can be obtained by reconfiguring the frequency response of the POF, as demonstrated for single-channel operation in [45].

4.5 Conclusions

In this chapter, three optical subsystems based on different photonic mixers were assessed.

An IFMS based on differentially delaying two copies of the input RF signal by τ, and mixing the resulting signals thereafter was implemented by means of signal remodulation. An OC was firstly modulated by the input RF signal, and, after a time interval of τ, remodulated by the input RF signal. Modulation and remodulation was obtained by a single EAM, enabled by the bidirectionality of such device. The RF power and RF frequency were measured from the average optical power of the modulated and remodulated optical signals, respectively, after OCS was performed on both signals. The RF frequency was measured unambiguously within 10 MHz, over a frequency range of 12 GHz. A peak-to-peak RF frequency error of 3 MHz was obtained. Such a low unambiguity was limited by the length of the patchcord that connected the EAM to the fiber mirror reflector. The lowest measurable RF frequency depends on the bandwidth of the OCS NFs, whereas the highest measurable RF frequency depends on the electrical bandwidth of the EAM and respective driving circuitry. The greatest advantages of the proposed photonic IFMS are its simplicity and incoherent operation. The latter advantage enables stable RF frequency measurement with high frequency resolution over a large frequency range, at the cost of reduced unambiguity.

Wavelength conversion in a PPLN waveguide was performed by mixing two CW pumps with an input 160 Gb/s OTDM signal by means of cSFG-DFG. The purpose of the experiment was to validate room-temperature operation over a broad bandwidth at very high pump powers, which could potentially induce photorefractive damage in the PPLN waveguide. Such a deleterious effect was not observed as error-free operation was measured in all tributaries of the converted optical signal, tuned at 1536, 1540, and 1565 nm. A maximum power penalty of 2.1 dB relatively to the input optical signal was obtained.

Flexible OTDM to WDM conversion was performed by FWM a multi-wavelength SPT with an input 160 Gb/s (4×40 Gb/s) OTDM signal in a HNLF. SPTs with an arbitrary disposition of SPs centered at different wavelengths was performed by multicasting an optical clock signal, and filtering the resulting SPs with a POF. A multi-wavelength multicasting scheme based on a MZI-SOA was employed. Since optical signals without data modulation were employed, patterning effects did not occur. However, the multicast SPs were impaired by ASE noise, limited CR, FWM and gain competition between channels. The tunable amplitude and phase responses of the POF individually reshaped and delayed each SP, thereby providing high quality SPTs. All converted WDM channels achieved error-free performance with a maximum power penalty of 6.3 dB at a BER of 10^{-9} relatively to the input optical signal. Intermediate rate conversion to two 80 Gb/s WDM channels was also achieved, simply by reconfiguring the amplitude response of the POF. The repetition rate of the SPs was doubled to 80 GHz by suppressing half of their spectral lines. The proposed OTDM to WDM converter addresses important issues such as wavelength tunability of the input and output optical signals, arbitrary OTDM tributary to WDM channel mapping, and modulation format and bit rate transparency. All issues except for the last two were addressed in the experiment. Modulation format transparency requires an improved FWM scheme. Bit rate tunability could be assessed using an OTDM signal generation scheme with continuously tunable bit rate.

Chapter 5

Conclusion and outlook

In this thesis several photonic systems have been presented with the purpose of performing optical and RF signal processing. Linear optical signal processing with MZDI-based optical filtering was firstly proposed to perform instantaneous RF frequency measurement. Two IFMSs sharing the same operation principle but differing in the implementation of the MZDI were presented [J1, J2]. The inclusion of TCR to the MZDI was explored in different applications which require TODLs. A photonic beamforming system [J3] and a TODC [J4, J5] were proposed. The last works done for this thesis were based on nonlinear optical signal processing. Signal remodulation, cSFG-DFG in a PPLN waveguide, and FWM in a HNLF served as basic photonic mixers for a novel IFMS [J6], wavelength conversion [J7] and OTDM to WDM conversion [J8], respectively. This short summary shows that this thesis has successfully focused on many diverse topics such as microwave photonics, optical dispersion compensation and ultrafast all-optical nonlinear signal processing.

The work done with MZDIs on IFMSs is fairly finished and future research directions should be based on the improved scheme shown in Fig. 2.8 (b). Such scheme enables a strong OCS independently of the laser's linewidth without attenuating the RF tones. Furthermore, the electrical circuitry which drives the electrodes of the DE DO MZM is simple. The required differential time delay decreases with the increase of the RF frequency measurement range, and can be tuned by the TEDL without destabilizing the system. Hence, this scheme is able to provide an IFMS with a tunable measurement range limited only by the bandwidth of the passive electrical circuitry, which can nowadays reach more than 50 GHz.

There is much future work to be done on the proposed photonic beamforming system, motivated by the observed stability problems. In this scope, there are two possible research directions. The first consists in designing a system based on incoherent operation enabled by SSB modulation, as done in the experiment of the TODC. This should require theoretical, simulation and experimental work. The other direction is to straightforwardly resort to integrated optics. The main disadvantage of the proposed system is the trade-off between maximum time delay, which increases with the number of antenna elements, and bandwidth. Another important issue is energy efficiency, which mainly depends on the losses, and E/O and O/E conversion efficiency of the system. Both issues cannot be neglected when thinking in novel beamforming systems based on MZDI-TCRs. Hybrid architectures using discretely TODLs [46], MZDI-TCRs, ring resonators [47] and phase shifters [48] can be conceived to explore the unique advantages of each technique. Such trade-off between bandwidth and maximum time delay also applies to the proposed TODC, in which maximum time delay gives

rise to maximum CD compensation range. This is also the main disadvantage of the TODC. Future work on this topic should be directed to enabling the use of DSB modulated signals, which requires coherent operation in the optical domain. Consequently, implementations in all-fiber or integrated optical devices should be considered with the purpose of avoiding a high sensitivity to the environmental conditions. Further work should also address multichannel operation. However, before thinking in these future directions a careful comparison between the proposed TODC and TEDC should be performed with the purpose of finding an adequate scenario in which the TODC fits [49]. State-of-the-art high capacity optical transport systems are already employing advanced modulation formats which explore all the three dimensions of light – amplitude, phase and polarization. Consequently, E/O conversion requires that the information present in all three dimensions of light is passed to the electrical domain. This automatically enables nearly ideal TEDC [17] and even compensation of nonlinear effects [50]. However, these features have a cost in complexity and power consumption. The proposed TODC and all TODCs in general are passive devices with reduced power consumption, thereby increasing the energy efficiency of the system. In addition, some TODCs allow multichannel operation. However, TODCs also have a cost in complexity, loss and component count. These statements show that the proposed TODC should be essentially investigated towards network scenarios in which multichannel CD compensation and high energy efficiency are required.

The operation principle behind the work done in nonlinear optical signal processing is to delay and mix the optical signals, instead of linearly delaying and adding them as done in the MZDIs. The first application using this operation principle was a photonic IFMS [J6], which in comparison with the ones proposed in [J1, J2] has two disadvantages and one advantage. The first disadvantage is the absence of two complementary average power measurements. As a result, the ACF is a cosine function instead of a tangent one, which in the logarithmic scale is quasi-linear over the entire RF frequency measurement range. The second disadvantage is that the length of the patchcord which connects the EAM to the fiber mirror reflector must be very short for unambiguous RF frequency measurement in the order of GHz. A length of approximately of 5 mm is required for a RF frequency measurement range of 10 GHz. Such a short length should be achievable only with integrated optical devices such as a reflective EAM. The main advantage of the proposed IFMS is its intrinsically incoherent operation, which provides robustness to the environmental conditions independently of how wide is the RF frequency measurement range. The proposed IFMS can be used together with a broad range, low-resolution IFMS such as the one proposed in [J2] with the purpose of providing a broad range, high-resolution IFMS. Ultrafast all-optical mixing was employed in the last two works presented in this thesis to achieve wavelength conversion and gating. Such operations serve as basis to optical packet switching (OPS), both for OTDM and WDM networks. As pointed in [51], OPS should be compared with conventional electronic packet switching in terms of energy consumption/efficiency, capacity, throughput and scalability. Therefore, the final conclusions drawn on [J7, J8] address these issues. The purpose of the work done in [J7] was simply to test the PPLN waveguide at room temperature, which was successfully achieved. A very low conversion efficiency was traded off for a broad conversion bandwidth. As a result, high-power EDFAs had to be used, thereby reducing the energy efficiency of the system. The capacity of the PPLN waveguide was limited by its conversion bandwidth of about 700 GHz, which was sufficiently broad to handle the 160 Gb/s intensity modulated input OTDM signal. Since such device is modulation format transparent higher capacities can be achieved using advanced modulation formats with higher spectral efficiencies without sacrificing con-

version efficiency. This is an interesting topic for future work. The throughput of an OPS system consists in its capacity to dynamically process input packets as a whole, and therefore mainly depends on the system's architecture. Nonetheless, the proposed wavelength converter is able to process an arbitrary number of packets of the input OTDM signal with a granularity down to a single OTDM tributary, as long as the involved optical signals do not exceed its conversion bandwidth. The scalability of an OPS system also mainly depends on its architecture. However, it is limited by future-proof features of its wavelength converters such as the operational bandwidth, modulation format transparency and energy consumption/efficiency. The PPLN waveguide offers modulation format transparency and an operational bandwidth much higher than the electronic devices present in an OPS system. Therefore, the throughput and scalability of an OPS system should not be limited by wavelength converter systems based on the used PPLN waveguide thanks to their ultrafast response, as long as the energy consumption/efficiency is improved in further research work.

The difference between the OTDM to WDM converter proposed in [J8] and [J7] is that in the first one each tributary of the input OTDM signal is selectively mapped to a given wavelength, whereas in the latter work all tributaries are mapped to a single wavelength. The proposed OTDM to WDM converter was designed to be flexible in terms of wavelength tunability of the input and output optical signals, OTDM tributary to WDM channel mapping, and modulation format and bit rate transparency. These issues enable future-proof operation, and are closely related with capacity, throughput and scalability. The capacity and throughput were mainly limited by the gain bandwidth of the EDFAs, which was completely filled by all optical signals. The use of enhanced EDFAs operating in both C and L bands or Raman amplification is a solution to increase capacity. Similarly to what was previously concluded on the wavelength converter, since the converter is modulation format transparent higher capacities can be achieved using advanced modulation formats with higher spectral efficiencies. The conclusions previously drawn on the wavelength converter about throughput also apply to the proposed converter. The scalability of the converter can be defined as its capacity to convert input OTDM signals with different bit rates, modulation formats and number of tributaries to an arbitrary number of output wavelengths. This should be done with a granularity down to a single OTDM tributary, and energy efficiency should also be addressed. FWM enables modulation format transparent operation over a large spectral width, which thereby enables bit rate transparent operation. The granularity of the system is limited by the minimum bandwidth of the POF. In order to map an arbitrary set of input OTDM tributaries to a given output WDM channel, the transfer function of the POF associated with the respective SP should be able to individually shape each spectral line [45]. The number of output wavelengths depends on how many wavelengths the MZI-SOA can handle. Even if wavelength multicasting performs differently at different wavelengths, spectral reshaping can be performed by the POF. In terms of energy efficiency, the energy consumption of the system increases with the symbol rate and number of output wavelengths, as the average power per input OTDM tributary and per output WDM channel should be kept relatively constant. Nonetheless, the energy efficiency can be improved by replacing the MZI-SOA by a single SOA. This requires additional spectral reshaping to be performed by the POF, which does not increase its power consumption. In terms of future work, it would be interesting to test the flexibility of the proposed OTDM to WDM converter as an interface between high bit rate core networks and lower bit rate passive optical access networks, both employing WDM and/or OTDM.

References

[1] Govind P. Agrawal. *Fiber-Optic Communication Systems*. John Wiley & Sons, 3rd edition, 2002.

[2] R.S. Tucker, G. Eisenstein, and S.K. Korotky. Optical time-division multiplexing for very high bit-rate transmission. *Lightwave Technology, Journal of*, 6(11):1737–1749, Nov. 1988.

[3] J. Armstrong. OFDM for optical communications. *Lightwave Technology, Journal of*, 27(3):189–204, Feb. 2009.

[4] P.J. Winzer and R.-J. Essiambre. Advanced optical modulation formats. *Proceedings of the IEEE*, 94(5):952–985, May 2006.

[5] A. E. Willner, O. F. Yilmaz, J. Wang, X. Wu, A. Bogoni, L. Zhang, and S. R. Nuccio. Optically efficient nonlinear signal processing. *Selected Topics in Quantum Electronics, IEEE Journal of*, 17(2):320–332, Mar. 2011.

[6] C.R. Giles. Lightwave applications of fiber bragg gratings. *Lightwave Technology, Journal of*, 15(8):1391–1404, Aug. 1997.

[7] N. Yan, J. del Val Puente, T.G. Silveira, A. Teixeira, A. Ferreira, E. Tangdiongga, P. Monteiro, and A. Koonen. Simulation and experimental characterization of SOA-MZI-Based multiwavelength conversion. *Lightwave Technology, Journal of*, 27(2):117–127, Jan. 2009.

[8] R. Morais, R. Meleiro, P. Monteiro, and P. Marques. OTDM-to-WDM conversion based on wavelength conversion and time gating in a single optical gate. In *Optical Fiber communication/National Fiber Optic Engineers Conference, 2008. OFC/NFOEC 2008. Conference on*, pages 1–3, Feb. 2008.

[9] Jianping Yao. Microwave photonics. *Lightwave Technology, Journal of*, 27(3):314–335, Feb. 2009.

[10] A. J. Seeds and K. J. Williams. Microwave photonics. *Lightwave Technology, Journal of*, 24(12):4628–4641, Dec. 2006.

[11] Xihua Zou, Shilong Pan, and Jianping Yao. Instantaneous microwave frequency measurement with improved measurement range and resolution based on simultaneous phase modulation and intensity modulation. *Lightwave Technology, Journal of*, 27(23):5314–5320, Dec. 2009.

[12] Xihua Zou and Jianping Yao. An optical approach to microwave frequency measurement with adjustable measurement range and resolution. *Photonics Technology Letters, IEEE*, 20(23):1989–1991, Dec. 2008.

[13] J. Dai, K. Xu, X. Sun, J. Niu, Q. Lv, J. Wu, X. Hong, W. Li, and J. Lin. A simple photonic-assisted microwave frequency measurement system based on MZI with tunable measurement range and high resolution. *Photonics Technology Letters, IEEE*, 22(15):1162–1164, Aug. 2010.

[14] C. Caucheteur, S. Bette, R. Garcia-Olcina, M. Wuilpart, S. Sales, J. Capmany, and P. Megret. Influence of the grating parameters on the polarization properties of fiber bragg gratings. *Lightwave Technology, Journal of*, 27(8):1000–1010, Apr. 2009.

[15] A. J. Seeds and K. J. Williams. Microwave photonics. *Lightwave Technology, Journal of*, 24(12):4628–4641, Dec. 2006.

[16] T. Kato, Y. Koyano, and M. Nishimura. Temperature dependence of chromatic dispersion in various types of optical fiber. *Opt. Lett.*, 25(16):1156–1158, Aug. 2000.

[17] C.R.S. Fludger, T. Duthel, D. van den Borne, C. Schulien, E.-D. Schmidt, T. Wuth, J. Geyer, E. De Man, Khoe Giok-Djan, and H. de Waardt. Coherent equalization and POLMUX-RZ-DQPSK for robust 100-GE transmission. *Lightwave Technology, Journal of*, 26(1):64–72, Jan. 2008.

[18] D. Fonseca, A.V.T. Cartaxo, and P. Monteiro. On the use of electrical precompensation of dispersion in optical single-sideband transmission systems. *Selected Topics in Quantum Electronics, IEEE Journal of*, 12(4):603–614, Jul.-Aug. 2006.

[19] Ana Patrícia Santos Ferreira and Tiago Gomes da Silveira. Projecto de um equipamento de terminal óptico de banda lateral única. Technical report, Departamento de Electrónica e Telecomunicações, Universidade de Aveiro, 2004.

[20] T. Erdogan. Fiber grating spectra. *Lightwave Technology, Journal of*, 15(8):1277–1294, Aug. 1997.

[21] Rogério N. Nogueira. *Redes de Bragg em fibra óptica.* PhD thesis, Departamento de Física, Universidade de Aveiro, 2005.

[22] M. Ibsen, M.K. Durkin, M.J. Cole, and R.I. Laming. Optimised square passband fibre bragg grating filter with in-band flat group delay response. *Electronics Letters*, 34(8):800–802, Apr. 1998.

[23] Govind P. Agrawal. *Nonlinear Fiber Optics.* Academic Press, 3rd edition, 2001.

[24] K. Inoue. Four-wave mixing in an optical fiber in the zero-dispersion wavelength region. *Lightwave Technology, Journal of*, 10(11):1553–1561, Nov. 1992.

[25] Robert W. Boyd. *Nonlinear Optics.* Elsevier, 2nd edition, 2003.

[26] C. Langrock, S. Kumar, J.E. McGeehan, A.E. Willner, and M.M. Fejer. All-optical signal processing using $\chi^{(2)}$ nonlinearities in guided-wave devices. *Lightwave Technology, Journal of*, 24(7):2579–2592, Jul. 2006.

[27] C.-S. Brés, A.O.J. Wiberg, B.P.-P. Kuo, J.M. Chavez-Boggio, C.F. Marki, N. Alic, and S. Radic. Optical demultiplexing of 320 Gb/s to 8×40 Gb/s in single parametric gate. *Lightwave Technology, Journal of*, 28(4):434–442, Feb. 2010.

[28] M. Asobe, O. Tadanaga, H. Miyazawa, Y. Nishida, and H. Suzuki. Multiple quasi-phase-matched device using continuous phase modulation of $\chi^{(2)}$ grating and its application to variable wavelength conversion. *Quantum Electronics, IEEE Journal of*, 41(12):1540–1547, Dec. 2005.

[29] Jie Huang, X. P. Xie, Carsten Langrock, R. V. Roussev, D. S. Hum, and M. M. Fejer. Amplitude modulation and apodization of quasi-phase-matched interactions. *Opt. Lett.*, 31(5):604–606, Mar. 2006.

[30] N. Sarkhosh, H. Emami, L. Bui, and A. Mitchell. Reduced cost photonic instantaneous frequency measurement system. *Photonics Technology Letters, IEEE*, 20(18):1521–1523, Sep. 2008.

[31] H. Emami, N. Sarkhosh, L. A. Bui, and A. Mitchell. Amplitude independent RF instantaneous frequency measurement system using photonic Hilbert transform. *Opt. Express*, 16(18):13707–13712, Sep. 2008.

[32] Lam A. Bui, Mark D. Pelusi, Trung D. Vo, Niusha Sarkhosh, Hossein Emami, Benjamin J. Eggleton, and Arnan Mitchell. Instantaneous frequency measurement system using optical mixing in highly nonlinear fiber. *Opt. Express*, 17(25):22983–22991, Dec. 2009.

[33] G.L. Li and P.K.L. Yu. Optical intensity modulators for digital and analog applications. *Lightwave Technology, Journal of*, 21(9):2010–2030, Sep. 2003.

[34] S.J.B. Yoo. Wavelength conversion technologies for WDM network applications. *Lightwave Technology, Journal of*, 14(6):955–966, Jun. 1996.

[35] Guo-Wei Lu, K.S. Abedin, and T. Miyazaki. Experimental demonstrations of all-optical phase-multiplexing using FWM-based phase interleaving in silica and bismuth-oxide HNLFs. *Lightwave Technology, Journal of*, 27(4):409–416, Feb. 2009.

[36] P.J. Winzer, A.H. Gnauck, C.R. Doerr, M. Magarini, and L.L. Buhl. Spectrally efficient long-haul optical networking using 112-Gb/s polarization-multiplexed 16-QAM. *Lightwave Technology, Journal of*, 28(4):547–556, Feb. 2010.

[37] Hao Hu, Evarist Palushani, Michael Galili, Hans Christian Hansen Mulvad, Anders Clausen, Leif Katsuo Oxenløwe, and Palle Jeppesen. 640 Gbit/s and 1.28 Tbit/s polarisation insensitive all optical wavelength conversion. *Opt. Express*, 18(10):9961–9966, May 2010.

[38] H. Hu, H. Suche, R. Ludwig, B. Huettl, C. Schmidt-Langhorst, R. Nouroozi, W. Sohler, and C. Schubert. Polarization insensitive all-optical wavelength conversion of 320 Gb/s RZ-DQPSK data signals. In *Optical Fiber Communication - incudes post deadline papers, 2009. OFC 2009. Conference on*, pages 1–3, Mar. 2009.

[39] Mathieu Charbonneau-Lefort, Bedros Afeyan, and M. M. Fejer. Optical parametric amplifiers using chirped quasi-phase-matching gratings I: practical design formulas. *J. Opt. Soc. Am. B*, 25(4):463–480, Apr. 2008.

[40] M.R. Lorenzen, D. Noordegraaf, C.V. Nielsen, O. Odgaard, L. Gruner-Nielsen, and K. Rottwitt. Suppression of Brillouin scattering in fibre-optical parametric amplifier by applying temperature control and phase modulation. *Electronics Letters*, 45(2):125–126, Jan. 2009.

[41] L.K. Oxenløwe, M. Galili, H.C.H. Mulvad, H. Hu, H. Ji, J. Xu, E. Palushani, J.L. Areal, A.T. Clausen, and P. Jeppesen. Ultra-high-speed optical signal processing of Tbaud data signals. In *Optical Communication (ECOC), 2010 36th European Conference and Exhibition on*, pages 1–6, Sep. 2010.

[42] H.C.H Mulvad, E. Palushani, M. Galili, J. Xu, H. Hu, A.T. Clausen, L.K. Oxenløwe, and P. Jeppesen. OTDM-WDM conversion based on time-domain optical fourier transformation with spectral compression. In *Optical Fiber Communication - incudes post deadline papers, 2011. OFC 2011. Conference on*, pages 1–3, Mar. 2011.

[43] M.A.F. Roelens, S. Frisken, J.A. Bolger, D. Abakoumov, G. Baxter, S. Poole, and B.J. Eggleton. Dispersion trimming in a reconfigurable wavelength selective switch. *Lightwave Technology, Journal of*, 26(1):73–78, Jan. 2008.

[44] K. Inoue. Polarization independent wavelength conversion using fiber four-wave mixing with two orthogonal pump lights of different frequencies. *Lightwave Technology, Journal of*, 12(11):1916–1920, Nov. 1994.

[45] M.A.F. Roelens, J.A. Bolger, D. Williams, S.J. Frisken, G.W. Baxter, A.M. Clarke, and B.J. Eggleton. Flexible and reconfigurable time-domain demultiplexing of optical signals at 160 Gb/s. *Photonics Technology Letters, IEEE*, 21(10):618–620, May 2009.

[46] E.N. Toughlian and H. Zmuda. A photonic variable RF delay line for phased array antennas. *Lightwave Technology, Journal of*, 8(12):1824–1828, Dec. 1990.

[47] P.A. Morton and J.B. Khurgin. Microwave photonic delay line with separate tuning of the optical carrier. *Photonics Technology Letters, IEEE*, 21(22):1686–1688, Nov. 2009.

[48] L. Jofre, C. Stoltidou, S. Blanch, T. Mengual, B. Vidal, J. Marti, I. McKenzie, and J.M. del Cura. Optically beamformed wideband array performance. *Antennas and Propagation, IEEE Transactions on*, 56(6):1594–1604, Jun. 2008.

[49] P. Mamyshev. Does optical dispersion compensation have a future? In *Optical Fiber Communication - incudes post deadline papers, 2010. OFC 2010. Conference on*, volume OSuF Workshop, Mar. 2010.

[50] Danish Rafique, Jian Zhao, and Andrew D. Ellis. Digital back-propagation for spectrally efficient WDM 112 Gbit/s PM m-ary QAM transmission. *Opt. Express*, 19(6):5219–5224, Mar. 2011.

[51] R.S. Tucker. Optical packet switching meets mythbusters. In *Optical Fiber Communication - incudes post deadline papers, 2011. OFC 2011. Conference on*, page 1, Mar. 2011.

Appendix A

Journal papers

[J1] - Photonic RF instantaneous frequency measurement system by means of a polarization-domain interferometer

Miguel V. Drummond, Paulo. P. Monteiro and Rogério N. Nogueira

OSA Optics Express, Vol. 17, No. 7, pp. 5433–5438, March 2009.

Photonic RF instantaneous frequency measurement system by means of a polarization-domain interferometer

M. V. Drummond[1,*], P. Monteiro[1,2] and R. N. Nogueira[1]

[1]*Instituto de Telecomunicações, Universidade de Aveiro, 3810-193 Aveiro, Portugal*
[2]*Nokia Siemens Networks Portugal, S.A., RTP NT NAB Photonic Networks SP, 2720-093 Amadora, Portugal*
[*]*Corresponding author: mvd@av.it.pt*

Abstract: A new photonic RF instantaneous frequency measurement system is proposed and experimentally demonstrated. A frequency measurement independent of the optical input power and microwave modulation index is achieved by using the constructive and destructive ports of a polarization-domain interferometer. Experimental tests yield a peak-to-peak frequency error lower than 200 MHz for a frequency range of 1-18 GHz.

OCIS codes: (0060.5625) Radio frequency photonics; (070.6020) continuous optical signal processing; (350.4010) Microwaves.

References and links

1. M. Aikawa and H. Ogawa, "Double-sided MICs and their applications," IEEE Trans. Microwave Theory Tech. **37**, 406-413 (1989).
2. A. J. Seeds and K. J. Williams, "Microwave Photonics," J. Lightwave Technol. **24**, 4628-4641 (2006).
3. L. V. T. Nguyen and D. B. Hunter, "A photonic technique for microwave frequency measurement," IEEE Photon. Technol. Lett. **18**, 1188-1190 (2006).
4. X. Zou and J. Yao, "An Optical Approach to Microwave Frequency Measurement with Adjustable Measurement Range and Resolution," IEEE Photon. Technol. Lett. **20**, 1989-1991 (2008).
5. N. Sarkhosh, H. Emami, L. Bui, and A. Mitchell, "Reduced Cost Photonic Instantaneous Frequency Measurement System," IEEE Photon. Technol. Lett. **20**, 1521-1523 (2008).
6. H. Emami, N. Sarkhosh, L. A. Bui, and A. Mitchell, "Amplitude independent RFinstantaneous frequency measurementsystem using photonic Hilbert transform," Opt. Express **16**, 13707-13712 (2008).
7. H. Chi, X. Zou, and J. Yao, "An Approach to the Measurement of Microwave Frequency Based on Optical Power Monitoring," IEEE Photon. Technol. Lett. **20**, 1249-1251 (2008).

1. Introduction

Modern electronic warfare such as RADAR warning receivers rely on instantaneous frequency measurement (IFM) systems with broad bandwidth and high resolution. Traditional implementations of IFM systems require electrical delay lines and mixers, thus being limited by distortion and unwanted radiation [1].

Microwave signal processing on the optical domain offers many advantages, such as low losses, high time bandwidth products, light weight and immunity to electromagnetic interference [2]. These unique properties have recently brought an increasing interest in photonic IFM systems [3-7]. In [3], two optical carriers are modulated by a RF signal. Each carrier then experiences a different amount of chromatic dispersion, leading to distinct dispersion-induced power fading after direct detection. The difference between the detected optical powers allows measuring the RF frequency. This technique has the downside of needing high-bandwidth photodetectors. An approach based on this idea with adjustable measurement range and resolution was presented in [4]. The chromatic dispersion experienced by each optical carrier is tuned by using tunable laser sources and taking advantage of the dispersion slope of a dispersive fiber. Photonic implementations of traditional electrical IFM

systems were proposed in [5] and [6]. The system presented in [6] allows measuring the RF frequency and power simultaneously and independently, by taking advantage of two orthogonal DC measurements; however, it uses a higher complexity setup in comparison to [5]. Although both systems require low-bandwidth photodiodes, two electrooptic modulators (EOMs) are needed, and their mathematical modeling is complex. A simple approach was presented in [7], in which two optical carriers modulated by the RF signal are filtered by a sinusoidal filter. One of the carriers is centered at a maximum of the filter's response, whereas the other is centered at a minimum. The relation between the optical powers of both modulated carriers is used to measure the RF frequency, independently of the RF input power and microwave modulation index. Although this technique uses low-bandwidth photodiodes and a single EOM, it requires two optical carriers along with a multiplexer and a demultiplexer. Moreover, different wavelength drifts arise from both optical sources, leading to measurement errors.

In this paper, we propose and experimentally demonstrate a simple, cost-effective photonic IFM system based on an interferometer that operates on the polarization domain. The system uses a single optical source, avoiding the need of multiplexers/demultiplexers and different wavelength drifts. A Mach-Zehnder modulator (MZM) up-converts the signal to the optical domain with suppressed optical carrier. The modulated optical signal is fed to a polarization-based interferometer, composed by a polarization maintaining fiber (PMF), a polarization beam splitter (PBS) and two polarization controllers (PCs). The relation between the average optical powers measured at the constructive and destructive output ports of the interferometer yields the RF frequency independently of the input optical power and microwave modulation index.

2. Operation principle

Figure 1 illustrates the proposed IFM system concept. A laser diode (LD) is used to generate a continuous wave (CW) probe with linear polarization. PC1 adjusts the state of polarization (SOP) of the CW probe with the transmission axis of the MZM. The MZM bias is set at the minimum transmission point, so that optical carrier suppressed modulation is achieved.

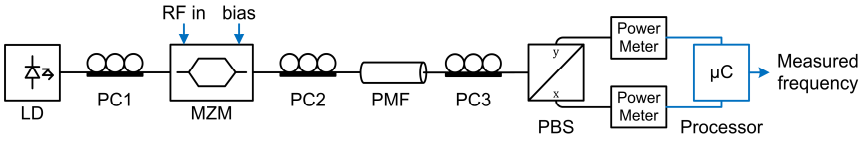

Fig. 1. (Color online) Scheme of the proposed IFM system.

The polarization-domain interferometer consists on the PC2, PMF, PC3 and PBS. The optical carrier suppressed signal at the output of the MZM can be written as

$$s(t) = E_{\mathrm{CW}} e^{j\omega_{\mathrm{CW}} t} \sin[\pi z v_{\mathrm{RF}}(t)], \tag{1}$$

where E_{CW} is the amplitude of the CW probe, ω_{CW} is the angular frequency of the optical carrier, z is the microwave modulation index and $v_{\mathrm{RF}}(t)$ is the RF signal voltage, assumed to have a null average value. Considering all PCs as ideal polarization rotators and the polarization axes x and y aligned with the fast and slow axes of the PMF, respectively, one can express the signal at the output of the PMF as

$$S_{\mathrm{PMF}}(f) = S(f)\{\cos(\theta_1)\hat{x} + \sin(\theta_1) e^{-j2\pi f\tau}\hat{y}\}, \tag{2}$$

where $\hat{x}$ and $\hat{y}$ are the unit vectors along the x and y directions, θ_1 is the polarization rotation angle imposed by PC2 and τ represents the differential group delay (DGD) of the

PMF. $S(f)$ is the Fourier transform of $s(t)$, where f is the RF frequency. The PC3 applies another polarization rotation according to an angle of θ_2. The signal at its output is given by

$$S_{PC3}(f) = S_{PMF}(f)\{\hat{x}\cdot[\cos(\theta_2)\hat{x} + \sin(\theta_2)\hat{y}] + \hat{y}\cdot[\cos(\theta_2)\hat{y} - \sin(\theta_2)\hat{x}]\}. \quad (3)$$

Using equation (2), (3) can be written as

$$S_{PC3}(f) = S(f)\{\cos(\theta_1)\cdot[\cos(\theta_2)\hat{x} + \sin(\theta_2)\hat{y}] + \sin(\theta_1)e^{-j2\pi f\tau}\cdot[\cos(\theta_2)\hat{y} - \sin(\theta_2)\hat{x}]\}. \quad (4)$$

The optical signals at the outputs of the PBS are given by

$$S_{PBS,x}(f) = S(f)\{\cos(\theta_1)\cos(\theta_2) - \sin(\theta_1)\sin(\theta_2)e^{-j2\pi f\tau} \quad (5)$$

$$S_{PBS,y}(f) = S(f)\{\cos(\theta_1)\sin(\theta_2) + \sin(\theta_1)\cos(\theta_2)e^{-j2\pi f\tau}. \quad (6)$$

Hence, the x output port of the PBS consists on the destructive port of the interferometer, whereas the y output port is the constructive port. The optical signals at the outputs of the PBS depend on $S(f)$, that in turn depends on the CW probe power and microwave modulation index. To achieve a measurement independent on these parameters, an amplitude comparison function (ACF) defined as $|S_{PBS,x}(f)/S_{PBS,y}(f)|$ is used to get the RF frequency.

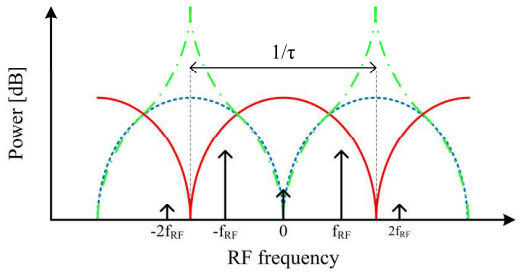

Fig. 2. (Color online) Operation principle of the polarization-based interferometer. Constructive port (solid line), destructive port (dashed line) and ACF (dashed-dotted line).

Figure 2 shows that unambiguous RF frequency measurement can be achieved for RF frequencies up to $1/2\tau$. The highest sensitivity is achieved for $\cos(\theta_1)\cos(\theta_2) = \sin(\theta_1)\sin(\theta_2)$ and $\cos(\theta_1)\sin(\theta_2) = \sin(\theta_1)\cos(\theta_2)$, which yields $\theta_1 = \theta_2 = (2k+1)\pi/4$, $k \in \mathbb{Z}$. In this case, the ACF power variation is theoretically infinite. In practice, the sensitivity is reduced by the limited accuracy in setting θ_1 and θ_2. Moreover, the extinction ratio of the output ports of the PBS and loss difference between both ports must be taken into account. Therefore, the ACF can be defined as

$$\mathrm{ACF}(f) = \left| \frac{S_{PBS,x}(f) + S_{PBS,y}(f)\cdot 10^{\frac{-ER_x}{20}}}{S_{PBS,y}(f) + S_{PBS,x}(f)\cdot 10^{\frac{-ER_y}{20}}} \right| \cdot \alpha, \quad (7)$$

where ER_x and ER_y are the extinction ratios of the x and y ports of the PBS, respectively. α is the loss difference between both ports. The RF frequency is extracted from the measured ACF value, through $f = \mathrm{ACF}^{-1}(f)$.

3. Experiment

An experimental setup similar to the scheme shown in Fig. 1 is considered. A CW laser with a wavelength of 1554.13 nm, 13 dBm of optical power and linewidth lower than 20 MHz is used. A MZM with 30 GHz electrical bandwidth and half-wave voltage of 2 V yields an optical signal with suppressed optical carrier. Low RF input powers are considered since the MZM has a built-in electrical amplifier placed at its RF input. The electrical amplifier has an approximated small signal gain of 26 dB and an output power compression of 16 dBm. It is designed not to significantly overdrive the MZM if carrier suppressed modulation is employed. The PMF is 20 meter long and produces a DGD of τ = 22 ps. PC1 and PC2 are manually adjustable three-plate polarization controllers, whereas PC3 is a polarization locker that allows automatic adjustment. The extinction ratios of the PBS are ER_x = 26 dB and ER_y = 25 dB. An optical switch and a power meter are used instead of the two power meters of Fig. 1. The insertion losses of the MZM, PMF, PBS and optical switch are 6 dB, 1 dB, 0.5 dB and 1 dB, respectively. The RF cable that connects the signal generator to the electrical amplifier has a loss of 1 dB. The measured loss difference between both output ports of the PBS is of α = -0.6 dB. The system calibration process is done automatically through a LabVIEW© interface that controls the RF input frequency and power, PC3 adjustment,

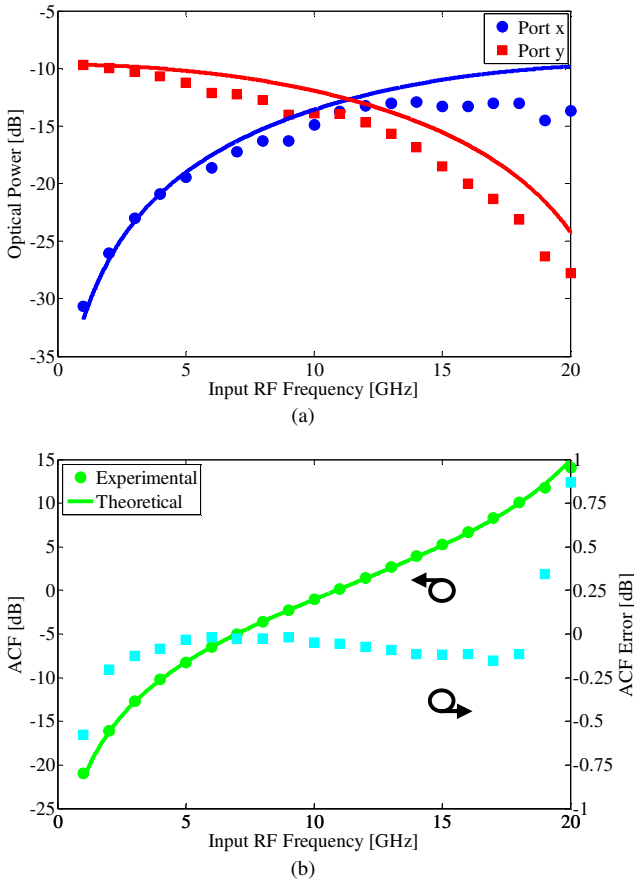

Fig. 3. (Color online) IFM system results. (a) Measured optical powers and (b) ACF for a RF input power of -9 dBm.

optical switch and power meter reading. The calibration process is completed in about 20 seconds (500 ms/GHz), limited mainly by the RF frequency generator settling time and power meter reading time. All the used devices are non polarization-maintaining, except the PMF and the PBS. Experimental results and theoretical curves derived from the mathematical model are presented in Fig. 3. All theoretical curves result from an optimization of θ_1 and θ_2 within a range of 40º to 50º, in order to achieve the lowest peak-to-peak frequency error. This optimization is done because it is impossible to experimentally set both angles at exactly 45º. Moreover, random temperature changes and mechanical vibrations affect PC2 and PC3, thus adding uncertainty to the real values of θ_1 and θ_2. Figure 3(a) shows that experimental optical powers deviate significantly from the theoretical predictions. This deviation is expected since $S(f)$ depends on the microwave modulation index, that in turn decreases with the increase of the RF frequency. Therefore, the measured optical powers decrease relatively to the theoretical predictions as the frequency increases. However, since the ACF does not depend on $S(f)$, theoretical and experimental ACF values agree, as shown in Fig. 3(b).

The measured RF frequency and frequency errors for various RF input powers are displayed in Fig. 4. For each RF power, the peak-to-peak frequency error is lower than 200 MHz, considering a frequency range of 1 to 18 GHz. Errors increase for high RF frequencies

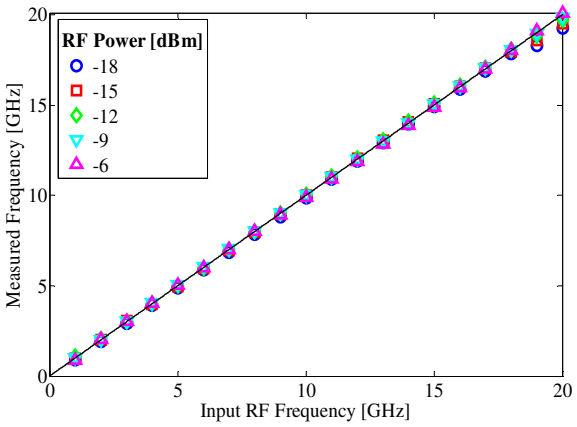

(a)

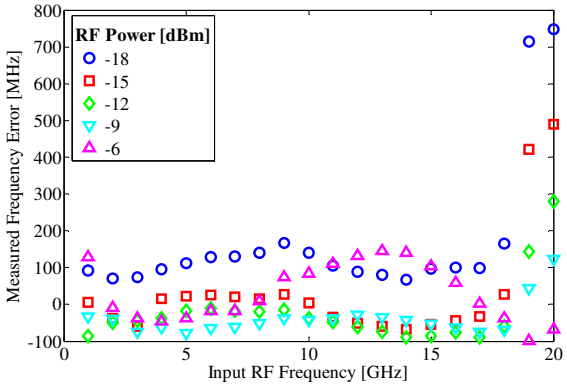

(b)

Fig. 3. (Color online) (a) Measured RF frequency and (b) frequency error for various RF input powers.

close to $1/2\tau$ = 22.7 GHz, since the residual power of the optical carrier interferes on the measurement taken at the constructive port. This situation is illustrated in Fig. 2. The lower peak-to-peak frequency error (50 MHz) is achieved for a RF input power of -9 dBm. For lower RF input powers, the optical carrier suppression ratio decreases. In this case, the power of the optical carrier cannot be neglected relatively to the power of the RF tones, causing a slight increase of the error. On the other hand, for RF input powers higher than -9 dBm, nonlinear distortion occurs in the modulation. The distortion arises mainly from gain saturation of the electrical amplifier and also from the nonlinear modulation transfer function of the MZM. As depicted in Fig. 2, this distortion results in increased power of the higher-order RF tones. This means that the optical signal has at least four spectral lines ($\pm 2f_{RF}$ and $\pm f_{RF}$), where it should ideally have just two, $\pm f_{RF}$. As such, the measurement accuracy is reduced for RF input powers higher than -9 dBm. RF signals with higher input powers can still be considered, at the cost of using an electrical attenuator.

The residual optical carrier derives from the bias drift and limited extinction ratio of the MZM. The MZM bias drift can be mitigated using an automatic bias control device. Another source of error that cannot be neglected is the instability of the signal's SOP, that can be mathematically described as a random variation of θ_1 and θ_2. The instability can be severely reduced using only PM devices and removing PC2 and PC3. Instead of using polarization controllers, a PMF with adjustable key connectors at both ends can be employed.

4. Conclusion

A new photonic RF instantaneous frequency measurement system based on a polarization-domain interferometer was presented and experimentally demonstrated. Since the system takes advantage of the constructive and destructive ports of the interferometer, only a single laser source is needed. This simplifies the system design and avoids different wavelength drifts from different sources. An experimental error lower than 200 MHz was achieved within a RF frequency range of 1-18 GHz. The range and resolution can be adjusted using a PMF with different DGD. The accuracy of the system can be further improved increasing the optical carrier suppression and using only PM devices.

Acknowledgments

THRONE (PTDC/EEA-TEL/66840/2006) Fundação para a Ciência e a Tecnologia (FCT) project and BONE Network of Excellence funded by the European Commission through the 7th ICT-Framework Programme are acknowledged. M. V. Drummond was supported by FCT under the SFRH/BD/40250/2007 scholarship.

[J2] - Photonic Instantaneous Frequency Measurement System Using Complementary Modulation

Miguel V. Drummond, Carlos A.F. Marques, Paulo. P. Monteiro and Rogério N. Nogueira

IEEE Photonics Technology Letters, Vol. 23, No. 3, pp. 143–145, February 2011.

Photonic Instantaneous Frequency Measurement System Using Complementary Modulation

Miguel V. Drummond, Carlos A. F. Marques, Paulo P. Monteiro, and Rogério N. Nogueira

***Abstract*—A novel photonic instantaneous frequency measurement system based on complementary modulation is proposed and experimentally demonstrated. A dual-electrode dual-output Mach–Zehnder modulator is used to simultaneously achieve electrooptical modulation and complementary modulation sideband (MS) filtering. By suppressing the optical carrier at one of the modulator outputs, complementary MS filtering is mapped into two complementary average optical powers from which the RF frequency is derived. The obtained frequency measurement is independent of both optical and RF powers, and is also robust to electrical circuitry imperfections.**

***Index Terms*—Complementary modulation, instantaneous microwave frequency measurement, microwave photonics.**

I. Introduction

ADVANCED electronic warfare systems rely on the analysis and control of large portions of the electromagnetic spectrum (EMS). The first step in the analysis of the EMS is the identification of the frequency and power of incoming RF signals. To this end, an instantaneous frequency measurement system (IFMS) can be employed. Such system should be able to provide real-time, high resolution operation over a wide bandwidth. These stringent requirements have been tackled by photonic IFMSs [1]–[9], which explore the advantages of microwave photonics techniques, such as broad bandwidth, low losses, light weight and immunity to electromagnetic interference [10].

Photonic IFMSs were initially based on well-known electronic techniques, such as the channelizer [1] and scanning receiver [2]. The recently proposed photonic IFMSs have been focused in all-optical signal processing [3]–[9]. In [3], chromatic dispersion is used to obtain RF power fading as function of the RF frequency. Photonic mixing between two delayed copies of the modulated RF signal is explored in [4]–[6]. The average power of the resulting signal depends on the RF frequency. A RF frequency to average power conversion scheme was proposed in [7]. A Mach–Zehnder modulator (MZM) biased in the minimum transmission point is used to modulate two optical sources. One modulated signal is high-pass filtered, whereas low-pass filtering is employed on the other. In this way, the average powers of the filtered optical signals depend on the RF frequency in a complementary way. The complementary nature of the average optical powers yields a frequency measurement independent of both optical and RF powers. Furthermore, the frequency measurement is not affected by the nonideal frequency response of the electrooptical modulator. A simplified scheme of this idea which uses a single optical source and a complementary filter pair (CFP) was presented in [8], [9]. However, it employs a polarization sensitive setup which is sensitive to environmental perturbations. Such perturbations result in deviations between the central frequency of the CFP and the optical carrier (OC). Since such deviations affect both complementary filters, the resulting frequency errors cannot be easily detected.

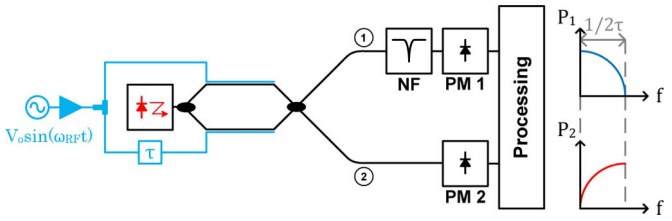

Fig. 1. Schematic of the IFMS. The graphics at the right depict the variation of the measured average optical powers with the RF frequency.

In this letter, we propose and experimentally demonstrate a photonic IFMS based on complementary modulation. The key component of the proposed scheme is a dual-electrode, dual-output MZM (DE-DO-MZM). By delaying the RF signal applied to one electrode relatively to the other, the MS power of the two modulated optical signals becomes dependent on the RF frequency. The bias voltage of the modulator is adjusted so that the OC is suppressed at output 2. As a result, the power of the MSs at output 2 increases with the RF frequency, while at output 1 such variation is opposite. As such, the proposed scheme shares the previously mentioned advantages of [7]. Since electrooptic modulation and complementary filtering are simultaneously achieved, complementary optical filters are not required.

II. Operation Principle

The schematic of the proposed IFMS is shown in Fig. 1. An OC is modulated by the RF signal using a DE-DO-MZM. The signals at the outputs of the modulator have a phase difference of đ, and are given by

$$\frac{E_{1,2}(t)}{E_{\text{in}}(t)} = \frac{1}{2}\left[e^{j(\pi/V_\pi)(v(t)+V_B)} \mp e^{j(\pi/V_\pi)(v(t-\tau)-V_B)}\right], \quad (1)$$

Manuscript received July 27, 2010; revised October 31, 2010; accepted November 13, 2010. Date of publication November 18, 2010; date of current version January 12, 2011. This work was supported by THRONE (PTDC/EEA-TEL/66840/2006) Fundação para a Ciência e Tecnologia (FCT) project.

The authors are with the Instituto de Telecomunicações, Universidade de Aveiro, Aveiro 3810-193, Portugal (e-mail: mvd@av.it.pt).

Color versions of one or more of the figures in this letter are available online at http://ieeexplore.ieee.org.

Digital Object Identifier 10.1109/LPT.2010.2093875

where $E_{\rm in}(t)$ is the electric field of the input OC, V_π is the modulator switching voltage, $v(t) = V_o \sin(\omega_{\rm RF} t)$ is the RF signal, where V_o is the RF amplitude and $\omega_{\rm RF} = 2\pi f_{\rm RF}$ is the RF angular frequency, V_B is the bias voltage and τ is the electrical time delay difference between both electrodes. Considering $V_B = (V_\pi/2)$ and applying the Jacobi–Anger expansion, (1) can be written as

$$\frac{E_{1,2}(t)}{E_{\rm in}(t)} = \frac{j}{2} \sum_{n=-\infty}^{n=+\infty} j^n J_n(z)[e^{jn\omega_{\rm RF} t} \pm e^{jn\omega_{\rm RF}(t-\tau)}], \quad (2)$$

where $J_n(z)$ is the nth Bessel function and $z = \pi(V_o/V_\pi)$ is the modulation index. As $J_{-n}(z) = (-1)^n J_n(z)$, (2) can be expressed as

$$\frac{E_{1,2}(t)}{E_{\rm in}(t)} = \frac{j}{2} \left\{ \begin{array}{c} k_{1,2} + 2 \sum\limits_{n=1}^{n=+\infty} j^n J_n(z). \\ [\cos(n\omega_{\rm RF} t) \pm \cos(n\omega_{\rm RF}(t-\tau))] \end{array} \right\}, \quad (3)$$

where $k_1 = 2J_0(z)$ and $k_2 = 0$. By applying trigonometric identities the electrical fields are given by

$$\frac{E_1(t)}{E_{\rm in}(t)} = j \left\{ \begin{array}{c} J_0(z) + 2 \sum\limits_{n=1}^{n=+\infty} j^n J_n(z). \\ \left[\cos\left(n\omega_{\rm RF}\left(t - \frac{\tau}{2}\right)\right) \cos\left(\frac{n\omega_{\rm RF}\tau}{2}\right)\right] \end{array} \right\} \quad (4.1)$$

$$\frac{E_2(t)}{E_{\rm in}(t)} = j \left\{ \begin{array}{c} -2 \sum\limits_{n=1}^{n=+\infty} j^n J_n(z). \\ \left[\sin\left(n\omega_{\rm RF}\left(t - \frac{\tau}{2}\right)\right) \sin\left(\frac{n\omega_{\rm RF}\tau}{2}\right)\right] \end{array} \right\}. \quad (4.2)$$

If low modulation indexes are considered, the series can be approximated by the first term. Therefore,

$$\frac{E_1(t)}{E_{\rm in}(t)} = j \left\{ \begin{array}{c} J_0(z) + 2jJ_1(z). \\ \left[\cos\left(\omega_{\rm RF}\left(t - \frac{\tau}{2}\right)\right) \cos\left(\frac{\omega_{\rm RF}\tau}{2}\right)\right] \end{array} \right\} \quad (5.1)$$

$$\frac{E_2(t)}{E_{\rm in}(t)} = j \left\{ \begin{array}{c} -2jJ_1(z). \\ \left[\sin\left(\omega_{\rm RF}\left(t - \frac{\tau}{2}\right)\right) \sin\left(\frac{\omega_{\rm RF}\tau}{2}\right)\right] \end{array} \right\}. \quad (5.2)$$

Equations (5.1) and (5.2) show that the MSs of the modulated optical signals are multiplied by a cosine or sine factor, which depends on the product $\omega_{\rm RF}\tau$. Therefore, the electrical time delay difference results in complementary MS filtering. Equation (5.2) also shows that the average optical power at the output 2 of the modulator, $P_2 = \overline{||E_2(t)||^2}$, is proportional to $\sin^2(\omega_{\rm RF}\tau/2)$. However, $P_1 = \overline{||E_1(t)||^2}$ is proportional to $\cos^2(\omega_{\rm RF}\tau/2)$ only if the OC is suppressed, which corresponds to the elimination of the first term in (5.1).

There are two methods to achieve OC suppression (OCS). The first consists on splitting the light generated by the optical source in two paths, one connected to the DE-DO-MZM, and the other coupled with the output 1 of the modulator. By adjusting the phase and amplitude of the CW signal going through the latter path, OCS is achieved at output 1 by destructive interference. This method enables wavelength-insensitive operation at the cost of requiring integrated optics to achieve stable operation. The method adopted in this work is based on suppressing the OC with a notch filter (NF). Even though wavelength-insensitive operation is achieved only at output 2, a deviation between the wavelengths of the optical source and NF can be easily monitored since it only affects P_1.

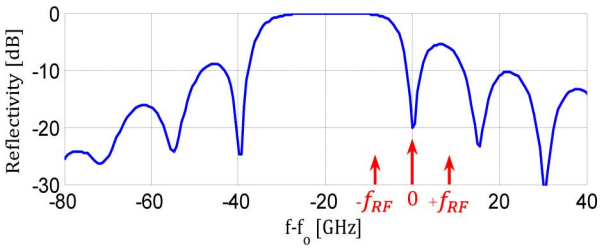

Fig. 2. Reflectivity of the FBG used as an NF. f_0 is the OC frequency.

With OCS performed at the output 1 of the modulator, an amplitude comparison function (ACF) can be defined as

$$\text{ACF}(\omega_{\rm RF}) = \frac{P_2}{P_1} = \tan^2\left(\frac{\omega_{\rm RF}\tau}{2}\right). \quad (6)$$

The ACF only depends on the product $\omega_{\rm RF}\tau$. Therefore, the measurement of the RF frequency through the ACF is independent of both the optical and RF powers.

III. Experimental Results and Discussion

A proof-of-concept experiment based on the schematic shown in Fig. 1 was performed. The input RF signal was firstly amplified using an electrical amplifier (EA) with a gain of 26 dB and a bandwidth of 40 GHz, and then divided in two by a 3-dB power splitter. An electrical tunable delay line (ETDL) was employed to set a time delay difference between electrodes of $\tau = 16.67$ ps, providing a measurement range of $1/2\tau = 30$ GHz. However, the electrical bandwidth of the system was limited to 20 GHz as electrical mismatches between the ETDL and RF cables induced a resonance at 21 GHz.

The optical source was an external cavity laser with a linewidth lower than 100 KHz. Since a DE-DO-MZM was not available, a DE single-output MZM with $V_\pi = 5.2$ V and a bandwidth of 30 GHz was used instead. Consequently, the experiment was divided in two parts. First, a bias voltage of $V_B = (V_\pi/2)$ was set and an optical power meter (PM) at the output of the modulator was used to measure P_2. The bias voltage was then increased by V_π. A NF was added to the output of the modulator. P_1 was measured at the output of the NF using a PM. The NF consisted on a uniform fiber Bragg grating (FBG) with a length of 7 mm and an average refractive index variation of 2×10^{-4}. The reflectivity of the grating was measured resorting to an optical network analyzer. As depicted in Fig. 2, the OC frequency was aligned with a first-order zero of the FBG reflectivity. Therefore, the OC was suppressed by 20 dB. The highest frequency zero was chosen since it provides the narrowest notch filtering. As the FBG filtering impacts each MS in a different way, its measured reflectivity was considered on the simulations of P_1, and thus of the ACF.

The experimental results taken for a RF input power of -12 dBm are shown in Fig. 3. Fig. 3(a) shows that the measured powers follow the simulation results. The differences between the measured powers and simulation lines are caused by ripple in the electrical amplitude response of the system. As shown in Fig. 3(b), the impact of these electrical imperfections is minimized on the ACF due to the complementarity of the measurements. Fig. 3(b) also shows that the simulated ACF

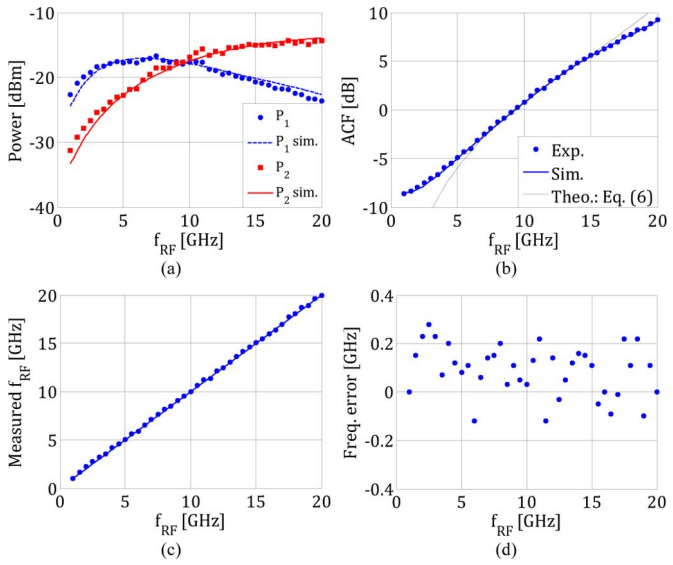

Fig. 3. Experimental results obtained for an RF input power of -12 dBm. (a) P_1 and P_2, (b) ACF, (c) measured frequencies, and (d) frequency errors.

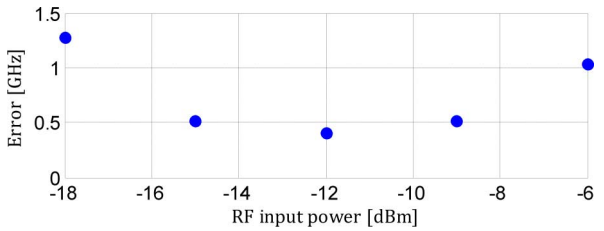

Fig. 4. Peak-to-peak frequency error for different RF input powers.

deviates significantly from (6) at low and high frequencies. At low frequencies the reason for this is limited OCS in P_2, which results from limited extinction ratio of the modulator. Furthermore, in P_1 the MSs are significantly attenuated by the nonideal notch filtering. At high frequencies P_1 is dominated by the residual OC power, which also results from nonideal notch filtering. The measured frequencies and frequency errors are shown in Fig. 3(c) and (d). A peak-to-peak frequency error of 400 MHz was achieved. Measurement errors were mainly caused by wavelength drifts between the laser source and FBG, and also by bias drifts of the modulator. Reduced frequency errors were obtained at low RF frequencies thanks to the narrow notch bandwidth of the FBG.

The RF frequency was measured for different RF input powers. As shown in Fig. 4, the lowest peak-to-peak frequency error of 400 MHz was achieved for a RF input power of -12 dBm. For lower RF powers the modulation index decreases, as does the power of the MSs. Hence, the power of the residual OC in P_1 becomes increasingly significant, which degrades the complementarity of the power measurements and also reduces the slope of the ACF. Consequently, the frequency measurements are impaired by the electrical imperfections of the system. For higher RF powers the frequency error increases as the experimental results deviate from the simulation predictions. This can be explained by the gain saturation of the EA, which was not considered on simulations.

IV. Conclusion

A novel IFMS based on complementary modulation was proposed and experimentally demonstrated. A differential time delay on the electrical RF signals applied to a DE-DO-MZM was employed to achieve simultaneous electrooptical modulation and complementary MS filtering. Since the OC was suppressed in only one of the modulator outputs, a simple uniform FBG was used to perform OCS on the other output. This enabled deriving the RF frequency from two complementary average optical power measurements, which are independent of the optical and RF powers. A peak-to-peak frequency error of 400 MHz was achieved over a measurement range of 1–20 GHz. Precise electrical impedance matching along with high OCS at both modulator outputs are key factors in minimizing frequency errors over larger frequency and RF power ranges.

Acknowledgment

The authors would like to thank M. Violas for support in the experiment.

References

[1] D. B. Hunter, L. G. Edvell, and M. A. Englund, "Wideband microwave photonic channelised receiver," in *Proc. 2005 Int. Topical Meeting Microwave Photonics Tech. Dig.*, Seoul, Korea, pp. 249–252.

[2] S. T. Winnall and A. C. Lindsay, "A Fabry–Pérot scanning receiver for microwave signal processing," *IEEE Trans. Microw. Theory Tech.*, vol. 47, no. 7, pt. 2, pp. 1385–1390, Jul. 1999.

[3] L. V. T. Nguyen and D. B. Hunter, "A photonic technique for microwave frequency measurement," *IEEE Photon. Technol. Lett.*, vol. 18, no. 10, pp. 1188–1190, May 15, 2006.

[4] L. Bui, M. Pelusi, T. Vo, N. Sarkhosh, H. Emami, B. Eggleton, and A. Mitchell, "Instantaneous frequency measurement system using optical mixing in highly nonlinear fiber," *Opt. Express*, vol. 17, no. 25, pp. 22983–22991, 2009.

[5] H. Emami, N. Sarkhosh, L. Bui, and A. Mitchell, "Amplitude independent RF instantaneous frequency measurement system using photonic Hilbert transform," *Opt. Express*, vol. 16, no. 18, pp. 13707–13712, 2008.

[6] N. Sarkhosh, H. Emami, L. Bui, and A. Mitchell, "Reduced cost photonic instantaneous frequency measurement system," *IEEE Photon. Technol. Lett.*, vol. 20, no. 18, pp. 1521–1523, Sep. 15, 2008.

[7] H. Chi, X. Zou, and J. Yao, "An approach to the measurement of microwave frequency based on optical power monitoring," *IEEE Photon. Technol. Lett.*, vol. 20, no. 14, pp. 1249–1251, Jul. 15, 2008.

[8] X. Zou, H. Chi, and J. Yao, "Microwave frequency measurement based on optical power monitoring using a complementary optical filter pair," *IEEE Trans. Microw. Theory Tech.*, vol. 57, no. 2, pp. 505–511, Feb. 2009.

[9] M. V. Drummond, P. Monteiro, and R. N. Nogueira, "Photonic RF instantaneous frequency measurement system by means of a polarization-domain interferometer," *Opt. Express*, vol. 17, no. 7, pp. 5433–5438, 2009.

[10] A. J. Seeds and K. J. Williams, "Microwave photonics," *J. Lightw. Technol.*, vol. 24, no. 12, pp. 4628–4641, Dec. 2006.

[J3] - Photonic True-Time Delay Beamforming Based on Polarization-Domain Interferometers

Miguel V. Drummond, Paulo. P. Monteiro and Rogério N. Nogueira

IEEE/OSA Journal of Lightwave Technology, Vol. 28, No. 17, pp. 2492–2498, September 2010.

Photonic True-Time Delay Beamforming Based on Polarization-Domain Interferometers

Miguel V. Drummond, *Student Member, IEEE*, Paulo P. Monteiro, *Member, IEEE*, and Rogério N. Nogueira, *Member, IEEE*

***Abstract*—In this paper, we propose a novel photonic true-time delay beamforming system for phased array antennas. The system relies on tunable delay lines which are based on Mach–Zehnder delay interferometers (MZDIs) with tunable coupling ratio. As the MZDIs are implemented on the polarization domain, a single optical source and a single piece of polarization maintaining fiber are required. The proposed implementation is theoretically assessed and beam squinting is investigated by simulation. A proof-of-concept experiment that validates the operation principle of the proposed delay lines is presented.**

***Index Terms*—Mach–Zehnder delay interferometer (MZDI), phased array antennas, photonic true-time delay beamforming.**

I. Introduction

DEMANDING wireless applications such as electronic warfare systems and broadband wireless networks require advanced antenna systems which can provide high sensitivity, broad bandwidth operation, and wide and precise angular control [1]. With this end, phased array antennas (PAAs) with photonic beamforming systems have been intensively investigated over the last years. Such systems share the advantages of microwave photonics, such as low losses, high time-bandwidth products, light weight and immunity to electromagnetic interference. As broad bandwidth operation is required, photonic true-time delay (TTD) beamforming should be used to avoid beam squinting.

Different photonic TTD beamforming techniques based on different optical delay lines have been proposed [2]–[10]. Optical fibers with different lengths can be used to provide discretely tunable delay lines [2]. The photonic beamforming system therefore consists on a switchable fiber optic network. This approach has scalability problems. For a PAA composed by several antenna elements, a fiber optic network with many fibers is required, which results in a bulky system. Another well known approach is to take advantage of chromatic dispersion [4]–[6]. In [4], N tunable laser sources are multiplexed and modulated by the input RF signal, where N is the number of antenna elements of the PAA. The multiplexed signals are then propagated in a dispersive medium, thus acquiring a time delay dependent on their wavelength. Tunable delays among the modulated signals are achieved by tuning the wavelength of the optical sources. This technique also has scalability problems, as the number of tunable lasers increases with the number of antenna elements of the PAA. The dispersive medium can be implemented with a chirped fiber Bragg grating (CFBG) [4] or a dispersive optical fiber [5]. A CFBG offers a compact implementation. However, the group delay ripple must be low to avoid signal distortion and beam squinting [7].

A novel technique based on ring resonators has recently introduced a new concept in [8]. Instead of having a constant time delay across the entire spectral bandwidth of the optical signal, the time delay only needs to be constant at the modulated RF carrier, as long as the phase of the optical carrier is adjusted. Such concept relaxes the bandwidth requirement of the tunable delay lines down to the spectral bandwidth of the data signal modulated onto the RF carrier. This is especially important when high-frequency RF carriers are employed. However, this concept is limited to optical single sideband signals with monochromatic optical carrier.

In this paper, we propose a novel photonic TTD beamforming technique based on an improved concept: the amplitude and group delay responses only need to be correct at the optical and RF carriers. The proposed scheme allows using double or single sideband signals with monochromatic or modulated optical carrier. The tunable delay lines are implemented with polarization-domain Mach–Zehnder interferometers. Each interferometer has a tunable coupling ratio, which allows tuning the time delay between 0 and τ, where τ is the differential group delay (DGD) of the polarization-domain interferometer (PDI). The optical and RF carriers are set at different maxima of the PDI's amplitude response, thus sharing the same frequency response. As a result, the bandwidth requirement of the tunable delay lines is relaxed down to the spectral bandwidth of the data signal modulated onto the RF carrier. The proposed beamformer structure uses only one optical source that needs not to be tunable and a single birefringent medium.

The remainder of this paper is organized as follows. A mathematical description of the proposed photonic beamforming system is presented in Section II. Section III presents simulation results which analyze the impact of beam squinting. A proof-of-concept experiment with the purpose of assessing the operation principle of one PDI is described in Section IV. Section V states the main conclusions of this work.

Manuscript received January 18, 2010; revised June 20, 2010 and June 28, 2010; accepted June 30, 2010. Date of publication July 15, 2010; date of current version August 18, 2010. This work was supported by the THRONE (PTDC/EEA-TEL/66840/2006) Fundação para a Ciência e Tecnologia (FCT) Project. The work of M. V. Drummond was supported by the FCT under the SFRH/BD/40250/2007 scholarship.

The authors are with the Instituto de Telecomuniçacões, Universidade de Aveiro, 3810-193 Aveiro, Portugal (e-mail: mvd@av.it.pt; paulo.1.monteiro@nsn.com; rnogueira@av.it.pt).

Color versions of one or more of the figures in this paper are available online at http://ieeexplore.ieee.org.

Digital Object Identifier 10.1109/JLT.2010.2057408

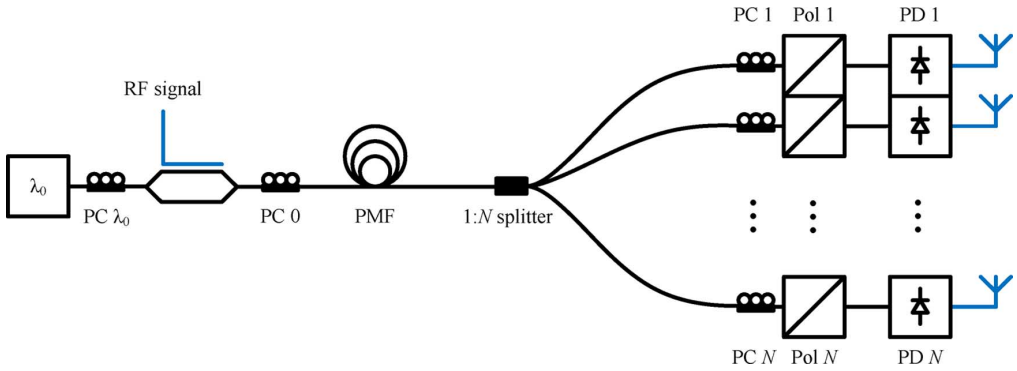

Fig. 1. Photonic TTD beamforming scheme considering a PAA with N antenna elements.

II. Operation Principle

The photonic TTD beamforming scheme is depicted in Fig. 1. A laser source provides a CW signal with a wavelength of λ_0. A Mach–Zehnder modulator is used to modulate the CW signal with the input RF signal. The polarization controller PC 0 sets the state-of-polarization (SOP) of the modulated signal at 45° with the slow axis of the polarization-maintaining fiber (PMF), which has a differential group delay of τ. Thus, at the output of the PMF there are two modulated signals delayed by τ, combined in orthogonal polarization. A 1: N optical splitter is used to replicate the PMF output signal, where N is the number of antenna elements of the PAA. Each output of the 1: N optical splitter is connected to a polarization controller (PC) and a polarizer. This allows performing a weighted addition of the polarization combined signals, therefore resulting in a Mach–Zehnder interferometer with tunable coupling ratio. The output signal of each polarizer is converted to the electrical domain using a photodetector (PD) and then fed to the respective antenna element. The photonic beamformer is thus composed by N PDIs. The coupling ratio of each PDI can be tuned by appropriately setting the corresponding PC.

The analysis of the beamforming scheme is divided in two steps. Firstly, the beamformer is theoretically described. Secondly, beam squinting analysis is conducted.

A. Theoretical Analysis

The tuning principle of the tunable delay lines implemented with PDIs is similar to the one presented in [11], with the difference that in this work time delays are considered instead of dispersive media.

The transfer function of one PDI is given by

$$H_i(f) = \frac{\sqrt{2}}{2}[\sin(\theta_i) + \cos(\theta_i)e^{-j2\pi f\tau}], \quad i = 1,2,\ldots,N \quad (1)$$

where θ_i is the angular difference between the slow axes of the PMF and polarizer i. The value of θ_i can be set by the PC i. The amplitude and group delay responses of the PDI can be derived from (1)

$$||H_i(f)||^2 = (1/2)[1 + 2\sin(\theta_i)\cos(\theta_i)\cos(2\pi f\tau)] \quad (2a)$$

$$\tau_i(f) = \tau\left\{\frac{\cos^2(\theta_i) + \sin(\theta_i)\cos(\theta_i)\cos(2\pi f\tau)}{1 + 2\sin(\theta_i)\cos(\theta_i)\cos(2\pi f\tau)}\right\}. \quad (2b)$$

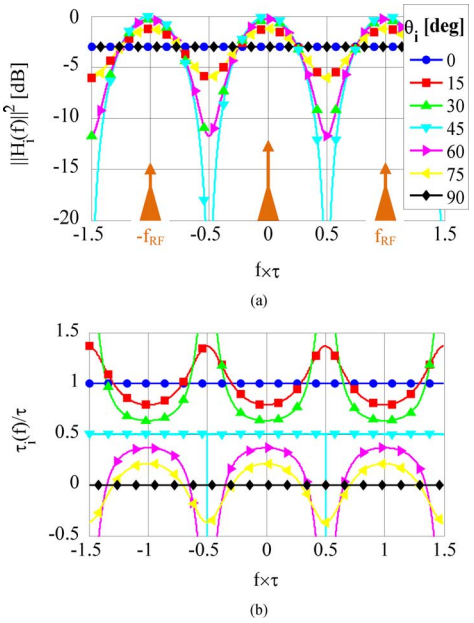

Fig. 2. Amplitude (a) and group delay (b) responses of the PDI for different values ofθ_i. As shown in (a), the carriers of the optical signal are centered at different maxima of the PDI's amplitude response.

Both responses are depicted in Fig. 2. A periodical behavior with a period of $1/\tau$ is obtained. Fig. 2(b) shows that the group delay can be changed with θ_i, however at the cost of also changing the amplitude response. There are two options for centering the optical signal with the response of the PDI. The first one is to set the optical signal within only one period of the frequency response. This approach limits the bandwidth of the optical signal to be lower than f_τ. Moreover, the attenuation of the RF carriers relatively to the optical carrier depends on θ_i. The other option is to center the optical and RF carriers at different maxima of the PDI's response, as depicted in Fig. 2(a). Mathematically this can be written as

$$f_{\mathrm{RF}}\tau = n, \quad n\epsilon\mathbb{N} \quad (3)$$

where f_{RF} is the frequency of the RF signal. In order to avoid signal distortion, the bandwidth of the signal modulated onto the RF carriers should be lower than $f\tau$. In comparison to the latter option, this relaxes the PDI's bandwidth requirement as the bandwidth of the optical signal is usually much higher than

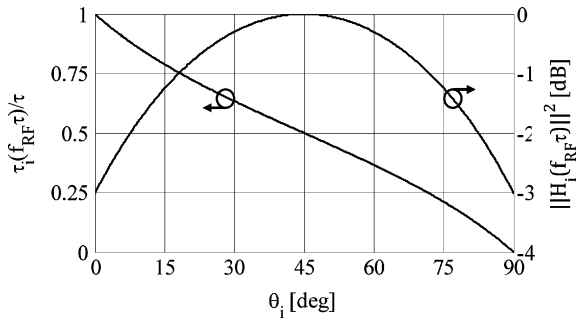

Fig. 3. Amplitude and group delay responses of the PDI for $f_{\mathrm{RF}}\tau = n, n\epsilon\mathbb{N}$.

the bandwidth of the signal modulated onto the RF carriers. Another advantage is that the amplitude and group delay responses are the same for all the carriers, for any value of θ_i. The variation of the group delay and amplitude responses with θ_i for all carriers is shown in Fig. 3.

The tunable time delay range required to achieve a beam steering tuning range of 180° can be derived from the array factor of a PAA, defined as

$$\mathrm{AF}(\Theta) = \frac{1}{N}\sum_{i=0}^{N-1} A_i e^{j[ikd\cos(\Theta)+\beta_i]} \tag{4}$$

where Θ is the spatial angle around the orientation axis of the PAA, A_i is the amplitude of the RF signal, $k = 2\pi/\lambda$ is the wavenumber of the RF signal, d is the distance between two adjacent antenna elements and β_i is phase shift applied to the respective antenna element. In case of a TTD beamformer

$$\beta_i = 2\pi f \tau_i \tag{5}$$

where τ_i is the time delay. In order to achieve a phase shift between 0 and 2π for $f = f_{\mathrm{RF}}, \tau_i$ should have a tuning range of $1/f_{\mathrm{RF}}$. This corresponds to the maximum time delay between two adjacent antennas. Therefore, the maximum delay required by the PAA is of

$$\tau_{\max} = \frac{N-1}{f_{\mathrm{RF}}}. \tag{6}$$

The tunable time delay range can be of $[0, \tau_{\max}]$, or of $[-\tau_{\max}/2, \tau_{\max}/2]$. In practice, the latter range only requires an absolute maximum delay of $\tau_{\max}/2$. In order to obtain positive delays one has $\tau_0 = 0, \tau_1 = \delta(1/f_{\mathrm{RF}}), \ldots, \tau_{N-1} = \delta(\tau_{\max})/(2)$, while for negative delays $\tau_{N-1} = 0, \tau_{N-2} = \delta(1/(f_{\mathrm{RF}}), \ldots, \tau_0 = \delta(\tau_{\max})/(2)$, where $\delta \in [0,1]$ is a constant defined by the target beampointing angle Θ_T. The DGD of the PDI should therefore be of $\tau = \tau_{\max}/2$. This condition complies with (3). However, the exponential term in (1) assumes negative values for even values of N, as $2\pi_{\mathrm{fRF}}\tau_{\max}/2 = \pi(N-1)$. In this case, the optical carrier is set at a minimum (maximum) of the amplitude response, whereas the RF carriers are set at maxima (minima). This situation can be resolved by considering a higher maximum delay of $\tau_{\max} = N/f_{\mathrm{RF}}$. According to these considerations, the DGD of the PDI is

$$\tau = \begin{cases} \frac{N-1}{2f_{\mathrm{RF}}}, & \text{when } N \text{ is odd} \\ \frac{N}{2f_{\mathrm{RF}}}, & \text{when } N \text{ is even.} \end{cases} \tag{7}$$

Equation (7) shows that the required τ is proportional to the number of antenna elements. On the other hand, the bandwidth of the amplitude response is inversely proportional to τ. As such, there is a tradeoff between maximum delay and bandwidth. Nonetheless, the bandwidth of the optical signal modulated onto the RF carrier usually increases at the cost of also increasing the RF carrier frequency, which according to (7) decreases the required τ. In this case, high signal bandwidths can be accommodated by the beamformer, since a low τ is required.

B. Beam Squinting Analysis

TTD operation can be demonstrated using the same analysis as in [4]. The modulated optical double sideband (DSB) signals at the input of the PDs, $s_i(t)$, can be written as a sum of three spectral lines,

$$s_i(t) = H_i f_o e^{j2\pi(f_o t)} + H_i(f_o + f_{\mathrm{RF}})e^{j2\pi(f_o+f_{\mathrm{RF}})t} + H_i(f_o - f_{\mathrm{RF}})e^{j2\pi(f_o-f_{\mathrm{RF}})t} \tag{8}$$

where f_o is the optical carrier frequency. After direct detection of $s_i(t)$, the photocurrent can be expressed by

$$E_i(t) = E_i(f_o, f_{\mathrm{RF}})e^{j(2\pi f_{\mathrm{RF}} t + \psi_i(f_o, f_{\mathrm{RF}}))} \tag{9}$$

and (10), shown at the bottom of the page, where $\phi_i(f)$ is the phase of $H_i(f)$. The phase of the photocurrent is given by (11), shown at the bottom of the page. As depicted in Fig. 2(a), $\|H_i(f_o)\| = \|H_i(f_o + f_{\mathrm{RF}})\| = \|H_i(f_o - f_{\mathrm{RF}})\|$. From (1), it

$$E_i(f_o, f_{\mathrm{RF}}) = \frac{1}{2}\|H_i(f_o)\| \cdot \left\{ \begin{bmatrix} \|H_i(f_o + f_{\mathrm{RF}})\|\cos(\phi_i(f_o + f_{\mathrm{RF}}) - \phi_i(f_o)) + \\ \|H_i(f_o - f_{\mathrm{RF}})\|\cos(\phi_i(f_o) - \phi_i(f_o - f_{\mathrm{RF}})) \end{bmatrix}^2 + \begin{bmatrix} \|H_i(f_o + f_{\mathrm{RF}})\|\sin(\phi_i(f_o + f_{\mathrm{RF}}) - \phi_i(f_o)) + \\ \|H_i(f_o - f_{\mathrm{RF}})\|\sin(\phi_i(f_o) - \phi_i(f_o - f_{\mathrm{RF}})) \end{bmatrix}^2 \right\}^{\frac{1}{2}} \tag{10}$$

$$\psi_i(f_o, f_{\mathrm{RF}}) = \mathrm{atan}\left[\frac{\|H_i(f_o + f_{\mathrm{RF}})\|\sin(\phi_i(f_o + f_{\mathrm{RF}}) - \phi_i(f_o)) + \|H_i(f_o - f_{\mathrm{RF}})\|\sin(\phi_i(f_o) - \phi_i(f_o - f_{\mathrm{RF}}))}{\|H_i(f_o + f_{\mathrm{RF}})\|\cos(\phi_i(f_o + f_{\mathrm{RF}}) - \phi_i(f_o)) + \|H_i(f_o - f_{\mathrm{RF}})\|\cos(\phi_i(f_o) - \phi_i(f_o - f_{\mathrm{RF}}))} \right] \tag{11}$$

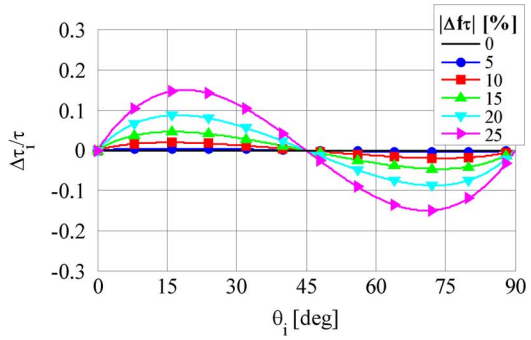

Fig. 4. Group delay variation with θ_i, considering different values of $|\Delta f\tau|$. The group delay variation is given by $\Delta\tau_i = \tau_i(\Delta f\tau) - \tau_i(0)$.

can be seen that $\phi_i(f_o+f_{\rm RF})-\phi_i(f_o) = \phi_i(f_o)-\phi_i(f_o-f_{\rm RF})$. Hence, (10) and (11) are simplified to

$$E_i(f_o, f_{\rm RF}) = \frac{1}{2}||H_i(f_o)||[||H_i(f_o+f_{\rm RF})|| + ||H_i(f_o-f_{\rm RF})||] = ||H_i(f_o)||^2 \quad (12)$$

$$\psi_i(f_o, f_{\rm RF}) = \frac{\phi_i(f_o+f_{\rm RF})-\phi_i(f_o-f_{\rm RF})}{2f_{\rm RF}} f_{\rm RF} \approx -\tau_i(f_o)\cdot 2\pi f_{\rm RF}. \quad (13)$$

Equation (13) shows that TTD operation is achieved across a given bandwidth, at which the approximation is valid. The obtained time delay depends on the optical carrier frequency. Fig. 4 shows that group delay error increases with the frequency shift, defined as $\Delta f\tau = f_{\rm int} - f_o$, where $f_{\rm int}$ is the frequency at which a maximum of the interferometer response should be located. The error also depends on θ_i, being maximum for of about 20° and 70°. Therefore, a frequency shift of the amplitude response maximum from f_o causes beam squinting. This can be particularly serious if the N PDIs have different frequency shifts. The amount of squinting also depends on the considered values of θ_i.

Equation (12) shows that the amplitude of the RF signal depends on the optical carrier frequency, i.e., $A_i = E_i(f_o, f_{\rm RF})$, and thus also of θ_i. Even when there is no frequency shift of the amplitude response, the amplitudes of the RF signals can differ up to 3 dB depending on θ_i. This is depicted in Fig. 3. Equation (4) shows that target beampointing angle Θ_t only depends on the phase of the RF signals, $\beta_i = \psi_i(f_o, f_{\rm RF})$. Hence, deviations of the RF amplitudes do not cause beam squinting, although beam shaping is obtained.

For RF signals with broad data bandwidth or with an RF frequency not compliant with (3) the approximation done in (13) is not valid. Under such conditions, the phase of the photocurrent is given by

$$\psi_i(f_o, f_{\rm RF}) = \phi_i(f_o+f_{\rm RF})-\phi_i(f_o) = \phi_i(f_o+f_{\rm RF})-\phi_i(f_{\max}) = \phi_i(f_o+f_{\rm RF})-2\pi f_{\max}\tau_i(f_{\max}) \quad (14)$$

where $f_{\max}$ is the frequency of the PDI's amplitude response maximum nearest to $f_o + f_{\rm RF}$. The phase of the detected RF signal mainly depends on the group delay of the optical carrier, as $\tau_i(f_{\max}) = \tau_i(f_o)$. The first term corresponds to the phase shift originated by the frequency detuning between the RF carrier and $f_{\max}$. If such detuning is zero, then $f_o + f_{\rm RF} = f_{\max}$ and $\phi_i(f_o+f_{\rm RF}) = 0$. Under such condition (14) can be written as (13).

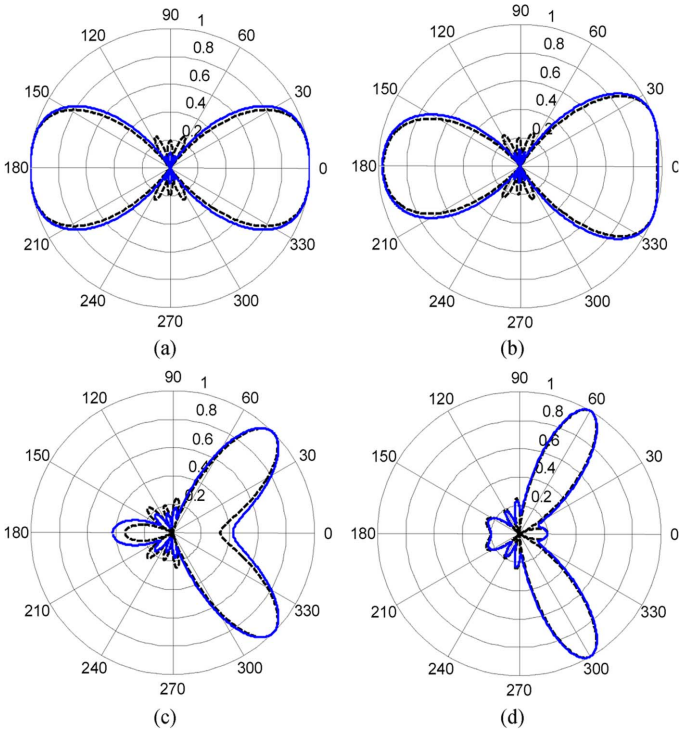

Fig. 5. Radiation diagrams for Θ_T of (a) 0°, (b) 20°, (c) 45°, and (d) 60°. The solid line represents the proposed beamformer; the dashed line represents an ideal TTD beamformer.

Finally, it should be noted that the analysis performed on (12)–(14) is also valid for single sideband signals. By suppressing the RF carrier at $f_o - f_{\rm RF}$, (12) and (13) become

$$E_i(f_o, f_{\rm RF}) = \frac{1}{2}||H_i(f_o)||||H_i(f_o+f_{\rm RF})|| = \frac{1}{2}||H_i(f_o)||^2 \quad (15)$$

$$\psi_i(f_o, f_{\rm RF}) = \phi_i(f_o+f_{\rm RF})-\phi_i(f_o) \approx -\tau_i(f_o)\cdot 2\pi f_{\rm RF}. \quad (16)$$

III. Simulation Results

The proposed beamformer was simulated considering a PAA with $N = 5$ antenna elements, $f_{\rm RF} = 60$ GHz, and a distance between two adjacent antenna elements of $d = \lambda_{\rm RF}/2 \approx 5$ mm. According to (7), $\tau = 2/f_{\rm RF} = 33.3$ ps. An optical DSB signal was considered. Thus, the amplitude and phase of the RF signals were obtained from (12) and (13). The radiation diagrams were obtained using (4). Results considering different target beampointing angles are shown in Fig. 5. Beam squinting is not observed. However, beam shaping arises from the dependence of the RF amplitudes with the required time delays. Even though the observed beam shaping is insignificant, it can be controlled using variable optical attenuators at the outputs of the 1:N optical splitter. Other option is to use RF amplifiers with variable gain after the PDs.

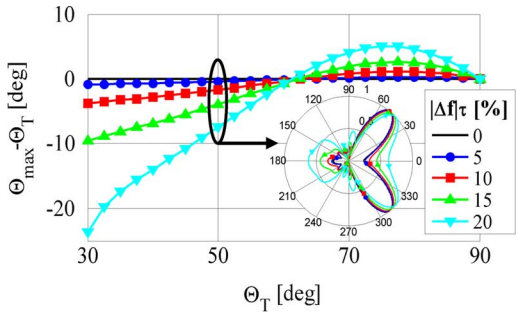

Fig. 6. Beam squinting considering different frequency shifts. Inset: radiation diagrams for $\Theta_T = 50°$.

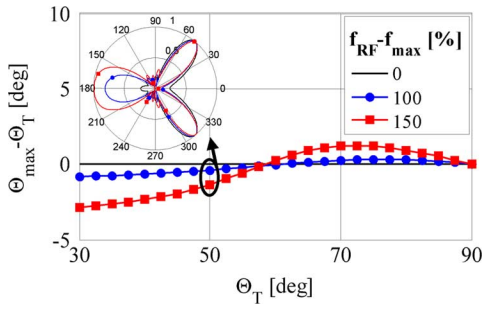

Fig. 7. Beam squinting considering different RF frequency detunings relatively to $f_{\max}$. The frequency detuning is normalized to the 3-dB cutoff frequency. Inset: radiation diagrams for $\Theta_T = 50°$.

Beam squinting and additional beam shaping occur when there is a frequency shift between the optical signal and the PDIs. Fig. 6 shows that beam squinting increases significantly with $|\Delta f\tau|$. The beam squinting is the same for $\pm\Delta f\tau$, as a result of the symmetry of the PDI's amplitude response with respect to its maxima. The additional beam shaping can severely distort the radiation diagram, as shown in the inset of Fig. 6. It should be noted that these results consist on the worst-case scenario, which corresponds to having the same frequency shift for all the N PDIs. Further simulations considering the same values of $|\Delta f\tau|$ have shown that beam squinting increases with the number of antenna elements. The increase of N results in the increase of the required τ. Thus, according to Fig. 4, a given frequency shift $|\Delta f\tau|$ yields a higher group delay variation, which explains the increase of the beam squinting.

As mentioned in the last subsection, the approximation of a PDI to an ideal delay line taken in (13) is only valid within a given bandwidth. This is particularly relevant for optical RF signals with broad data bandwidths or with optical RF carriers located away from the maxima of the PDI's amplitude response. The impact of the RF frequency and data bandwidth was assessed considering different RF frequencies. The RF phases were calculated using (14). The results are shown in Fig. 7. Fig. 7 shows that the detuning of the RF frequency results in reduced beam squinting. However, the radiation diagrams show that the power of the sidelobes increases. The results displayed in Figs. 6 and 7 show that a frequency shift between the optical signal and the PDIs results in stronger beam distortion in comparison to having an RF frequency different from $f_{\max}$.

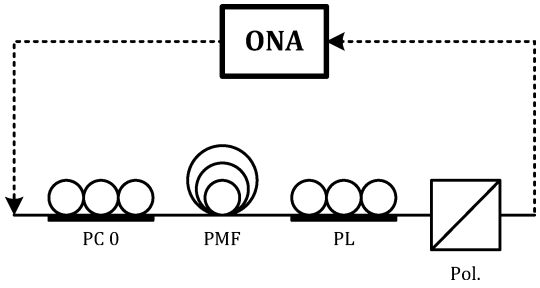

Fig. 8. Experimental setup. ONA—optical network analyzer; PL—polarization locker.

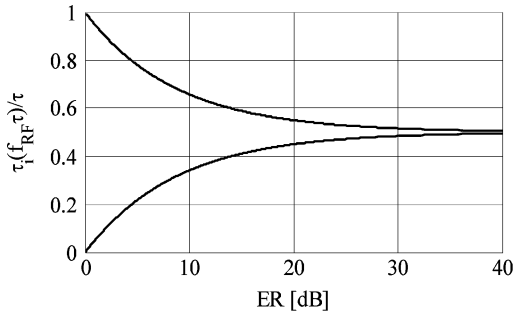

Fig. 9. Group delay at the maxima of the amplitude response as function of the extinction ratio.

IV. Experiment

A proof-of-concept experiment with discrete components was performed in order to assess the operation principle of the PDI. The experimental setup is depicted in Fig. 8. A PMF with a DGD of 33.3 ps was used. PC 0 was a manual PC with three wave plates, used to set the state-of-polarization (SOP) of the input signal at 45° relatively to the slow axis of the PMF. The PC placed after the PMF output was a deterministic polarization locker (PL), which allowed transforming any input SOP to any output SOP. An optical network analyzer (ONA) was used to measure the amplitude and group delay responses of the PDI. As the ONA can only measure relative values of the group delay, the absolute group delay was derived from the obtained extinction ratio (ER) of the amplitude response. The ER is the difference in dB between the optical powers of the maxima and minima of the amplitude response. Fig. 9 shows that there are two possible group delays for the same ER. However, both delays can be distinguished as the corresponding group delay responses are symmetric with respect to $\tau_i(f_{\mathrm{RF}}\tau)/\tau = 0.5$. This is depicted in Fig. 2(b).

The frequency response of the PDI was measured considering different ERs. The results are shown in Fig. 10. The angle $\theta_i = \theta_1$ increases from 0° up to 90° with the measurement number, thus proving that the group delay can be tuned from 0 up to $\tau = 33.3$ ps. A maximum ER of 29.5 dB was obtained for $\theta_1 \approx 45°$. The ER was limited to such value due to the inability of setting θ_1 at exactly 45°, and also due to the limited ER of the polarizer [12]. Fig. 10(b)–(d) shows that a good agreement was obtained between the experimental and theoretical curves. Fig. 10(d) shows that the group delay response had positive and negative values at different minima of the amplitude response. As depicted in Fig. 2(b), slight variations of θ_1

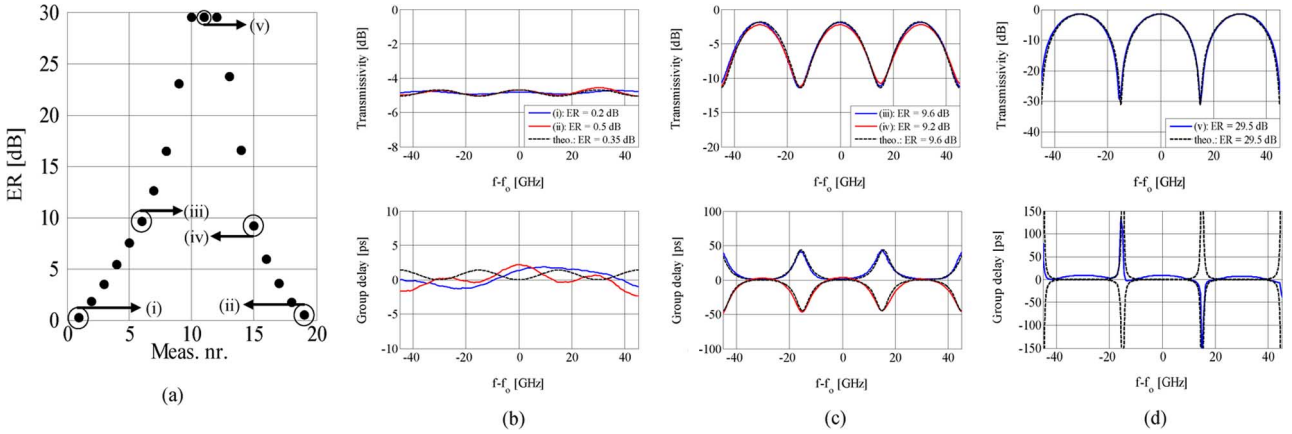

Fig. 10. Measured (a) ERs and (b)–(d) selected amplitude and group delay responses.

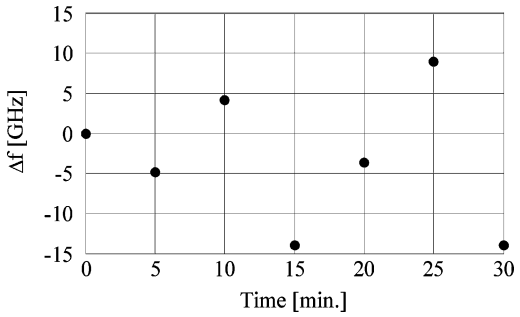

Fig. 11. Temporal variation of the amplitude response's frequency shift.

around 45° cause the group delay at the minima of the amplitude response to switch between positive and negative values. Although the employment of the PL resulted in a stable output SOP, the short patch cord that connected the PL to the polarizer was responsible for slight variations of θ_1 that in turn resulted in the observed group delay variations.

As proved in Section II, frequency shifts on the interferometer response are deleterious since they lead to beam squinting. Instabilities on the experimental setup can result in frequency shifts. In order to assess the stability of the experimental setup the PL was firstly adjusted to obtain a maximum ER of 29.5 dB, and then unlocked. Measurements were taken during 30 minutes, with a time interval of 5 minutes between them. The variation of the ER during the 30 minutes was less than 1 dB. However, as shown in Fig. 11 the frequency response drifted significantly over time. These results show that although θ_1 was stable, there was a random phase shift $\psi(t)$ on the PDI's response which can be modeled on (1) as

$$h_i(f) = \frac{\sqrt{2}}{2}\left[\sin(\theta_i) + \cos(\theta_i)e^{-j2\pi f\tau}e^{j\Psi(f)}\right] \qquad (17)$$

where $\Psi(f)$ is the Fourier transform of $\psi(t)$. Such phase shift resulted from environmental instabilities at the patch cord that connected the PL to the polarizer. Therefore, stable operation without the need of polarization tracking can be achieved simply by connecting the PL directly to the polarizer, without a patch cord.

V. Conclusion

In this paper, a novel photonic TTD beamforming system was presented. The proposed system relies on tunable delay lines, which are based on Mach–Zehnder delay interferometers. The time delays are continuously tunable by changing the coupling ratio of the interferometers. The optical bandwidth of the interferometers needs only to be higher than the bandwidth of the data signal modulated onto the RF carriers. This significantly relaxes the required bandwidth, as the spectral bandwidth of the optical signal is usually much higher than the bandwidth of the data signal. The proposed beamforming scheme implements the interferometers on the polarization domain. As a result, it only requires one optical source that needs not to be wavelength tunable and a single piece of PMF.

A detailed mathematical analysis of the system and numerical simulations have proven that squint-free operation is achieved over a significant bandwidth under frequency-stable operation of the interferometers. The optical carrier and frequency response of the interferometers should be properly centered in order to avoid beam squinting and beam distortion.

A proof-of-concept experiment validated the operation principle of the proposed delay line. It was observed that polarization instabilities on the setup cause random frequency shifts. The polarization instabilities originated from the patchcord connecting the PL and the polarizer. Hence, stable operation without the need of polarization tracking can be easily achieved with the suppression of such connection.

The evolution of the proof-of-concept setup with discrete components into an implementation in integrated optics should bring additional benefits such as intrinsically stable operation, low tuning time, low power consumption, compactness and low weight. The PCs can be implemented with polarization-sensitive phase modulators, which are basically polarization modulators. Furthermore, since all the waveguides can be birefringent, an implementation in $LiNbO_3$ technology is promising.

References

[1] R. C. Hansen, *Phased Array Antennas*. New York: Wiley, 1998.

[2] W. Ng, A. A. Walston, G. L. Tangonan, J. J. Lee, I. L. Newberg, and N. Bernstein, "The first demonstration of an optically steered microwave phased array antenna using true-time-delay," *J. Lightw. Technol.*, vol. 9, no. 9, pp. 1124–1131, Sep. 1991.
[3] E. N. Toughlian and H. Zmuda, "A photonic variable RF delay line for phased array antennas," *J. Lightw. Technol.*, vol. 8, no. 12, pp. 1824–1828, Dec. 1990.
[4] B. Ortega, J. L. Cruz, J. Capmany, M. V. Andres, and D. Pastor, "Variable delay line for phased-array antenna based on a chirped fiber grating," *IEEE Trans. Microw. Theory Tech.*, vol. 48, no. 8, pp. 1352–1360, Aug. 2000.
[5] J. Yongqiang, B. Howley, S. Zhong, Z. Qingjun, R. T. Chen, M. Y. Chen, G. Brost, and C. Lee, "Dispersion-enhanced photonic crystal fiber array for a true time-delay structured X-band phased array antenna," *IEEE Photon. Technol. Lett.*, vol. 17, no. 1, pp. 187–189, Jan. 2005.
[6] P. Q. Thai, A. Alphones, and D. R. Lim, "A novel simplified dual beam-former using multichannel chirped fiber grating and tunable optical delay lines," *J. Lightw. Technol.*, vol. 26, no. 15, pp. 2629–2634, Aug. 2008.
[7] P. Q. Thai, A. Alphones, and D. R. Lim, "Limitations by group delay ripple on optical beam-forming with chirped fiber grating," *J. Lightw. Technol.*, vol. 27, no. 24, pp. 5619–5625, Dec. 2009.
[8] P. A. Morton and J. B. Khurgin, "Microwave photonic delay line with separate tuning of the optical carrier," *IEEE Photon. Technol. Lett.*, vol. 21, no. 22, pp. 1686–1688, Nov. 2009.
[9] M. A. Piqueras, G. Grosskopf, B. Vidal, J. Herrera, J. M. Martinez, P. Sanchis, V. Polo, J. L. Corral, A. Marceaux, J. Galiere, J. Lopez, A. Enard, J. L. Valard, O. Parillaud, E. Estebe, N. Vodjdani, C. Moon-Soon, J. H. den Besten, F. M. Soares, M. K. Smit, and J. Marti, "Optically beamformed beam-switched adaptive antennas for fixed and mobile broadband wireless access networks," *IEEE Trans. Microw. Theory Tech.*, vol. 54, no. 2, pp. 887–899, Feb. 2006.
[10] L. Jofre, C. Stoltidou, S. Blanch, T. Mengual, B. Vidal, J. Marti, I. McKenzie, and J. M. del Cura, "Optically beamformed wideband array performance," *IEEE Trans. Antennas Propag.*, vol. 56, no. 6, pp. 1594–1604, Jun. 2008.
[11] M. V. Drummond, R. N. Nogueira, P. Monteiro, M. Violas, C. Sterner, and P.-Y. Fonjallaz, "Novel opto-electrical tunable dispersion compensator for IM signals," presented at the The 35th Eur. Conf. Opt. Commun., Vienna, Austria, 2009.
[12] M. V. Drummond, P. Monteiro, and R. N. Nogueira, "Photonic RF instantaneous frequency measurement system by means of a polarization domain interferometer," *Opt. Exp.*, vol. 17, no. 7, pp. 5433–5438, 2009.

Miguel V. Drummond (S'09) was born in Porto, Portugal, in 1984. He received the Diploma degree in electronics and telecommunications engineering from the University of Aveiro, Aveiro, Portugal, in 2007, where he is currently working toward the Ph.D. degree.

Since 2008, he has been with the Optical Communications Research Group, Institute of Telecommunications, Aveiro. His main research interests include all-optical signal processing techniques applied to high bitrate optical communication systems and microwave photonic devices.

Paulo P. Monteiro (M'06) was born in Coimbra, Portugal, in 1964. He received the diploma degree in electronics and telecommunications from the University of Aveiro, Aveiro, Portugal, the M.Sc. degree from the University of Wales, Wales, U.K., and the Ph.D. degree in electronics and telecommunications from the University of Aveiro.

He is a Research Manager with Nokia Siemens Networks, Amadora, Portugal, and an Associate Professor with the University of Aveiro, where he has been teaching courses of telecommunications. He is also a Researcher with the Institute of Telecommunication, University of Aveiro. His main research interests include high-speed optical communications for access and core networks and fixed-mobile convergence. He has acted as a reviewer for *Electronics Letters*, *ETRI Journal*, and the *Journal of Optical Networking*. He has participated in several national and European projects and he is currently the Project Coordinator of the large-scale integrating project FUTON (FP7 ICT-2007-215533). He has authored or coauthored more than 15 patent applications and over 200 refereed papers and conference contributions.

Dr. Monteiro has been a reviewer for the JOURNAL OF LIGHTWAVE TECHNOLOGY.

Rogerio N. Nogueira (M'08) received the degree in physics engineering and Ph.D. degree in physics from the University of Aveiro, Aveiro, Portugal, in 1998 and 2005, respectively.

He is now an Assistant Researcher with the Institute of Telecommunications where he has been working in the field of fiber optics since 1999, participating in several projects financed by national, EU organizations and private companies. In 2009, he joined Nokia Siemens Networks, Amadora, Portugal, as an R&D expert in the field of optical communications. He has authored or coauthored one book chapter, more than 30 papers in international scientific journals, and more than 100 papers in international conferences. His research interests include design and production of optical components, fiber optical communication systems and fiber optical sensors.

[J4] - Tunable Optical Dispersion Compensator Based on Power Splitting Between Two Dispersive Media

Miguel V. Drummond, Rogério N. Nogueira, Paulo P. Monteiro, Manuel A. Violas, Carola Sterner and Pierre-Yves Fonjallaz

IEEE/OSA Journal of Lightwave Technology, Vol. 28, No. 8, pp. 1164–1175, April 2010.

Tunable Optical Dispersion Compensator Based on Power Splitting Between Two Dispersive Media

Miguel V. Drummond, *Student Member, IEEE*, Rogério N. Nogueira, *Member, IEEE*, Paulo P. Monteiro, *Member, IEEE*, Manuel A. Violas, Carola Sterner, and Pierre-Yves Fonjallaz

***Abstract*—In this paper, we propose and experimentally demonstrate a novel tunable optical dispersion compensator (TODC). Dispersion compensation is achieved by splitting the input signal between two dispersive media and adding the resulting signals thereafter. Tunable compensation is attained by controlling the power splitting ratio of the input signal between both dispersive media. The frequency response of the TODC is theoretically assessed considering signal addition in the optical and electrical domains. The latter case is enabled by using optical single sideband (OSSB) modulation, which allows preserving the phase information of dispersive media output signals after direct detection. This is the only case experimentally tested, since it avoids stability problems related with coherent addition of optical signals. A TODC with a tuning range of -340 to 0 ps/nm was designed and experimentally assessed for a 40 Gb/s nonreturn-to-zero OSSB signal. The tunable power splitter consisted of an automatic polarization controller and a polarization beam splitter, which offered a tuning time lower than 150 μs. A bit error rate lower than 10^{-8} was measured on the entire compensation range with a maximum power penalty of 3.3 dB relatively to an SSB signal in back-to-back.**

***Index Terms*—Chromatic dispersion (CD), optical communication systems, single sideband (SSB), tunable dispersion compensation.**

I. Introduction

CHROMATIC DISPERSION (CD) is a critical impairment in current lightwave transmission systems. A fourfold increase on the bit rate corresponds to a CD tolerance reduction of about 16 times [1]. Therefore, precise dispersion compensation is needed for high-perchannel bit-rate lightwave systems in order to allow the detection of information data with reduced bit error rate (BER). There are three main reasons why a static optical dispersion compensator (ODC) may not be sufficient to guarantee a precise compensation. First, in reconfigurable networks, signals travel through different paths that may have different cumulative dispersion. Second, optical power variations of the signal itself and other channels result in a variation of the nonlinear phase shift, that in turn changes the optimum amount of dispersion compensation [2]. Third, the fluctuation of environmental conditions such as the ambient temperature may also change the cumulative dispersion of a given path [3]. As such, tunable dispersion compensation should be employed to provide precise compensation, with increased robustness to variation of transmission conditions.

Tunable optical dispersion compensators (TODCs) based on different passive techniques have been proposed. Infinite impulse response (IIR) all-pass filters based on ring resonators are reported in [4]. Compensation tunability is achieved by varying the coupling ratio and phase of the ring relatively to the line. Finite impulse response filters implemented with cascaded Mach–Zehnder interferometers, and parallel tapped delay lines are discussed in [5] and [6], respectively. Similar tuning processes to IIR filters are considered. Chirped fiber Bragg gratings (CFBGs) are investigated in [7] and[8]. Tunable compensation is obtained by applying a temperature [7] or strain [8] gradient to the grating. Angularly dispersive gratings are proposed in [9] and[10]. Tunable angularly dispersive gratings are implemented with movable parts [9], or by using adjustable lens [10].

In this paper, we propose and experimentally assess a novel passive TODC that presents a different tuning process from the aforementioned ones. It is based on splitting the signal by two dispersive media with different cumulative dispersions. Tunability is achieved by varying the splitting ratio. The compensated signal consists of the addition of the dispersive media output signals. Since the experimental assessment of the proposed TODC is done using discrete components, stability problems associated with optical coherent addition can arise. In order to avoid such problems, the addition of the dispersive media output signals is done in the electrical domain. The dispersive media output signals are combined in orthogonal polarizations and then directly detected with a photodiode. Since phase preservation is needed after direct detection to correctly perform the addition, single sideband modulation (SSB) is employed [11]. This is achieved through sideband suppression filtering (SSF)[12]. The power splitting ratio between both dispersive media is varied using a polarization controller (PC) followed by a polarization beam splitter (PBS). Depending on the state of polarization (SOP) rotation enabled by the PC,

Manuscript received August 31, 2009; revised December 18, 2009. First published February 08, 2010; current version published March 17, 2010. This work was supported by THRONE (PTDC/EEA-TEL/66840/2006) Fundação para a Ciência e Tecnologia (FCT) Project, and ISIS and BONE Networks of Excellence, funded by the European Commission. The work of M. V. Drummond was supported by FCT under the SFRH/BD/40250/2007 Scholarship.

M. V. Drummond and M. A. Violas are with the Instituto de Telecomunicações, University of Aveiro, 3810-193 Aveiro, Portugal (email: mvd@av.it.pt).

R. N. Nogueira and P. P. Monteiro are with the Instituto de Telecomunicações, University of Aveiro, 3810-193 Aveiro, Portugal, and also with Nokia Siemens Networks Portugal S.A., 2720-093 Amadora, Portugal.

C. Sterner and P.-Y. Fonjallaz are with Acreo AB, SE-164 40 Kista, Sweden, and also with Kista Photonics Research Center, Royal Institute of Technology, SE-164 40 Kista, Sweden.

Color versions of one or more of the figures in this paper are available online at http://ieeexplore.ieee.org.

Digital Object Identifier 10.1109/JLT.2010.2042031

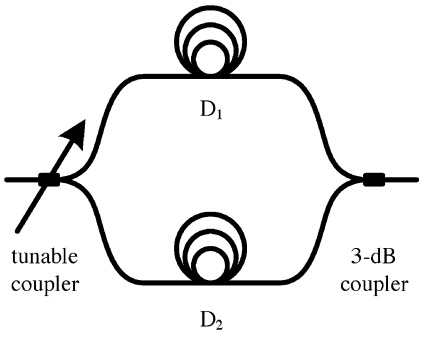

Fig. 1. General scheme of the TODC employing coherent addition of the dispersive media D_1 and D_2 output signals.

the signal is coupled to both dispersive media with different splitting ratios. In order to reduce the polarization sensitivity that results from using a PBS, an automatic PC is used. With the aid of a feedback loop, it sets a given output signal SOP independently of the input signal SOP. Moreover, a low tuning time in the order of tens of microseconds is achieved, since it only depends on the polarization rotation speed imposed by the automatic PC.

The remainder of this paper is organized as follows. The operation principle of the system is presented in Section II. A mathematical model of the TODC and analytical validation of the signal addition performed on the electrical domain with an input optical SSB (OSSB) signal are presented. Section III presents the optimization of the TODC and SSF parameters, where a 40 Gb/s nonreturn-to-zero (NRZ) is considered. Transmission simulations are presented in order to analyze the compensation effectiveness. In Section IV, the experiment is described. The compensation effectiveness is experimentally assessed through eye diagram analysis and BER measurements. Section V presents the final conclusions.

II. Operation Principle

Fig. 1 presents the TODC general scheme. The input signal is divided into two paths. The optical power in each path depends on the coupling ratio set by the tunable coupler. Both paths contain a dispersive medium with cumulative dispersions of D_1 and D_2. A 3-dB coupler coherently adds the output signals of both dispersive media.

The mathematical analysis of the operation principle presented in this section is first presented for the case where the dispersive media output signals are coherently added. In the second part of this section, the case where SSB modulation is employed and the signal addition is performed in the electrical domain is assessed.

A. Mathematical Analysis Considering Coherent Addition of the Dispersive Media Output Signals

Assuming that both dispersive media have unitary amplitude response for all considered wavelengths, the electric field transfer function of the TODC depicted in Fig. 1 can be written as

$$\begin{aligned} H(f) &= H_{D_1}(f) + H_{D_2}(f) \\ &= \alpha e^{-j2\pi[k_1 f^2 + \tau_1 f]} + \beta e^{-j2\pi[k_2 f^2 + \tau_2 f]}. \end{aligned} \tag{1}$$

Equation (1) neglects the 3 dB loss added by the 3 dB coupler. α and β are constants defined by the coupling ratio, through $\alpha = \sqrt{1-\beta^2}f$ is the detuned frequency relatively to the optical central frequency f_0. $\tau_{1,2}$ are the time delays associated with each dispersive medium. $k_{1,2}$ represent the cumulative dispersion of the dispersive media through the relation

$$k_{1,2} = \frac{D_{1,2}\lambda_0^2}{2c} \tag{2}$$

where $D_{1,2}$ are the cumulative dispersion of the dispersive media, λ_0 is the optical central wavelength, and c is the speed of light in vacuum. The amplitude response of (1) is given by

$$||H(f)||^2 = \alpha^2 + \beta^2 + 2\alpha\beta\cos(\mathrm{A}_1 - \mathrm{A}_2) \tag{3}$$

where

$$\mathrm{A}_{1,2} = 2\pi[k_{1,2}f^2 + \tau_{1,2}f]. \tag{4}$$

Equation (3) shows that the amplitude response is periodical. The period varies with the frequency and is dependent on the difference between k_1 and k_2, as well as τ_1 and τ_2. This is easily understandable if one looks at the TODC as an interferometer with a time-delay difference between both arms that varies with the frequency. The optical bandwidth is defined by the last term in (3). As such, the bandwidth is also dependent on the difference between k_1 and k_2 as well as τ_1 and τ_2. Independently of these differences, the lowest optical bandwidth is achieved when the last term in (3) is maximized, i.e., $\alpha = \beta = \sqrt{0.5}$.

The group-delay response can be obtained by derivating the phase response $\phi(f)$ through the relation $\tau(f) = (1/2\pi)(d\phi/df)$. In this way, the group-delay response is given by

$$\tau(f) = \frac{1}{2\pi}\frac{\alpha^2\mathrm{B}_1 + \beta^2\mathrm{B}_2 + \alpha\beta(\mathrm{B}_1 + \mathrm{B}_2)\cos(\mathrm{A}_1 - \mathrm{A}_2)}{\alpha^2 + \beta^2 + 2\alpha\beta\cos(\mathrm{A}_1 - \mathrm{A}_2)} \tag{5}$$

where

$$B_{1,2} = 2\pi[2k_{1,2}f + \tau_{1,2}]. \tag{6}$$

Similarly to (3), (5) shows that the group delay has a periodical response with a frequency-dependent period. The group-delay response is linear with respect to the frequency when the cosine terms are annulled. This occurs for $\alpha = 0, \sqrt{0.5}$, and 1. For $\mathrm{A}_1 - \mathrm{A}_2 \approx 0$, (5) can be approximated by

$$\tau(f) \approx \frac{1}{2\pi}\frac{(\alpha^2 + \alpha\beta)\mathrm{B}_1 + (\beta^2 + \alpha\beta)\mathrm{B}_2}{\alpha^2 + \beta^2 + 2\alpha\beta}. \tag{7}$$

As $\alpha^2+\beta^2=1$, (7) can be written as

$$\tau(f)\approx\frac{(\alpha^2+\alpha\sqrt{1-\alpha^2})\mathrm{B}_1+(1-\alpha^2+\alpha\sqrt{1-\alpha^2})\mathrm{B}_2}{2\pi(1+2\alpha\sqrt{1-\alpha^2})}. \tag{8}$$

According to (8), when the first term increases, i.e., α increases, the second term decreases. This shows that the TODC total cumulative dispersion and time delay depend on the optical power coupling ratio between both dispersive media. It is important to note that the frequency range that complies with the approximation $\mathrm{A}_1-\mathrm{A}_2\approx 0$ increases with the decrease of the cumulative dispersion and time-delay differences between both dispersive media.

Since in practice dispersive media can have group delay ripple (GDR), which is generally the case of CFBGs, it is useful to consider such parameter in the analysis. This can be done considering

$$H_{D_{1,2}}(f)=e^{-j2\pi[k_{1,2}f^2+\tau_{1,2}f+\xi_{1,2}(f)]} \tag{9}$$

where $\xi_{1,2}(f)$ represents the phase ripple of dispersive medium 1 and 2, respectively. Analogously, to the group delay, the GDR is related to the derivative of the phase ripple in order to the frequency, here designated $\xi'_{1,2}(f)$. In this way, (6) can be rewritten as

$$B_{1,2}=2\pi[2k_{1,2}f+\tau_{1,2}+\xi'_{1,2}(f)]. \tag{10}$$

By using (10) on (8), it can be seen that the GDR also depends on the optical power coupling ratio between both dispersive media. This means that within the approximation $\mathrm{A}_1-\mathrm{A}_2\approx 0$, the GDR of the TODC depends only of the GDR of both dispersive media.

B. Mathematical Analysis Considering SSB Modulation and Addition of the Dispersive Media Output Signals Performed in the Electrical Domain

The analysis performed in the last section considers a coherent addition of the output signals of both dispersive media. In this section, it is demonstrated that the same analysis is valid for the scheme depicted in Fig. 2, if the input signal is SSB modulated. The output signals of both dispersive media are combined in orthogonal polarizations using a polarization beam combiner (PBC). The PBC output signal is detected by a photodiode with a responsivity of $\Re$. The frequency response of the photodiode is neglected in the following analysis. The photodiode output current is given by

$$I(t)=I_x(t)+I_y(t)=\Re\{\|E_x(t)\|^2+\|E_y(t)\|^2\} \tag{11}$$

where E_x and E_y represent the orthogonally polarized signals in the x and y polarization axis, respectively. According to Fig. 2, E_x and E_y are the output signals of the dispersive medium D_1 and D_2, respectively. Equation (11) shows that the dispersive media output signals are first subject to direct detection and added afterward. For double sideband (DSB) modulation, the phase information of the optical signal is lost after direct detection. As such, the signals are added without phase information. Since cumulative dispersion affects the phase of optical signals, the dispersion compensation performed by signal addition is thereby invalidated. On the other hand, there is phase preservation after direct detection for SSB signals.

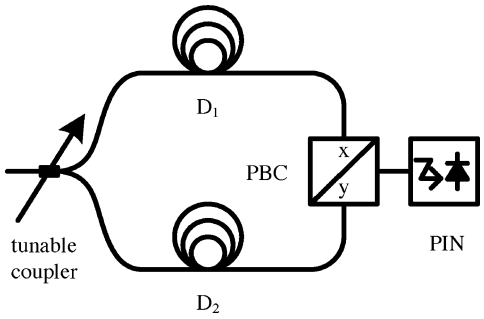

Fig. 2. TODC scheme with the addition of the dispersive media output signals performed in the electrical domain. PBC, p-i-n—photodiode.

The photodiode output current of an SSB signal propagated in a dispersive line can be written as [13]

$$\begin{aligned}I(f)=\Re P\{&\delta(f)+zH_f^*(f)X_L(f)\\&+zH_f(f)X_U(f)\\&+z^2[H_f^*(f)X_L(f)]\circledast[H_f(f)X_U(f)]\}\end{aligned} \tag{12}$$

where P is the optical power and z is the modulation depth. $X_L(f)$ and $X_U(f)$ are the lower and upper sidebands of the information signal $X_{\mathrm{inf}}(f)$, respectively. The symbol $\circledast$ represents the convolution operation. The phase response of the dispersive line is given by $H_f(f)=e^{-j2\pi k_f f^2}$, where $k_f=D_f\lambda_0^2/2c$. D_f is the cumulative dispersion of the dispersive line. The time delay of the dispersive line is not defined since it is irrelevant for the dispersion compensation. Using (11) and (12), the photocurrent generated by the signal $E_x(t)$ can be written as

$$\begin{aligned}I_x(f)=\alpha^2\Re P\{&\delta(f)+zH_{f+D_1}^*(f)X_L(f)\\&+zH_{f+D_1}(f)X_U(f)\\&+z^2[H_{f+D_1}^*(f)X_L(f)]\\&\circledast[H_{f+D_1}(f)X_U(f)]\}\end{aligned} \tag{13}$$

where $H_{f+D_1}(f)=e^{-j2\pi((k_f+k_1)f^2+\tau_1 f)}$. A similar expression can be written for $I_y(f)$ considering β and $H_{f+D_2}(f)$ instead of α and $H_{f+D_1}(f)$, respectively, in which $H_{f+D_2}(f)=e^{-j2\pi((k_f+k_2)f^2+\tau_2 f)}$. The photocurrent generated by both orthogonal signals is then written as

$$\begin{aligned}I(f)=\Re P\{&(\alpha^2+\beta^2)\delta(f)\\&+zX_L(f)[\alpha^2H_{f+D_1}^*(f)+\beta^2H_{f+D_2}^*(f)]\\&+zX_U(f)[\alpha^2H_{f+D_1}^*(f)+\beta^2H_{f+D_2}^*(f)]\\&+z^2(\alpha^2[H_{f+D_1}(f)X_L(f)]\\&\circledast[H_{f+D_1}(f)X_U(f)]\\&+\beta^2[H_{f+D_2}^*(f)X_L(f)]\\&\circledast[H_{f+D_2}(f)X_U(f)])\}.\end{aligned} \tag{14}$$

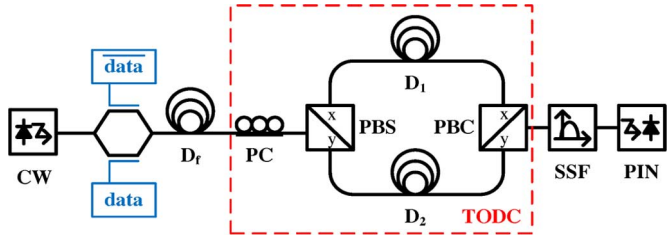

Fig. 3. Scheme considered for system optimization. CW—continuous-wavelength laser; D_f—dispersive fiber; PC; PBS; SSF.

Equation (14) shows that the upper sideband is affected by the dispersive line and TODC according to

$$\alpha^2 H_{f+D_1}(f) + \beta^2 H_{f+D_2}(f) = H_f(f)\left[\alpha^2 H_{D_1}(f) + \beta^2 H_{D_2}(f)\right]. \quad (15)$$

As such, the dispersive line is compensated with a transfer function that is given by (1), with the exception that α and β are squared. The same analysis is valid for the lower sideband. This proves that the compensation principle presented in the previous section is valid for the present case depicted in Fig. 2. The first three terms in (14) fully reconstruct the compensated data signal, since they represent the optical carrier and lower and upper sidebands, respectively. The fourth term consists of the beat between the optical sideband carrying information with itself. As pointed in [13], phase preservation is not kept for this term. Even in back-to-back situation it represents distortion due to direct detection of the OSSB signal. Furthermore, since there is no phase preservation, additional distortion arises if a dispersive line and the TODC are considered. If an OSSB signal is used with the TODC scheme depicted in Fig. 1, this drawback does not exist since phase preservation is not required after direct detection. However, there is a 3 dB loss intrinsic to the coherent addition of two optical signals.

III. System Optimization

The system optimization is based on the scheme presented in Fig. 3. The optimization is performed in two steps. First, the TODC parameters are optimized to achieve proper compensation for a 40 Gb/s NRZ OSSB signal. Second, the SSF parameters are optimized taking into account the TODC optimized parameters. The optimized system performance is assessed through transmission simulations. The implementation of one dispersive medium and SSF using FBGs is discussed in the last part of this section.

A. TODC Optimization

The TODC parameters are the splitting ratio, dispersive media cumulative dispersions and time delays. Since the frequency response variation depends only on $D_1 - D_2$ and $\tau_1 - \tau_2$, in the remaining of this work, it is considered that the dispersive medium 1 is purely dispersive, and that the dispersive medium 2 is nondispersive, being a tunable delay line. As such, $\tau_1 = 0$ and $D_2 = 0$. The power splitting ratio depends on

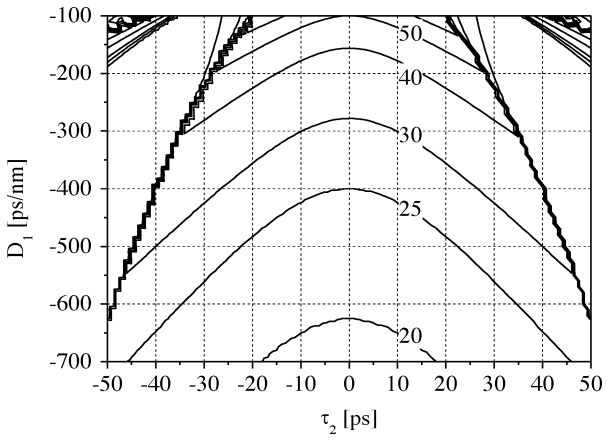

Fig. 4. Optical -3 dB bandwidth (in GHz) of the TODC for various values of τ_2 and D_1.

the polarization rotation imposed by the PC. Assuming that the input signal at the TODC is linearly polarized along the x-axis, then $\alpha = |\cos(\theta)|$. θ is the polarization rotation angle imposed by the PC.

According to (3), the optical bandwidth of the TODC depends on D_1 and τ_2. Fig. 4 presents the optical -3 dB bandwidth for various cumulative dispersions D_1 and time delays τ_2, considering $\theta = 45°$. This is the case where the lowest bandwidth is achieved, since it implies that $\alpha = \sqrt{0.5}$. As it is pointed in the previous section, the optical bandwidth decreases with the increase of $|D_1|$, since $D_2 = 0$. For a given dispersion value D_1, the bandwidth can be increased by optimizing τ_2. This means temporally displacing the optical pulses at the output of the dispersive media so that the coherent addition of both results in a pulse with increased bandwidth. Since it is the relative displacement between one pulse to the other that is important, the optimum delay can be either positive or negative. For a given value of D_1, the optimum delay τ_2 that maximizes the bandwidth depends on the splitting ratio. However, if a single delay value is considered for all splitting ratios, then the optimum delay corresponding to $\alpha = \sqrt{0.5}$ should be the one used. Such delay guarantees that the lowest bandwidth is maximized.

Since the optimized system should achieve proper compensation for a 40 Gb/s NRZ OSSB signal, the TODC should have an optical bandwidth higher than 20 GHz. Such a low-bandwidth requirement is enabled by the SSB modulation, which reduces the optical bandwidth of the signal to half the one of the original DSB signal. According to Fig. 4, an optical bandwidth of 20 GHz enables the compensation of at least 620 ps/nm of cumulative dispersion. However, the system optimization only taking into account the optical bandwidth is insufficient. The shape of the amplitude response should be considered. Moreover, (5) shows that the group delay response varies nonlinearly with the frequency. Therefore, the impact of D_1 and τ_2 in the group-delay response should also be analyzed.

The amplitude, group delay, and cumulative dispersion responses for four values of τ_2 considering $D_1 = -340$ ps/nm are shown in Fig. 5. In order to observe the nonlinear response of the group delay, the parameter α must be different of 0, $\sqrt{0.5}$, and 1. A value of $\alpha = \sqrt{0.25}$ is used. The increase of the delay

produces three effects. First, there is a shift of the frequency response toward higher frequencies. This shift can be neglected since the central frequency depends on the optical central frequency f_0, which in turn can be readjusted. Second, the increase of the delay results in a higher bandwidth, as corroborated by Fig. 4. However, this implies the formation of a valley located at the center of the amplitude response. For a given positive or negative delay value, the valley reaches -3 dB, resulting in an abrupt reduction of the -3 dB optical bandwidth. This can be also observed in Fig. 4, where these points represent the maximum bandwidth for a given value of D_1. The third effect is analog to the second one, with the exception that the cumulative dispersion is considered instead of the amplitude response. The increase of the delay results in the increase of the frequency range where the cumulative dispersion is near the compensation value. In the case of Fig. 5, the compensation value is of $D_1/4 = -85$ ps/nm. However, the increase of such frequency range results in the formation of a peak. Nevertheless, the average value of the dispersion on the given frequency range is approximately the compensation value.

In summary, there are tradeoffs among various parameters. The bandwidth increases with the decrease of D_1. It also increases with the increase of τ_2, at the cost of amplitude and phase response degradation imposed by the formation of a valley and peak, respectively. Since the OSSB signal has a bandwidth of about 20 GHz, the TODC should have a bandwidth significantly higher than 20 GHz. In the further simulation and experimental tests, it is considered $D_1 = -340$ ps/nm. This cumulative dispersion results in a -3 dB optical bandwidth of about 27 GHz for $\tau_2 = 0$. Such a high bandwidth avoids signal degradation originated by narrow optical filtering. Moreover, since this bandwidth is achieved for $\tau_2 = 0$, amplitude and phase response degradations driven by time-delay optimization are also alleviated.

B. SSF Optimization

The modulation of OSSB signals can be achieved resorting to electro-optic [11], [14] or all-optical techniques [12]. Electro-optic techniques include special electro-optic modulators [15] or electro-optic filters [14]. Both techniques are wavelength transparent. However, the maximum bit rate is inherently limited by the electrical circuitry frequency response. All-optical techniques enable SSB modulation at high bit rates. The simplest all-optical technique consists on using SSF [12]. This technique is considered in this work.

The SSB modulation achieved through SSF depends on the filter parameters, which are the amplitude response and central frequency detuning from the optical carrier. In this paper, the frequency response of the SSF is modeled by a super-Gaussian function given by

$$H(f) = e^{-\left(2\ln(2)\frac{f-\delta_f}{\mathrm{BW}}\right)^{2N}} \tag{16}$$

where δ_f is the frequency detuning relatively to the optical carrier, BW is the -3 dB bandwidth, and N is the order.

The simulation scheme used for the optimization of the SSF parameters is shown in Fig. 3. The data signal consists of a De Bruijn sequence with a length of 2^9 bits and a bit rate of

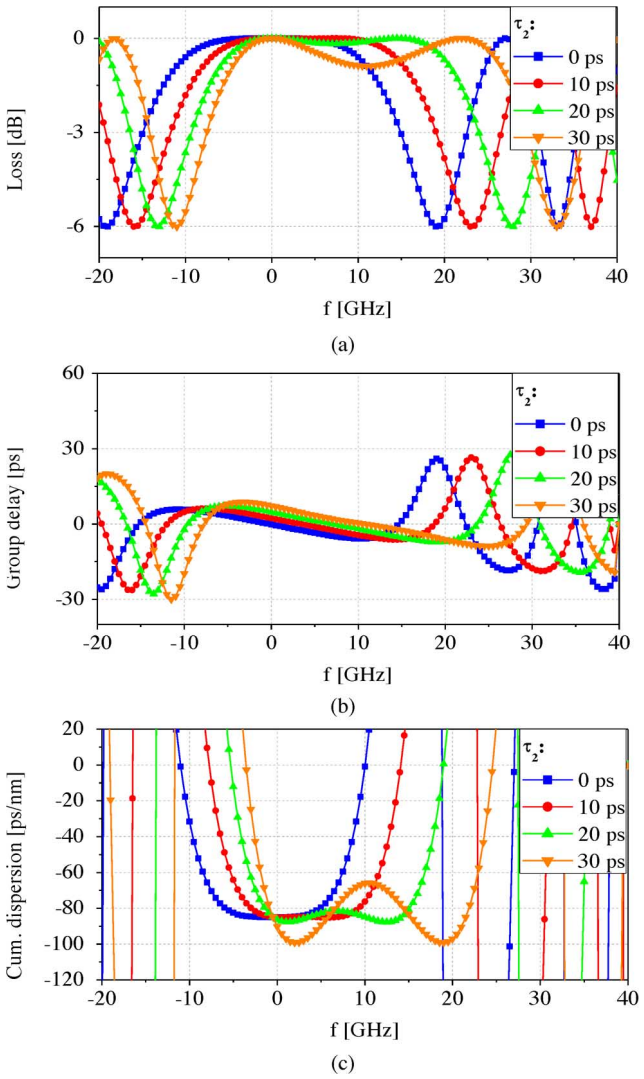

Fig. 5. (a) Amplitude, (b) group delay, and (c) dispersion responses of the TODC corresponding to four values of τ_2, considering $D_1 = -340$ ps/nm and $\alpha = \sqrt{0.25}$.

40 Gb/s. The data signal and corresponding negated version are used to drive a Mach–Zehnder modulator (MZM) in chirp-free operation. The frequency response of the MZM is modeled by a third-order Bessel filter with a -3 dB cutoff frequency of 30 GHz. The DSB optical signal at the output of the MZM has an extinction ratio (ER) of 10 dB. The dispersive media D_f, D_1, and D_2 have the following transfer function

$$H_{D_i}(f) = e^{-j2\pi[k_i f^2 + \tau_i f]} \tag{17}$$

where k_i is given by (2). The PBS and PBC have infinite polarization ER. The SSF is polarization insensitive. The p-i-n has a unitary responsivity, and its frequency response is modeled by a third-order Bessel filter with a -3 dB cutoff frequency of 30 GHz.

The performance criteria are the eye-opening penalty (EOP) [14], sideband suppression ratio (SSR) and filtering loss. The EOP is given by

$$\mathrm{EOP} = 10\log_{10}\left\{\frac{I_1 - I_0}{I_{1,\mathrm{ref}} - I_{0,\mathrm{ref}}}\right\} \tag{18}$$

where I_1 and I_0 are the lowest and highest currents corresponding to the symbols "1" and "0" at the optimum sampling time of the eye diagram at the output of the p-i-n, respectively. The eye aperture is thereby given by $I_1 - I_0$. $I_{1,\mathrm{ref}} - I_{0,\mathrm{ref}}$ is the eye aperture of the reference signal, which is a DSB signal in back-to-back with $\mathrm{ER} = 9$ dB. The SSR is given by the power difference (in dB) of the spectral components 20 GHz apart the carrier frequency. The filtering loss is the difference (in dB) between the average optical powers of the SSF input and output signals.

The filter parameters are optimized considering the case where the TODC bandwidth is the lowest. As such, $D_f = 170$ ps/nm, $D_1 = -340$ ps/nm, and $\theta = 45°$. A time delay of $\tau_2 = -30$ ps is considered in order to achieve a bandwidth of 35 GHz without significant distortion of the frequency response. Fig. 6 presents the optimization results considering a second-order filter $(N = 2)$. The frequency detuning is given by $\delta_f = \mathrm{BW}/2 + \delta$. Fig. 6(a) shows that high EOPs are obtained for low bandwidths due to narrow filtering effect. For each bandwidth, there is an optimum detuning. Lower detunings result in poor sideband suppression, which in turn reduces the compensation effect. On the other hand, higher detunings cause considerable carrier suppression, which results in the collapse of the eye diagram. The SSR and filtering loss both increase with the detuning, as asserted in Fig. 6(b) and (c), respectively. A bandwidth of 40 GHz and a detuning of 23 GHz are considered (blue dot in Fig. 6), since such settings provide low EOP, high SSR, and low filtering losses. Similar optimization procedures with different filter orders do not yield significant improvement over all three performance criteria. As such, a filter order of $N = 2$ is considered.

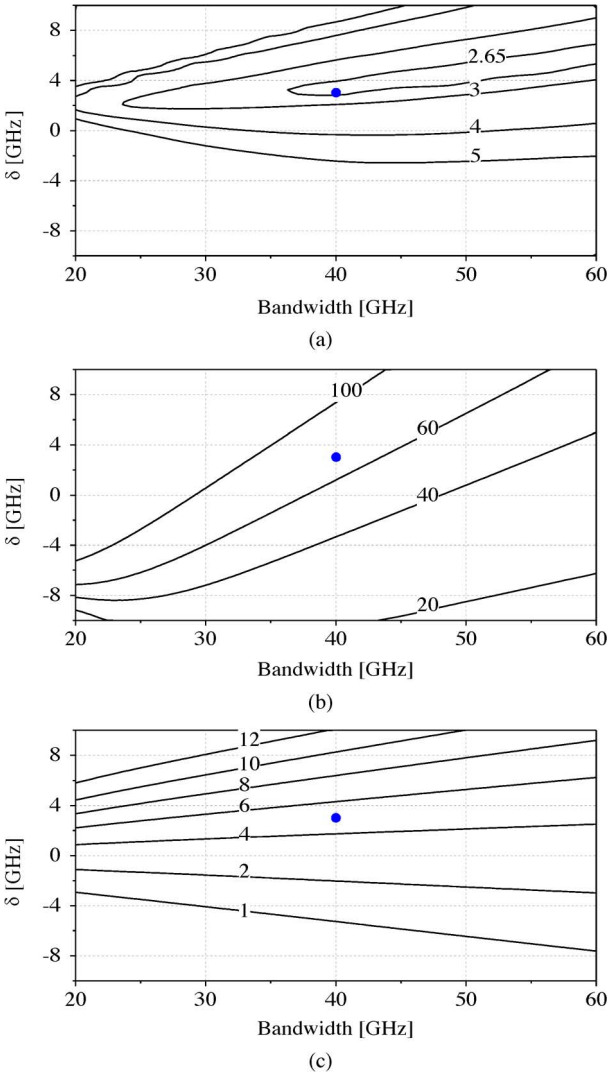

Fig. 6. (a) EOP, (b) SSR, and (c) filtering loss for various SSF−3 dB bandwidths and detunings. The frequency detuning is given by $\delta_f = \mathrm{BW}/2 + \delta$. The blue dot represents the chosen SSF parameters.

C. Transmission Simulations Using the TODC and SSF Optimum Settings

The transmission simulation setup is depicted in Fig. 3. The TODC and SSF settings correspond to the optimized values found in the last two sections. The simulation results are shown in Fig. 7. Fig. 7(a) shows that in back-to-back, the uncompensated SSB signal presents a penalty of 0.96 dB relatively to the uncompensated DSB signal. Such penalty is due to degradation induced by SSF, as seen in insets (i) and (ii). However, a lower increase of the EOP with the fiber length is obtained for the SSB signal due to its stronger resilience to CD in comparison to DSB signaling.

The frequency response of the TODC has limited optical bandwidth and nonideal phase response. Thus, dispersion compensation also induces signal distortion. Since the TODC minimum bandwidth is high, signal distortion is mainly caused by nonideal phase response. Analysis of (5) shows that the phase response of the TODC presents the worst nonlinear behavior for polarization rotation angles near 22.5° and 67.5°. This explains the deviation of the optimized and theoretical curves on Fig. 7(b) near such angles. A maximum compensation penalty of 1.38 dB is achieved for a fiber length of 10 km, with an optimum polarization rotation angle of $\theta = 45°$ [inset (iii)]. Such an angle results in the lowest optical bandwidth. Equal penalties are obtained for fiber lengths having the same absolute difference relatively to the intermediate fiber length of 10 km (e.g., 5 and 15 km). For fiber lengths obeying to this condition, the theoretical optimum polarization rotation angles are complementary (for the given example, these angles are of 70° and 20°, respectively). According to (3), for complementary angles the amplitude responses are equal. In addition, the group-delay response nonlinear terms are also equal. In (5), these terms correspond to the denominator and the last term in the nominator. Hence, compensation-induced distortions and subsequent EOPs are equal for fiber lengths compliant with the aforementioned condition.

Simulations are shown for the previously fixed time delay of $\tau_2 = -30$ ps, and for a time delay optimized for each given fiber length. Fig. 7(a) shows that the time-delay optimization results in negligible gain. Moreover, the average optimum delay is about -30 ps, as seen in Fig. 7(c). As such, the time delay can be fixed for the entire compensation range.

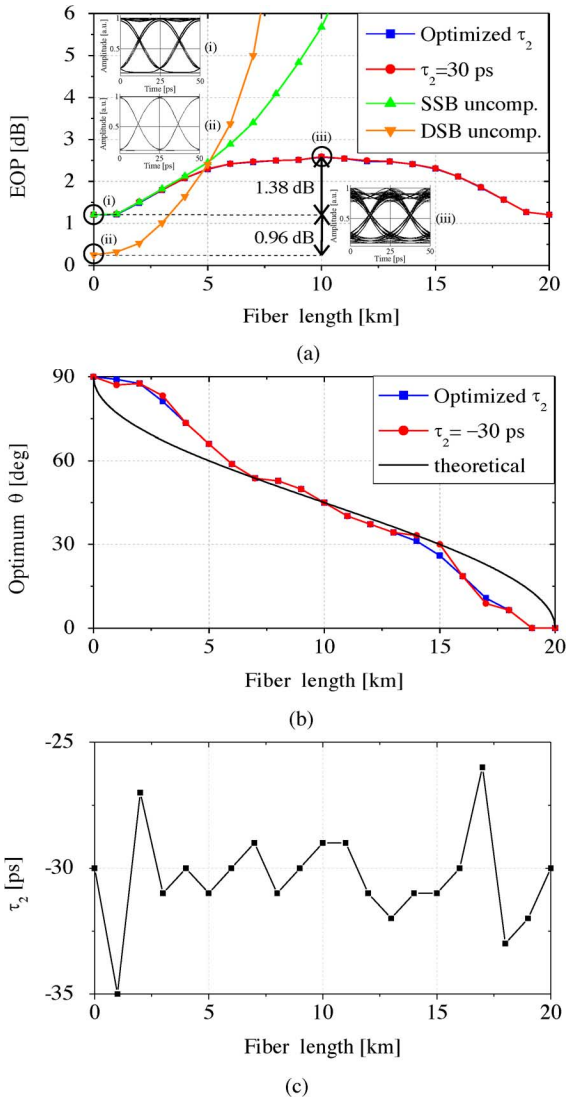

Fig. 7. (a) EOP, (b) optimum θ, and (c) optimum time delay for the considered fiber lengths. The EOP is calculated for compensated SSB signals with optimized and fixed time delays, and uncompensated SSB and DSB signals. The signals at the input of the TODC have a cumulative dispersion of $D_f = 17$. Fiber length [ps/nm]. The insets in (a) are the eye diagrams of the detected signal. In (b), the theoretical line is derived using (7).

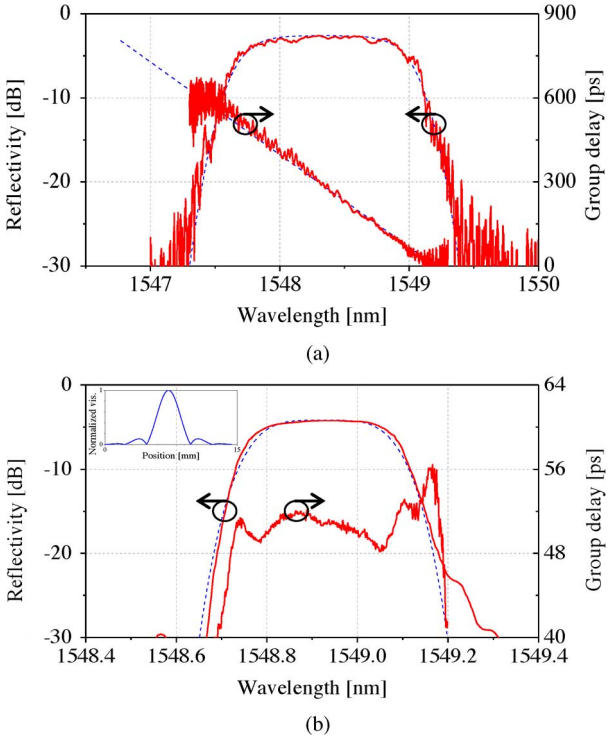

Fig. 8. Reflectivity and group-delay responses of the (a) CFBG and (b) shaded-sinc FBG. The dashed lines correspond to the designed responses, whereas solid lines are experimental data. Experimental reflectivities include the circulator insertion losses. The inset in (b) is the visibility profile of the apodized-sinc FBG. A phase shift of π is set at each zero of the sinc function.

D. Implementation of One Dispersive Medium and SSF Using FBGs

The dispersive media can be implemented using CFBGs since such devices present attractive features such as simplicity, negligible nonlinear effects, and small size.

The TODC compensation range is of $D_1 = -340$ ps/nm up to $D_2 = 0$. The CFBG designed to implement D_1 presents a second-order super-Gaussian reflectivity with a -3 dB bandwidth of 160 GHz. Such a broad bandwidth avoids signal distortion imposed by narrow filtering. A length of $L = 86.6$ mm and chirp of -96 pm/cm are considered. The apodization profile consists of a fourth-order super-Gaussian function with a full-width at half-maximum of $L/3$. The average effective refractive index variation is $\overline{\delta_{n_{\text{eff}}}} = 1.1 \times 10^{-4}$. The designed and experimental frequency responses of the CFBG are shown in Fig. 8(a). A slightly higher cumulative dispersion of -370 ps/nm is achieved. Such dispersion offset does not present a limitation to the experiment. A maximum reflectivity of -2.6 dB, -3 dB bandwidth of 177 GHz, and average reflectivity and GDRs of 1.6 dB and 9.5 ps are achieved, respectively. Since the dispersive medium D_2 presents no cumulative dispersion, it basically consists of an all-pass filter with linear phase response. Although such filter can be implemented using FBGs, a simpler implementation is considered. A fiber mirror is used instead since it presents nearly ideal phase response, broad bandwidth, and low insertion loss.

The SSF should present a second-order super-Gaussian reflectivity with a -3 dB bandwidth of 40 GHz, and a flat group-delay response. Both requirement are met using an advanced visibility profile described in [16] as apodized-sinc. If a sinc-shaped visibility is used, then an approximately square reflectivity is obtained. A super-Gaussian reflectivity with selectable order can be achieved by apodizing the sinc-shaped visibility with a given super-Gaussian function. The visibility profile used to achieve the SSF required parameters, as shown in the inset of Fig. 8(b). One important detail is that the dispersion at the transition bands of the filter increases with the maximum reflectivity. Since the purpose of the filter is to perform sideband suppression, a high dispersion at the transition bands of the filter would induce signal degradation. As such, the filter is designed to have a low maximum reflectivity of -3 dB. A length of $L = 12.8$ mm, and an average effective refractive index variation of $\overline{\delta_{n_{\text{eff}}}} = 1.8 \times 10^{-4}$ are considered. The reflectivity and group-delay responses of the apodized-sinc FBG are shown in

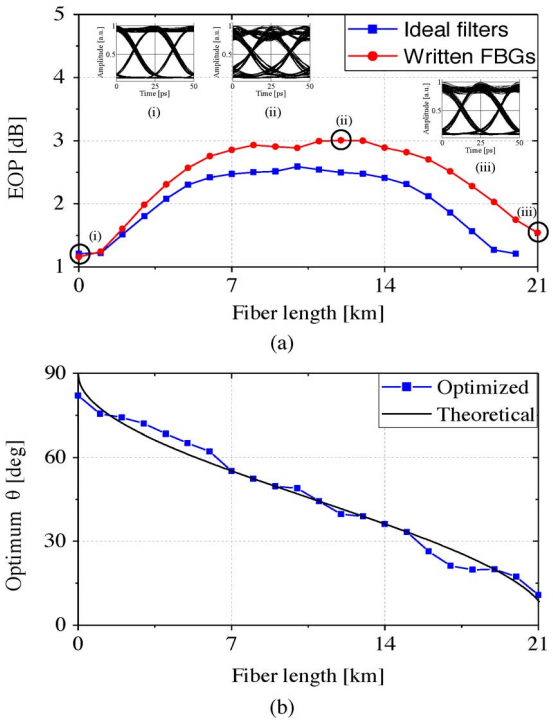

Fig. 9. (a) EOP for the considered fiber lengths using ideal filters and $\tau_2 = -30$ ps, and using the frequency response of the written FBGs; (b) optimum θ obtained when using the written FBGs response. The theoretical line is derived using (7).

Fig. 8(b). A maximum reflectivity of -4.2 dB, -3 dB bandwidth of 42 GHz, and a peak-to-peak group delay lower than 5 ps are achieved.

Transmission simulations are performed using the frequency responses of the written FBGs, which were obtained resorting to an optical network analyzer (ONA). The apodized-sinc FBG detuning is optimized in order to obtain a similar EOP when using an ideal filter. The CFBG detuning is optimized with the purpose of minimizing the EOP, using the apodized-sinc FBG as the SSF, and considering a fiber length of 21.5 km. Such a fiber length matches the cumulative dispersion of the CFBG. Both detunings consist of the difference between the central frequencies of the FBGs with the optical carrier frequency. The time delay is adjusted considering an intermediate fiber length of 10.75 km and $\theta = 45°$. These three optimizations yield SSF and CFBG detunings of 22 and 15 GHz, respectively, and a time delay of 30 ps. Simulation results are presented in Fig. 9. Negligible penalty is obtained in back-to-back, since the frequency response of the SSF is nearly ideal. Increasing degradation is observed as the fiber length increases. This is due to the amplitude and GDR of the CFBG. Furthermore, higher compensation penalty is expected since a slightly broader compensation range is considered.

IV. Experiment

The experimental setup is shown in Fig. 10. A continuous wave (CW) source with a wavelength of 1549.32 nm and an average power of 13 dBm was used. A dual-electrode nearly chirp free MZM with a -3 dB cutoff frequency of 30 GHz was

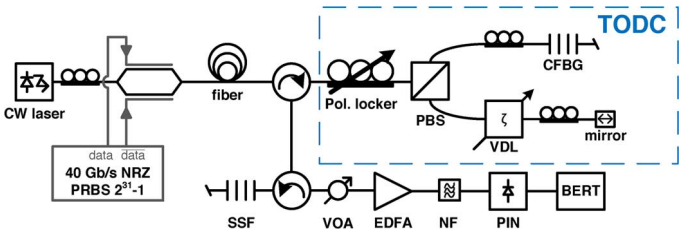

Fig. 10. Experimental setup. PRBS; VDL; VOA—variable optical attenuator; EDFA—erbium-doped fiber amplifier; NF—noise filter with a bandwidth of 100 GHz; p-i-n—photoreceiver; BERT—bit error rate tester.

used to obtain a 40 Gb/s DSB NRZ signal. A pseudorandom binary sequence (PRBS) with $2^{31} - 1$ bits was used. Spools of standard single-mode fiber (SSMF) with a dispersion parameter of 17 ps/nm/km were used in order to add a given cumulative dispersion to the signal. An automatic polarization locker was used instead of a manual PC. This equipment is able to set any input SOP to any output SOP in less than 150 μs, with a precision of 10°. Since the tuning time of the TODC corresponds to the settling time of the PC, a very low tuning time is enabled. Moreover, input SOP variations are accommodated by the polarization locker. The dispersive media consisted of a fiber mirror with zero cumulative dispersion and 50% reflectivity, and a CFBG with a frequency response depicted in Fig. 8(a). The CFBG central wavelength was optimized by inducing a strain to the grating. A variable delay line (VDL) was used in order to adjust the delay between both arms of the TODC. Since both dispersive media are reflective, the PBS works as a PBC for the dispersive media reflected signals. The SSF was the FBG with a frequency response, as shown in Fig. 8(b). The SSF was detuned by 22 GHz relatively to the optical carrier resorting to a controllable heater. The SSB signal was detected by an optically pre-amplified receiver. The -3 dB cutoff frequency of the photoreceiver is of 33 GHz.

The frequency response of the TODC was investigated using an ONA. Different polarization rotation angles were considered. The results are shown in Fig. 11. These results show that the dispersion decreases from 0 to -365 ps/nm when θ is varied from 90° to 0°. For $\theta = 0°(\theta = 90°)$, the TODC input signal is directed only to the CFBG (fiber mirror). The amplitude and GDRs decrease as θ increases, since the fiber mirror has nearly ideal amplitude and group-delay responses. The intrinsic limitations of the TODC amplitude and group-delay responses depicted in Fig. 5 are not observed due to the sweeping nature of the measurement. Therefore, the measured frequency response is the weighted average between both dispersive media frequency responses.

The measured eye diagrams and polarization rotation angles for uncompensated and compensated signals are presented in Fig. 12. The experimental eye diagrams agree with the simulation results [see insets of Fig. 9(a)]. The eye diagrams considering fiber lengths of 15 and 20 km and $\theta = 90°$ are not shown as only distortion is observed. The eye of the SSB signal in back-to-back is slightly tilted due to residual chirp induced by the electro-optic modulation. The eye diagrams shown in the second and third columns correspond to the case where fixed

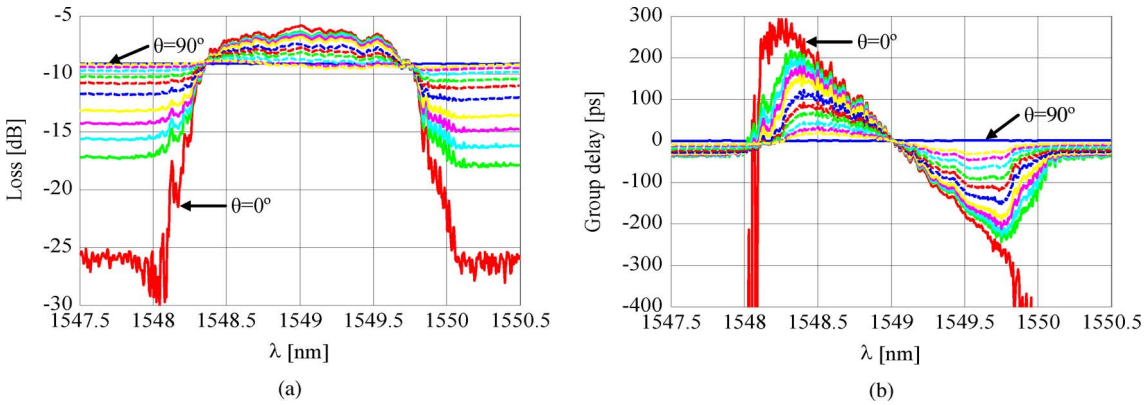

Fig. 11. (a) Amplitude and (b) group delay of the TODC for various polarization rotation angles.

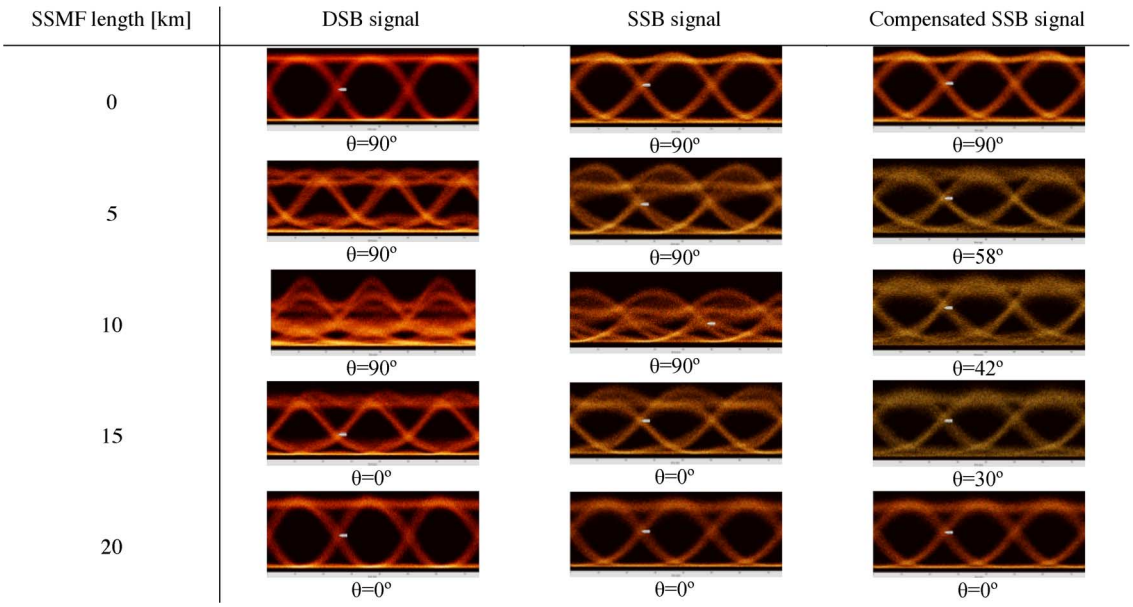

Fig. 12. Eye diagrams and measured polarization rotation angles for the detected DSB and SSB signals considering different SSMF lengths.

compensations is employed, i.e., θ is 0° or 90°. As such, nonoptimum compensation is obtained for 5, 10, and 15 km. For these cases, lower distortion is observed when SSB modulation is employed. This is due to the higher tolerance to CD provided by SSB modulation. The fourth column presents the eye diagrams of the properly compensated signals. Improved eye openings for 5, 10, and 15 km of fiber were obtained. For 0 and 20 km, fixed compensation is the already optimum case.

For the remaining fiber lengths, the polarization rotation angles were fine tuned in order to obtain low eye distortion. The measured polarization rotation angles are up to 7° lower than the simulated values because the residual chirp induced during electro-optic modulation is partially compensated by the CFBG group delay response. Another reason is the difference between the cumulative dispersion of the fiber spools and the values considered in simulations. The optical spectra of the DSB and SSB signals in back-to-back is shown in Fig. 13. An SSR of 28 dB was obtained for the SSB signal.

The system performance was quantitively assessed using BER measurements. The BER results are shown in Fig. 14. The results corresponding to back-to-back and simultaneously fixed and optimum compensation are presented in Fig. 14(a). The dispersion compensation performed by the CFBG induces no observable power penalty. The SSB signals present a power penalty of 1.3 dB relatively to DSB due to degradation caused by SSF. The results corresponding to a fiber length of 5 km are shown in Fig. 14(b). A low compensation gain of 0.4 dB is achieved with the optimum compensation in comparison to fixed compensation. Such a low compensation gain is due to the low cumulative dispersion experienced by the SSB signal. Since the DSB signal presents lower tolerance to CD, a higher compensation gain of 1.3 dB is obtained. It should be noted that this compensation gain already takes into account the 1.3 dB power penalty caused by SSF. A similar analysis is valid for a fiber length of 15 km, as shown in Fig. 14(d), with 0.1 dB higher compensation gains. Fig. 14(c) shows the case where the approximately intermediate fiber length of 10 km is employed. In this case, CD induces high signal distortion, even when fixed compensation is used. As a result, the BER of the DSB signal could not be measured, and the SSB signal with fixed compensation presented a BER floor of 10^{-6}. The employment of optimum compensation resulted in a BER lower than 10^{-8}.

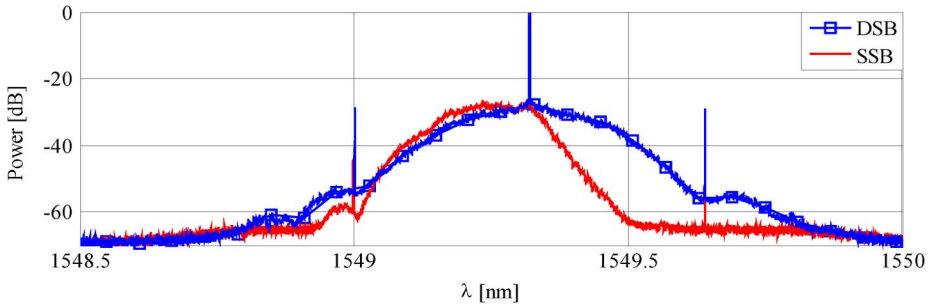

Fig. 13. Optical spectra of the DSB and SSB signals.

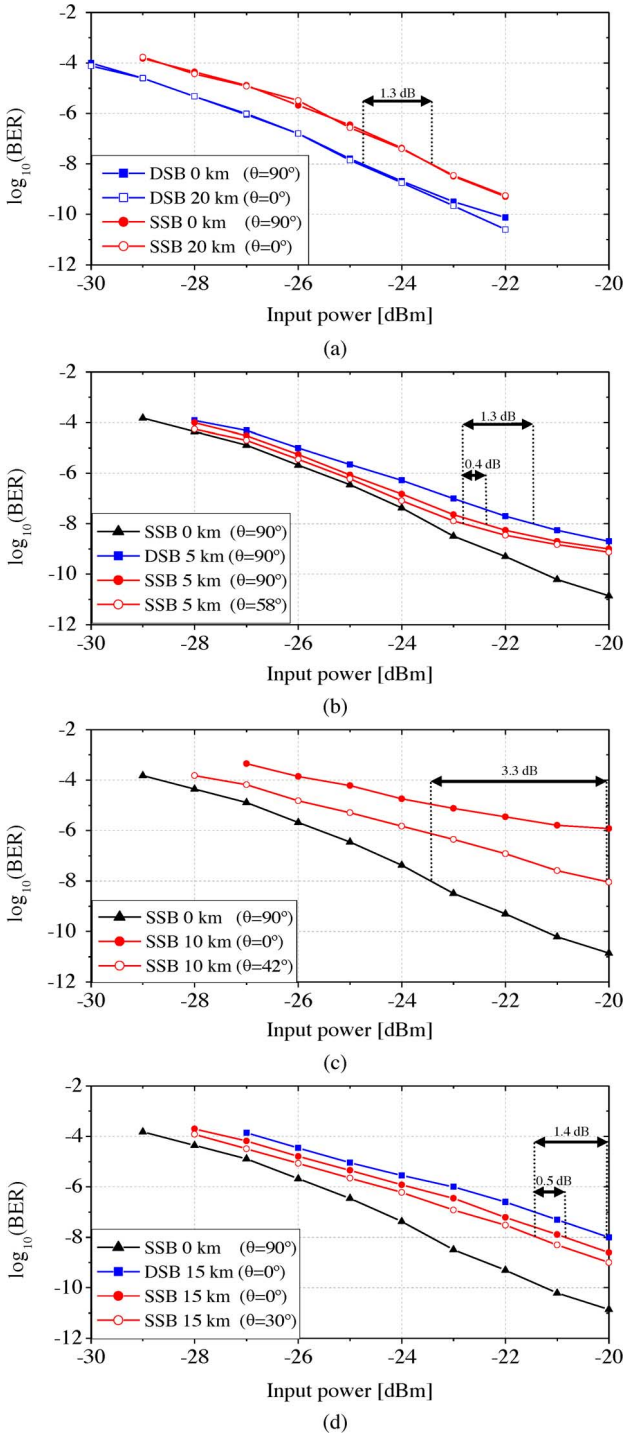

Fig. 14. BER results for different input powers at the output of the VOA, considering fiber lengths of (a) 0 and 20 km, (b) 5 km, (c) 10 km, and (d) 15 km.

In comparison to back-to-back situation, the compensated signal presented a power penalty of 3.3 dB considering a BER of 10^{-8}. Since this is the case where an intermediate fiber length is used, it is expected that a maximum power penalty of 3.3 dB on the compensated signal relatively to the SSB back-to-back signal is achieved for the entire compensation range. If a DSB signal in back-to-back is considered instead, this penalty is increased by 1.3 to 4.6 dB. Furthermore, optimum compensation enables achieving a BER on the order of 10^{-9} on the entire compensation range.

V. Conclusion

A TODC based on a novel operation principle was proposed and experimentally demonstrated. Dispersion compensation is obtained by splitting the input signal by two dispersive media, and adding the resulting signals afterward. Theoretical analysis of the TODC proved that tunable dispersion is achieved by varying the power splitting ratio between both dispersive media. In order to avoid coherence problems related to signal addition in the optical domain, a scheme where signal addition is performed in the electrical domain was proposed. The dispersive media output signals are combined in orthogonal polarizations and directly detected. Since the phase information of both signals needs to be preserved after direct detection, SSB modulation is used with this end. Theoretical validation of this approach was also presented.

The main limitation of the TODC is the tradeoff that exists between bandwidth and compensation range. This limitation was taken into account on the optimization of the TODC settings considering a 40 Gb/s NRZ SSB signal. DSB to SSB conversion was performed through SSF. The SSF and one dispersive medium were implemented using FBGs, which presented frequency responses very similar to the designed ones. The other dispersive medium consisted of a fiber mirror with ideal frequency response.

An experiment was performed using a 40 Gb/s NRZ signal and a TODC with a compensation range of -340 to 0 ps/nm. This compensation range allows compensating the dispersion associated with up to 20 km of SSMF. The compensation effectiveness was investigated after transmitting the signal by SSMF spools of 5, 10, 15, and 20 km. A BER lower than 10^{-8} was achieved for the entire compensation range, with a maximum power penalty of 3.3 dB relatively to the SSB signal in back-to-back. As predicted on simulations, the maximum power penalty occurred when half of the tuning range was employed. In this

situation, the TODC bandwidth is the lowest, whereas in zero or maximum compensation the bandwidth is the highest.

Depending on the fiber length, the power splitting ratio between both dispersive media was adjusted resorting to an automatic PC and a PBS. The automatic PC makes the TODC insensitive to the SOP of the input signal, while enabling tuning times lower than 150 μs. In fact, one of the main advantages of the presented TODC is its fast response. Depending on the power splitting method, such as using fast PCs [17] and a PBS, ultra-low tuning times in the picosecond range required for packet switching applications can be successfully achieved.

REFERENCES

[1] G. P. Agrawal, *Fiber-Optic Communication Systems*, 3rd ed. New York: Wiley-Interscience, 2002.

[2] T. N. Nielsen, B. J. Eggleton, J. A. Rogers, P. S. Westbrook, P. B. Hansen, and T. A. Strasser, "Dynamic post dispersion optimization at 40 Gb/s using a tunable fiber Bragg grating," *IEEE Photon. Technol. Lett.*, vol. 12, no. 2, pp. 173–175, Feb. 2000.

[3] W. Hatton and M. Nishimura, "Temperature dependence of chromatic dispersion in single mode fibers," *J. Lightw. Technol.*, vol. LT-4, no. 10, pp. 1552–1555, Oct. 1986.

[4] C. K. Madsen, G. Lenz, A. J. Bruce, M. A. Cappuzzo, L. T. Gomez, and R. E. Scotti, "Integrated all-pass filters for tunable dispersion and dispersion slope compensation," *IEEE Photon. Technol. Lett.*, vol. 11, no. 12, pp. 1623–1625, Dec. 1999.

[5] K. Takiguchi, K. Okamoto, and K. Moriwaki, "Planar lightwave circuit dispersion equalizer," *J. Lightw. Technol.*, vol. 14, no. 9, pp. 2003–2011, Sep. 1996.

[6] H. Kawashima, N. Matsubara, and K. Nara, "Tunable dispersion compensator using PLC type optical transversal filter," *Furukawa Rev.*, vol. 29, pp. 13–18, 2006.

[7] B. J. Eggleton, A. Ahuja, P. S. Westbrook, J. A. Rogers, P. Kuo, T. N. Nielsen, and B. Mikkelsen, "Integrated tunable fiber gratings for dispersion management in high-bit rate systems," *J. Lightw. Technol.*, vol. 18, no. 10, pp. 1418–1432, Oct. 2000.

[8] Y. J. Lee, J. Bae, K. Lee, J.-M. Jeong, and S.-B. Lee, "Tunable dispersion and dispersion slope compensator using strain-chirped fiber Bragg grating," *IEEE Photon. Technol. Lett.*, vol. 19, no. 10, pp. 762–764, May 2007.

[9] S. Cao, C. Lin, G. Barbarossa, and C. A. Y. C. Yang, "Dynamically tunable dispersion slope compensation using a virtually imaged phased array (VIPA)," in *Proc. Adv. Semicond. Lasers Appl./Ultraviolet Blue Lasers Their Appl./Ultralong Haul DWDM Transmiss. Netw./WDM Compon., Dig. LEOS Summer Top. Meetings*, 2001, p. 2, .

[10] C. R. Doerr, S. Chandrasekhar, and L. L. Buhl, "Tunable optical dispersion compensator with increased bandwidth via connection of a Mach–Zehnder interferometer to an arrayed-waveguide grating," *IEEE Photon. Technol. Lett.*, vol. 20, no. 8, pp. 560–562, Apr. 2008.

[11] M. Sieben, J. Conradi, and D. E. Dodds, "Optical single sideband transmission at 10 Gb/s using only electrical dispersion compensation," *J. Lightw. Technol.*, vol. 17, no. 10, pp. 1742–1749, Oct. 1999.

[12] K. Yonenaga and N. Takachio, "A fiber chromatic dispersion compensation technique with an optical SSB transmission in optical homodyne detection systems," *IEEE Photon. Technol. Lett.*, vol. 5, no. 8, pp. 949–951, Aug. 1993.

[13] D. Fonseca, A. V. T. Cartaxo, and P. Monteiro, "On the use of electrical precompensation of dispersion in optical single-sideband transmission systems," *IEEE J. Sel. Topics Quantum Electron.*, vol. 12, no. 4, pp. 603–614, Jul./Aug. 2006.

[14] D. Fonseca, A. V. T. Cartaxo, and P. Monteiro, "Adaptive optoelectronic filter for improved optical single sideband generation," *IEEE Photon. Technol. Lett.*, vol. 18, no. 2, pp. 415–417, Jan. 2006.

[15] D. Fonseca, A. V. T. Cartaxo, and P. Monteiro, "Optical single-sideband transmitter for various electrical signaling formats," *J. Lightw. Technol.*, vol. 24, no. 5, pp. 2059–2069, May 2006.

[16] M. Ibsen, M. K. Durkin, M. J. Cole, and R. I. Laming, "Optimised square passband fibre Bragg grating filter with in-band flat group delay response," *Electron. Lett.*, vol. 34, no. 8, pp. 800–802, Apr. 1998.

[17] K. Benjamin, H. Ariya, M. Vitali, Z. Hongbin, S. David, and N. Reinhold, "Robust, wavelength and temperature-insensitive 14 krad/s endless polarization tracking over 2.5 grad," presented at the Optical Fiber Communications Conf., San Diego, CA, 2009, Paper JThA63.

Miguel V. Drummond (S'09) was born in Porto, Portugal, in 1984. He received the Diploma degree in electronics and telecommunications engineering from the University of Aveiro, Aveiro, Portugal, in 2007, where he is currently working toward the Ph.D. degree.

Since 2008, he has been with the Optical Communications Research Group, Institute of Telecommunications, University of Aveiro. His current research interests include all-optical signal processing techniques applied to high-bit-rate optical-communication systems and microwave photonic devices.

Rogerio N. Nogueira (M'03) graduated in physics engineering and received the Ph.D. degree in physics from the University of Aveiro, Aveiro, Portugal, in 1998 and 2005, respectively.

He is currently an Assistant Researcher at the Institute of Telecommunications, University of Aveiro, where he has been engaged in research on the field of fiber optics since 1999, participating in several projects financed by national, EU organizations and private companies. Since 2009, he has also been an R&D expert at Nokia Siemens Networks Portugal S.A., Amadora, Portugal, where he is engaged in research on the field of optical communications. He is the author or coauthor of one book chapter, more than 30 papers published in international scientific journals and more than 100 papers published in international conferences. His research interests include design and production of optical components, fiber optical communication systems, and fiber optical sensors.

Paulo P. Monteiro (M'98) was born in Coimbra, Portugal, in 1964. He received the Diploma and Doctoral (Ph.D.) degrees in electronics and telecommunications from the University of Aveiro, Aveiro, Portugal, and the M.Sc. degree from the University of Wales, U.K.

He is currently a Research Manager at Nokia Siemens Networks Portugal S.A., Amadora, Portugal, and an Associate Professor at the University of Aveiro, where he has been teaching courses of telecommunications, and where he is also a Researcher at the Institute of Telecommunications. He has participated in several national and European projects and he is currently the Project Coordinator of the large-scale integrating project FUTON (FP7 ICT-2007-215533). He is the author or coauthor of more than 15 patent applications and more than 200 refereed papers and conference contributions. His main research interests include high-speed optical communications for access and core networks, fixed-mobile convergence.

Dr. Monteiro has served as a Reviewer of the IEEE JOURNAL OF LIGHTWAVE TECHNOLOGY, *Institution of Electrical Engineers Electronics Letters*, *Electronics and Telecommunications Research Institute Journal*, and *Optical Society of America Journal of Optical Networking*, and *International Society for Optical Engineers Optical Engineering*.

Manuel A. Violas received a degree in electronics and telecommunications engineering from the University of Aveiro, Aveiro, Portugal, in 1982, the M.Sc. degree from the University of Coimbra, Coimbra, Portugal, 1988, and the Ph.D. degree in electrical engineering from University of Aveiro, in 1999.

From 1990 to 1992, he was with British Telecom, where he was involved in research on very broadband optical receivers. Since 1982, he has been with the Department of Electronics and Telecommunications, University of Aveiro, Portugal, where he is currently a Researcher at the Institute of Telecommunications, where he has been involved in National and International Projects in optical communications. His main research interests include microwave and RF circuit design, microwave circuit/system simulation, electrical signal processing for very high speed lightwave communications systems, and radio over fiber, for distributed antenna system, with focus on model electro-optical devices such as direct-modulated lasers and receiver optical subassembly.

Carola Sterner was born in Umea, Sweden, on April 11, 1968. She received the Master's degree in engineering physics from the University of Uppsala, Uppsala, Sweden, in 1993, and the Ph.D. degree from the Department of Solid-State Electronics, Ångström Laboratory, Uppsala University, in 1998.

She is currently a Senior Scientist at Acreo AB, Kista, Sweden. She is a member of the Fiber Department working with fiber components mainly based on fiber Bragg gratings. She is also with Kista Photonics Research Center, Royal Institute of Technology, Kista, Sweden. She has long experience in optoelectronic applications from past positions as Development Engineer at Ericsson Microelectronics and Optillion AB. At Ericsson's Optoelectronic Division, she was responsible for details in 10 Gbit/s laser products. At the start-up company Optillion AB, she was responsible for the "in-house" carrier manufacturing for 10 Gbit/s transceivers. At the Ångström Laboratory, Uppsala University, she was a Researcher and Teacher.

Pierre-Yves Fonjallaz was born in France, on August 20, 1966. He received the Master's degree in physics and the Ph.D. degree in physics from the Swiss Federal Institute of Technology, Zurich, Switzerland, in 1990 and 1995, respectively.

In 1995, he joined the Royal Institute of Technology (KTH), Kista, Sweden, as a Postdoctoral Fellow for one year, and then joined the Institute of Optical Research, which became in 1999 the Research Institute Acreo AB after merging with the Industrial Microelectronics Centre. Since 2000, he has been the Head of the Fiber Optics Group, Acreo AB, Kista, Sweden. Since 2003, he has been the Director of Kista Photonics Research Center (KPRC), KTH, which is an umbrella organization facilitating the collaboration between Acreo and KTH in the field of optics and photonics. He is active in different European organizations such as the European Optical Society, where he is now the treasurer, and in the European Technology Platform Photonics21, where he is supporting the chairs of the working group 6 on Design and Manufacturing of Photonic Components and Systems. He is also in the Board of the Swedish Optical Society since 2008.

[J5] - All-optical generation of 40 Gb/s single sideband signals using a fiber Bragg grating

Miguel V. Drummond, Rogério N. Nogueira, Paulo P. Monteiro, Manuel A. Violas, Carola Sterner and Pierre-Yves Fonjallaz

Elsevier Optics Communications, Vol. 283, No. 12, pp. 2492–2495, 2010.

Optics Communications 283 (2010) 2492–2495

Contents lists available at ScienceDirect

Optics Communications

journal homepage: www.elsevier.com/locate/optcom

All-optical generation of 40 Gb/s single sideband signals using a fiber Bragg grating

Miguel V. Drummond [a,*], Rogério N. Nogueira [a,b], Manuel Violas [a], Paulo P. Monteiro [a,b], Carola Sterner [c,d], Pierre-Yves Fonjallaz [c,d]

[a] Instituto de Telecomunicações, 3810-193 Aveiro, Portugal
[b] Nokia Siemens Networks Portugal S.A., 2720-093 Amadora, Portugal
[c] ACREO AB, Electrum 229, SE-164 40 Kista, Sweden
[d] Kista Photonics Research Center, Royal Institute of Technology, Electrum 229, SE-164 40 Kista, Sweden

ARTICLE INFO

Article history:
Received 5 January 2010
Received in revised form 10 February 2010
Accepted 10 February 2010

Keywords:
Optical single sideband
Detuned filtering
Fiber Bragg gratings
Optical communication systems

ABSTRACT

In this work, we demonstrate a reliable all-optical technique for performing optical double sideband (ODSB) to single sideband (OSSB) format conversion of a 40 Gb/s non-return-to-zero signal. It is based on the optimization of a detuned optical filter, which was implemented on a fiber Bragg grating (FBG) with a complex apodization profile. An OSSB signal with negligible distortion was obtained, as the FBG presented a nearly ideal frequency response. Higher tolerance to chromatic dispersion enabled by the OSSB signal in comparison to the ODSB signal was demonstrated on both simulation and experimental results.

1. Introduction

Advanced optical modulation formats have been investigated with the purpose of increasing the capacity of wavelength-division-multiplexing networks [1]. Among such modulation formats, optical single sideband (OSSB) modulation presents the attractive features of allowing direct detection, linear electronic dispersion compensation [2] and having about twice the spectral efficiency and tolerance to chromatic dispersion (CD) in comparison to optical double sideband (ODSB) intensity modulated signals [3].

The generation of OSSB signals can be achieved with complex modulators [3], optoelectronic filters [4], or all-optical techniques [5–7]. Complex modulators generally add the ODSB signal with its Hilbert transform, thus generating an OSSB signal. Optoelectronic filters phase modulate the input ODSB signal with its Hilbert transform. All-optical techniques can be either linear or non-linear. An example of the latter case is using self-phase modulation on a semiconductor optical amplifier to induce gain in one sideband of an ODSB signal [6]. For high per-channel bitrates, all-optical techniques are the only possible solution, as the other ones are hampered by electrical bandwidth limitations. The simplest linear all-optical technique consists on using a detuned optical filter to suppress one of the signal's sidebands [5,7]. Even though such technique is impaired by wavelength drifts of the input ODSB signal, wavelength drift requirements relax with the increase of the bit rate. The filter's amplitude and group delay responses should be carefully tailored with the purpose of obtaining an undistorted OSSB signal with high sideband suppression. More specifically, the filter's response should have an optimum amplitude roll-off and reduced group delay variation.

In this letter, we design and experimentally test a fiber Bragg grating (FBG) filter with the aim of performing detuned optical filtering on a 40 Gb/s non-return-to-zero (NRZ) signal. A complex FBG apodization profile [8] was used to achieve the optimized roll-off on the amplitude response with negligible group delay variation. The generated OSSB signal was characterized by measuring its tolerance to CD.

2. Optimization of the filter settings

The optimization of the filter settings was performed taking into account the simulation setup depicted in Fig. 1. A dual-electrode Mach–Zehnder modulator (MZM) is used to generate a chirp-free ODSB signal with an extinction ratio (ER) of 10 dB. CD is added to the signal using spools of linear standard single mode fiber (SSMF), with a dispersion parameter of 17 ps/nm/km. Detuned filtering is performed at the receiver side. The frequency responses of the MZM and receiver are both modeled by a third-order Bessel filter with a −3 dB cutoff frequency of 30 GHz. The detuned filter (DF) is modeled by a second-order super-Gaussian

* Corresponding author. Address: Instituto de Telecomunicações; Campus Universitário de Santiago, 3810-193 Aveiro, Portugal. Tel.: +351 234 377900; fax: +351 234 377901.
E-mail address: mvd@av.it.pt (M.V. Drummond).

0030-4018/$ - see front matter © 2010 Elsevier B.V. All rights reserved.
doi:10.1016/j.optcom.2010.02.023

Fig. 1. Simulation and experimental setup. Inset: operation principle of detuned filtering operation. SSMF – standard single mode fiber; DF – detuned filter; RX – receiver.

function with linear phase response. The −3 dB optical bandwidth and frequency detuning relatively to the optical carrier are optimized considering a SSMF length of 5 km. The performance criteria are the eye opening penalty (EOP), sideband suppression ratio (SSR) and filtering loss. The EOP is given by

$$\mathrm{EOP} = -10\log_{10}(O_s/O_{\mathrm{ref}}), \tag{1}$$

where O_s and O_{ref} are the eye apertures obtained at the input of the decision circuit of the analyzed and reference signals, respectively. The reference signal is an ODSB signal in back-to-back with an ER of 9 dB. The SSR is given by the power difference (in dB) of the spectral components 20 GHz apart the carrier frequency. The filtering loss is the difference (in dB) between the average optical powers of the DF input and output signals. The results are shown in Fig. 2. Fig. 2a and b shows that high EOPs are obtained for low bandwidths, due to narrow filtering effect. An optimum detuning is obtained for each given bandwidth. A lower detuning results in poor sideband suppression (Fig. 2c), which causes a reduction on the tolerance to CD and signal degradation due to narrow filtering. On the other hand, an extremely high SSR has the cost of filtering out significant spectral content near the carrier frequency, with consequent high filtering losses. As such, the optimum filter settings should enable reduced signal distortion in back-to-back, high tolerance to CD and low filtering losses. According to these guidelines, a −3 dB bandwidth of 40 GHz and a frequency detuning of 23 GHz were considered as optimum settings. Simulations considering different filter orders yielded higher EOPs for the same bandwidth and detuning ranges. This means that the second-order super-Gaussian filter function presents optimum steepness after the −3 dB cutoff frequency. As mentioned in [9], the shape of the filter's amplitude response plays an important role in minimizing the distortion that arises from detuned filtering. Therefore, different shapes such as Blackman or hyperbolic tangent with different orders were also assessed, however without any improvement relatively to the chosen super-Gaussian response. Moreover, such shapes can be well approximated by a super-Gaussian response with an adequate order. The optimum filter shape can only be found by a point-to-point optimization, where the filter is divided in a given number of slices with respect to the frequency. The amplitude of the slices should thus be optimized to provide reduced signal distortion and high sideband suppression. Such optimization procedure is very complex, and it should be noted that ultimately optimization results depend on the considered binary sequence.

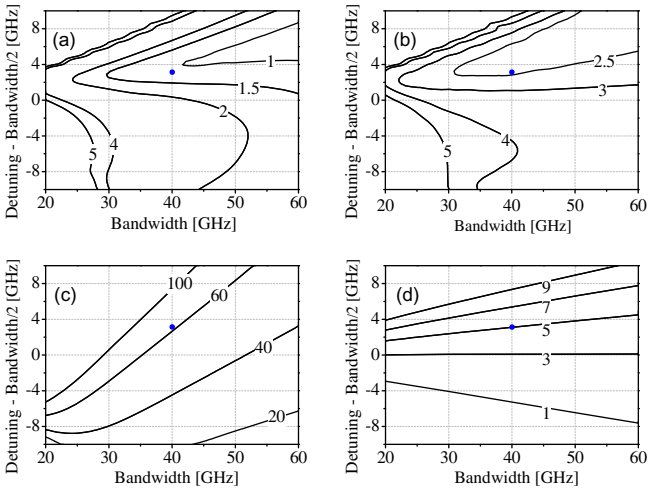

Fig. 2. DF Optimization results. (a) EOP in back-to-back, (b) EOP with 5 km of SSMF, (c) SSR and (d) filtering loss (in dB) for different −3 dB bandwidths and detunings. The dot represents the optimized DF parameters (Bandwidth = 40 GHz and Detuning = 23 GHz).

3. FBG design

According to the optimization results, the FBG should present a second-order super-Gaussian reflectivity with a −3 dB bandwidth of 40 GHz. Additionally, the group delay response should be constant in order to avoid signal distortion. Since the reflectivity should present a Gaussian shape, then a Gaussian apodization profile could be employed. This approach was followed in [5]. However, such apodization profile results in a large variation of the group delay for frequencies near the −3 dB cutoff frequency. In order to mitigate this problem, a complex apodization profile was used.

Considering the Fourier transform relation that exists between the apodization profile and reflectivity response for weak gratings, if a sinc apodization profile is employed, the reflectivity should present a square-like response [8]. A super-Gaussian reflectivity can be obtained if the sinc apodization profile is apodized by a second-order Gaussian function. As such, the final apodization profile is the product between a sinc and Gaussian functions, given by

$$A(z) = \left|\mathrm{sinc}\frac{z-L/2}{T}\right| \cdot \exp\left(-2\ln(2)^{1/N}\left[\frac{z-L/2}{\mathrm{FWHM}}\right]^N\right), \tag{2}$$

where z is the position along the grating, L is the grating length and T defines the period of the sinc function. By changing the order N and the full-width at half maximum (FWHM) of the Gaussian function, a super-Gaussian reflectivity with controllable order is obtained. For obtaining the target order and bandwidth, the parameters T, FWHM and maximum refractive index variation must be optimized simultaneously. The decrease of the filter's order also results in the mitigation of the Gibbs effect [8], i.e., the amplitude and group delay ripples originated from the truncation of the sinc function are reduced. The FBG was designed with a length of L = 12.8 mm and a maximum refractive index variation of 3.6×10^{-4}. The T parameter of the sinc function was of 2.5 mm. A second-order super-Gaussian apodization function with FWHM = 3.46 mm was

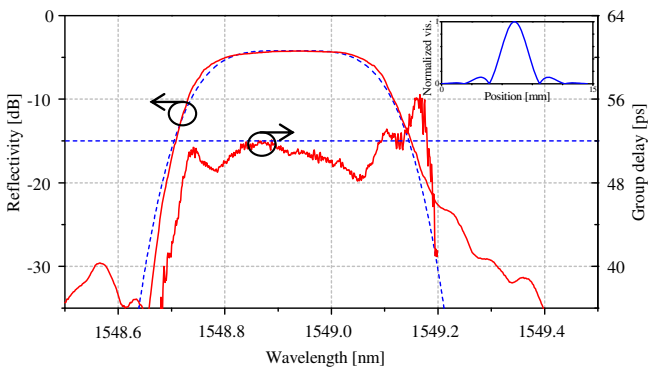

Fig. 3. Target super-Gaussian response (dashed line) and reflectivity and group delay responses of the written FBG. The experimental reflectivity includes the circulator insertion losses. The inset is the apodization profile.

considered. The target super-Gaussian response and reflectivity and group delay responses of the written FBG are shown in Fig. 3. The obtained reflectivity closely matches the target function. A low group delay ripple of about 8 ps was achieved for the −10 dB passband. An expected maximum reflectivity of −4.2 dB was obtained. A low reflectivity was intended as the group delay variations decreases with the maximum reflectivity.

4. Detuned filter performance

The performance of the DF was firstly assessed through simulations taking into account an ODSB signal, and OSSB signals obtained using an ideal filter and the frequency response of the written FBG. Different lengths of SSMF were considered. The EOP of the detected signals is shown in Fig. 4. According to the simulation results, the ODSB signal is outperformed by both OSSB signals after 6 km of SSMF. For lower lengths of SSMF, the ODSB signal outperforms the OSSB signals due to signal degradation originated from detuned filtering. For SSMF lengths higher than 6 km this situation is inverted, as the ODSB signal presents a lower tolerance to CD.

Experimental tests were performed for SSMF lengths of 0, 5 and 10 km. The measured optical spectra and eye diagrams are presented in Fig. 5. The OSSB signal presents a SSR of 28 dB. The SSR is limited by the amplitude response's decay deviation of the FBG relatively to the ideal response, as shown in Fig. 3. Nevertheless, to the best of the authors' knowledge, such a high SSR has never been reported for 40 Gb/s NRZ signals. Fig. 5 also shows that the unsuppressed sideband of the OSSB signal was reshaped in comparison with the same sideband of the ODSB signal. This spectral reshaping is similar to a slight high-pass filtering effect, opposing to signal degradation caused by sideband suppression. This reshaping effect is dependent on the order of the filter's amplitude response, which in this case is of 2. If a higher order is considered instead, then a higher SSR is achieved. However, the observed spectral reshaping is less significant. Oppositely, for lower orders, the SSR is lower and more significant spectral reshaping will even induce additional signal degradation. Fig. 5b–i presents the comparison between the simulation and experimental eye diagrams. The results for ODSB signals in back-to-back show that lower rise/fall-times are achieved in the experimental results. This means that the experimental ODSB signal presents a higher power on the high frequency spectral components. However, since such spectral components of the signal are removed after detuned filtering, the OSSB signals in back-to-back are very similar. The experimental eye diagram of the OSSB signal in back-to-back is slightly tilted due to residual chirp induced by the electro-optic modulation. The eye diagrams of the signals propagated by 5 and 10 km of SSMF also agree very well. The performance of the generated OSSB signal

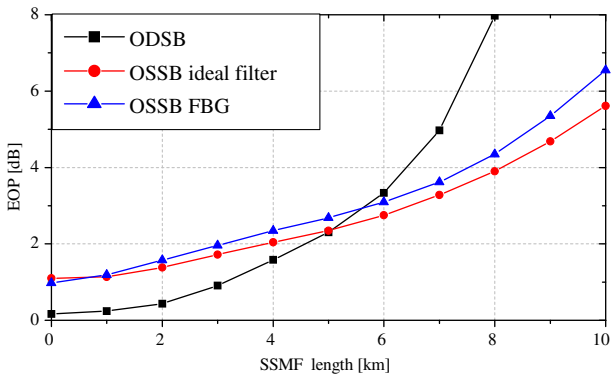

Fig. 4. EOP of the detected signal for different SSMF lengths.

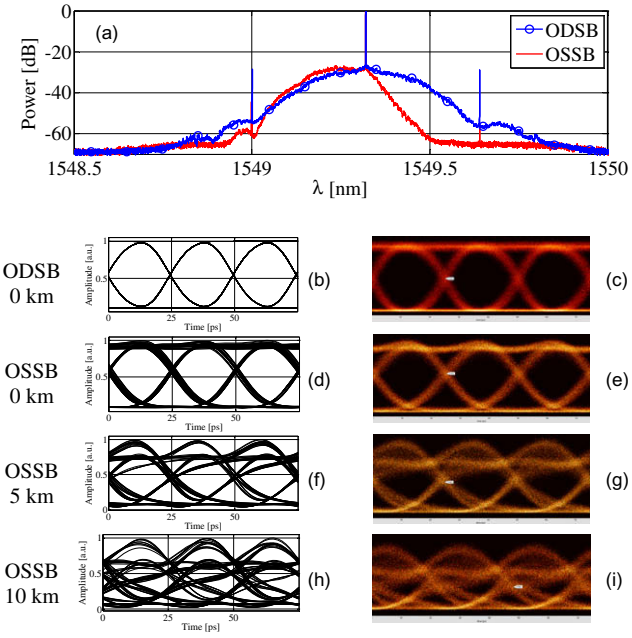

Fig. 5. (a) Optical spectra of the ODSB and OSSB signals. (b–i) Simulated (left) and experimental (right) eye diagrams for different lengths of SSMF.

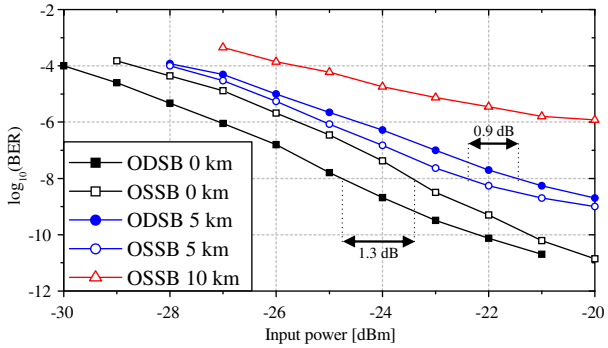

Fig. 6. BER results of the ODSB and OSSB signals.

was quantitatively compared with the ODSB signal through bit error rate (BER) measurements. An optically pre-amplified RX was considered. Fig. 6 shows that BER results present the same tendencies as simulation results, found in Fig. 4. Back-to-back results show that detuned filtering induces a power penalty of 1.3 dB, considering a BER of 10^{-8}. When 5 km of SSMF is employed, the OSSB signal outperforms the ODSB signal by 0.9 dB. Although on simulations the ODSB signal is outperformed only after 6 km of SSMF, such a length difference is acceptable due to residual chirp induced by electro-optic modulation. For 10 km of SSMF the BER of the ODSB signal could not be measured due to severe signal degradation induced by CD. Nonetheless, for such a fiber length, the OSSB signal achieves a minimum BER of 10^{-6}.

5. Conclusions

The optimization of a detuned optical filter for ODSB to OSSB format conversion of a 40 Gb/s NRZ signal was presented and experimentally validated. The optimization parameters were the detuning, bandwidth and order of the filter's super-Gaussian response. The filter was implemented on a FBG, using a complex apodization profile. Such profile allows controlling the order of the

response while reducing the group delay variation at the edges of the amplitude response. The latter feature is essential in order to prevent additional signal distortion during detuned filtering. The control of the order has also proven to be important since this parameter can be used to provide advantageous spectral reshaping asides sideband suppression. The experimental OSSB signal presented a SSR of 28 dB. A power penalty of 1.3 dB in back-to-back was obtained relatively to the ODSB signal. A BER of 10^{-6} was achieved after using 10 km of SSMF. The presented optimization and implementation method offers better results in comparison to other techniques presented so far at 40 Gb/s, while having a simple implementation at a relative low cost. Moreover, its passive all-optical nature allows easily achieving bitrates beyond 40 Gb/s.

Acknowledgments

This work was supported by THRONE (PTDC/EEA-TEL/66840/2006) Fundação para a Ciência e Tecnologia (FCT) project, and ISIS and BONE Networks of Excellence, funded by the European Commission. Miguel V. Drummond was supported by the FCT SFRH/BD/40250/2007 scholarship.

References

[1] P.J. Winzer, R.J. Essiambre, Proceedings of the IEEE 94 (5) (2006) 952.
[2] D. Fonseca, A.V.T. Cartaxo, P. Monteiro, IEEE Journal of Selected Topics in Quantum Electronics 12 (4) (2006) 603.
[3] M. Sieben, J. Conradi, D.E. Dodds, Journal of Lightwave Technology 17 (10) (1999) 1742.
[4] D. Fonseca, A.V.T. Cartaxo, P. Monteiro, IEEE Photonics Technology Letters 18 (2) (2006) 415.
[5] K. Yonggyoo, K. Sangil, L. Inkyo, J. Jichai, IEEE Journal of Selected Topics in Quantum Electronics 10 (2) (2004) 371.
[6] T.G. Silveira, A.L.J. Teixeira, A.P.S. Ferreira, P.M.N.P. Monteiro, IEEE Photonics Technology Letters 18 (21) (2006) 2212.
[7] K. Schuh, B. Franz, B. Junginger, P. Klose, E. Lach, Serial 107 Gbit/s (2 × 53.5 Gbit/s NRZ-VSB-Polmux) transmission over 15 km SSMF with electronic dispersion compensation, in: 34th European Conference on Optical Communication, ECOC, 2008.
[8] M. Ibsen, M.K. Durkin, M.J. Cole, R.I. Laming, Electronics Letters 34 (1998) 800.
[9] D.F. Hewitt, Design and performance of optical vestigial sideband (VSB) filters in digital 40 Gbit/s systems, in: Conference on the Optical Internet/Australian Conference on Optical Fibre Technology, 2003: EA Books.

[J6] - Photonic Instantaneous Microwave Frequency Measurement System Based on Signal Remodulation

Miguel V. Drummond, Carlos A.F. Marques, Paulo. P. Monteiro and Rogério N. Nogueira

IEEE Photonics technology Letters, Vol. 22, No. 16, pp. 1226–1228, August 2010.

Photonic Instantaneous Microwave Frequency Measurement System Based on Signal Remodulation

Miguel V. Drummond, Carlos A. F. Marques, Paulo P. Monteiro, and Rogério N. Nogueira

***Abstract*—A novel photonic instantaneous microwave frequency measurement system based on signal remodulation is proposed and experimentally demonstrated. Modulation and remodulation are achieved using a single electroabsorption modulator operating bidirectionally. The RF power and frequency are derived from the RF tone powers of the modulated and remodulated signals, respectively. The incoherent operation principle of the proposed system enables a high resolution measurement with reduced ambiguity over a large frequency range.**

***Index Terms*—Instantaneous microwave frequency measurement, microwave photonics, remodulation.**

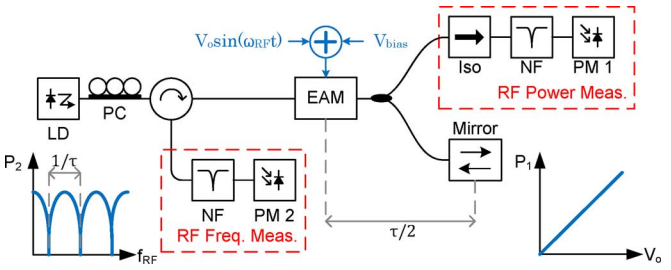

Fig. 1. Schematic of the IFM system based on signal remodulation. The bottom graphs show how the RF frequency and power can be derived from the average optical powers measured by PM 2 and PM 1, respectively.

I. Introduction

MODERN electronic warfare systems such as radar receivers rely on the analysis of incoming RF signals. Such analysis starts by providing a real-time identification of the frequency and power of incoming RF signals over a broad frequency range with high resolution. This task can be done by an instantaneous frequency measurement system (IFMS). Photonic implementations of IFMSs are particularly attractive since they benefit from many advantages inherent to microwave photonics, such as low losses, high bandwidth, light weight, and immunity to electromagnetic interference [1].

The first proposed photonic IFMSs were based on an optical channelizer [2] and a scanning receiver [3]. However, both systems cannot simultaneously provide real-time, broadband, and high-resolution operation. Recently, techniques which accomplish all these three features have been presented [4]–[9]. In [4], chromatic dispersion is used to obtain two complementary RF power fading curves as a function of the RF frequency. In [5] and [6], two complementary optical filters are employed to obtain RF frequency to average optical power conversion. The methods presented in [7]–[9] are based on mixing two copies of the optical signal delayed between them, and then measuring the average power of the resultant signal. These techniques have succeeded in achieving a measurement range up to 40 GHz with resolutions on the order of 100 MHz. However, it is difficult to obtain higher resolutions, even by reducing the measurement range. In [4], large values of chromatic dispersion and low-noise broadband photoreceivers would be required. The measurement resolution in [5] and [6] could only be increased using highly stable, narrow linewidth lasers. The techniques presented in [7]–[9] involve complex setups and have low sensitivity, as the measured average power has a dominant constant factor added to the RF frequency-dependent one.

In this letter, we propose and experimentally demonstrate a simple photonic IFMS with a resolution lower than 10 MHz over a measurement range of 12 GHz. Similar to [9], the operation principle relies on mixing the optical signal with a delayed copy. The mixing process is obtained by remodulating a delayed optical signal. Modulation and remodulation are simultaneously achieved resorting to a single electroabsorption modulator (EAM) operating bidirectionally. The RF power and frequency are derived from the RF tone power of the modulated and remodulated optical signals, respectively. The RF tone powers are measured by optical power meters (PMs), which is enabled by optical carrier suppression (OCS) performed by optical notch filtering. As a result, the use of low-noise broadband photoreceivers is avoided and a high measurement sensitivity is obtained.

II. Operation Principle

The schematic of the proposed IFMS is shown in Fig. 1. An optical carrier is modulated by the incoming RF signal resorting to an EAM. Assuming that the EAM provides a linear, chirp-free modulation, the power of the modulated signal is given by

$$P_{\mathrm{mod}}(t) = P_{\mathrm{in}} L_{\mathrm{mod}} |V_o \sin(\omega_{\mathrm{RF}} t) + V_{\mathrm{bias}}| \qquad (1)$$

where P_{in} is the average optical power of the laser diode (LD) source, L_{mod} is a loss factor which includes the insertion losses of the circulator and EAM, V_o is the RF amplitude voltage, ω_{RF} is the angular RF frequency, and V_{bias} the bias voltage. The RF power is measured at the upper output of the 3-dB coupler. An

Manuscript received April 23, 2010; revised May 19, 2010; accepted May 29, 2010. Date of publication June 10, 2010; date of current version July 23, 2010. This work was supported by the THRONE (PTDC/EEA-TEL/66840/2006) Fundação para a Ciência e Tecnologia (FCT) project. The work of M. V. Drummond was supported by FCT under the SFRH/BD/40250/2007 Scholarship.

The authors are with Instituto de Telecomunicações, Universidade de Aveiro, 3810-193 Aveiro, Portugal (e-mail: mvd@av.it.pt; cmarques@av.it.pt; paulo.1.monteiro@nsn.com; rnogueira@av.it.pt).

Color versions of one or more of the figures in this letter are available online at http://ieeexplore.ieee.org.

Digital Object Identifier 10.1109/LPT.2010.2052099

optical notch filter (NF) is used to perform OCS. In this way, the signal at the input of PM 1 is given by

$$P_1(t) = P_{\text{in}} L_1 |V_o \sin(\omega_{\text{RF}} t)| \tag{2}$$

where L_1 is a loss factor. The PM 1 yields the average optical power of its input optical signal

$$P_1 = P_{\text{in}} L_1 V_o \cdot \frac{2}{\pi}. \tag{3}$$

The lower output of the 3-dB coupler is connected to a mirror. Therefore, the modulated optical signal is reflected and remodulated. This operation can be regarded as mixing the modulated signal with a delayed copy, where such delay is proportional to the fiber length between the EAM and the mirror. Since bidirectional modulation is required, an EAM was used instead of a Mach–Zehnder modulator. The signal at the output of the circulator is given by

$$P_{\text{remod}}(t) = P_{\text{in}} L_{\text{remod}} |V_o \sin(\omega_{\text{RF}} t) + V_{\text{bias}}| \cdot |V_o \sin(\omega_{\text{RF}}(t-\tau)) + V_{\text{bias}}| \tag{4}$$

where L_{remod} is a loss factor and τ is the time delay between the modulated and remodulated signals. Equation (4) can be written as

$$P_{\text{remod}}(t) = P_{\text{in}} L_{\text{remod}} \left| V_{\text{bias}}^2 + \frac{1}{2} V_o^2 \cos(\omega\tau) + 2 V_o V_{\text{bias}} \cos\left(\frac{\omega\tau}{2}\right) \sin\left(\omega t - \frac{\omega\tau}{2}\right) - \frac{1}{2} V_o^2 \cos(2\omega t - \omega\tau) \right|. \tag{5}$$

The first term of (5) corresponds to the dc component. Since this term is dominated by V_{bias}^2, a frequency measurement based on it presents reduced sensitivity, as observed in [7]–[9]. The employment of OCS allows surpassing this problem, as the first term is annulled. Under small signal condition, $V_o \ll V_{\text{bias}}$, PM 2 yields

$$P_2 = P_{\text{in}} L_{\text{remod}} V_o V_{\text{bias}} \left| \cos\left(\frac{\omega\tau}{2}\right) \right| \cdot \frac{4}{\pi}. \tag{6}$$

The RF frequency can thus be measured with high sensitivity from (6), whereas the RF power is extracted from (3).

III. Experimental Results and Discussion

An experiment based on the schematic shown in Fig. 1 was performed. An external cavity laser with a linewidth lower than 100 KHz was used. A polarization controller (PC) was used to minimize the optical power reflected by the EAM facet. An EAM with a 40-GHz bandwidth was biased at −0.75 V, which enabled quasi-linear modulation and a reduced insertion loss of 13 dB. The RF signal and bias were added with a 20-GHz bandwidth bias tee. The NFs consisted on a 5-cm uniform fiber Bragg grating (FBG) operating in transmission, with a notch depth of 27 dB and attenuation higher than 3 dB over a bandwidth of 14 GHz. A time delay of $\tau = 47.375$ ns was induced by a patchcord length of 4.91 m between the EAM and mirror.

The IFMS was first tested for an RF frequency range of 20 MHz around a central frequency of 10 GHz, considering various RF input powers. The results are shown in Fig. 2. Fig. 2(a) and (b) shows that P_1 varies only with the RF power, whereas P_2 is dependent on both V_o and f_{RF}, as predicted in (3) and (6). Fig. 2(c) shows that P_1 increases linearly with V_o for RF powers higher than −8 dBm. For lower RF powers, P_1 is higher than expected due to limited OCS performed by the NF. Fig. 2(b) and (d) shows that $P_{2,\max} - P_{2,\min}$ and, therefore, the sensitivity of the RF frequency measurement are maxima for $V_o = 6$ dBm. The increase of $P_{2,\max}$ and P_1 with V_o are similar. However, $P_{2,\min}$ also increases with V_o, which is justified by the third term in (5). As such, the optimum measurement sensitivity results from a tradeoff between having high OCS and reduced optical power on the spectral components at $\pm 2 f_{\text{RF}}$.

RF frequencies from 1 to 25 GHz with a 1-MHz step were measured for RF powers of −6, 0, and 6 dBm. The results are shown in Fig. 3. It can be observed that P_1 is approximately

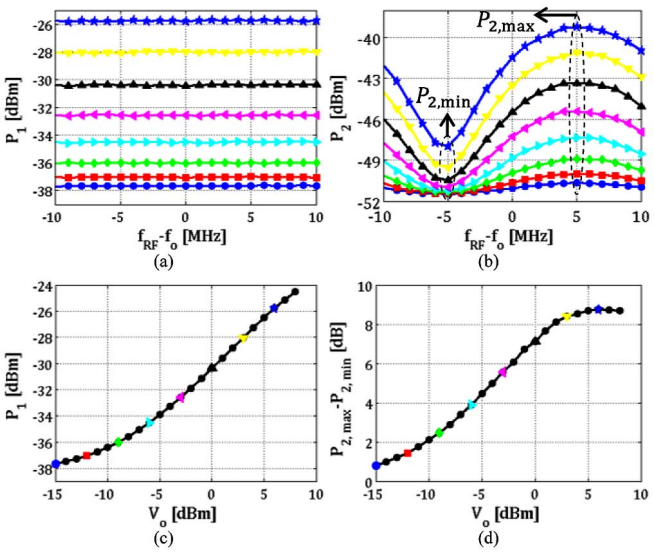

Fig. 2. (a) P_1 and (b) P_2 as function of the RF frequency, for various RF powers, indicated in (c) and (d). The central frequency is $f_o = 10$ GHz. (c) P_1 and (d) P_2 peak-to-peak amplitude as function of V_o.

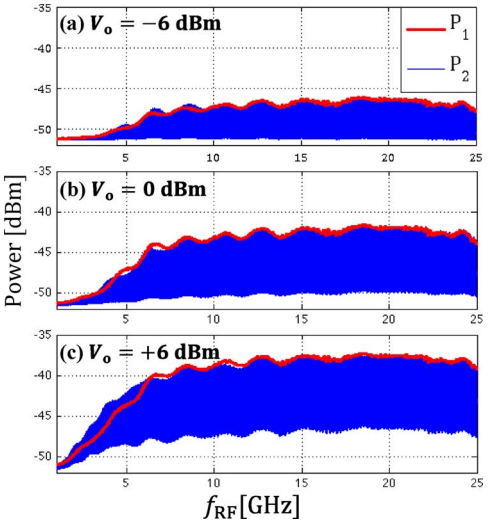

Fig. 3. Measured average optical powers. P_1 has an offset of −12.8 dB.

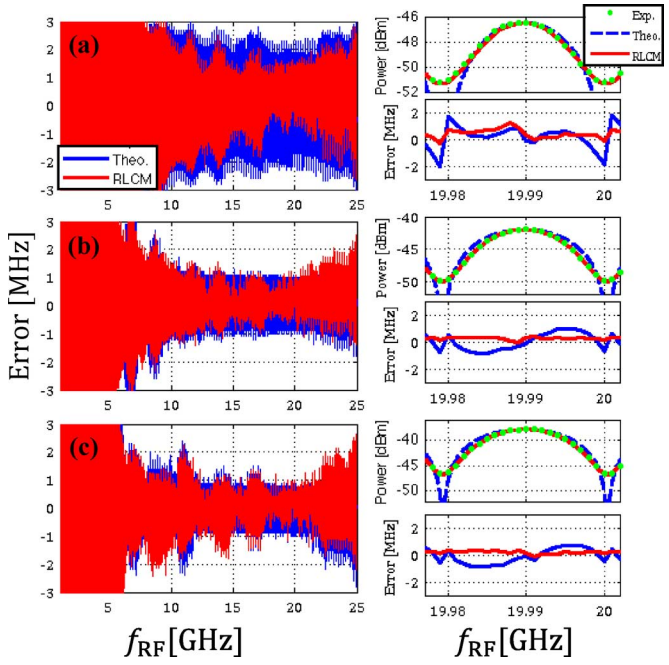

Fig. 4. Measured frequency error for an input RF power of (a) −6, (b) 0, and (c) 6 dBm. Upper right insets: measured, theoretical and RTCM powers at a frequency interval of 19.977–20.002 GHz.

constant for an RF frequency interval of 10–22 GHz. For lower frequencies, the FBG NF significantly attenuates the RF tones, whereas the bias tee limits the maximum input RF frequency to approximately 20 GHz. The oscillations observed on P_1 are the result of electrical imperfections, which cause a frequency-dependent attenuation of the RF power. As the RF power is measured through P_1, the frequency-dependent attenuation of the RF power is automatically taken into account. Such electrical imperfections are critical in [8] and [9] since long RF paths are employed.

The RF frequency was measured by comparing P_2 with the theoretical curve, given by the absolute value of the cosine term in (6). P_1 was used to provide the correct optical power offset to the theoretical curve. As the theoretical curve assumes infinite OCS and small signal operation, the RF frequency was also measured by comparing all lobes of P_2 with a reference lobe, located between the local minima at 15.040 and 15.061 GHz. Such a reference lobe comparison method (RLCM) is a much simpler approach than considering either a simultaneously small and large signal theoretical model, or obtaining a theoretical curve through simulation where the FBG NF and EAM specifications are taken into account. The results are shown in Fig. 4. The upper right insets show that the experimental results deviate from the theoretical cosine curve as the RF power increases. Such deviations and limited OCS result in systematic frequency errors, which are reduced when the RLCM is considered. The measured frequency errors are shown in Table I. Lower errors are obtained for the RLCM. The lowest peak-to-peak errors are achieved for $V_o = 0$ dBm. This was expected since for

TABLE I
FREQUENCY ERROR WITHIN 10–22 GHz

RF Power [dBm]	Peak-to-peak error [MHz]		Average absolute error [MHz]	
	Theo.	RLCM	Theo.	RLCM
−6	5.9	5.1	0.7	0.6
0	3.1	3.0	0.6	0.3
+6	4.7	4.1	0.6	0.2

$V_o = 6$ dBm P_1 and $P_{2,\max}$ do not match perfectly, as shown in Fig. 3(c). The reason for this is that modulation and remodulation under large signal operation cannot be assumed as purely linear. Under such conditions, P_1 and P_2 increase unequally with V_o.

IV. CONCLUSION

A novel IFMS based on optical signal remodulation was proposed and experimentally demonstrated. The RF power and frequency are obtained from the modulated and remodulated signals, respectively. The bidirectional operation of an EAM enables simultaneous modulation and remodulation with the advantages of having incoherent operation, requiring short RF paths and a single laser source. The RF frequency was measured with an ambiguity of only ∼10 MHz over a frequency range of 12 GHz. A peak-to-peak error of 3 MHz was obtained. The measurement range can be significantly increased by employing a narrower NF and a bias tee with higher bandwidth.

The conjugation of the proposed system with broad range, low-resolution photonic IFMSs opens the way for broad range, high-resolution photonic IFMSs.

REFERENCES

[1] A. J. Seeds and K. J. Williams, "Microwave photonics," *J. Lightw. Technol.*, vol. 24, no. 12, pp. 4628–4641, Dec. 2006.
[2] D. B. Hunter, L. G. Edvell, and M. A. Englund, "Wideband microwave photonic channelised receiver," in *Proc. Int. Topical Meeting Microwave Photonics Tech. Dig.*, Seoul, Korea, 2005, pp. 249–252.
[3] S. T. Winnall and A. C. Lindsay, "A Fabry-Perot scanning receiver for microwave signal processing," *IEEE Trans. Microw. Theory Tech.*, vol. 47, no. 7, pp. 1385–1390, Jul. 1999.
[4] M. Attygalle and D. B. Hunter, "Improved photonic technique for broadband radio-frequency measurement," *IEEE Photon. Technol. Lett.*, vol. 21, no. 4, pp. 206–208, Feb. 15, 2009.
[5] M. V. Drummond, P. Monteiro, and R. N. Nogueira, "Photonic RF instantaneous frequency measurement system by means of a polarization-domain interferometer," *Opt. Express*, vol. 17, no. 7, pp. 5433–5438, 2009.
[6] X. Zou, H. Chi, and J. Yao, "Microwave frequency measurement based on optical power monitoring using a complementary optical filter pair," *IEEE Trans. Microw. Theory Tech.*, vol. 57, no. 2, pp. 505–511, 2009.
[7] L. Bui, M. Pelusi, T. Vo, N. Sarkhosh, H. Emami, B. Eggleton, and A. Mitchell, "Instantaneous frequency measurement system using optical mixing in highly nonlinear fiber," *Opt. Express*, vol. 17, no. 25, pp. 22983–22991, 2009.
[8] H. Emami, N. Sarkhosh, L. Bui, and A. Mitchell, "Amplitude independent RF instantaneous frequency measurement system using photonic Hilbert transform," *Opt. Express*, vol. 16, no. 18, pp. 13707–13712, 2008.
[9] N. Sarkhosh, H. Emami, L. Bui, and A. Mitchell, "Reduced cost photonic instantaneous frequency measurement system," *IEEE Photon. Technol. Lett.*, vol. 20, no. 18, pp. 1521–1523, Sep. 15, 2008.

[J7] - Error-free wavelength conversion at 160 Gbit/s in PPLN waveguide at room temperature

Miguel V. Drummond, Jacklyn D. Reis, Rogério N. Nogueira, Paulo. P. Monteiro, António L.J. Teixeira, Satoshi Shinada, Naoya Wada and Hiromasa Ito

IEE Electronics Letters, Vol. 45, No. 22, pp. 1135–1137, October 2009.

Error-free wavelength conversion at 160 Gbit/s in PPLN waveguide at room temperature

M.V. Drummond, J.D. Reis, R.N. Nogueira, P.P. Monteiro, A.L. Teixeira, S. Shinada, N. Wada and H. Ito

Tunable wavelength conversion of a 160 Gbit/s signal by means of cascaded sum frequency generation/difference frequency generation was performed on a periodically-poled lithium niobate waveguide. Operation at room temperature (25°C) is demonstrated. A maximum power penalty of 2.1 dB for a bit error rate of 10^{-9} was achieved over a wavelength range of 29 nm.

Introduction: Ultrafast all-optical signal processing has attracted significant interest as a potential enabler to increase the per-channel bit rate of optical communication systems well beyond the bit rates imposed by electronic bandwidth limitations. Recently, considerable attention has been given to ultrafast nonlinear signal processing in compact waveguides [1, 2], mainly because such devices are suitable for integration. Nonlinear signal processing techniques such as optical time division signal multiplexing [3], demultiplexing [2], add/drop [2] and wavelength conversion [4] have been reported using periodically-poled lithium niobate (PPLN) waveguides at bit rates up to 320 Gbit/s. These applications all take advantage of the ultrafast response and high efficiency offered by compact PPLN waveguides.

In PPLN waveguides, tunable wavelength conversion is achieved through cascaded sum frequency generation/difference frequency generation (cSFG/DFG), enabled by the second-order nonlinearity of the material. The main limitation of PPLN waveguides is that SFG only occurs within a limited bandwidth, defined by the quasi-phase matching condition (QPM). There are two ways of increasing such bandwidth. The first is to trade maximum efficiency for bandwidth on the PPLN design. The second is to resort to pump depletion phenomena [2]. Although the latter approach has enabled operation at 320 Gbit/s, it presents additional complexity since it requires a clocked pump synchronised with the input signal. On the other hand, the problem of having a broad bandwidth and low efficiency is that high pump powers are required. Furthermore, in order to reduce photorefractive damage induced by high pump powers, operation temperatures higher than 150°C are usually required. This is a major drawback owing to the high power consumption needed to heat the device.

In this Letter we demonstrate wavelength conversion of a 160 Gbit/s signal by means of cSFG/DFG on a 45 mm-long PPLN waveguide at 25°C. The PPLN waveguide presents a broad bandwidth of about 5 nm in the C-band, and a low second harmonic generation (SHG) efficiency of 80%/W. Error-free operation was achieved with a maximum power penalty of 2.1 dB over a wavelength range of 29 nm, thus proving that photorefractive damage was effectively mitigated when using high pump powers.

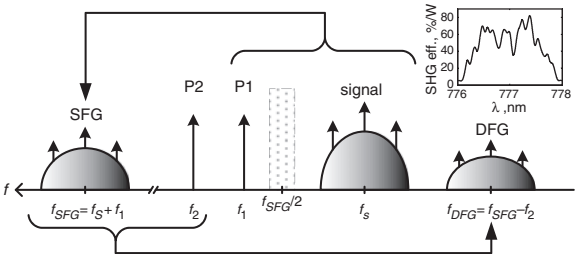

Fig. 1 *Operation principle of wavelength conversion via cSFG/DFG*
Inset: experimentally measured SHG efficiency

Operation principle: The operation principle of wavelength conversion via cSFG/DFG is depicted in Fig. 1. Two CW pumps, P1 and P2, and a modulated signal with wavelengths (frequencies) of λ_1, λ_2, λ_s (f_1, f_2, f_s) are set at the PPLN input. Since the nonlinear interactions of interest are SFG and DFG, the input signals should not individually obey the QPM condition in order to avoid SHG. The wavelength of P1 is adjusted so that SFG between P1 and the modulated signal falls within the QPM-imposed bandwidth. The inset shows that for the PPLN device used, the generated SFG signal should be centred at about 777 nm and should have a maximum spectral width of about 1.3 nm. At the C-band, this corresponds to a maximum input modulated signal bandwidth of about 5 nm. The SFG signal interacts with P2 by DFG, resulting in the converted signal. Wavelength tunability is achieved by changing λ_2. The power of the converted signal is approximately given by $P_{conv} \simeq 4P_sP_1P_2\eta_{SHG}^2$, where P_s, P_1 and P_2 are the powers of the input signal, P1 and P2, respectively, and η_{SHG} is the SHG efficiency, depicted in the inset of Fig. 1.

Experiment: The experimental setup is depicted in Fig. 2. A mode-locked laser diode (MLLD) provided an optical clock signal at 10 GHz with a central wavelength of 1547 nm and a full-width at half maximum (FWHM) of 2.2 ps. The clock signal was intensity modulated with a pseudorandom binary sequence (PRBS) using a Mach-Zehnder modulator. An optical time domain multiplexer (OTDM) was used to increase the bit rate from 10 to 160 Gbit/s. The modulated signal and two CW pumps were inputted to the PPLN. The wavelength of the signal and P1 were fixed at 1547 and 1560.92 nm, respectively. λ_2 was set at 1572.3, 1568.1 and 1543 nm in order to achieve a converted signal at 1536, 1540 and 1565 nm, respectively. As such, a wavelength range spanning 29 nm was tested. The average powers of the modulated signal, P1 and P2 at the input of the PPLN were 21.6, 27.8 and 30.3 dBm, respectively, totalling an input power of 32.6 dBm. Each channel of the 160 Gbit/s converted signal was demultiplexed through four wave mixing with control pulses on a HNLF. The 10 GHz control pulses were achieved by intensity modulating a wavelength tunable CW laser. Two cascaded EAMs were used with this end. Pulses with a FWHM of 4.5 ps were obtained. The demultiplexed channel was detected using an optically pre-amplified receiver.

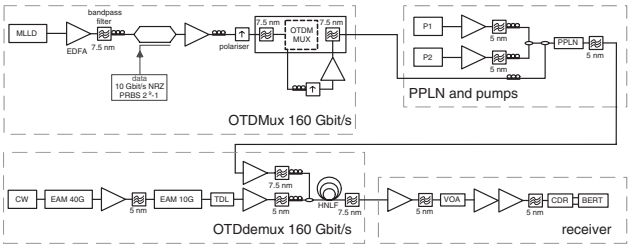

Fig. 2 *Experimental setup*
MLLD – mode-locked laser diode; EDFA – erbium-doped fibre amplifier; PRBS – pseudorandom binary sequence; OTDM – optical time domain multiplexing; EAM–electroabsorption modulator; TDL – tunable delay line; HNLF – highly nonlinear fibre; VOA – variable optical attenuator; CDR – clock and data recovery; BERT – bit error rate tester.

The 45 mm-long PPLN waveguide was fabricated using the proton-exchange technique on a 5 mol% MgO-doped lithium niobate wafer. Such MgO doping enabled a high photorefractive damage threshold, which in turn allowed operation of the device at room temperature with high input powers. The polarisation inversion period was chirped from 18.96 to 19.04 μm. The waveguide width was 11.5 μm. The PPLN waveguide presented an insertion loss of 3.3 dB, which included the losses of the input and output focussing lenses.

Results: The experimental results are shown in Fig. 3. The spectrum of the signals at the output of the PPLN (Fig. 3*a*) shows that a conversion efficiency of −25 dB was obtained. This value was expected considering the used pump powers and a SHG efficiency of about 50%/W was found to be in the centre of the QPM response (see inset of Fig. 1). The conversion efficiency was constant within the entire wavelength range. Fig. 3*b* and *c* show the spectrum of the input and converted signal. It can be seen that negligible spectral distortion was achieved and that wavelength conversion was correctly performed for all five tones of the signal. It should be noted that in contrast to [4], no spectral reshaping scheme was needed. Significant photorefractive damage would yield an efficiency lower than expected and further spectral distortion. Thus, no significant photorefractive damage was observed. The eye diagrams of the back-to-back and converted signals are shown in Fig. 3*d*–*g*. Aside from the addition of optical amplified spontaneous emission noise, negligible signal distortion is observed. This means that the QPM-bandwidth associated with SFG was broad enough in order to avoid narrow filtering effects on the converted signal. It should be noted that the signal-to-noise ratio of the converted signals depended on their

wavelength owing to the gain spectral response of the EDFAs. Moreover, the tested wavelength range was limited only by the gain spectral response of the EDFAs. Fig. 3*h* shows the average BER of the 16 demultiplexed channels of each 160 Gbit/s signal. Error-free operation was achieved for all channels of all of the converted signals. A maximum power penalty of 2.1 dB for a BER of 10^{-9} was obtained for the converted signals relatively to back-to-back, confirming that negligible distortion occurred during wavelength conversion.

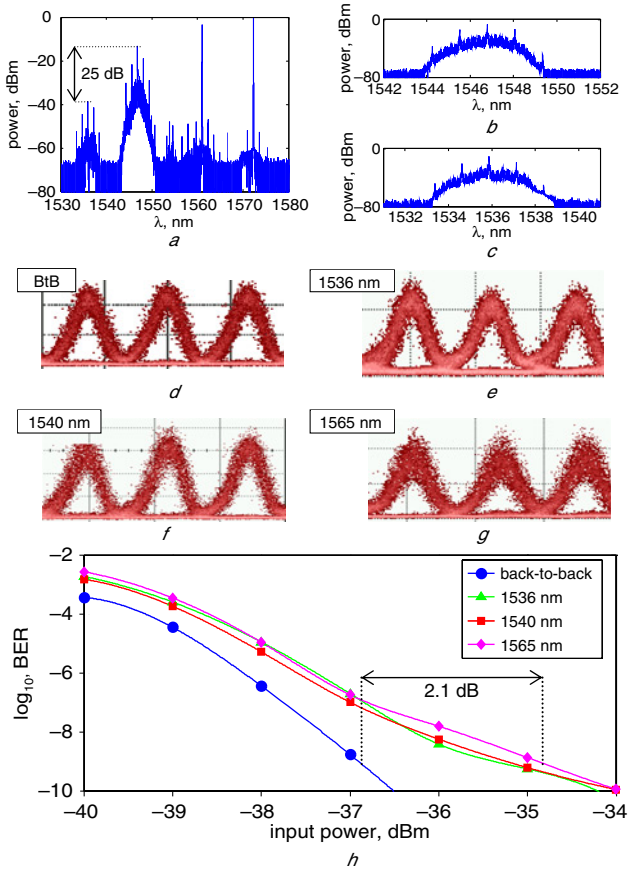

Fig. 3 *Experimental results*

a Spectra of signals at PPLN output
b, c spectra of input and converted signal at 1536 nm
d-g Eye diagrams of back-to-back (BtB), and converted signals (5 ps/div)
h Average BER of 16 channels of demultiplexed back-to-back and converted signals

Conclusion: Wavelength conversion of a 160 Gbit/s signal was performed at room temperature using a PPLN waveguide. A maximum power penalty of 2.1 dB for a BER of 10^{-9} was obtained within a wavelength range of 29 nm, proving that signal distortion was negligible. No photorefractive damage was observed. This experiment proves that PPLN waveguides with broad QPM bandwidth and low SHG efficiency can effectively operate at low temperatures with high pump powers, enabling wavelength efficient conversion at bit rates of 160 Gbit/s and beyond.

Acknowledgments: The authors acknowledge OPTOQUEST Co., Ltd. for experimental support. This work was partially supported by the European Commission through BONE and EUROFOS networks of excellence, and by Fundação para a Ciência e Tecnologia THRONE project (PTDC/EEA-TEL/66840/2006).

16 August 2009
doi: 10.1049/el.2009.2383

M.V. Drummond, J.D. Reis, R.N. Nogueira, P.P. Monteiro and A.L. Teixeira (*Instituto de Telecomunicações, Aveiro 3810-193, Portugal*)

E-mail: mvd@av.it.pt

S. Shinada and N. Wada (*National Institute of Information and Communications Technology, Tokyo 184-8795, Japan*)

H. Ito (*RIKEN, Sendai, 519-1399, Aramaki Aoba, Aoba-ku, Sendai 980-0845, Japan*)

A.L. Teixeira: Also with Nokia Siemens Networks Portugal S.A., IE WSM, 2720-093 Amadora, Portugal

R.N. Nogueira and P.P. Monteiro: Also with Nokia Siemens Networks Portugal S.A., RT TAF ON, 2720-093 Amadora, Portugal

H. Ito: Also with Research Institute of Electrical Communication (RIEC), Tohoku University, Sendai 980-8577, Japan

References

1 Galili, M., Xu, J., Mulvad, H.C., Oxenløwe, L.K., Clausen, A.T., Jeppesen, P., Luther-Davies, B., Madden, S., Rode, A., Choi, D.-Y., Pelusi, M., Luan, F., and Eggleton, B.J.: 'Breakthrough switching speed with an all-optical chalcogenide glass chip: 640 Gbit/s demultiplexing', *Opt. Express*, 2009, **17**, (4), pp. 2182–2187

2 Bogoni, A., Wu, X., Fazal, I., and Willner, A.E.: 'Photonic processing of 320 Gbits/s based on sum-/difference-frequency generation and pump depletion in a single PPLN waveguide', *Opt. Lett.*, 2009, **34**, (12), pp. 1825–1827

3 Ohara, T., Takara, H., Shake, I., Yamada, T., Ishii, M., Ogawa, I., Okamoto, M., and Kawanishi, S.: 'Highly stable 160-Gb/s OTDM technologies based on integrated MUX/DEMUX and drift-free PLL-type clock recovery', *IEEE J. Sel. Top. Quantum Electron.*, 2007, **13**, (1), pp. 40–48

4 Furukawa, H., Nirmalathas, A., Wada, N., Shinada, S., Tsuboya, H., and Miyazaki, T.: 'Tunable all-optical wavelength conversion of 160-Gb/s RZ optical signals by cascaded SFG-DFG generation in PPLN waveguide', *IEEE Photonics Technol. Lett.*, 2007, **19**, (6), pp. 384–386

[J8] - Flexible OTDM to WDM Conversion based on a Programmable Optical Processor

Miguel V. Drummond, António L.J. Teixeira, Paulo P. Monteiro and Rogério N. Nogueira

OSA Optics Express, submitted.

Flexible OTDM to WDM Converter enabled by a Programmable Optical Processor

Miguel V. Drummond,[1,*] António L.J. Teixeira,[1,2] Paulo P. Monteiro,[1,2] and Rogério N. Nogueira[1,2]

[1]*Instituto de Telecomunicações, Universidade de Aveiro, 3810-193 Aveiro, Portugal*
[2]*Nokia Siemens Networks Portugal S.A., 2720-093 Amadora, Portugal*
[*]*mvd@av.it.pt*

Abstract: We propose an OTDM to WDM converter which enables wavelength tunability, flexible OTDM tributary to WDM channel mapping and modulation format transparency. The converted signals are obtained by four-wave mixing (FWM) the input 160 Gb/s OTDM signal with a multi-wavelength sampling pulse train (SPT). The generation of the multi-wavelength SPT starts by multicasting an optical clock signal. The multicast pulses are then individually delayed and reshaped by a programmable optical processor (POP), resulting in flexible generation of the SPT. Error-free performance was achieved in different OTDM tributary to WDM channel mappings. In addition, intermediate rate conversion (2x80 Gb/s) was also achieved simply by reconfiguring the POP.

OCIS codes: (060.4510) Optical communications; (190.4380) Nonlinear optics, four-wave mixing.

References and links

1. M.S. Alfiad, M. Kuschnerov, S.L. Jansen, T. Wuth, D. van den Borne, H. de Waardt, "11x224-Gb/s POLMUX-RZ-16QAM Transmission Over 670 km of SSMF With 50-GHz Channel Spacing," *IEEE Photon. Technol. Lett.* **22**, 1150–1152 (2010).
2. H. Mulvad, M. Galili, L. Oxenløwe, H. Hu, A. Clausen, J. Jensen, C. Peucheret, P. Jeppesen, "Demonstration of 5.1 Tbit/s data capacity on a single-wavelength channel," *Opt. Exp.* **18**, 1438–1443, (2010).
3. L.K Oxenløwe, M. Galili, H.C. Mulvad, H. Hu, H. Ji, J. Xu, E. Palushani, J. Areal, A. Clausen, P. Jeppesen, "Ultra-high-speed optical signal processing of Tbaud data signals," in *Proc. ECOC'10*, paper Mo.1.A.1.
4. T. Hirooka, M. Okazaki, T. Hirano, P. Guan, M. Nakazawa, S. Nakamura, "All-Optical Demultiplexing of 640-Gb/s OTDM-DPSK Signal Using a Semiconductor SMZ Switch," *IEEE Photon. Technol. Lett.* **21**, 1574–1576, (2009).
5. H. Hu, H.C. Mulvad, M. Galili, E. Palushani, J. Xu, A.T. Clausen, L.K. Oxenløwe, P. Jeppesen, "Polarization-Insensitive 640 Gb/s Demultiplexing Based on Four Wave Mixing in a Polarization-Maintaining Fibre Loop," *J. Lightw. Technol.* **28**, 1789–1795, (2010).
6. T.D. Vo, H. Hu, M. Galili, E. Palushani, J. Xu, L.K. Oxenløewe, S.J. Madden, D.-Y. Choi, D. Bulla, M.D. Pelusi, J. Schroder, B. Luther-Davies, B.J. Eggleton, "Photonic chip based 1.28 Tbaud transmitter optimization and receiver OTDM demultiplexing," in *Proc. OFC'10,* Post-deadline paper PDPC5.
7. C. Brés, A. Wiberg, B. Kuo, J. Chavez-Boggio, C. Marki, N. Alic, S. Radic, "Optical Demultiplexing of 320 Gb/s to 8x40 Gb/s in Single Parametric Gate," *J. Lightw. Technol.,* **28**, 434–442, (2010).
8. A.H. Gnauck, R.M. Jopson, R.W. Tkach, C.J. McKinstrie, S. Radic, "Serial-to-Parallel Demultiplexing Using WDM Sampling Pulses," *IEEE Photon. Technol. Lett.* **21**, 97–99, (2009).
9. G. Lei, C. Shu, M. Fok, "All-Optical OTDM-to-WDM Signal Conversion Using Cross-Absorption Modulation With Time- and Wavelength-Interleaved Short Pulses," *IEEE Photon. Technol. Lett.* **22**, 571–573, (2010).
10. K. Lee, S. Liu, F. Parmigiani, M. Ibsen, P. Petropoulos, K. Gallo, D. Richardson, "OTDM to WDM format conversion based on quadratic cascading in a periodically poled lithium niobate waveguide," *Opt. Exp.* **18**, 10282–10288, (2010).
11. M.A.F Roelens, J.A. Bolger, D. Williams, S.J. Frisken, G.W. Baxter, A.M. Clarke, B.J. Eggleton, "Flexible and Reconfigurable Time-Domain Demultiplexing of Optical Signals at 160 Gb/s," *IEEE Photon. Technol. Lett.* **21**, 618–620, (2009).

12. N. Yan, J. Val del Puente, T.G. Silveira, A. Teixeira, A. Ferreira, E. Tangdiongga, P. Monteiro, A. Koonen, "Simulation and Experimental Characterization of SOA-MZI-Based Multiwavelength Conversion," *J. Lightw. Technol.* **27**, 117–127, (2009).
13. M. Roelens, S. Frisken, J. Bolger, D. Abakoumov, G. Baxter, S. Poole, B. Eggleton, "Dispersion Trimming in a Reconfigurable Wavelength Selective Switch," *J. Lightw. Technol.,* **26**, pp 73–78, (2008).

1. Introduction

A significant part of the research in high capacity optical networks has been driven towards 100Gb and 1Tb Ethernet standards. The required capacity increase of optical links has been relying in the increase of the spectral efficiency. This is true in both wavelength division multiplexing (WDM) [1] and optical time division multiplexing (OTDM) systems [2]. While more than 1 Tb/s has already been achieved in both systems, it is still uncertain how such systems can work together [3]. Nevertheless, the interface between both systems should certainly include multiplexing scheme conversion between OTDM and WDM [2-10].

OTDM single-tributary to WDM single-channel conversion has been implemented using different techniques [2-6]. Such techniques are based on different nonlinear subsystems such as nonlinear optical loop mirror [2], Mach-Zehnder interferometer semiconductor optical amplifier (MZI-SOA) [4], highly nonlinear fiber (HNLF) [5] and photonic chip [6]. OTDM multiple-tributary to WDM multichannel conversion can be achieved by parallelizing single-channel conversion techniques. However, parallel architectures present problems in synchronization and scalability [7]. As a result, alternative multichannel conversion techniques have been presented [7-10]. Even though such techniques rely on different operation principles, they have limitations concerning the wavelength tunability of the converted signals, OTDM tributary to WDM channel mapping, or modulation format transparency. The first two limitations are generally related with the generation of the sampling signals, whereas the latter depends on the used nonlinear process.

In this paper, we propose and experimentally assess an OTDM to WDM converter which addresses these limitations. The generation of the sampling pulses (SPs) is flexible both on time and wavelength domains thanks to the tunable frequency response of a POP. The SPs are mixed with the input OTDM signal by means of degenerate FWM in a HNLF, enabling modulation format transparent OTDM to WDM conversion.

2. Operation Principle

The operation principle of the OTDM to WDM converter is depicted in Fig. 1. Part of the input data signal is used to feed a clock recovery subsystem, which outputs a clean optical clock signal at the tributary rate. The optical clock signal is then multicast into *N* different wavelengths. *N* is the number of tributaries of the input OTDM signal, which are four in the illustration of Fig. 1. The resulting SPs are processed by a POP. Such device enables designing an arbitrary transfer function over a large frequency range within a given frequency resolution. The phase of the transfer function is adjusted to control the time delay imposed to each SP. In addition, the SPs can be reshaped through the adjustment of the POP's amplitude response. This is very useful in compensating signal distortions caused by the wavelength multicasting system. The optimization of the frequency response of a POP with the purpose of

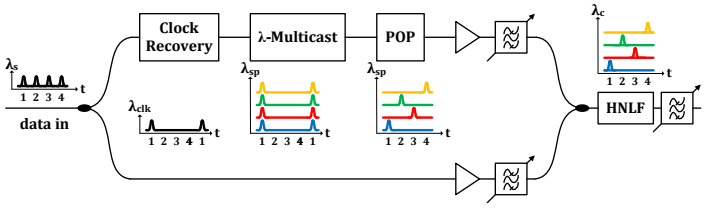

Fig. 1. Operation principle of the proposed OTDM to WDM converter.

producing SPs was already reported in [11]. However, only single-channel operation was investigated. After amplification and noise filtering the input data signal and SPs are launched in a HNLF. The *N* converted WDM signals are the product of FWM between the input data signal and SPs. The output tunable optical filter (TOF) filters the converted WDM signals.

3. Experiment

The experimental setup of the 160 Gb/s OTDM to WDM converter is shown in Fig. 2. As the converter was tested in back-to-back (BtB), a clock recovery system was not required. A mode locked fiber laser (MLFL) provided a 40 GHz optical clock signal centered at 1539 nm. The full width at half maximum of the clock pulses was of 1.5 ps. The optical clock signal was split in two copies. One was used to produce a 160 Gb/s intensity modulated (IM) OTDM signal, and the other was fed to a wavelength multicasting system.

The optical clock signal was multicast by a multi-wavelength conversion scheme employing a MZI-SOA [12]. The optical clock signal was converted to three CW signals spaced by 600 GHz. The fourth CW signal, centered at 1564.42 nm, was not considered for two reasons. First, since the maximum output power of the erbium doped fiber amplifier (EDFA) 2 was of only 50 mW, the addition of the fourth CW signal would significantly degrade the power budget related with the FWM process in the HNLF. Second, the idler resulting from FWM in the HNLF would have a wavelength of 1517.21 nm, which is out of the gain bandwidth of the used C-band EDFAs. The MZI-SOA had a low yet observable polarization sensitivity. The polarization of each CW signal was adjusted while the other lasers were turned off with the purpose of maximizing the gain provided by the MZI-SOA. Such procedure resulted in approximately co-polarized SPs. The shape and pulse width of the SPs were optimized through the adjustment of the tunable optical delay lines (TODLs), variable optical attenuators (VOAs) and also by the phase shifters integrated in the MZI-SOA.

As shown in Fig. 3 (a1), the POP was firstly programmed to produce three rectangularly shaped bandpass filters, each with a bandwidth of 400 GHz, centered at the three CW wavelengths. The phase responses of the programmed bandpass filters centered at λ_1, λ_2 and λ_3 were defined to achieve a constant group delay response of 12.50, 6.25 and 0 ps, respectively. The purpose was to obtain a SPT with wavelengths of λ_3, λ_2 and λ_1. The optical spectrum and waveforms of each SP and of the resulting SPT are shown in Fig. 3 (b1)-(f1). Each one of the SPs shown in Fig. 3 (c1), (d1) and (e1) were obtained by programming only one of the three bandpass filters. All SPs have a pulse width of 3.5 ps. Both the group delay response and the waveforms show that the pulses are properly delayed by steps of 6.25 ps. However, the amplitude response of the POP shows that the insertion losses are different for each SP. This is explained by the tradeoff between insertion loss and added time delay, which is inherent to the POP's operation principle [13]. Furthermore, the power of the SPs at the output of the MZI-SOA is not identical for the three wavelengths. The conjunction of these non-

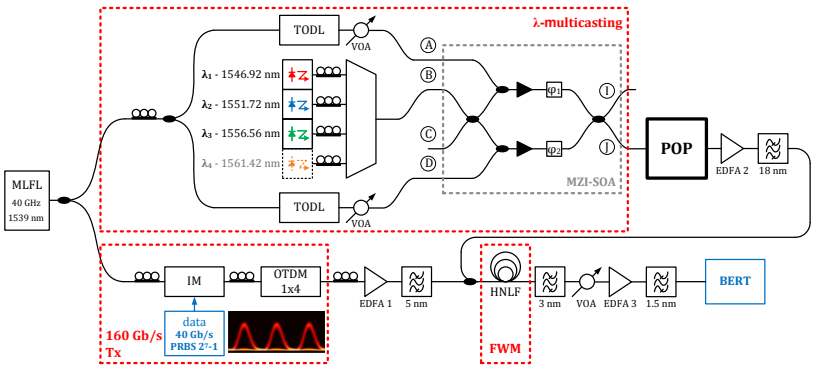

Fig. 2. Experimental setup. Inset: eye diagram of the 160 Gb/s input OTDM signal.

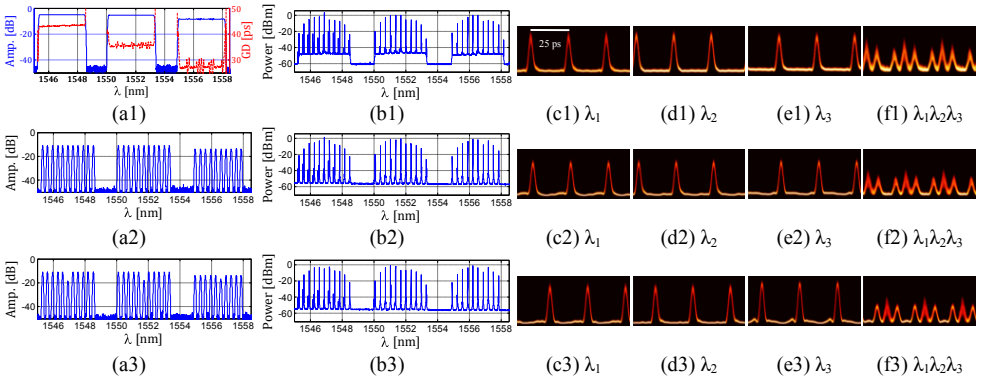

Fig. 3. (a) frequency responses of the POP measured by an optical network analyser, (b) optical spectra of the SPT, waveforms of the (c)-(e) SPs and (f) SPTs obtained for the POP configured to produce (1) rectangular bandpass filtering, (2) line-by-line filtering and (3) improved CR.

uniformities results in a SPT with unequalized amplitudes, as shown in Fig. 3 (f1). The employed multicasting scheme has very attractive features such as inherent gain and possibility of individually tuning the wavelength of the SPs. Furthermore, there are no patterning effects as the input optical signal is not modulated. On the other hand, the SOAs add amplified spontaneous emission (ASE) noise to the SPs, which results in noise floors observed in Fig. 3 (b1). In addition, the nonlinear response of the SOAs induces FWM between the high power input optical clock signal and SPs [12]. The FWM idlers can be observed in Fig. 3 (b1). The idlers have the highest power on the signal centered at λ_1, as it is the closest one to the input optical clock signal. As shown in Fig. 3 (f1), this results in a thicker pulse trace which can ultimately impair the OTDM to WDM conversion.

The impairments caused by the MZI-SOA on the SPs were mitigated by reconfiguring the POP. The insertion losses of the amplitude responses related with each SP were individually adjusted, thereby providing amplitude equalization of the SPT. The ASE noise floor and FWM idlers added by the SOAs were filtered out by setting the amplitude response of the programmed bandpass filters to maximum attenuation between the spectral lines of the SPs. The results are shown in Fig. 3 (a2)-(f2). The group delay response of the POP could not be measured due to the discontinuities introduced in the amplitude response. Nevertheless, Fig. 3 (f2) shows that the POP's time delay response is correct, and that the amplitude equalization has improved. The second SP at λ_2 falsely appears noisy and unequalized as the used large bandwidth optical sampling scope was able to capture the crosstalk between the pulse itself and the zero level of the neighboring pulses. The quality of the SPs has significantly improved, particularly at λ_1. Fig. 3 (b2) shows that the noise floor and a considerable number of FWM idlers were suppressed. The idlers close to the spectral lines of the SPs could not be suppressed due to the limited frequency resolution of the POP. The minimum achievable –3 dB bandwidth of the bandpass filters centered at each spectral line was of about 7.5 GHz.

The SPs shown in Fig. 3 (c1)-(e1) have a contrast ratio (CR) between 9.5 and 11 dB. The CR of the pulses shown in Fig. 3 (c2)-(e2) improved by 2 dB. It is important to have a high CR of the SPs, as it directly affects the extinction ratio (ER) of the converted WDM signals. The CR can be improved by again reconfiguring the amplitude response of the POP. The CR of an optical clock signal mainly depends on the power of the central spectral line. Therefore, the CR of the SPs was improved by adjusting the insertion loss of the bandpass filters located at λ_1, λ_2 and λ_3. The results are shown in the last row of Fig. 3. The CRs of the SPs at λ_1, λ_2 and λ_3 improved to 15.7, 16.8 and 18.6 dB, respectively. Such a high contrast ratio obtained at λ_3 resulted in amplitude ripple just before the pulse's rising edge. The shape of the SPs could be further improved by individually optimizing each spectral line.

The SPs and input OTDM signal were amplified, filtered and then coupled into a HNLF with a length of 150 m, a nonlinear coefficient of 10.5 $W^{-1}km^{-1}$, zero dispersion wavelength of 1550 nm and a dispersion slope of 5 $fs/nm^2/km$. The input powers of the SPs and OTDM signal were of 13 dBm and 21 dBm, respectively. OTDM to WDM conversion was obtained by degenerate FWM, which produces two sets of idlers. The set located at higher wavelengths enables modulation format transparent conversion, whereas the set located at lower wavelengths does not as the phase of each idler is twice the phase of the corresponding OTDM tributary. However, the idlers at higher wavelengths could not be considered as they lie outside the gain bandwidth of the available C-band EDFAs. Although the employed FWM scheme is polarization sensitive, it is possible to have polarization insensitive operation using the scheme proposed in [5]. The eye diagrams and optical spectra of the FWM idlers are shown in Fig. 4 (a2)-(a4) and Fig. 4 (e), respectively. A FWM conversion efficiency of –20 dB was obtained. Even though the idlers are undistorted, the adjacent OTDM tributaries were not completely suppressed. This was mainly caused by the significant power of the zero level right before and after the SPs. The idlers were also impaired by the reduced roll-off of the TOFs used after the HNLF, tight channel spacing and noise added by the high power EDFA 1. Nonetheless, high *Q*-factors of 16.5 dB were measured in all converted signals.

The phase response of the POP was readjusted to obtain a SPT with wavelengths of λ_1, λ_2 and λ_3. The amplitude of the SPs was again equalized due to the changes made in the phase response of the POP. The SPs and obtained FWM idlers are shown in Fig. 4 (b1)-(b4). Properly delayed SPs and undistorted converted signals were obtained. SPTs with wavelengths of λ_3, λ_2 and λ_1 or λ_1, λ_2 and λ_3 could be obtained simply by using a purely dispersive medium at the output of the MZI-SOA with a negative or positive dispersion sign, respectively. However, a purely dispersive medium cannot produce a SPT with an arbitrary arrangement of wavelengths, such as λ_2, λ_1 and λ_3. The phase response of the POP was adjusted to achieve such SPT. The results shown in Fig. 4 (c1)-(c4) demonstrate that the configured phase response did not degrade the SPs. As a result, undistorted converted signals were obtained. This demonstrates that the POP can produce a SPT with an arbitrary arrangement of wavelengths. The proposed OTDM to WDM converter can also be used to multicast one OTDM tributary to different wavelengths. This requires that all SPs are overlapped in time. The phase response of the POP was adjusted to add identical time delays to all SPs, yielding overlapped SPs as shown in Fig. 4 (d1). The measured *Q*-factors of the

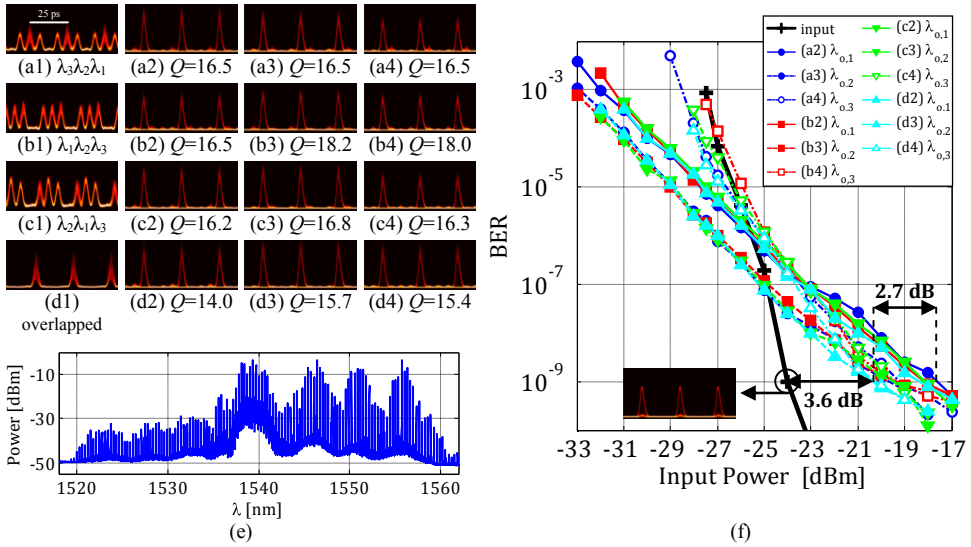

Fig. 4. (a)-(d) SPTs and corresponding 40 Gb/s converted WDM signals located at (2) $\lambda_{o,1}$=1532.7 nm, (3) $\lambda_{o,2}$=1528.2 nm and (4) $\lambda_{o,3}$=1523.1 nm. The *Q*-factors are in dB. (e) Spectrum at the HNLF output. (f) BERs of the input and

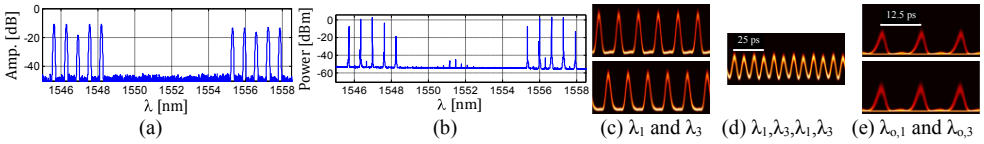

(a) (b) (c) λ_1 and λ_3 (d) λ_1,λ_3,λ_1,λ_3 (e) $\lambda_{o,1}$ and $\lambda_{o,3}$

Fig. 5. Results obtained for intermediate rate (80 Gb/s) conversion. (a) frequency response of the POP, (b) optical spectra and (c)-(d) waveforms of the SPs and SPTs. (e) converted optical signals at $\lambda_{o,1}$ (up) and $\lambda_{o,3}$ (down).

converted signals are significantly lower in comparison with the previous cases. The reason is that the crosstalk produced by the adjacent WDM channels now overlaps in time with the pulses of the converted WDM signal, resulting in a thicker pulse trace.

The bit error rates (BERs) of the converted optical signals at 40 Gb/s as function of the average power at the input of EDFA 3 are plotted in Fig. 4 (f). Error-free operation (BER< 10^{-9}) was achieved in all signals. The power penalty of the converted signals relatively to BtB varies from 3.6 dB to 6.3 dB. The performance of the converted signals does not vary significantly among the different configurations. The highest power penalties are obtained for $\lambda_{o,1}$ since it is the converted signal closest to the high-power input OTDM signal. The power penalties obtained for $\lambda_{o,2}$ and $\lambda_{o,3}$ are identical. The converted signal at $\lambda_{o,2}$ has two adjacent converted signals, whereas the converted signal at $\lambda_{o,3}$ has only one. However, the central wavelength of the latter signal is located at the lower limit of the gain bandwidth of the used EDFAs. Even though low *Q*-factors were measured in Fig. 4 (d1)-(d4), the corresponding BERs do not reveal a performance penalty. This can be explained by the bandwidth of 30 GHz of the photoreceiver used in the BER measurements. Such a low bandwidth resulted in the mitigation of the interchannel crosstalk previously captured by the optical sampling scope.

The repetition rate of the SPs can be doubled by suppressing half the spectral lines of each SP, leaving the remaining ones spaced by 80 GHz. The resulting SPs can be used to perform intermediate rate conversion, i.e., 160 Gb/s to 2x80 Gb/s WDM signals. The amplitude response of the POP was configured to achieve intermediate rate conversion, as shown in Fig. 5 (a). As only two WDM channels are required, the SPs centered at λ_2 were suppressed. Fig. 5 (b) shows that the suppression of half the spectral lines of the SPs also provided additional suppression of the FWM idlers induced by the SOAs. Properly delayed, undistorted SPs were obtained, as shown in Fig. 5 (c), (d). As a result, the converted optical signals presented an undistorted eye diagram with high *Q*-factors of 16.6 dB ($\lambda_{o,1}$) and 16.9 dB ($\lambda_{o,3}$).

4. Conclusion

We have proposed and experimentally assessed a 160 Gb/s OTDM to 4x40 Gb/s WDM converter based on FWM between the input optical signal and a multi-wavelength SPT. The SPs were obtained by multicasting a 40 GHz ultrashort pulse train into different wavelengths using a MZI-SOA. The multicast pulses were flexibly delayed and reshaped by a POP, which resulted in the suppression of ASE noise and FWM crosstalk, and also in the improvement of the CR. SPTs with different arrangement of wavelengths were produced, yielding undistorted converted WDM signals. All converted optical signals achieved error-free performance with a maximum power penalty of 6.3 dB relatively to BtB. Lower power penalties can be obtained by relaxing the channel spacing and by using TOFs with higher roll-off. The POP was also reconfigured to produce two 80 GHz time-interleaved SPs, enabling intermediate-rate conversion. Undistorted converted signals at 80 Gb/s with *Q*-factors higher than 16.5 dB were obtained.

Acknowledgements

This work was supported by the Fundação para a Ciência e Tecnologia project CONTACT (PTDC/EEA-TEL/114144/2009). The authors acknowledge Infractive and Finisar for loaning a Waveshaper 4000S.